The Relationship Between Structure and Core-Level Shifts in Thin Epitaxial Films of CaF_2 and SrF_2 on Si(111)

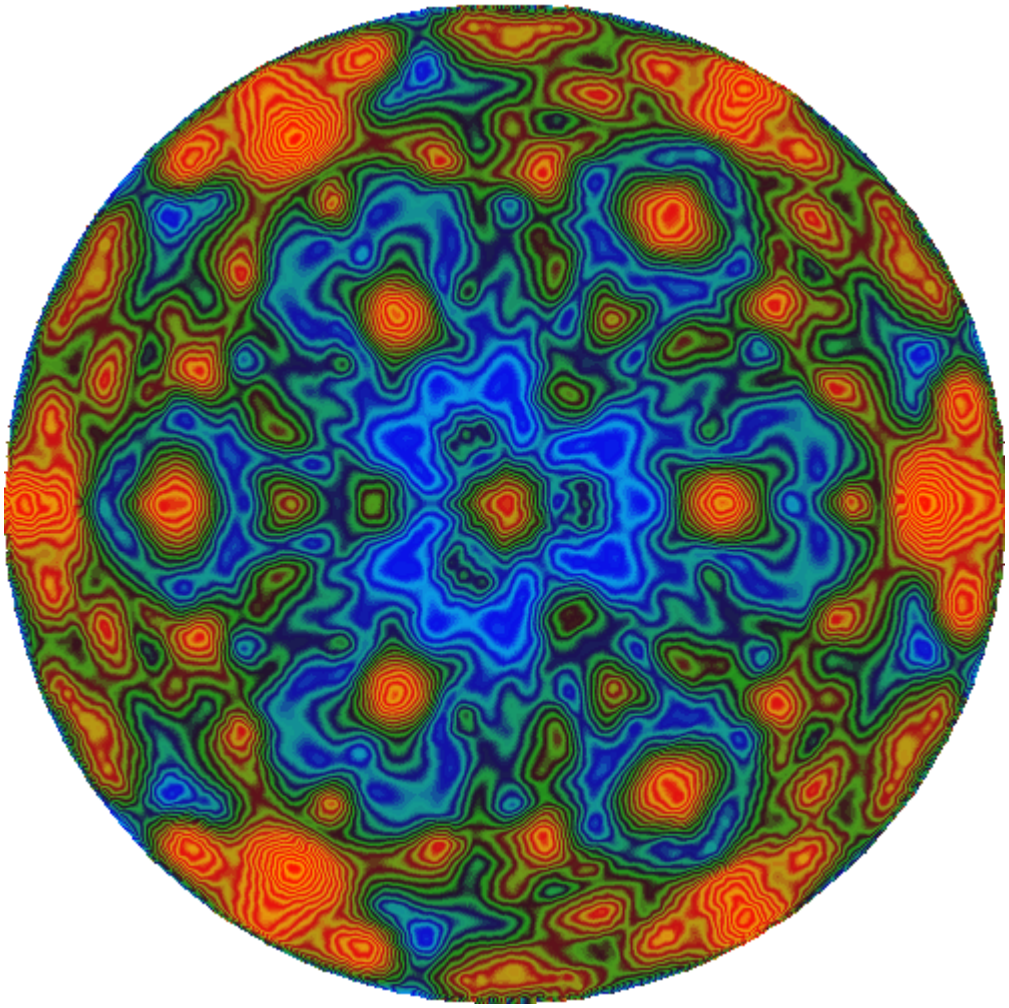

Eli Rotenberg

Department of Physics
University of California at Berkeley
1993

(Electronic Version Created April 1998)

Abstract

The Relationship Between Structure and Core-Level Shifts
in Thin Epitaxial Films of CaF_2 and SrF_2 on Si(111)

by

Eli Rotenberg

Doctor of Philosophy in Physics

University of California at Berkeley

Professor Marjorie A. Olmstead, Co-Chair
Professor Peter Y. Yu, Co-Chair

To lowest order, x-ray photoelectron spectroscopy (XPS) gives elemental composition of thin films and surfaces. To higher order, it provides chemical states and atomic structure; however, a theoretical model must be constructed to interpret these effects. In this thesis, we construct such a model for insulator surfaces and thin films. We have carried out experimental measurements of core-level shifts (CLSs) in thin films of CaF_2 and SrF_2 on the (111) surface of silicon, and have found good agreement between the theory and experiment. Our interpretation of these experiments improves upon published results of similar insulating compounds, because it does not require surface chemical changes to account for the measurements.

Theoretically, we conclude that initial- and final-state effects (Madelung potential and polarization-relaxation response, respectively) contribute equally to CLSs in ionic solids. The formalism for determining the final-state shift is shown to be accurate, since it reproduces experimentally observed shifts in rare-gas films where only final-state effects are important.

CLS measurements and sample characterization were facilitated by the x-ray photoelectron diffraction (XPD) technique. In turn, the XPS results were used to refine the XPD analysis to identify separately the atomic structure near interface, bulk and surface atoms.

This combination yielded the growth morphology of films as a function of growth rate and temperature. The dependence of growth morphology on the preparation conditions is shown to be dominated by kinetic processes, and a simple model (consistent with the theoretical Madelung shifts) is presented which accounts for some of the results.

Investigations were carried out for various film morphologies, and several conclusions are drawn. The simplest model for the CaF_2 and SrF_2 surfaces, which assumes no altered surface chemical states, is sufficient to explain the data. At the fluoride/substrate interface, chemical effects are of only minor importance to the observed ICLSs. In films which consist of CaF_2 islands atop a Si-Ca-F layer, we resolve the CLSs between the buried and exposed interface atoms; we interpret the results in terms of disorder in the interface layer which is removed upon being buried. For films which have been oxidized, new CLSs appear at the interface between the film and the oxide layer, which are associated with structural rearrangement of the CaF_2 surface atoms and/or chemical interactions with the overlayer. For CaF_2 films buried by a Si overlayer, preliminary measurements and interpretation are presented.

We also explored the origin of XPS satellite peaks observed for interface Ca and Sr atoms. The model most consistent with all of the data is a "molecular" model in which the satellites are intrinsic to the interface atoms and are due to excitations of the interface electronic states in the presence of the core hole.

The Relationship Between Structure and Core-Level Shifts
in Thin Epitaxial Films of CaF_2 and SrF_2 on Si(111)

by

Eli Rotenberg

B. S. (Cornell University) 1987
M. A. (University of California) 1989

A dissertation submitted in partial satisfaction of the
requirements for the degree of

Doctor of Philosophy

in

Physics

in the

GRADUATE DIVISION

of the

UNIVERSITY of CALIFORNIA at BERKELEY

Committee in charge:

Professor Marjorie A. Olmstead, Co-chair
Professor Peter Y. Yu, Co-Chair
Professor Steven G. Louie
Professor John D. Porter

The dissertation of Eli Rotenberg is approved:

Professor Marjorie A. Olmstead, Co-Chair	Date
Professor Peter Y. Yu, Co-Chair	Date
Professor Steven G. Louie	Date
Professor John D. Porter	Date

University of California at Berkeley

1993

Contents

Figures

Tables

Acknowledgements

I gratefully acknowledge the following for their contributions to this thesis:

(in alphabetical order)

Prof. Mark S. Cooper

For valuable assistance regarding choices, and for image analysis assistance.

Dr. Jonathan D. Denlinger

For helping develop many of the ideas in this thesis, for taking much of the data, for staying up 24 hours with me at the synchrotron, for drawing some figures in this thesis, for listening critically to my ideas, for simultaneously putting up with me and putting me up in his apartment in Seattle for 6 months, and for being my friend.

Dr. (to be) Susanna P. B. Gordon

For everything.

Dr. (to be) Uwe Hessinger, and Dr. (to be) Michael Leskovar

For assistance in data collection, and for many useful conversations. Also thanks to Mike for taking care of my cat Elvis while I gallavanted around the country.

Dr. Mark S. Hybertson

For suggesting the molecular model in Appendix B.

Prof. Steven G. Louie

For useful discussions regarding the CaF_2/Si(111) interface.

Prof. Marjorie A. Olmstead

Simply put, for teaching me how to do physics. Also, for being my advisor and friend, and for sticking by me through tough times.

Aharon Rotenberg and Varda Rotenberg (my parents)

For making it all possible.

Dr. (to be) Gerard C. L. Wong

For stimulating discussions, as well as for collecting the LBL XPS data and analysis of the TEM pictures referenced in §5.4.

Prof. Peter Yu

For kindly taking me into his group as my local advisor, while I did my research at Lawrence Berkeley Laboratory and at the University of Washington. For critically listening to my ideas and helping to prepare me for my qualifying exam.

The Relationship Between Structure and Core-Level Shifts
in Thin Epitaxial Films of CaF_2 and SrF_2 on Si(111)

by

Eli Rotenberg

Introduction 1

1.1 Motivation

This thesis explores the relationship between the atomic structure of a thin film and the electronic properties measured by core-level electron spectroscopy. Figure 1.01 illustrates the interplay between the physical systems examined (thin crystalline films, upper panels) and the experimental techniques employed (x-ray photoelectron spectroscopy (XPS) and x-ray photoelectron diffraction (XPD)). It also serves as a guide to the organization of this thesis.

XPS is one of the most powerful techniques currently available for studying thin films (~few atomic layers) and surfaces. To lowest order, it gives elemental composition with extremely high sensitivity. To higher order, it provides information about the different chemical states present in a system as well as the atomic structure of films; however, a theoretical model must be constructed to interpret these effects. In this thesis, we construct such a model for insulator surfaces and thin films; this model predicts the outcome of spectroscopic experiments. We have carried out an experimental investigation of thin films of CaF_2 and SrF_2 (ionic insulators) on the (111) surface of silicon, and have found good agreement between theory and experiment. Our interpretation of these experiments improves upon published results of similar insulating compounds, because it does not require surface chemical changes to account for the measurements.

The remainder of this section motivates the subject in more detail; the following sections give a literature review of the relevant topics. The final section of this chapter provides an overview and summary of the thesis.

1.1.1 XPS "Desiderata"

Epitaxy is the growth of crystalline (epitaxial) films upon a substrate. In the early stages of growth (the first 1-10 monolayers (MLs)) of any epitaxial system, the questions of

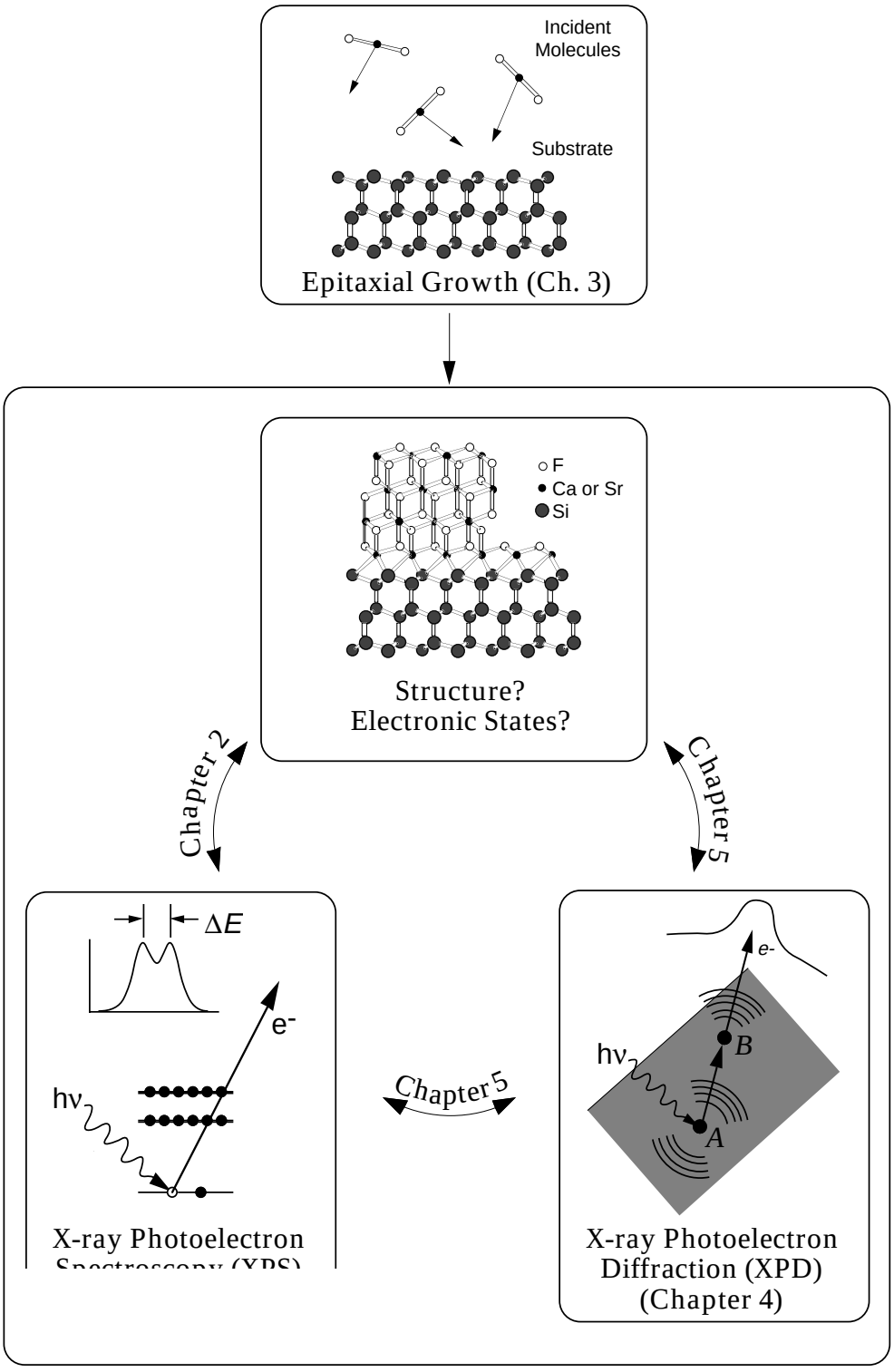

Figure 1.01. Thesis block diagram.

general interest are:

(i) What is the structure? This question asks not only about local atomic arrangements at the film's surface, interior, and interface with the substrate, but also about the larger-scale morphology of the films. How rough are the films? Are they perfectly two-dimensional, or are there variations in thickness, such as illustrated in Figure 1.01? Are the interfaces abrupt, or is there intermixing between layers? Under what conditions of crystal growth (temperature, growth rate, etc.) do the atomic structure and morphology change?

(ii) What are the electronic properties? This question asks how the solid is bonded together, and how this bonding varies at the surface, interface, and interior of the film.

Traditionally, XPS (lower left panel) is a powerful technique which has been used to answer these questions [Bri77, Car 78, Bri83, Ege87]. In this technique, incident x-ray photons excite a bound atomic core-level electron into the vacuum; the energy spectrum of these ejected electrons corresponds directly to the bound states in the atom. Splittings ΔE in core-level energies are observed which can be ascribed to electron emission from different atomic sites in the solid, e.g. surface and bulk atoms. These splittings are called core-level shifts (CLSs) and have been a subject of much study over the past ~20 years.

These splittings have traditionally been interpreted as chemical state differences between the different atoms in the film. This is because the electrostatic interaction between an atom's valence electrons and the deeper, core-level electrons changes as the valence population changes. Therefore, a theoretical link is needed to translate the answers that the XPS technique provides (the CLSs) into answers to the important questions ((i) and (ii) above). Theoretical estimates of this interaction have allowed the mapping of energy splittings to the different valence occupations, which in turn are used to describe the bonding in the solid.

This *chemical* or *intra-atomic* energy is not the only contribution to the observed XPS splittings ΔE. In addition, there are contributions which arise from *extra-atomic* factors

related to the geometric arrangement of atoms near the electron-emitting atom. In Chapter 2, we discuss two such extra-atomic interactions which are important for the insulating films considered in this study: electrostatic fields and the relaxation response, both of which are altered at surfaces and interfaces. Not only are these interactions as important as the altered intra-atomic interaction for determining the observed shifts, but for the films studied in this thesis, they are dominant.

1.1.2 Experimental considerations

The measurement of CLSs poses practical experimental problems. First, the shifts observed are quite small (compared to the linewidths) and are difficult to measure. The XPD technique [Ege90, Cha91] is used to help measure these shifts. A (very) simplified view of the XPD experiment is illustrated in the lower right panel of Figure 1.01. The electron wave isotropically emitted from atom *A* travels through the solid, encountering atom *B*. The electron scatters from *B*, which modifies the isotropic electron wavefront so that the intensity is peaked along the interatomic axis between *A* and *B* (this effect is called *forward focussing*). The XPD technique measures this emission profile; because different atoms have different arrangements of neighboring atoms, a method is suggested to aid the measurement of small CLSs. XPS spectra taken at special angles identified with the XPD technique can be used to selectively enhance spectral peaks from particular atoms; this makes the measurement of small shifts considerably easier. The XPS and XPD techniques are discussed individually in Chapter 4, while this useful link between them is discussed in Chapter 5.

The second problem with measuring CLSs is to correlate them independently with the atomic structure of the film. How is it certain that a given peak may be ascribed to a given atomic site? Furthermore, how can we be sure our films have a definite, simple morphology (i.e., uniformly thick)? We again use the XPD technique to answer these questions. In our films, large CLSs occur for the interface atoms, which can unambiguously be assigned using the electron attenuation through the film (Chapter 4). Each of these XPS peaks (interface

and bulk peaks) have separate XPD profiles, and the interpretation of these profiles will be used to characterize the film morphologies (flat *vs.* islanded). Moreover, once the smaller surface CLS is resolved using XPS/XPD as discussed above, the measured energy splitting is fed back into the XPD analysis to confirm the surface atom assignment. Thus, a complicated interplay between the XPS and XPD techniques is used to determine simultaneously both the CLSs and the atomic structure and morphology.

1.1.3 Why CaF_2 and SrF_2 on Si(111)?

The ultimate objective of this thesis is to understand the theoretical link between the atomic structure near an atom, and the kinetic energy distribution of electrons emitted from that atom. To that end, the combined XPS/XPD technique was developed to quantitatively measure the spectrum. The program employed in the study was first, to grow a film, second, to simultaneously determine its morphology, structure, and core-level energy shifts, and last, to compare these shifts to theoretical predictions. In order to isolate the extra-atomic effects, we concentrate on surface core-level shifts (SCLSs) because at a surface it is clear that the extra-atomic properties abruptly changes, while for an "ideal" surface the intra-atomic energies remain approximately constant. For such a surface, this provides a way to isolate the extra-atomic effects. Interface CLSs (ICLSs), on the other hand, may have additional intra-atomic contributions due to chemical bonds with the substrate whose effects are difficult to separate from the extra-atomic effects.

Insulators such as CaF_2 and SrF_2 are excellent prototypes for studying surface core-level shifts for two reasons. First, their surfaces have simple bulk termination. Second, in such ionic insulators, the charges are localized to the ions since the atoms are fully ionized to rare-gas configurations. This implies the outer electrons occupation should be fairly insensitive to the nearby arrangement of atoms. For these reasons, we expect the intra-atomic effects to be minimal at the CaF_2 or SrF_2 surfaces. Furthermore, their technological relevance has led to considerable effort in understanding their epitaxy on silicon (111) substrates, so that

clean, reproducible (111) surfaces may be readily prepared. In addition, we will see in Chapter 2 that the important contributions to SCLSs for these and other strongly ionic insulators are easily modeled; this is an additional consequence of the valence electrons being localized to individual atoms.

Semiconductors and metals, on the other hand, are difficult surfaces for measuring extra-atomic energies. Semiconductor surfaces are driven towards radical reconstructions by the large covalent character of the bonding. These reconstructions are normally accompanied by changes in surface chemical states, which we are trying to avoid. Metal surfaces, on the other hand, often do not reconstruct, but the observed SCLSs are very small [Cit83a-b, Nyh91], and the relative weight of initial- *vs.* final- state effects is still under dispute [Nyh91]. The situation is complicated by the fact that the conduction electrons are delocalized, so that surface density of states as well as electron spillover into the vacuum must be properly accounted for.

1.1.4 Implications for future work

For the films in this study, the main result is that chemical, or intra-atomic effects, are unimportant in the observed SCLSs. The importance of intra-atomic effects is secondary for ICLSs. This has broad implications for the general analysis of XPS data, which has traditionally ascribed *all* of the CLSs to chemical effects. It will also serve as a useful test of theories [e.g. Wat83] which predict surface chemical effects.

Some authors [Chi86, Bro88, Sto88, Liu89, Kow92, Hud93] considered the importance of final-state effect, but lacked a reliable method of estimating its magnitude. For ionic insulators, we know of no other work than this thesis which has combined the initial- and final-state effects to successfully explain ionic insulator SCLSs. We provide a useful approximation to the final-state shift in Chapter 2, which says that the polarization of a dielectric in response to a core hole may be given by a simple image charge (even if the core hole is within 1Å of the surface!). This will allow others to estimate the final-state effect without performing

the full calculation.

By understanding the relationship between structure and CLSs, we make XPS a more powerful tool for understanding complicated structures. For example, future work in the CaF_2/Si(111) system will address the growth of Si layers on top of the insulator for various preparation conditions (preliminary results will be presented in this thesis). New Ca and F CLSs are observed, which will be used to answer important questions: How abrupt is the new Si/CaF_2 interface? What is the morphology of the Si overlayer (flat *vs.* islanded *vs.* islands atop a flat layer), and how does it vary with different preparation techniques? Are there any interesting new electronic interface states at the new interface, and what are their origins? These questions will be examined in light of the techniques developed in this thesis.

1.2 Literature Review: Contributions to Core-Level Shifts

Egelhoff has reviewed the various contributions to CLSs in solids [Ege87]; another useful review is by Cardona and Ley [Car78b]. Surface and interface CLSs (SCLSs and ICLSs, respectively) arise from a number of sources. In addition to the broad division into chemical (intra-atomic) and structural (extra-atomic) effects, contributions to core-level shifts may also be divided into initial- and final-state effects. The initial-state energy is determined by the electrostatic potential acting on an electron before it is emitted from the solid, and thus is determined by the intra-atomic electron-electron interaction as well as the long-range electrostatic potential due to the extra-atomic arrangement of ions. The final-state energy is determined by the relaxation of both the intra-atomic electron orbitals as well as the neighboring (extra-atomic) electron orbitals in response to the sudden creation of a core hole at the source atom.

Figure 1.02 illustrates the division of contributions to CLSs into these categories. First, we compare the CLS between free ions and ions in bulk ionic solids. Fadley *et al.* [Fad68] and Citrin and Thomas [Cit72] considered the Madelung potential to be the principal initial-state contribution. This is just the potential of the alternating positive and

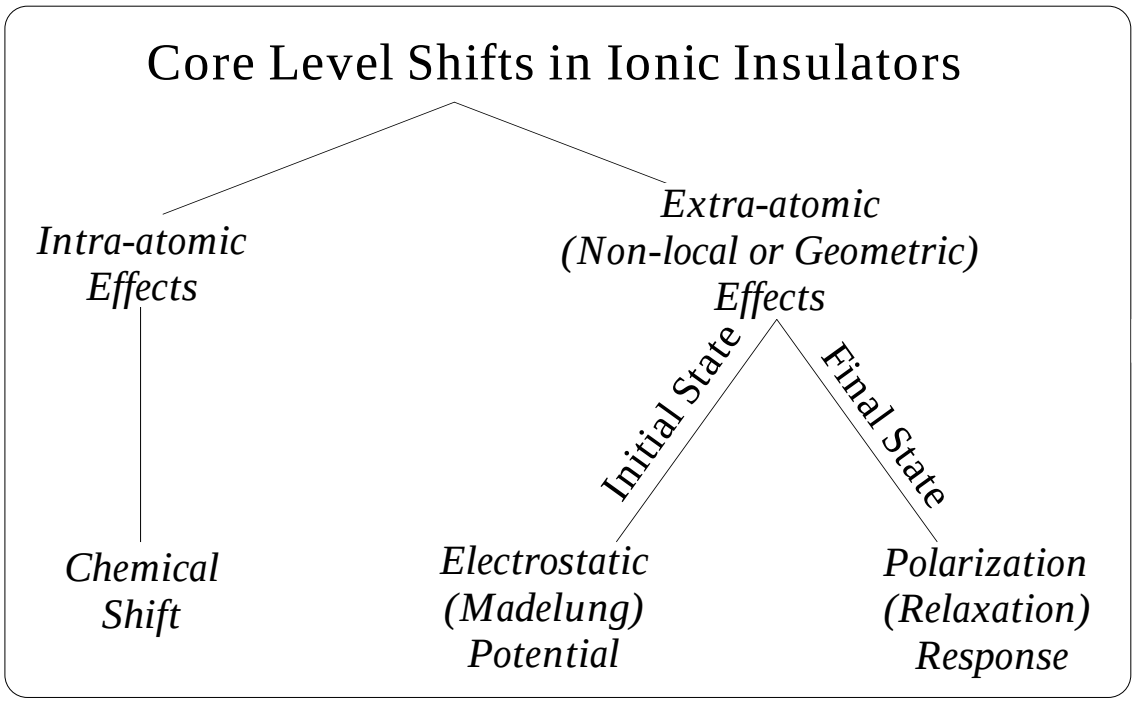

Figure 1.02. Summary of contributions to core-level shifts.

negative charges forming the ionic lattice, and determines most of the solid's cohesive energy. For the final state, they considered the polarization response of the solid to the sudden creation of the core hole. Using these terms, plus estimates of the electron affinities of the constituent atoms, they were able to account for the CLSs between free neutral atoms and the corresponding ions for a variety of chlorides and halides.

Various authors have considered the changes of these energies at a crystal surface as a way to account for experimentally observed SCLSs. Watson *et al.* [Wat81] considered the Madelung potential as the principle extra-atomic initial-state contribution to CLSs for ionic solids. They suggested that by calculating the change in Madelung potential at the surfaces, any difference between the calculation and the observed SCLSs could be attributed to intra-atomic effects. We are aware of several experimental studies in which SCLSs are interpreted in terms of the Madelung potential. Mönch [Mön86] and Hinkel *et al.* [Hin88, Wil88] modeled SCLSs at III-V (110) surfaces as due almost entirely to the altered Madelung

potential at the surface, where the surface ions have the same net charge as the bulk ions. This assignment was somewhat controversial, because tight-binding calculations [Pri87] predicted significant alterations of surface charges (0.2 to 0.3 e^-) and could also account for the observed SCLSs. More recent calculations support the chemical shift model [Rod90].

Another interesting system is the "co-adsorption" system (K, CO) on transition metal surfaces discussed by Schultz *et al.* [Sch89]. Upon adsorbing the two materials together, CLSs are observed relative to the adsorption of one or the other individual species. When co-adsorbed, the reaction $K + CO \rightarrow K^+ + CO^-$ was theoretically expected to occur, but this chemical shift alone could not account for the observed CLSs. Schultz *et al.* showed that if the contribution of the Madelung potential was accounted for at each atomic site, then the charge transfer could account for the rest of the CLSs.

The oxide surface $SrTiO_3(100)$ surface was studied by Courths *et al.* [Cou90]. From measured SCLSs corrected for Madelung shifts, they determined that considerable deviations between bulk and surface ionicities occur.

Some measurements of SCLSs in Ba compounds have been achieved. Quite recently, Hudson *et al.* [Hud93] used a similar argument to interpret SCLSs in $BaTiO_3(100)$ as was used for the $SrTiO_3$ experiment discussed above. Two independent measurements of Ba SCLSs at the $YBa_2Cu_3O_{7-x}(001)$ surface have been reported [Sto88, Liu89]. Liu *et al.*'s work attempted to interpret the observed shifts in terms of surface Madelung shifts although without success.

With regards to crystals with the fluorite (CaF_2) structure, little work on CLSs has been done. Kowalski [Kow92] observed CLSs in $Cd_{1-x}Pb_xF_2$ as x was varied. They found they could model their data using a combination of chemical shift plus Madelung shift.

All of these authors have considered the initial-state Madelung energy to be the main extra-atomic contribution to SCLSs. Some authors have considered the change in the final-state energy as a possible contribution [Sto88, Liu89, Kow92, Hud93], although none of

these have estimated its relative magnitude. But in one class of insulators, no charge transfer occurs anywhere (within the bulk or at the surface), so CLSs are determined solely by the final-state relaxation. These insulators are composed of rare-gas atoms crystallized on metallic substrates at low temperatures. After some debate in the literature [Jac82], it was demonstrated by Chiang *et al.* [Chi86] that the surface and interface core-level shifts in these insulating films could be accounted for completely by the altered screening properties in these environments as compared to the interior of the films, i.e. only the final-state effect is important. One of the important results of this thesis is the quantification of this effect. Recently, we applied the final-state model (Chapter 2) to these films, in which we accurately computed the screening changes using the local-field response to the creation of a core hole in the insulating film; our computed CLSs are in complete agreement with Chiang *et al.*'s measurements. [Rot92].

In ionic insulators, we predict (Chapter 2 and [Rot92]) that the altered relaxation energy at the surface is comparable to the Madelung energy. For the ionic insulators CaF_2 and SrF_2 on Si(111), we confirm this prediction experimentally. This suggests that interpretation of SCLSs in terms of only the chemical and Madelung shifts alone is incomplete, e.g. in the discussion of $SrTiO_3$ and $BaTiO_3$ mentioned above. The importance of the relaxation energy was also recognized by Browning *et al.* for SiO_2 films on Si [Bro88]. They were able to model ICLSs as due to the polarization response of the Si substrate, thus calling into question chemical effects as the sole cause of the observed CLSs. Their analysis is essentially similar to ours for CaF_2 on Si(111) (Chapter 6), except that their calculation was approximate and ignored any Madelung effects.

1.3 Literature Review: CaF_2 and SrF_2 films on Si(111)

As discussed above, thin films of CaF_2 and SrF_2 are probed experimentally. in this thesis This section reviews what is known about these materials from previous authors' works. The main parameters that are of concern in this thesis are the atomic structure of the

films, as well as the nature of the bonding. We are interested in these properties not only within the bulk materials, but also within the interface and surface layers. The other aspects of these films which are not specifically discussed here relate to the development of technological devices from these materials (such as device fabrication, electrical characteristics, etc.); these and other topics have been reviewed by Schowalter [Sch89] and Sinharoy [Sin90].

1.3.1 Atomic Structure.

SrF_2, CaF_2 and Si have similar face-centered-cubic structures; CaF_2 (SrF_2) has a lattice constant 0.6% (6.8%) larger than Si. Figure 1.03 illustrates our working model of the CaF_2 on Si(111) structure, for which most experimental studies in this thesis have been performed. The differences between SrF_2 and CaF_2 films will be pointed out in the following discussion.

The monolayer structure (Figure 1.03(a)) was found by ion scattering [Tro88], photoemission [Rie86, Olm87, Olm90], x-ray standing waves [Zeg90], and x-ray scattering [Luc93b] to consist of a reacted Si-M-F layer (where M=Sr or Ca). Evidently, some chemical reaction during formation of the monolayer is responsible for this structure; one possible mechanism is that the incident MF_2 molecules etch the substrate, while evolving SiF_x species and leaving behind the non-stoichiometric fluoride layer. Ca atoms have been found to rest in the 4-fold coordinated (*T*4) site [Tro88], although some evidence has been cited for partial occupation of the 3-fold hollow (*H*3) site for both CaF_2 and SrF_2 [Zeg90, Den91].

Thicker films (Figure 1.03(b)) consist of F-M-F triple layers (TLs) arranged above the initial reacted layer [Bat88, Luc93]. The CaF_2 overlayers are rotated 180° about [111] relative to the substrate (so-called type-*B* epitaxy) [Asa83] although for some growth conditions, this rotation is found not to occur (type-*A* epitaxy) [Cho91, Hon93]. SrF_2 and mixed alloy $Ca_xSr_{1-x}F_2$ films on Si or Ge show a wide variety of orientations (*A*, *B*, and mixed *A*/*B*) depending on growth conditions and lattice mismatches [Asa83, Asa83b, Tsu85, Den93, see also Chapter 4]. Our previous results [Den93, Den93(b, c)] using XPD indicate the first TLs

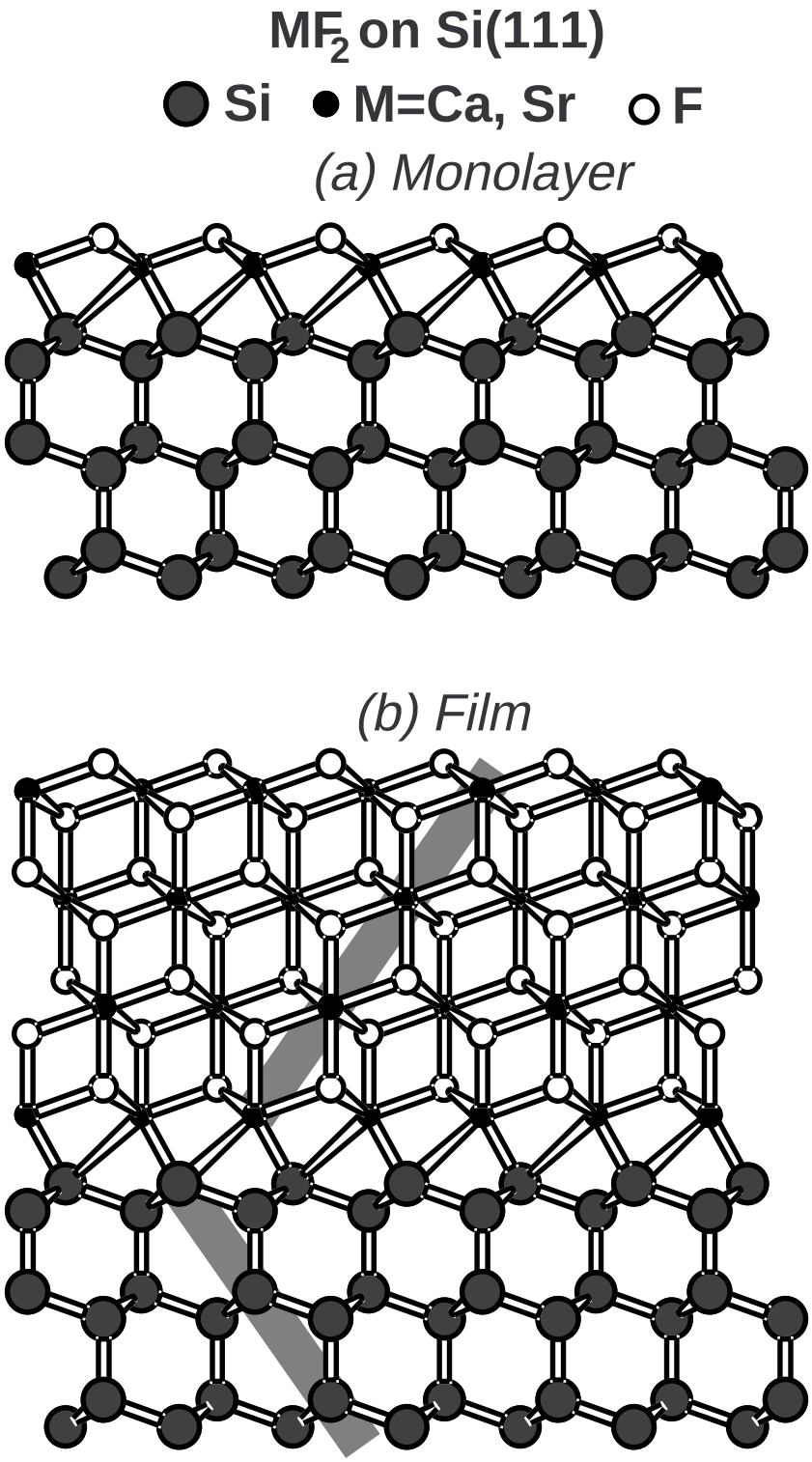

Figure 1.03. Ball-and-stick model of (a) monolayer and (b) thicker film of MF_2 on Si(111), where M=Ca or Sr. In (b), the Type-*B* overlayer orientation is indicated by the grey lines.

stack on top of the interface in the simple fashion shown in Figure 1.03; however, for CaF_2, Lucas *et al.* recently presented evidence for a second non-stoichiometric F-Ca layer between the interface and the bulk-like layers for films measured ex-situ after capping with amorphous silicon [Luc93]. The development of the interface structure they saw might be associated with contamination or some other alteration after removal of the samples from the growth chamber.

The surface structures of CaF_2 and SrF_2 have also been examined. Scanning probe microscopies have been applied to the surfaces of cleaved SrF_2(111) single crystals [Die92] and CaF_2 on Si(111) [Avo89]. In the CaF_2 experiment, scanning tunnelling microscopy (STM) showed unoccupied conduction band states at ~3.5 V positive bias, which corresponds closely to the conduction band offset of CaF_2 on Si(111) inferred by photoemission. These studies, combined with direct structural information obtained with surface component-resolved XPD in this work (Chapter 5 and [Den93c]) strongly support the notion that the surfaces of these insulators are bulk-terminated, with no structural reconstructions or unusual electronic states.

1.3.2 Film Morphology

Growth Kinetics. In the initial formation of the reacted Si-Ca-F layer, the overlayer atoms were found clustered at the substrate step edges [Avo89]. For most of the growth conditions in this study, it has been shown with photoemission that this layer is complete before nucleation of additional TLs begins [Rie86, Olm87, Olm90]. The growth morphology of subsequent layers of CaF_2/Si(111) depends strongly on the kinetic parameters of substrate temperature and incident flux [Den93b, Won93]. For the conditions used in this study, we have shown using x-ray photoelectron diffraction (XPD) that the initial growth mode is Stranski-Krastanov, in which the substrate is uniformly covered by a single F-Ca-Si interface layer, on top of which grow 2 TL high, bulk-like terraces which merge together to form a uniform film. This film becomes a template for subsequent layer-by-layer growth.

Because of this novel growth mode, the minimum thickness for a well-defined, two-dimensional geometry occurs when the 2 TL islands converge, a thickness which we refer to as 3 TL thick (even though the interface is missing one fluorine layer). If the growth rate is too slow, then nucleation of bulk islands occurs before the 2 TL completely merge, thus forming a very rough surface, with large regions of exposed Si-Ca-F layer.

Crystallinity. The optimal temperature for growth of thick CaF_2 films has been characterized using Rutherford backscattering [Ish81], where it was found that temperatures in excess of 600°C gave the most crystalline films. More recently, it has been understood that only the first few layers must be grown at this temperature; such a film forms a "template" for subsequent growth at room temperature. This template method has been characterized by x-ray standing wave fluorescence [Alv92, Zeg93], x-ray scattering [Luc92], and XPD (Chapter 5) to yield films of equal or superior quality to those grown at a uniform high temperature. The reason the films are superior is that for strained films (in which the film's lattice constant differs from the substrate's) defects associated with strain relief are created beyond the so-called critical thickness. Due to the mismatch of thermal expansion coefficients between CaF_2 and Si, the critical thickness for defect onset is lower at high temperature (~12 TLs [Luc92, Tro93]) than at RT (≥55 TLs [Won93]). Therefore, films grown with the template method may be grown thicker without formation of strain-relieving defects.

1.3.3 Electronic Properties

The bandgaps of Silicon and CaF_2 or SrF_2 are quite different (1.1 *vs.* ~12 eV). How does this property make a transition from the semiconductor to the insulator side of the interface? The valence band offset is ~8.3 eV for both CaF_2 and SrF_2 as measured by photoemission [Rie86, Olm87, Olm90] and by scanning tunnelling spectroscopy[Avo89].

Because of the absence of a F layer at the interface, the electron that would have been transferred to it from the interface Ca is available for formation of an interface state. Such a state has been seen both for CaF_2 and SrF_2 using photoemission [Mcl89, Olm90]. The

currently accepted model is that this state derives from a covalent bond between the interface Ca and Si atoms (see §1.3.4). The dispersion of this bonding state in CaF_2 has been measured with angle-resolved photoemission [Mcl89], and the optical bandgap of the state (between bonding and anti-bonding levels) has been found with sum frequency generation to be ~ 2.4 eV [Hei89]. The maximum energy of this interface state is just below the top of the Si valence band.

Another important property of the interface is the density of defect states. Although the interface state described above is insulating, with a 2.4 eV bandgap, the photoemission measurements have shown that the Fermi level is pinned just above the Silicon valence band after CaF_2 and SrF_2 growth. This pinning has been attributed to a high density of interface defects, such as extra F at the interface. Such an interface defect was imaged as depressions in the STM experiment [Avo89], although a detailed structure of these defects has not been proposed.

1.3.4 Theoretical Studies

CaF_2/Si(111) Interface. The interface structure shown in Figure 1.03 was by no means the only one suggested by early authors. Many of the theoretical studies were performed for a variety of competing models for the interface structure and compared to experimental results. Generally, all models with stoichiometric CaF_2 molecules at the interface are immediately ruled out because such interfaces (from an electron-counting argument) would be metallic in the absence of an interface reconstruction, whereas the observed interface state was not reconstructed and had a 2.4 eV bandgap.

Nath and Anderson [Nat88] showed with tight-binding calculations that type-*B* growth was energetically favored over type-*A* growth, although they exclusively considered Ca in the top site, directly interacting with Si dangling bonds. This bonding site was ruled out by the experimental measurements discussed above. Satpathy and Martin [Sat89] found the type-*B* interface favored over type-*A*, but they found that both *T*4 and top-site adsorption

were equally favored.

There have been three detailed studies of the interface state using the linear muffin-tin orbitals method within the atomic sphere approximation (LMTO-ASA). Fujitani and Asano [Fuj89] showed that the *T*4-bonded interface (Figure 1.03) had an interface state whose dispersion agreed with the experimental results. They concluded that the top-bonded interface was in better agreement with the observed Si ICLSs (see §4.1.2 and Figure 4.0.3), although this conclusion is questionable since final-state effects were not accounted for in their model.

Ossicini *et al.* [Oss91] found similar results for Si-Ca-F monolayer structures. Interestingly, to improve the agreement between calculated Si ICLSs with experiment, they explicitly included the initial-state Madelung potential at the Si lattice sites as a correction to the computed core-level binding energies. They were able to model the ICLSs better with their correction, although their analysis is questionable for three reasons: (i) The assignment of interface charge density, which is distributed over spheres in the LMTO-ASA approximation, to point charges is questionable. Furthermore, the charge density between spheres is unaccounted for. (ii) They neglected final-state effects in their analysis, which we show in this thesis can be a major contributor to CLSs. (iii) The Si ICLSs which they compare to [Rie86] have not proved repeatable in other experiments. While the Si-Ca feature seen in [Rie86] is also seen in our work (e.g. Figure 4.03 and , the Si-F feature they saw at 0.8 eV to higher binding energy than the bulk peak is not.

Salehpour and Satpathy independently studied CaF_2 on Si(111) using the same LMTO-ASA method as Ossicini, but for thicker coverages (interface layer + 3 TLs) [Sal91]. The main result is that for three possible bonding sites (*T*4, top-site, *H*3) the computed interface state band dispersion agrees with the experimental observation. Of further use is the information on the wave functions which they provide. They showed that the interface state has ~80% of its density concentrated on the Si side of the interface; this will be useful to us in

the discussion in Chapter 6.

Fluoride Surfaces. An important consideration in this thesis is the extent to which the surface atoms differ from the bulk. This question has two parts: (i) Is there a deviation from the simple bulk-termination? and (ii) Are there chemical differences between the surface and bulk atoms?

The first question was addressed for the fluorides by Tasker [Tas80]. Using a shell-model, he showed that there was a slight contraction of the distance between the outermost F and metal atoms for CaF_2, SrF_2, and BaF_2 (111) surfaces. These contractions were 0.5%, 1.4%, and 4.4%, respectively. For CaF_2 and SrF_2, these contractions are minor and will be neglected in this thesis. Tasker's calculation assumed full surface ionicity, and found the predicted surface energies to be in good agreement with experimental cleavage energies.

The second question has not been addressed theoretically to our knowledge for the fluorides (the calculations by Fujitani and Salehpour used a supercell method, so that there was no free CaF_2 surface). However, the general question has been examined by Watson *et al.* [Wat81]. They showed that the altered Madelung potential at the surfaces of ionic crystals can drive a small charge transfer from anions back to cations. Although they examined a wide variety of surfaces, they did not consider the fluorite structures, so that we do not know if their mechanism leads to charge transfer at CaF_2 or SrF_2(111). Such a charge transfer could have dramatic effects on our calculations; however, our results (Chapter 6) account for experimental CLSs without including such a charge transfer.

1.4 Thesis Overview and Summary

Chapter 2 discusses the link between observed CLSs and the atomic structure of insulators. The main conclusion drawn is that final-state effects are as important as initial-state effects in determining CLSs in ionic solids. The formalism for determining the final-state shift is shown to be accurate, since it reproduces experimentally observed shifts in rare-gas films where only final-state effects are important.

Chapter 3 discusses the apparatus used for growing and characterizing CaF_2 and SrF_2 films.

Chapter 4 discusses the XPS and XPD techniques, and details the many experimental considerations for measurements and quantitative analysis.

Chapter 5 shows how XPD was used to enhance the resolution in the XPS technique. This yields the SCLS measurements which are to be compared to experiment. In turn, the XPS results were used to refine the XPD analysis to identify separately the atomic structure near interface, bulk and surface atoms. Using this combination, we were able to determine the growth morphology of films as a function of growth rate and temperature, so that well-defined surfaces could be reliably prepared. The dependence of growth morphology on the preparation conditions is shown to be dominated by kinetic processes, and a simple model (consistent with the surface Madelung shifts) is presented which accounts for some of the results.

Chapter 6 presents and tabulates the SCLS results, and compares them to theoretical predictions. The investigations were carried out for various film morphologies, and the following conclusions are drawn:

(i) The simplest model for the CaF_2 and SrF_2 surfaces, which assumes no altered surface chemical states, is sufficient to explain the data. We are also able to show that not only is the sum of initial- and final-state energies predicted correctly, but that the individual terms are correct.

(ii) At the interfaces with the substrate, the chemical bond between Ca or Sr and Si is of only minor importance to the observed ICLSs. The polarization response of the substrate dominates the observed ICLSs, with chemical effects being of secondary importance. We interpret this result as a consequence of the charge density of the two-dimensional interface state, which is distributed mainly over the topmost Si layers and not in the insulator.

(iii) In CaF_2 films which consist of islands atop a Si-Ca-F layer, we resolve the CLSs

between the buried and exposed interface atoms; we interpret the results in terms of disorder in the interface layer which is removed upon being buried. This was corroborated by both XPS linewidth analysis and XPD results.

(iv) For films which have been oxidized, new CLSs appear at the interface between the film and the oxide layer. These shifts can only be accounted for by structural rearrangement of the CaF_2 surface atoms and/or chemical interactions with the overlayer.

(v) For CaF_2 films buried by a Si overlayer, preliminary measurements and interpretation are presented. The SCLSs are found to be altered after Si deposition. This system will be the subject of future publications [Hes94, Les94].

(vi) Comparing SrF_2 and CaF_2 SCLSs, we find that they have similar magnitude in spite of the greater polarizability of SrF_2. By modeling the SrF_2 SCLSs as a function of strain in the film, we show that this extra polarizability is compensated for by the effect of the strain field within the overlayer. Measurements of the SrF_2 lattice constant using *in situ* low energy electron diffraction confirms this picture.

Appendix A gives the detailed relationship between the lattice mismatch with the substrate, the elastic properties of cubic crystals and the strain field, and the observed strain fields.

Appendix B presents models for the origin of XPS satellite peaks observed for interface Ca and Sr atoms. The model most consistent with all of the data is a "molecular" model in which the satellites are intrinsic to the interface atoms and are due to excitations of the interface electronic states in the presence of the core hole.

Appendix C summarizes the CaF_2 and SrF_2 samples grown in this study.

Theory of Core Level Shifts 2

2.0 Introduction

In our photoemission measurements, monochromatized incident x-ray light induces transitions from bound electron states to the vacuum. For a typical solid, the experiment is outlined in Figure 2.01. An electron spectrometer is used to measure the energy distribution of the emitted electrons; a schematic of a typical spectrum is shown in Figure 2.01(c). Plotted in the spectrum is the electron yield as a function of the electron kinetic energy, where two main features are observed: (i) There are sharp peaks which generally correspond to bound states in the solid. Upon closer inspection, the sharp peaks are observed to be split into two or more components; the mechanisms behind the splitting are discussed in this chapter. (ii) There is a large secondary electron background which is the inelastic scattering spectrum. The discussion of this background and its implications for spectroscopy are discussed in Chapter 4.

There are two categories of peaks which contribute to the observed spectrum. The first (Figure 2.01(a)) corresponds to bound states in the solid; a direct correspondence between the observed kinetic energies and the binding energies of the states may be inferred because the incident radiation is monochromatic. States which are bound by more than ~15 eV are called *core levels*; since these electrons are strongly bound to atoms in the solid, their peaks yield information about the local environment within particular atoms. These core-level peaks are the main subject of study of this thesis. If states are bound by less than ~15 eV, they are derived from valence (and, for metals, conduction) band electrons. These states are broadened by band effects and hence give information about the long-range electronic properties of solids. These levels are not studied with the laboratory x-ray sources we employed because for our energies the cross-section for excitation of these peaks is low,

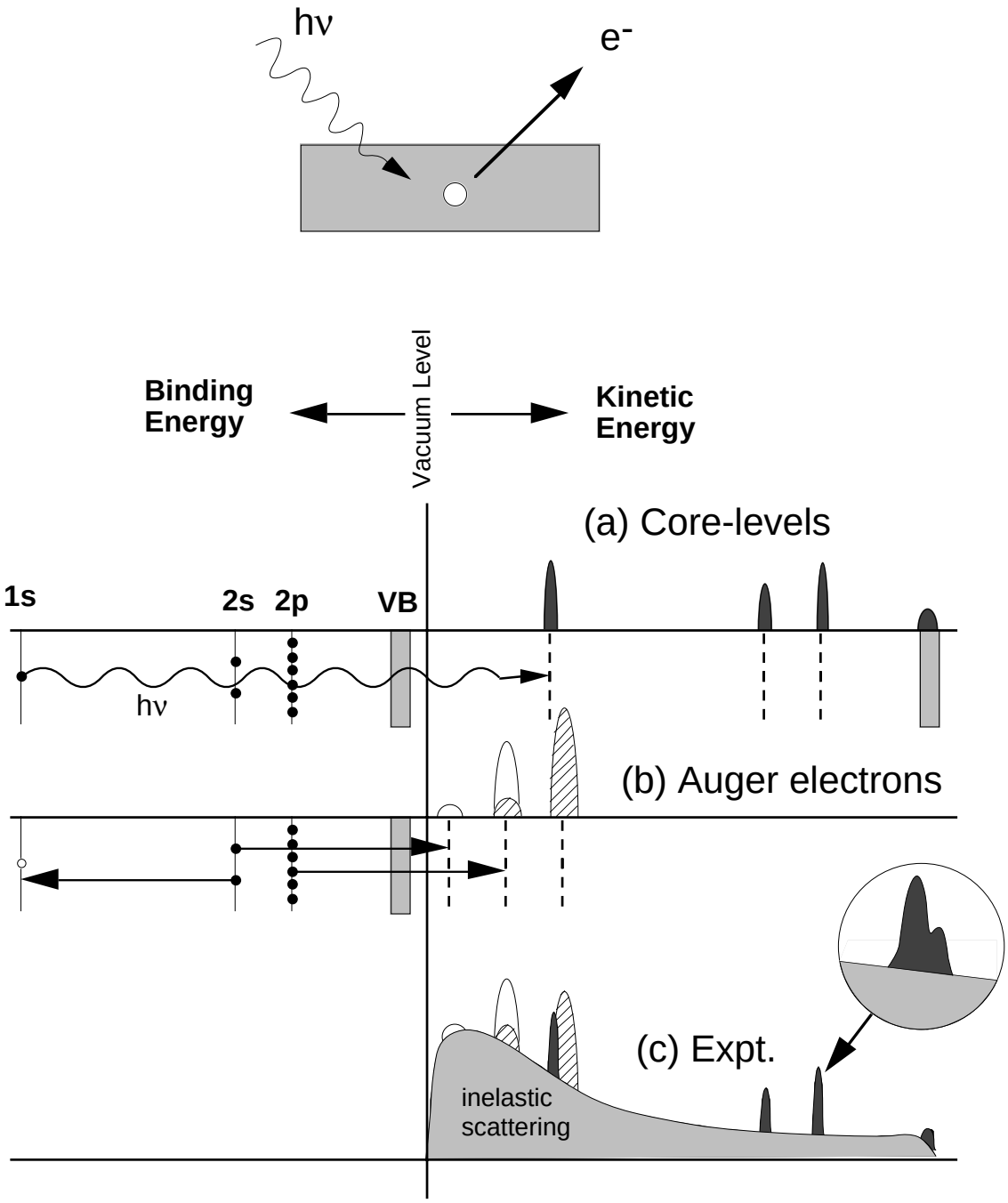

Figure 2.01. X-ray photoemission spectroscopy (XPS) schematic. (a) Core-level spectrum due to direct photoexcitation, (b) Auger-electron spectrum, due to decay of excited atoms, (c) Total spectrum, including inelastic background.

and because our x-ray source is not monochromatic enough to observe the small shifts associated with band effects.

The second category of peaks in the electron emission spectrum are not directly excited by the x-ray radiation, but instead are emitted as decay products of excited atoms. These electrons are called *Auger electrons* and a typical Auger decay event is illustrated in Figure 2.01(b). Prior to the decay, a photoemission event has created a core hole in the bound 1*s* state. A bound 2*s* electron has a transition into the core-hole; the energy liberated by the event raises another bound electron (either 2*s* or 2*p*) into the vacuum (unhatched peaks). A similar event ($2p \rightarrow 1s$ liberating 2*s* or 2*p*) leads to another pair of Auger electrons of higher kinetic energy (hatched peaks). The Auger electron spectrum is independent of the exciting photon energy.

A compact notation is commonly used to refer to Auger peaks [Bri83]. Generically, the event is called *ijk* when the electron *j* has a transition to core-hole *i* liberating electron *k*. In practice, the spectroscopic notation for principle quantum numbers (1, 2, 3…) → (K, L, M…) is used so that all the Auger electrons in the above example are labelled KLL (In the cases where a participating level is the valence band of the solid, the letter "V" is used, e.g. KLV or KVV). To distinguish angular momentum states, the following mapping is used: ($s_{1/2}$, $p_{1/2}$, $p_{3/2}$, $d_{1/2}$, $d_{3/2}$…) → (1, 2, 3, 4, 5…). The two unhatched Auger peaks in Figure 2.01(b) are uniquely identified as KL_1L_1 and $KL_1L_{2,3}$, while the hatched peaks are labelled $KL_{2,3}L_1$ and $KL_{2,3}L_{2,3}$. The $KL_{2,3}L_1$ and $KL_1L_{2,3}$ peaks are degenerate because they have identical initial and final states and hence the combination is referred to as $KL_1L_{2,3}$.

When a either a core-level or Auger peak is composed of several components, the energy difference between the components is called a *core level shift* (CLS), which is usually measured relative to the dominant component. CLSs arise in solids where the same element occurs in distinct chemical forms or lattice sites. For example, electrons bound to the two Cu sites in high-T_c superconductors have slightly different binding energies due to their different

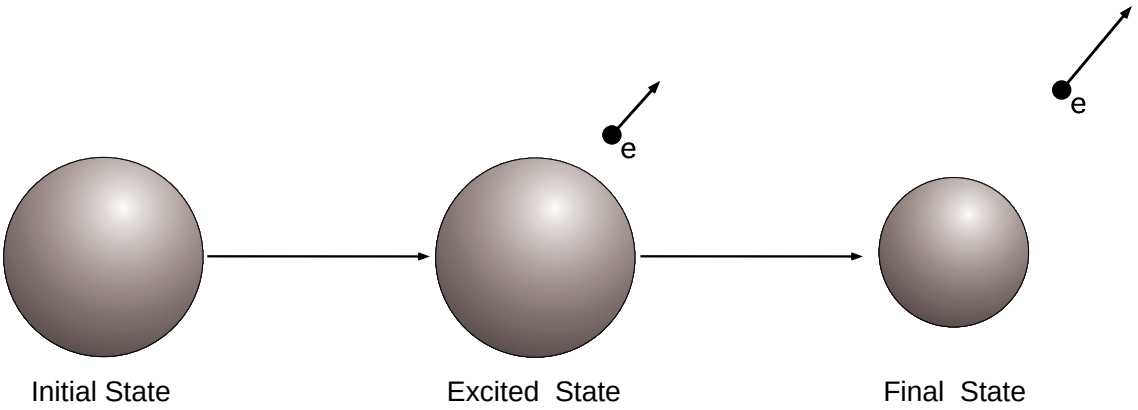

Figure 2.02. Initial/Final state picture of XPS for free atoms. In the first step, the core electron is removed while leaving the other electrons frozen in their original orbitals. In the second step,. the other electrons are allowed to relax. This relaxation contributes additional kinetic energy to the outgoing electron.

chemical state and local environments. Solids in which all atoms of an element are identical may still exhibit core-level shifts because the truncation of the solids at surfaces and interfaces can introduce new chemical states and structural environments. Such energy shifts are called surface core-level shifts (SCLSs) or interface core-level shifts (ICLSs), respectively.

To understand these shifts, we consider the so-called initial/final state picture [Shi78, Ege87], illustrated in Figure 2.02 for a free atom. The photoemission is considered to occur in two steps. In the first step, the electron is removed from the atom, and the remaining electron orbitals are held "frozen" in their initial state configuration. The binding energy one would compute for the electron depends only on the nuclear potential and the wave functions of the other orbitals before the incident photon arrived. Such effects are termed *intial state effects*. The binding energy computed in this way is equivalent to the Hartree-Fock eigenvalue ε_i described by Koopman's theorem [Ege87].

In the second step, the remaining orbitals are allowed to relax to their final state configuration. For free atoms, this relaxation generally consists of a contraction of the outer orbitals. This contraction may be approximated using the "$Z+1$ rule," namely that the sudden appearance of the core hole effectively increases the atomic number of the nucleus as

far as the outer electrons are concerned, so that the contracted orbitals are approximately those of the next atom in the periodic table (in the first ionization state). Assuming that the orbitals relax to their final state before the electron has left the vicinity of the atom, then the kinetic energy of the outgoing electron is boosted by the relaxation energy of the bound orbitals.

In both steps, the computed energies are strong functions of the occupation of the valence orbitals. The change in the initial state potential as a function of valence may be estimated classically by assuming that the valence orbitals form a spherical shell of radius r around the core hole. From simple electrostatics, these valence electrons reduce the electron binding energy by eQ/r. If by a chemical reaction the valence occupation changes by δQ then the initial-state binding energy correspondingly changes by $e\delta Q/r$. The change in final state energy also depends on the valence occupation, since a less occupied valence configuration can relax more than a fully occupied one. Detailed quantum mechanical computations of the atomic orbitals before and after core-hole creation are usually performed to arrive at the initial and final state changes simultaneously [Ege87].

For atoms in solids, there are extra-atomic contributions to core-level energies as well. These are illustrated in Figure 2.03. An external potential is applied to the atom by the other atoms in the solid (left part of figure). In covalently-bonded solids, this external potential is weak and short-ranged, but in ionic solids, the arrangement of positive and negative ions creates a strong electrostatic field at each core-level. This potential, which contributes to the initial-state binding energy, is called the *Madelung potential* and is discussed in detail in §2.1. We will show that the Madelung potential varies significantly between surface atoms and bulk atoms in the interior of a film.

The extra-atomic final state contribution is determined by the relaxation of orbitals on neighboring atoms (right part of figure). This relaxation is manifested as a polarization of these neighboring atoms into dipoles oriented approximately towards the core hole. This

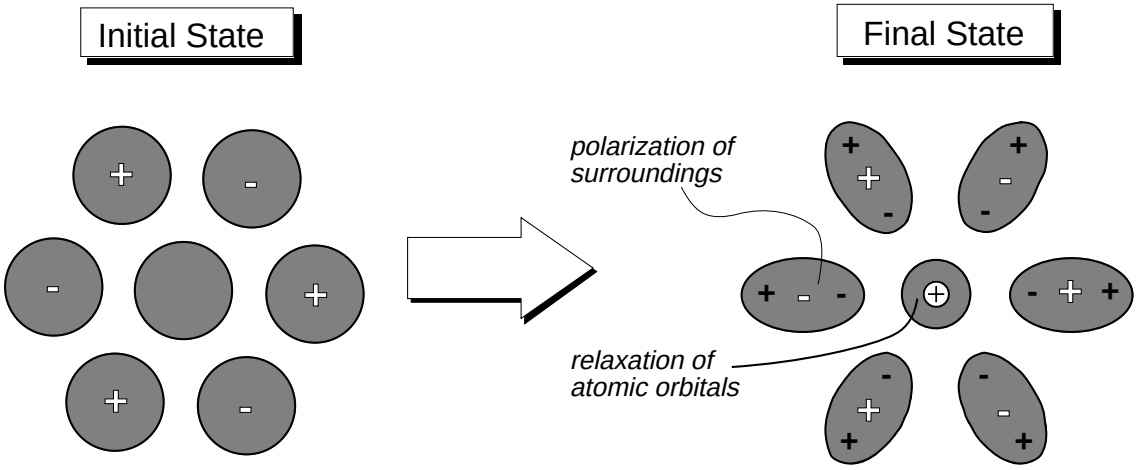

Figure 2.03. Initial/Final state picture of XPS for atoms in solids. (Left) the distribution of neighboring ions creates a potential at the core electron which can alter the electron's binding to the nucleus. (Right) after core hole creation, the neighboring atoms polarize in response to the creation of the core hole.

polarization contribution is discussed in detail in §2.2. One issue is whether or not this relaxation happens quickly enough to interact with the outgoing electron. If the relaxation is complete while the electron is still in the vicinity of the core hole, then this condition is called the *fully relaxed* case. This question was considered theoretically by Bechstedt (including retardation), who found full relaxation to occur for solids [Bec82]. Furthermore, our calculation of this relaxation are in good agreement for solid Xe (this chapter) and CaF_2 and SrF_2 films (Chapter 6). Therefore, the results in this thesis also support the fully relaxed condition.

Clearly the extra-atomic energies should depend on the geometrical arrangement of atoms near the atom in question. The geometry can also affect the chemical state and hence the intra-atomic (within the atom) contribution to the CLS. At an interface between very different materials, for example, the chemical states of the interfacial atoms are expected to differ from those in either bulk material and hence there should be important intra-atomic contributions to the binding energies of interface core levels.

For surface atoms, it is not always clear whether the chemical states are significantly

altered or not. Hence it should not be clear whether observed SCLSs are due to extra-atomic or intra-atomic effects. For materials like semiconductors which exhibit surface reconstructions, it is often the case that the recontructions are accompanied by chemical state changes, and the assignments of extra- *vs.* intra-atomic contributions are difficult to make [Mcl90]. In this thesis, however, we specialize to simple insulator surfaces which exhibit bulk-like terminations. In a theoretical study of ionic insulator surfaces, Watson and Davenport found significant alterations in surface valence states, i.e. $0.0 < |\delta Q/Q| < 0.2$ [Wat83]. These changes in charge state are driven by a competition between the molecular cohesive energy, which tries to maintain the bulk ionicity at the surface, and the Madelung potential near the surface which can act to reduce the surface ionicity. This occurs for certain geometries in which reconfiguring the surface charge states lowers the total electrostatic energy of the solid.

For CaF_2 and SrF_2 (111) surfaces which are the main subject of this thesis, there have been no theoretical calculations of altered surface chemical states to date. These low-energy surfaces are known from both theoretical [Tas80] and experimental [Die92] work to have simple bulk-like terminations. In this chapter, we will assume that the chemical states are not altered at the surfaces, and we will calculate only the extra-atomic initial- and final-state contributions to the binding energy assuming simple bulk-like surface terminations. In Chapter 6 we will find good agreement between computed and observed SCLSs in these materials, from which we conclude that the chemical states are not altered between the surface and bulk atoms. At the interface atoms, though, we will find deviations between the observed ICLSs and the ICLS predicted from extra-atomic effects only. These deviations can then be used to put limits on the magnitude of the intra-atomic contributions.

Figure 2.04 summarizes the scheme for calculation. The core-level shifts are determined by intra-atomic and extra-atomic effects. Of these, the latter is easiest to calculate and this calculation is a major result of this thesis. Furthermore, at the surfaces of ionic insulators, it is expected to be the most important. Within this picture, then, the observed CLSs for

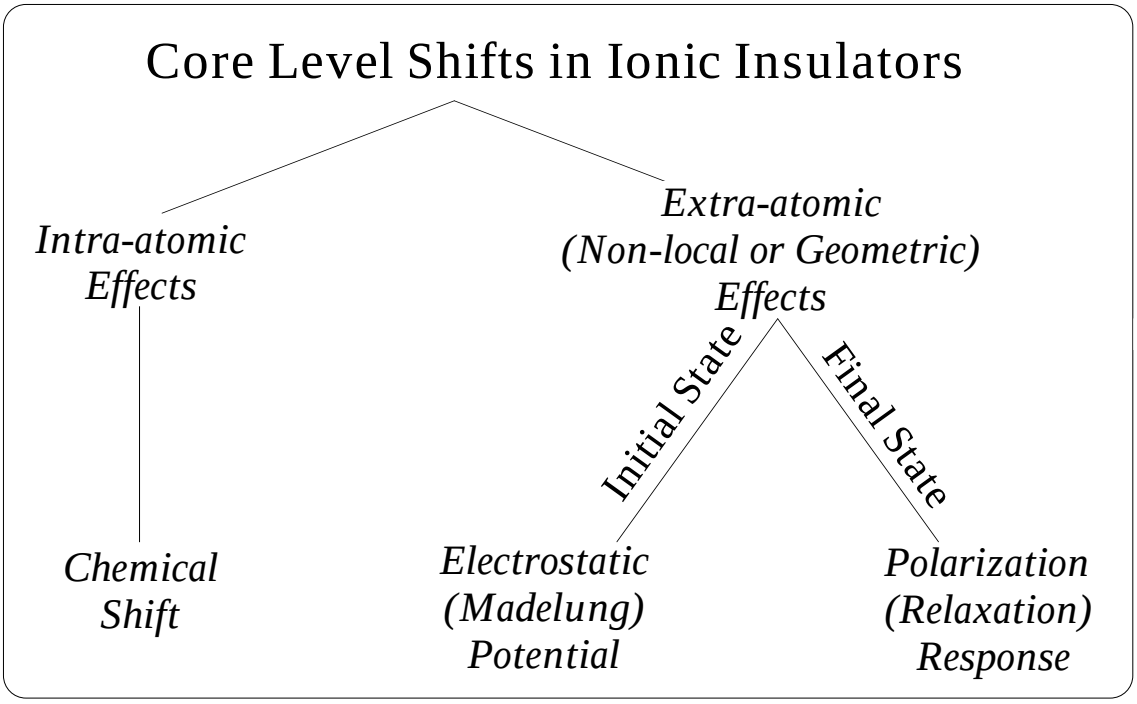

Figure 2.04. Summary of contributions to core level shifts.

photoelectrons (PE) and Auger electrons (AE) are written as

$$\Delta E = \begin{cases} \Delta(Initial\ State)_{PE} + \Delta(Final\ State)_{PE} & Photoelectrons \\ \Delta(Initial\ State)_{AE} + \Delta(Final\ State)_{AE} & Auger\ Electrons \end{cases}, \tag{2.1a}$$

where we take as convention $\Delta E>0$ means *less* kinetic energy. In this chapter we will compute only the extra-atomic effects of the Madelung potential and the polarization response. Therefore, (2.1a) becomes

$$\Delta E = \begin{cases} \Delta(e\Phi_M)_{PE} + \Delta(R)_{PE} & Photoelectrons \\ \Delta(e\Phi_M)_{AE} + \Delta(R)_{AE} & Auger\ Electrons \end{cases}, \tag{2.1b}$$

where Φ_M is the Madelung potential (computed in §2.1) and R is the relaxation energy (computed in §2.2).

Equation (2.1b) may be simplified as follows by relating the Auger terms to the photoemission terms [Wag75, Hoh85]. It will be shown in this chapter that $\Phi_M \propto Q$ and $R \propto Q^2$, where Q charge of the emitting atom with a core hole. For Auger decay, the system

has already relaxed to the initial core hole charge $Q=e$; afterwards, the system responds to the final core-hole charge $2e$. Therefore the net relaxation for Auger electrons is $(2^2\text{-}1)\Delta(R)_{PE}=3\Delta(R)_{PE}$. The initial state energy $e\Delta\Phi_M$ only scales as Q, so that the net initial state energy shift is just $(2\text{-}1)e\Delta(\Phi_M)_{PE}=e\Delta(\Phi_M)_{PE}$. Therefore, the final equation for the observed shifts becomes

$$\Delta E = \begin{cases} e\Delta\Phi_M + \Delta R & \textit{Photoelectrons} \\ e\Delta\Phi_M + 3\Delta R & \textit{Auger Electrons} \end{cases}. \tag{2.1c}$$

Chapter 6 compares the theory to experimental results, where we find good agreement at the fluoride surfaces, and reasonable agreement at the fluoride/Silicon interface.

2.1 Madelung Potential

2.1.1 Formulation

The Madelung potential at an atomic site in an infinite solid is given by

$$\Phi = e\Phi_M = e\sum_{\mathbf{R}}^{crystal}\left[\sum_{t}^{\substack{unit\\cell}}\frac{q_t}{(\mathbf{r}_t+\mathbf{R})}\right], \tag{2.2a}$$

where the lattice translation vectors $\{\mathbf{R}\}$ sum over the unit cells in the solid, t sums over the atoms within a unit cell, and q_t and $\mathbf{r}_t$ are the charge and position of the t^{th} atom in the unit cell. The vectors $\mathbf{r}_t$ are specified relative to the atom of interest in the unit cell.

In the standard Ewald method [Kit86], the summation (2.2a) is broken into separate summations in real and reciprocal space:

$$\Phi_M = \frac{4\pi}{\Delta}\sum_{\mathbf{G}}\frac{S(\mathbf{G})}{G^2}\exp(-G^2/4\eta) + e\sum_{\mathbf{R}}^{crystal}\left[\sum_{t}^{\substack{unit\\cell}} q_t / (\mathbf{r}_t + \mathbf{R})\,\mathrm{erfc}\left((\mathbf{r}_t + \mathbf{R})/\sqrt{\eta}\right)\right], \qquad (2.2b)$$
$$-2q_0\sqrt{\eta/\pi}$$

where {**G**} is a set of reciprocal lattice vectors and Δ is the volume of the unit cell. The third term in (2.2b) is a correction which effectively excludes the central atom from the potential computed. The computed potential is independent of the parameter η, which is chosen so that the two summations converge in roughly the same number of terms (typically $\eta \approx 0.5$Å^{-1}). The structure factor S(**G**) is given by

$$S(\mathbf{G}) = \sum_{t}^{\substack{unit\\cell}} q_t \exp(-i\mathbf{G}\cdot\mathbf{r}_t). \qquad (2.3)$$

To model thin films, we exploit the translational symmetry in the direction parallel to the surface, and allow for any arbitrary arrangement of atoms in the perpendicular direction. The direct lattice of the film is described by two-dimensional lattice vectors {$\mathbf{R}_\parallel$}, with a corresponding set of reciprocal space vectors {$\mathbf{G}_\parallel$}. The perpendicular direction z is normal to the film surface. To remove the translational symmetry in the z-direction from (2.2b), we replicate the film periodically in the z-direction with repeat-distance a_z. We then take the limit

$$\sum_{\mathbf{G}} \rightarrow \sum_{\mathbf{G}_\parallel}\sum_{G_\perp} \xrightarrow{a_z\rightarrow\infty} \sum_{\mathbf{G}_\parallel}\int_{G_z} \qquad (2.4)$$

in (2.2b). Then this equation becomes

$$\Phi_M = \sum_{\mathbf{G}_\parallel}\sum_t S_t\left(\eta,\mathbf{G}_\parallel\right)\exp\left(-i\mathbf{G}_\parallel\cdot\mathbf{r}_{t,\parallel}\right)$$
$$+\sum_{\mathbf{R}_\parallel}\sum_t q_i/\left|\mathbf{R}_\parallel+\mathbf{r}_t\right|\mathrm{erfc}\left(\left|\mathbf{R}_\parallel+\mathbf{r}_t\right|\sqrt{\eta}\right), \tag{2.5}$$
$$-2q_0\sqrt{\eta\ \pi}$$

where now the unit cell incorporates all film atoms in the z-direction. The structure factor S_t contains information perpendicular to the surface and is given by

$$S_t\left(\eta,\mathbf{G}_\parallel\neq 0\right)=q_t\left(\frac{\pi}{\Delta_\parallel G_\parallel}\right)\left\{e^{-G_\parallel r_{t,z}}\,\mathrm{erfc}\left(\frac{G_\parallel-2\eta r_{t,z}}{2\sqrt{\eta}}\right)\right.$$
$$\left.+e^{G_\parallel r_{t,z}}\,\mathrm{erfc}\left(\frac{G_\parallel+2\eta r_{t,z}}{2\sqrt{\eta}}\right)\right\}, \tag{2.6}$$

where $\Delta_\parallel$ is the area of the unit cell in real space and $r_{t,z}$ is the position of the t^{th} basis atom in the direction normal to the film surface. Particular attention must be paid to the case of $\mathbf{G}_\parallel$=0, when the first term in Eq. (2.5) becomes

$$\sum_{\mathbf{G}_\parallel}\sum_t \rightarrow \frac{2\pi}{\Delta_\parallel}\sum_{t\neq 0} q_t\left\{\left(\eta\pi\right)^{-1/2}\left(1-\exp\left(-\eta r_{t,z}^2\right)\right)-r_{t,z}\,\mathrm{erf}\left(\sqrt{\eta}r_{t,z}\right)\right\}. \tag{2.7}$$

Derivation of (2.7) assumes that the unit cell of the lattice must be charge-neutral and that $\mathbf{r}_o$=0. Eq. (2.7) is zero only in the case where the unit cell has no net charge in any given plane parallel to the film.

2.1.2 Examples of the Madelung potential

Figure 2.05 illustrates the contribution of the Madelung potential to the observed binding energy at the near-surface atoms of NaCl(100). The calculation assumed that these ions had their formal valences (q_{Na}=+1 and q_{Cl}=-1). We enumerate a number of features:

(1) Because the Na and Cl sites are geometrically equivalent, their Madelung potentials are equal (and opposite). This is in constrast to the CaF_2(111) case discussed below.

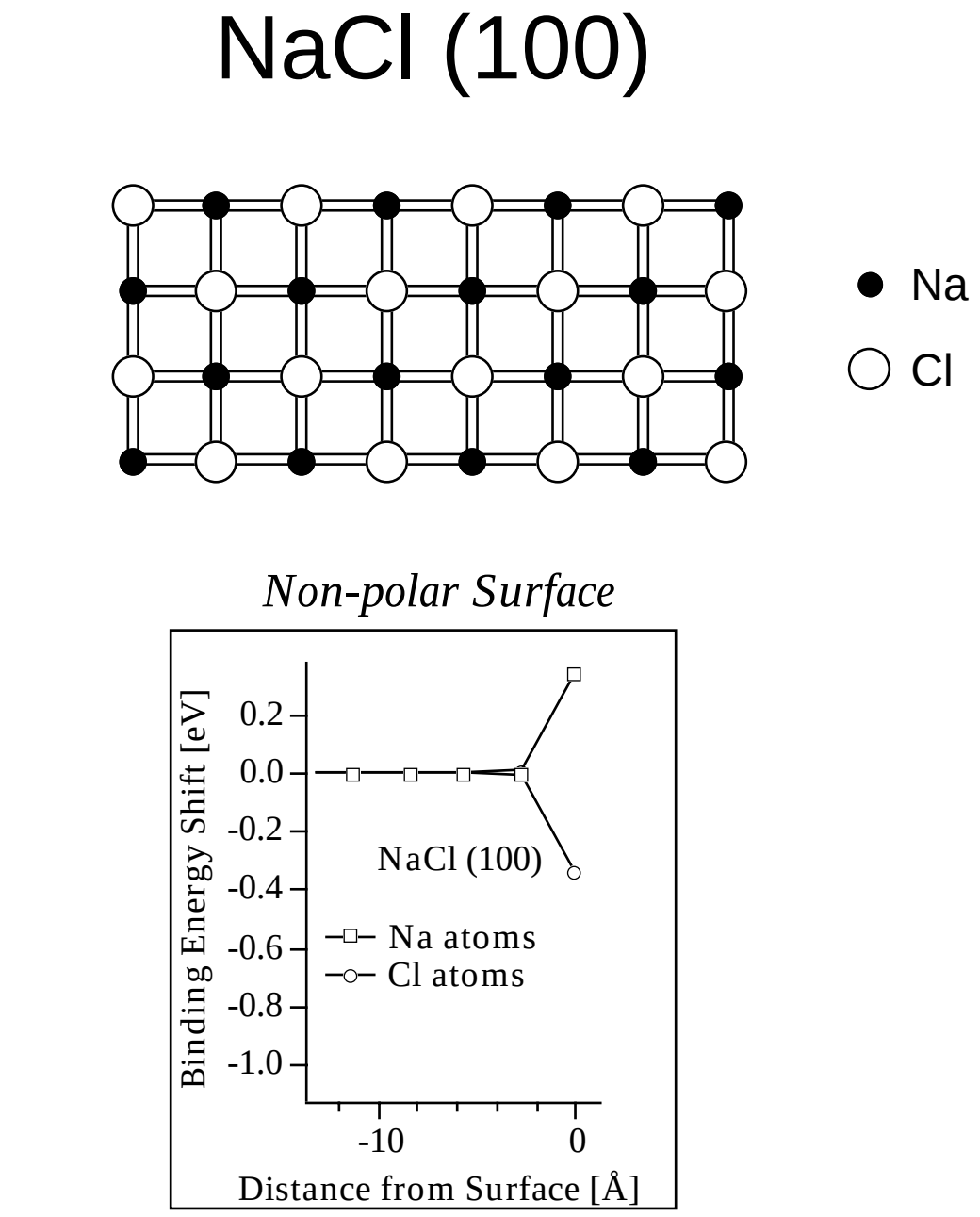

Figure 2.05. Surface Madelung shifts for NaCl(100). Shown are the predicted binding energy shifts of surface *vs.* bulk atoms as would be predicted by the Madelung potential alone.

(2) The cation binding energy is enhanced at the surface relative to the bulk atoms. This is because the Madelung potential is always negative at cation sites (the condition for stability of the ionic lattice), which leads to a destabilization of the cation orbitals. At the surface, this destabilization is reduced, so that electrons are more bound to surface cations than to bulk ones. A similar argument explains the net reduction in binding energy for surface anions.

(3) For a surface with simple bulk-termination, the surface Madelung shift is just minus the potential of the "missing" atoms above the surface at the site of the atom in question. Therefore since the bulk Madelung potential is known, the shifts shown in Figure 2.05 can be used to give us the potential *outside* of a semi-infinite crystal as well as inside. An example of this will be given below.

(4) The shifts in binding energy are confined to the surface atoms. Since the potential energy shift is equivalent to the potential of the "missing" above-surface atoms, and because the crystal is neutral, this potential drops off exponentially fast with characteristic length ≤ 1 atomic spacing [Wat84] the further one is from these missing atoms. This accounts for the surface shifts being negligible (< 0.01 eV) for sites further than about 1.5 Å from the surface.

Figure 2.06 shows the resulting Madelung energies for CaF_2(111). The calculation again assumes the formal valences (q_{Ca}=+2 and q_F=-1). Because the F atoms protrude further into the vacuum than Ca, the surface Madelung shift is larger for F than Ca. Furthermore, the geometry leads to a much stronger F shift than was the case for anions in NaCl(100).

2.1.3 Surface corrugation potentials

An important application of the formalism in this section is computation of surface corrugation potential, which can be computed directly using the formalism described above. The kinetics of crystal growth by MBE depend on the motion of free CaF_2 molecules on the surface, which in turn depends on the potential barrier for the CaF_2 molecule to hop from site to site. This will be discussed further in Chapter 5. For a single CaF_2 molecule adsorbed to

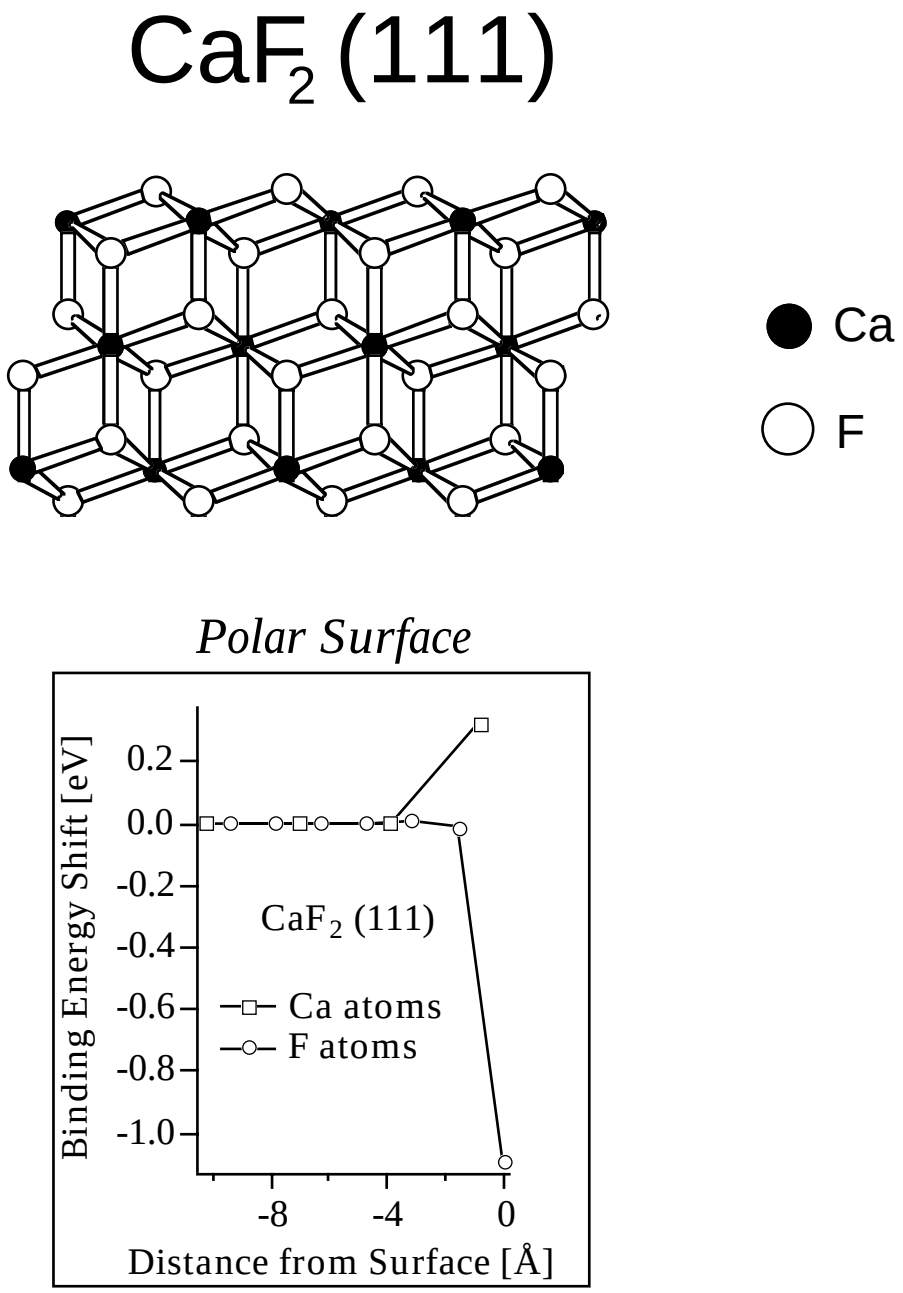

Figure 2.06. Surface Madelung shifts for $CaF_2(111)$. Shown are the predicted binding energy shifts of surface *vs.* bulk atoms as would be predicted by the Madelung potential alone.

the surface, the "binding energy" due to electrostatic attraction is just

$$-\sum q \cdot \Delta\Phi_M = -\left[(-1)*(-1.087\ eV)+(+2)(0.323\ eV)+(-1)(0.013\ eV)\right], \quad (2.08)$$
$$= -1.75\ eV$$

where the energies are those plotted in Figure 2.06. It is assumed that the repulsive potential is hard-sphere so that no repulsive terms appear in (2.08). We calculated this energy as a function of displacement of the molecule parallel to the surface. Figure 2.07(a) shows a contour plot of this potential field. The (straight-line) direction with the smallest barrier to motion is illustrated with a heavy line in Figure 2.07(a); the potential along this line is plotted in Figure 2.07(b). From this plot, we see that the peak-to-peak potential barrier for in-plane motion is 2.29 eV. This overestimates the barrier since the molecule also has the freedom to leave the surface (to where the potential is zero) and return to a different unit cell. Therefore the actual barrier to the motion is just 1.75 eV.

This discussion assumed that (a) the CaF_2 molecule is linear, and (b) that it maintains its 20° orientation to the surface during motion. There has been some controversy in the past as to whether in fact the free CaF_2 molecule is straight or bent. Recent calculations [Sal90, Sze90] suggest that the molecule is linear, although the energy difference between linear and bent is small (<< 0.1 eV/molecule) and depends on the Ca *d*-orbital occupation, which may change for adsorbed molecules. If the molecule were allowed to bend, rotate, or change its tilt, then in principle the barrier for hopping from site-to-site would change, although we have not corrected for this type of motion.

2.1.4 Application to work function calculation

For ionic solids, the crystal work function has a contribution from the distribution of charges in the solid. For example, simple electrostatics suggests that a surface dipole will raise or lower the potential of states in the solid relative to vacuum [Jac86]. Bulk-termination of CaF_2(111) does not yield such a dipole moment; however since the solid is composed of F-Ca-F triple layers (with charges (-)(++)(-)); this leads to an alternating potential in the solid.

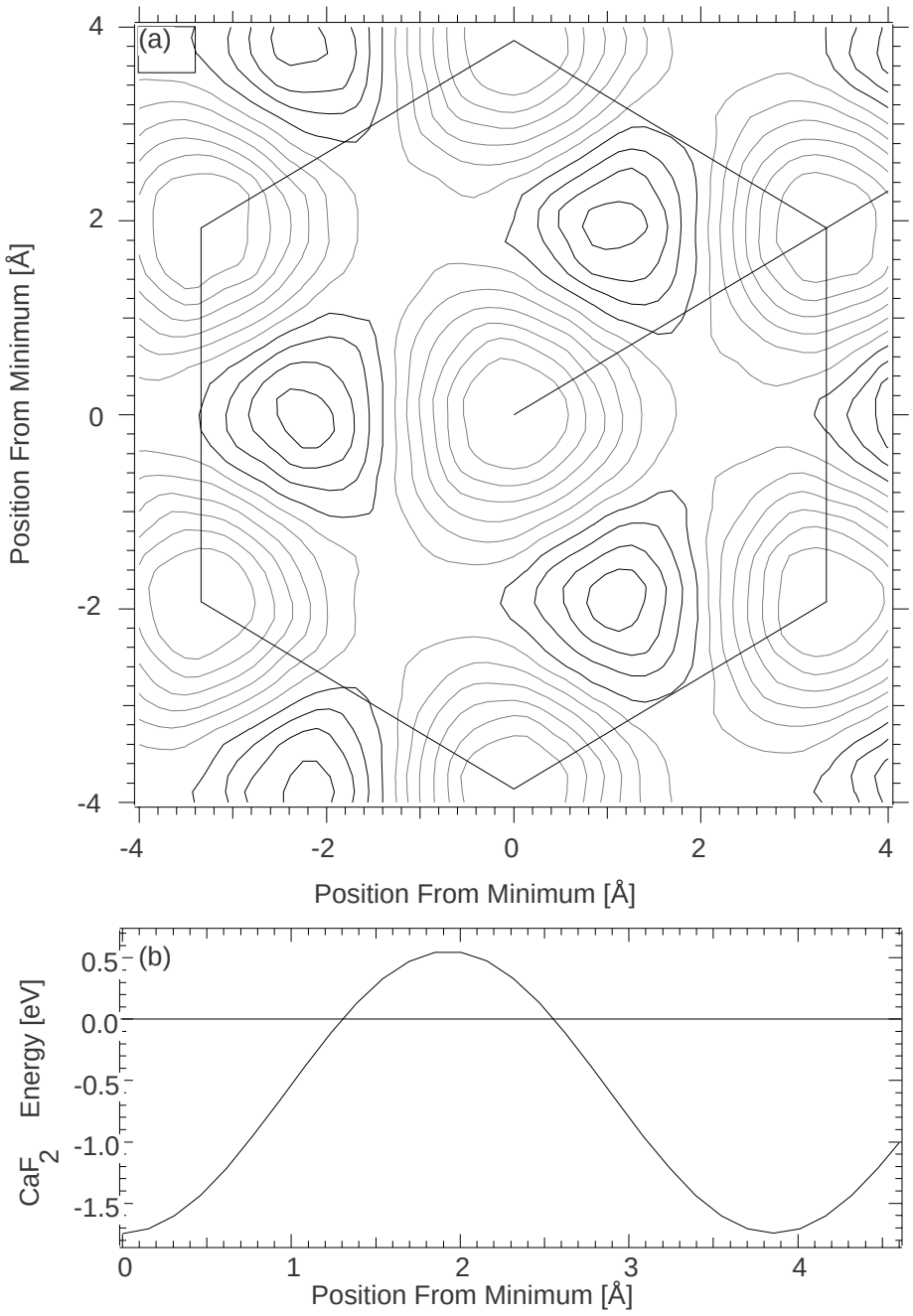

Figure 2.07. The binding energy due to Madelung interaction between an isolated CaF_2 molecule bound to the $CaF_2(111)$ surface. (a) A contour plot of the binding energy as a function of the molecule's position in the surface plane (grey=negative, solid=positive energies). Each contour represents a 0.3 eV change in binding energy. (b) The energy along the straight line indicated in part (a).

This yields a work-function contribution of ~2.8 eV, which is.just the average potential energy seen by an electron as it traverses a F-Ca-F triple layer in the [111] direction.

2.2 Relaxation Calculation

2.2.1 Local vs. Macroscopic Fields

The relaxation shift ΔR is computed in real space because translational symmetry is lost when the system responds to the core hole. Conceptually, the model is illustrated in Figure 2.08(a). A continuous dielectric medium responds to the sudden appearance of a core hole Q by developing a polarization field $\mathbf{P}$ directed radially away from the core hole. The energy of this configuration is given by the standard expression [Jac86 Eq. (4.93)],

$$R = -\tfrac{1}{2}\int \mathbf{P}\cdot\mathbf{E}_0 d^3x\,, \tag{2.09}$$

where $\mathbf{E}_0$ is the field of the core hole in the absence of the dielectric. The factor $1/2$ accounts for the work done in creating the polarization field. For this simple system, the following equations hold for the macroscopic fields:

$$\begin{aligned}\mathbf{E}_0 &= Q\hat{\mathbf{r}} / r^2 \\ \mathbf{E} &= \mathbf{E}_0 / \varepsilon_\infty \\ \mathbf{D} &= \varepsilon_\infty \mathbf{E} = \mathbf{E} + 4\pi\mathbf{P}\end{aligned} \quad . \tag{2.10}$$

We have used the dynamic dielectric constant ε_∞ because the time scale (0.1 to 1 fs) allows only electronic, not phonon, relaxation to occur while the photo- or Auger electron is in the vicinity of the core hole. Integration of (2.09) then leads to the simple expression (for bulk solids),

$$R_{r>\rho}^{bulk} = -\frac{1}{2}\left(1-\varepsilon_\infty^{-1}\right)\frac{Q^2}{\rho}. \tag{2.11}$$

The parameter ρ was introduced because the integral (2.09) diverges when the volume of integration includes the core-hole. Therefore a sphere of radius ρ around the core hole was excluded from the integration. Application of (2.11) to compute the relaxation energy is

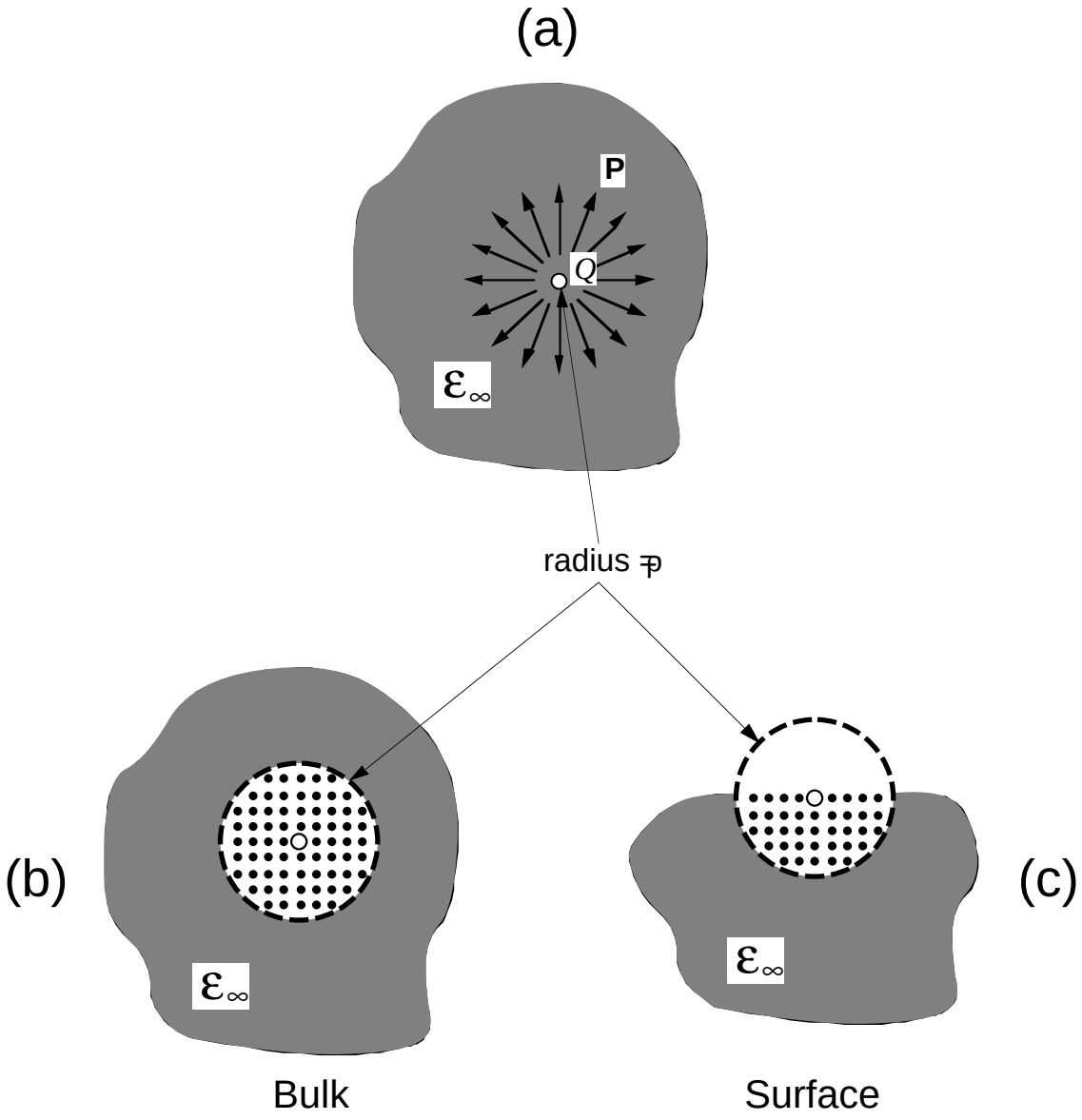

Figure 2.08. Schematic of relaxation in solids for a core hole Q in (a) a continuous dielectric, (b) a cluster embedded in a continuous dielectric, and (c) a cluster at the surface of a continuous dielectric.

impossible because of the introduction of this arbitrary parameter. The results of the full calculation detailed below for CaF_2 and NaCl, where we find $R \approx 2$ eV, show that the screening distance ρ is on the order of the insulator lattice constant. The derivation of the macroscopic fields (2.10), however, assumes that these fields are slowly varying on the atomic scale. This is because the *local fields* (the actual fluctuating fields at each dipole in the lattice) fail to have a simple relationship to the macroscopic fields (2.10) when the former vary on too small a length scale [Jac86 §4.5]. Therefore, the macroscopic formalism should fail to describe the problem, since the relevant length scale ρ is too small.

The situation is remedied by considering the alternate systems in Figure 2.08(b, c). The radius ρ is enlarged to enclose a cluster of atoms. Within the cluster, we compute the relaxation energy $R_{r<\rho}$ self-consistently using the correct local fields within the cluster, and we use (2.09) only for the region outside the cluster. The total relaxation R is just

$$R = R_{r<\rho} + R_{r>\rho}. \tag{2.12}$$

The change in this quantity ΔR at the surface is just given by the difference in polarization energies between the configurations in Figures 2.08(b, c).

2.2.2 References to Relaxation Calculations

Although a reciprocal-space calculation for $R_{r<\rho}$ has been presented [Mah80], it is difficult to generalize this method to arbitrary film geometries. The basic idea for the real-space calculation is due to Mott [Mot38]; calculations and comparisons to experiment for bulk solids are presented by Kao [Kao91] and Moretti [Mor90]. In the latter two papers, the calculations were carried out over very limited cluster sizes, and without corrections for finite clusters. Therefore the accuracies are limited, although some success was found in comparison with experiment. A calculation using a sufficiently large cluster was presented by Wang [Wan80] for NaCl. The reciprocal-space calculation by Mahan [Mah80] does away with the problem altogether. Our calculations are in full agreement with these latter two papers when we compare our calculation for bulk NaCl-structure solids. As far as we know, this work

presents the first calculation for two-dimensional structures [Rot92].

2.2.3 Formulation

The lattice consists of a set of polarizable atoms or ions, whose dipole moments (angle and magnitude) in the presence of the core hole are to be calculated. The relaxation energy ΔR thus depends on the geometry and the polarizabilities α_+ and α_- of the cation and anion, respectively. We calculate the dipole moment at the i^{th} atom in the cluster as

$$\mathbf{E}^i_{loc} = \mathbf{E}^i_{fixed} + \sum_{j \neq i} \frac{3\mathbf{R}^{ij}(\mathbf{p}^j \cdot \mathbf{R}^{ij})}{|\mathbf{R}^{ij}|^5} - \frac{\mathbf{p}^j}{|\mathbf{R}^{ij}|^3}, \tag{2.13}$$

where $\mathbf{p}^i$ is the i^{th} dipole moment, $\mathbf{E}^i_{loc}$ is the local field at the i^{th} dipole, $\mathbf{E}^i_{fixed}$ is the fixed field $\mathbf{E}_o = Q\mathbf{r}/r^3$ from the core hole, plus any other fixed fields (see below), and $\mathbf{R}^{ij} = (\mathbf{R}^i - \mathbf{R}^j)$ is the vector from the j^{th} dipole to the i^{th} dipole. The last term sums over the electric fields from other dipoles in the cluster.

The dipole configuration for a finite cluster of atoms is then given self-consistently by the matrix equation [Mot38, Wan80, Mor90],

$$\mathbf{p}^i = \alpha_i \mathbf{E}^i_{loc} = \alpha_i \mathbf{E}^i_{fixed} + \sum_{j \neq i} \ddot{\mathbf{M}}^{ij} \cdot \mathbf{p}^j. \tag{2.14}$$

This equation may be inverted to solve for the dipole moments $\mathbf{p}^i$. Starting from (2.13), the matrix $\ddot{\mathbf{M}}^{ij}$ which encodes the locations and polarizabilities of the dipoles is given by

$$M^{ij}_{\alpha\beta} = \alpha_j \left(\frac{3R^{ij}_\alpha R^{ij}_\beta}{|\mathbf{R}^{ij}|^5} - \frac{1}{|\mathbf{R}^{ij}|^3} \right) \tag{2.15}$$

(Throughout this discussion, roman letters (i, j) are used to enumerate dipoles, while greek letters (α, $\beta = 1...3$) are used for components of vectors and matrices). Once the dipole configuration is known, the relaxation energy for the cluster is simply the discrete version of (2.09),

$$R_{r<\rho} = -\tfrac{1}{2}\sum_j \mathbf{p}^j \cdot \mathbf{E}_0 \,. \tag{2.16}$$

The size of the matrix in (2.09-10) may be greatly reduced by grouping together similar dipoles whose orientations are related by symmetry. For a group of n such dipoles in either $CaF_2(111)$ or NaCl(100) films, the i^{th} dipole's position and dipole moment is related to the first dipole through a simple matrix $\mathbf{C}^i$, which is either a rotation or a rotation followed by an inversion. If we define the vectors,

$$\begin{aligned} \mathbf{p}^{j\sigma} &= \mathbf{C}^\sigma \cdot \mathbf{p}^j \\ \mathbf{R}^{ij\sigma} &= \mathbf{R}^i - \mathbf{C}^\sigma \cdot \mathbf{R}^j \,, \\ \mathbf{v}^{ij\sigma} &= (\mathbf{C}^\sigma)^{-1}\mathbf{R}^{ij\sigma} \end{aligned} \tag{2.17}$$

then (2.10) becomes,

$$\mathbf{p}_i = \alpha_i \mathbf{E}_{fixed,i} + \sum_j \sum_{\sigma=1+\delta_{ij}}^{n} \mathbf{h}^{ij\sigma} \cdot \mathbf{p}^j \,, \tag{2.18}$$

where δ_{ij} is the Kronecker delta, and the elements of the matrix $\mathbf{h}^{ij\sigma}$ are given by

$$h_{\alpha\beta}^{ij\sigma} = \alpha_j \left(\frac{3 R_\alpha^{ij\sigma} v_\beta^{ij\sigma}}{|\mathbf{R}^{ij\sigma}|^5} - \frac{C_{\alpha\beta}^\sigma}{|\mathbf{R}^{ij\sigma}|^3} \right). \tag{2.19}$$

2.2.4. Boundary Conditions

We illustrate the calculation and the question of boundary conditions with an example. We consider the surface Na atom at NaCl(100). We computed the dipole configuration for a hemispherical cluster with radius ρ=28 Å; the polarizabilities used are summarized in Table 2.01. This cluster encompasses ~2000 atoms. Figure 2.09(a) shows the resulting dipole angles (left) and the magnitudes (right) in the cluster. The angles are measured relative to the radial vector from the core hole, and the magnitudes are normalized to the source field strength $\mathbf{E}_0 \propto r^{-2}$ Clearly the polarization suffers a discontinuity at the

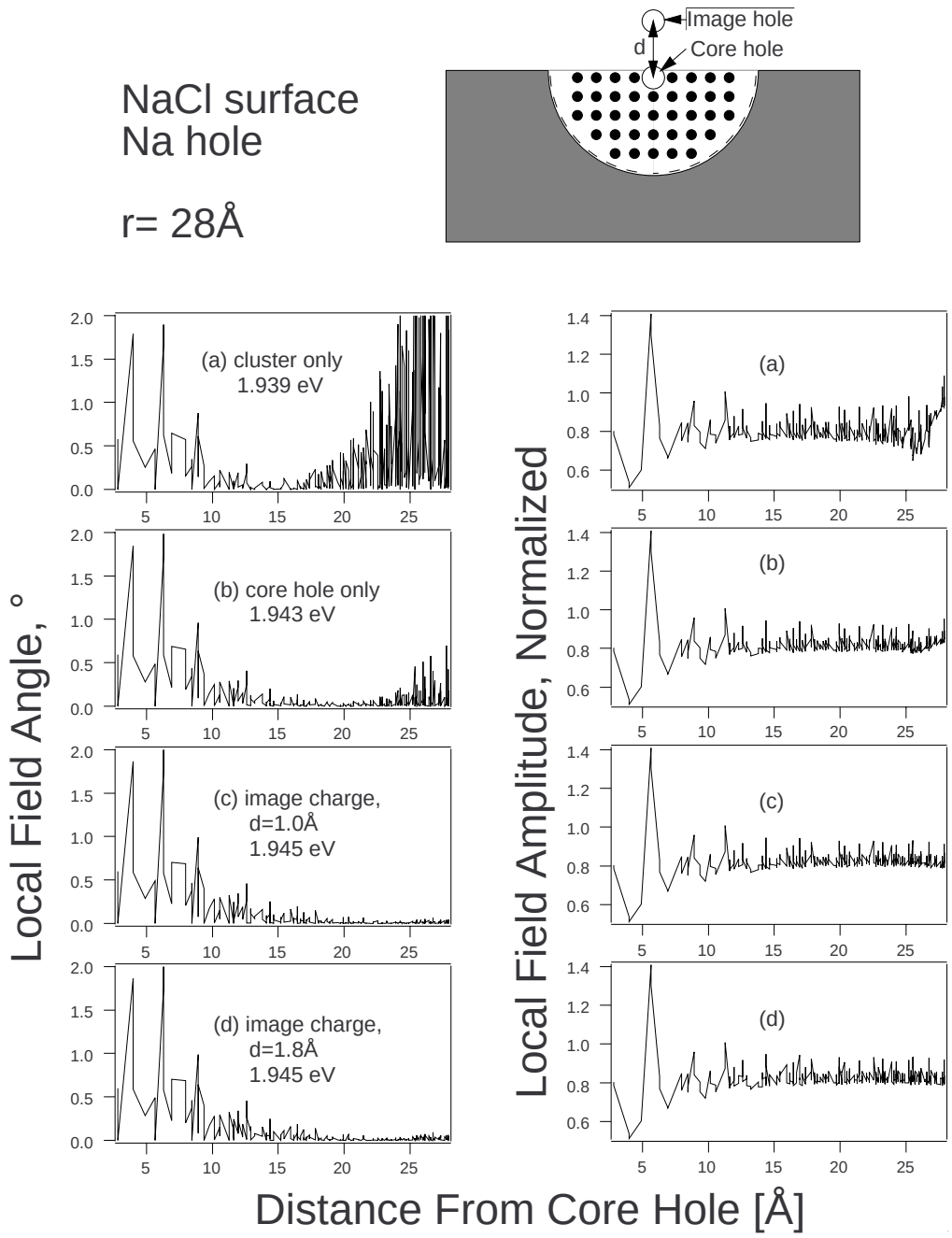

Figure 2.09. Effect of polarization boundary conditions on the relaxation calculation. For Na atoms at the NaCl(100) surface, the dipoles' angles (left) and magnitudes (right) are shown for various boundary conditions: (a) an isolated hemispherical cluster, (b) a cluster embedded in a hemispherical dielectric which "sees" only the core hole, (c) same but with an additional image charge 1.0 Å from the surface atom, and (d) same, 1.8 Å from the surface atom.

cluster surface, as can be seen by the fluctuations in the dipoles there; this violates the requirement that the polarization field **P** should be continuous at the cluster/continuum boundary. We removed this discontinuity by adding a term to $\mathbf{E}^i_{fixed}$ in (2.13) or (2.18) which includes the effect of the region $r>\rho$ on the cluster dipoles.

This method, due to Mott and Littleton [Mot38], is also detailed in Mott and Gurney's monograph [Mot40]. Far from the core hole, the dipole orientation should be uniform, and parallel to the macroscopic polarization vector **P**. From (2.10), we have

$$\begin{aligned}\mathbf{P} &= \frac{1}{4\pi}\left(1-\frac{1}{\varepsilon_\infty}\right)\mathbf{E}_0 \\ &= \frac{\mathbf{p}_+ + \mathbf{p}_-}{v}\end{aligned}, \tag{2.20}$$

where $\mathbf{p}_+$ and $\mathbf{p}_-$ are the cation and anion dipole moments, and v is the volume per molecule. Since $\mathbf{p}_\pm \propto \alpha_\pm$, we must have

$$\mathbf{p}_\pm = \frac{\alpha_\pm}{\alpha_{tot}}\frac{v}{4\pi}\left(1-\frac{1}{\varepsilon_\infty}\right)\mathbf{E}_0. \tag{2.21}$$

Therefore, we enclose the cluster within a larger shell formed of "fixed" dipoles given by (2.21). The fields from each of the fixed dipoles is then added to the dipoles in the cluster via the term $\mathbf{E}^i_{fixed}$ in (2.13).

Near surfaces and interfaces, the core-hole field $\mathbf{E}_0$ does not accurately describe the polarization, so that a better description of the dipoles in the far region $r > \rho$ is needed. The actual polarization includes the effect of a sum of image charges, so that in (2.20-21), the field $\mathbf{E}_0$ is replaced by

$$\mathbf{E}_0 \rightarrow \mathbf{E}_0 + \sum_{i=1} Q_i \mathbf{r} / r^3, \tag{2.22}$$

where the total number of image charges is 1 for a single surface or interface, and infinite for a thin film [Kum89].

Figure 2.09(b-d) illustrates how the polarization discontinuity is removed with this correction. In (b), the discontinuity is almost completely eliminated simply by using (2.21) as is, even though the geometry includes a surface. Only a modest correction to the energy $R_{r<\rho}$ was obtained, however (1.939 → 1.943 eV). In (c), we see the effect of correctly including a single image charge 1 Å away from the surface core hole. The discontinuity is now completely eliminated, although the energy computed has only insignificantly changed (1.943 → 1.945 eV). Implicit in this model is the distance between the core hole and the image charge, which amounts to a definition of the surface position. The calculation turns out to be insensitive to this position, as indicated in (d), where we moved the image charge significantly away from the core hole, and did not compute any difference in the relaxation calculation.

We conclude that the polarization boundary condition gives only a small (<0.5 %) correction to the computed energies, most of which is accomplished through the lowest-order term in the polarization. Most of the calculations in this chapter include the correction; for some calculations, however, we have simply neglected the correction altogether (which is much smaller than the experimental uncertainties, or the uncertainties in the calculation due to the polarizabilities).

2.2.5 Convergence

We conclude this section with a discussion of the convergence properties of the relaxation calculation. How large a cluster size is needed to achieve accurate results? Figure 2.10 shows results for the Ca core hole both in (a) bulk CaF_2 and (b) at the CaF_2(111) surface. We have plotted the cluster relaxations $R_{r<\rho}$ (2.16) for various cluster sizes. We see that the relaxation amplitude converges quite slowly over the range of cluster radii chosen(although the surface relaxation is clearly converging faster than the bulk). To continue the calculation for larger clusters would be prohibitive (the largest clusters shown correspond to inverting a 1000×1000 matrix, even exploiting the symmetry). However, we

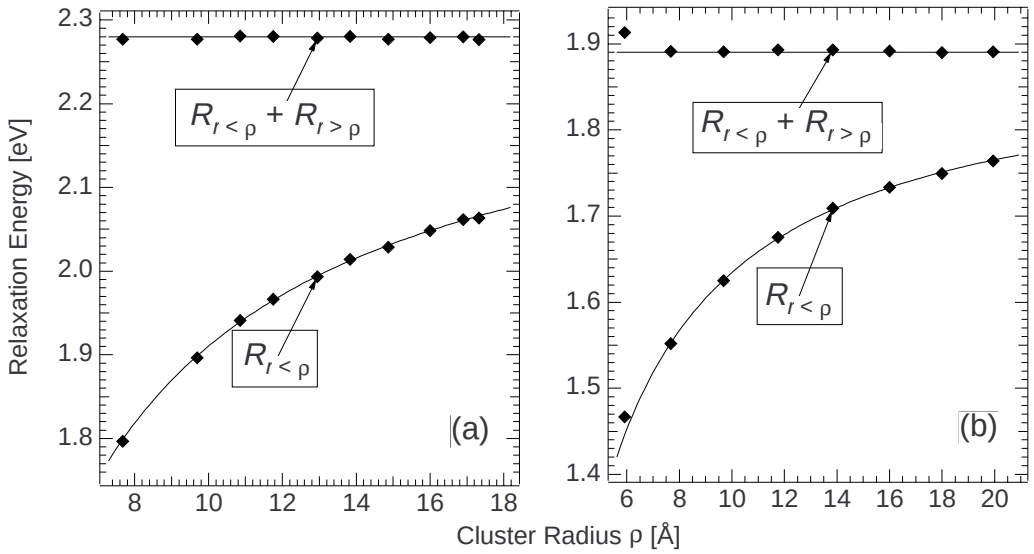

Figure 2.10. Convergence properties of relaxation calculation for Ca atoms in (a) bulk CaF_2 and (b) at the CaF_2(111) surface. The symbols labelled $R_{r<\rho}$ represent the relaxation energy within the clusters, the symbols labelled $R_{r<\rho} + R_{r>\rho}$ represent the total relaxation energy.

can determine that the *shape* of these curves has converged relatively rapidly: upon addition of the continuum relaxation $R_{r>\rho}$ (2.09), the resulting total relaxation (2.12) has converged to a flat line.

For the bulk and surface geometries, the continuum part of the relaxation (2.09) is

$$R_{r>\rho}^{bulk} = -\frac{1}{2}\left(1-\frac{1}{\varepsilon_\infty}\right)\frac{Q^2}{\rho}, \tag{2.23a}$$

$$R_{r>\rho}^{surf} = \begin{cases} R_{r>\rho}^{bulk}\left[\left(\frac{1}{2}+\frac{d_s}{4\rho}\right)+\frac{Q'}{Q}\left(\frac{1}{2}-\frac{d_s}{4\rho}\right)\right] & d_s \le \rho \\ R_{r>\rho}^{bulk}\left[4-\frac{\rho}{d_s}\left(1-\frac{Q'}{Q}\right)\right] & d_s > \rho \end{cases} \tag{2.23b}$$

where for the surface expression, the core hole is a distance d_s from the surface, and $Q'=Q(\varepsilon_\infty-\varepsilon_{vsc})/(\varepsilon_\infty+\varepsilon_{vac})$ is an image charge reflected across the surface. We find that the surface expression in (2.23) again introduces an arbitrary parameter—the distance d_s between

the core-hole and the surface. To add this expression to the cluster relaxation curve in Figure 2.10(b), we allowed this distance to vary in order to give the best fit to $R_{r>\rho}+R_{r<\rho}$=constant. The fitted d_s was within ~1-2 Å of the actual distance, and the converged energy was not very sensitive to its value. For a thin film geometry, the relaxation energy $R_{r>\rho}$ becomes

$$R_{r>\rho}^{\text{film}} = R_{r>\rho}^{\text{bulk}}\left[\left(\frac{d_i+d_s}{4\rho^2}\right)+\sum_{\substack{n=-\infty\\ n\neq 0}}^{\infty}\frac{Q_n}{2Q}\Big(f_1(n)+f_2(n)+f_3(n)+f_4(n)\Big)\right], \qquad (2.23c.i)$$

where

$$f_1(n)=\frac{-1/2}{2d_i+d_n},\quad f_2(n)=\frac{1/2}{-2d_s+d_n},\quad f_3(n)=\frac{\left(d_i+d_n\right)\left[2d_id_n+d_n^2+\rho^2\right]^{\frac{1}{2}}}{\left(2d_i+d_n\right)\left(d_n\rho\right)} \text{ (ii)}$$

$$f_4(n)=\frac{\left(\rho^2-d_n^2\right)\left[-2d_sd_n+d_n^2+\rho^2\right]^{\frac{1}{2}}-\left[-2d_sd_n+d_n^2+\rho^2\right]^{\frac{3}{2}}}{\left(-2d_s+d_n\right)\left(2d_n^2\rho\right)}\ , \qquad (2.23c.iii)$$

and where d_i and d_s are the distances from the core hole to the interface and surface, respectively, and it is assumed that $d_i + d_s \leq \rho$. This equation derives from the interaction between the far dipoles and an infinite series of image charges (distributed on either side of the film) whose positions (relative to the core hole) and charges are given by [Kum89]:

$$d_n = n(d_i+d_s)+\frac{d_i-d_s}{2}\left((-1)^n-1\right)$$

$$Q_n = Q\begin{cases}\xi^{|n|/2} & n \text{ even}\\ \xi^{(n-1)/2}\dfrac{\varepsilon_{film}-\varepsilon_{vac}}{\varepsilon_{film}+\varepsilon_{vac}} & n \text{ odd},\ n>0\\ \xi^{(-n-1)/2}\dfrac{\varepsilon_{film}-\varepsilon_{sub}}{\varepsilon_{film}+\varepsilon_{sub}} & n \text{ odd},\ n<0\end{cases}. \qquad (2.23c.iv)$$

where

$$\xi = \frac{\varepsilon_{film} - \varepsilon_{sub}}{\varepsilon_{film} + \varepsilon_{sub}} \cdot \frac{\varepsilon_{film} - \varepsilon_{vac}}{\varepsilon_{film} + \varepsilon_{vac}}. \qquad (2.23c.v)$$

We always followed the procedure in Figure 2.10 in order to obtain converged results: the calculation proceeded for a sequence of clusters, and the converged relaxation was calculated from them. For most calculations, we found adequate convergence in a modest amount of computation time (~10 matrix inversions, 2-3 hrs. time on a personal computer, with the largest matrix ~720×720 (240 atoms)).

2.3 Surface and Thin Film Calculations

We have performed calculations for four insulating systems: solid Xe, NaCl, CaF_2, and SrF_2. For all of these solids, the relaxation calculation contributes to core-level shifts. Only for the ionic solids NaCl, CaF_2, and SrF_2 does the Madelung calculation apply. Table 2.01 summarizes the relaxation calculation results for core holes at bulk atoms in these solids. Shown are the near-neighbor distances, the polarizabilities, and the resulting relaxation energies for cations and anions.

2.3.1 Surface relaxation shifts: theory

In Figure 2.11 we show calculated results for Xe(111), NaCl(100), and CaF_2(111) surface regions (symbols), where we plot extra-atomic relaxation energies relative to the bulk relaxations in Table 2.01. The binding energy shows an apparent increase at the surface for

Table 2.01. Parameters and results for bulk relaxation calculation, where d_0 is the nearest-neighbor distance, $\alpha(\pm)$ are the polarizabilities of the cation and anion, $R(\pm)$ are the computed relaxations (ignore the $\pm$ signs for neutral Xe).

Insulator	d_0 [Å]	α_+ [Å^3]	α_- [Å^3]	$R(+)$ [eV]	$R(-)$ [eV]
Xe	4.33	4.043[a]	———	1.37	———
NaCl	2.82	0.255[b]	2.974[b]	2.48	1.60
CaF_2	2.36	0.979[c]	0.759[c]	2.24	2.19
SrF_2	2.51	1.542[a]	0.759[c]	2.02	2.22

[a]From Clausius-Mosotti relation [b][Tes53] [c][Cat82, p.133]

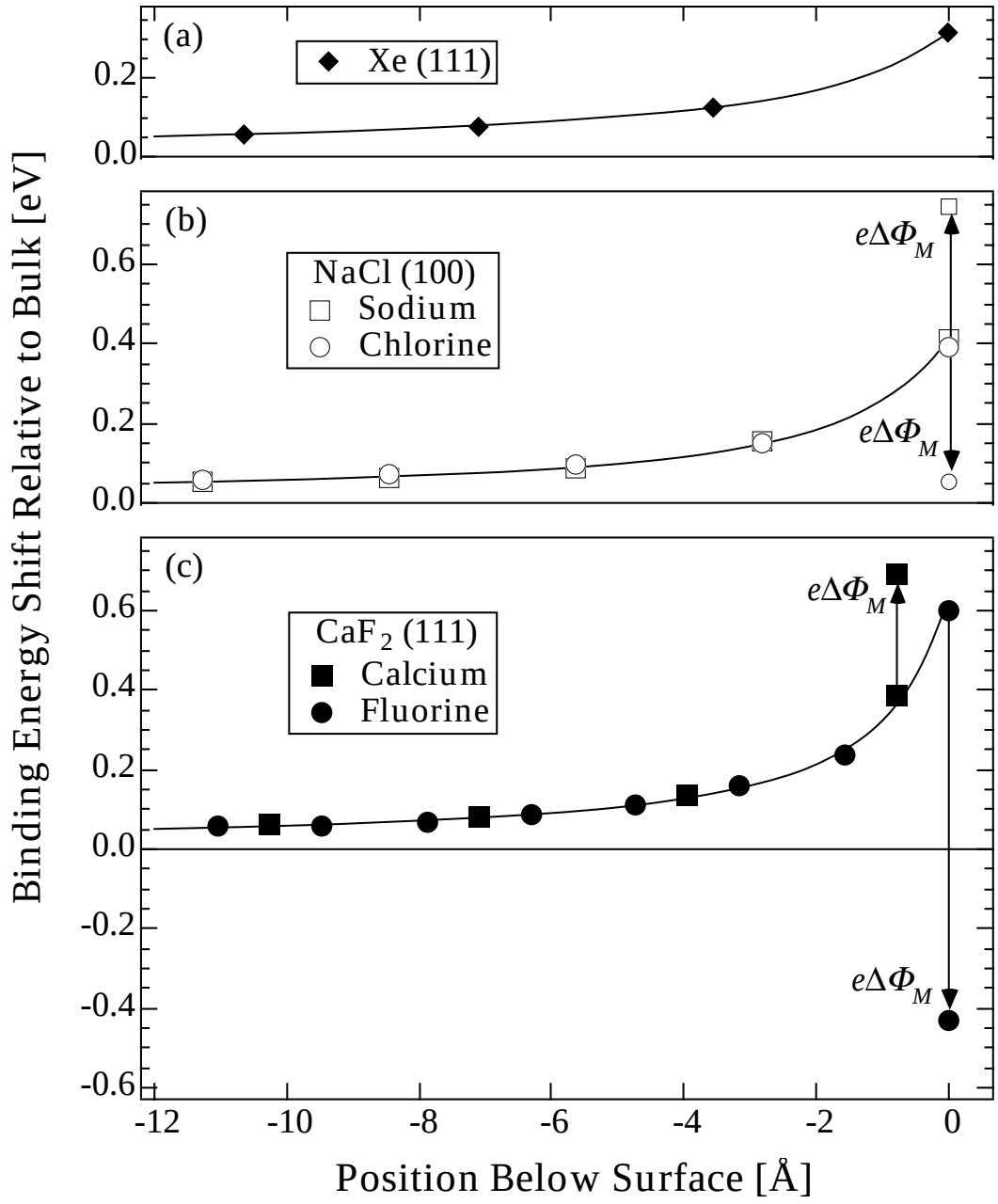

Figure 2.11. Predicted surface relaxation ΔR (symbols) for (a) Xe(111), (b) NaCl(100), and (c) CaF_2(111) surfaces. The curves are a simplified theory for the relaxation shift as discussed in the text. The arrows labelled $e\Delta\Phi_M$ represent the contribution from Madelung shifts, which are negligible for atoms other than those shown.

all atoms in the proximity of the non-polarizable vacuum. In these calculations, we assumed bulklike positions, valences, and polarizabilities for the surface atoms; these assumptions are not always valid for ionic crystal surfaces. The latter two assumptions are coupled: a slight departure from closed-shell configuration will greatly change the cation polarizability. This modifies the plotted results, in addition to introducing a new chemical shift and altering the Madelung energy. Our model can accomodate the removal of these restrictions, although we will see in Chapter 6 that the current model is sufficient to explain our $CaF_2(111)$ data.

The change in relaxation ΔR from the bulk to the surface, while confined in large part to the surface layers, penetrates somewhat into the crystals. The observed dependence of ΔR on the atom position is

$$\Delta R(z) = -Q^2(\varepsilon_\infty - 1)/[4\varepsilon_\infty(\varepsilon_\infty + 1)(z - z_0)], \qquad (2.24)$$

which, when z_0=0, is the same as predicted for a point charge in a continuous dielectric. The correction z_0 represents an effective distance of the sample surface above center of the highest atom. We have plotted (2.24) for comparison with the computed results in Figure 2.11 (solid lines) where z_0 was picked by least-squares fit to the computed points for Xe, NaCl, and CaF_2 (z_0=2.0, 1.5, and 1.0 Å, respectively). For these materials, z_0 is roughly equal to half the near-neighbor bond length, a rule which is useful in estimating $\Delta R(z)$ *a priori*. The agreement between (2.24) and the full calculation shows that the image charge approximation has validity even for core holes at solid surfaces.

The Madelung potential corrections $e\Delta\Phi_M$ have also been shown in Figure 2.11 (indicated by arrows) using the valences Na^+, Cl^-, Ca^{2+}, F^- (for other layers, $e\Delta\Phi_M < 0.015$eV). Relaxation will always act to enhance (diminish) surface core-level shifts for cations (anions) as predicted by the Madelung potential alone. Near interfaces with a more polarizable medium, such as semiconductors or metals, this conclusion is reversed. In either case, the relaxation shifts ΔR significantly modify the predicted core-level shifts based on the Madelung potential alone.

2.3.2 Xe surfaces: theory vs. experiment

Xe was chosen for the calculation because the rare-gas solids have minimal chemical or Madelung effects [Chi86, Jac88]. Experimental data supporting our surface computation were reported by Chiang, Kaindl, and Mandel (CKM), who found a surface-minus-bulk energy shift ΔR=0.26±0.04 eV for Xe 4d core levels [Chi86]. Using the measured electron escape depth of 3.65 Å, a weighted average of subsurface data of Figure 2.11(a) yields ΔR=0.22 eV, which is in satisfactory agreement with experiment. CKM, who model their data with (2.24) find a slightly better agreement (ΔR=0.25 eV) with experiment. However, they have arbitrarily chosen the free parameter z_0=1.8 Å; only experimentally verifiable parameters have gone into our calculation.

2.3.3 Effect of strain

Another important consideration in computing $\Delta\Phi_M$ and ΔR for heteroepitaxial films is the possibility of strain-induced lattice distortion induced by lattice mismatch between overlayer and substrate crystals. In this section we explore the effect of strain on the theory for CaF_2 and SrF_2, which are the subjects of experiments in this thesis. The normal and planar strains in tetragonally strained films are related by

$$e_\perp = -Ae_\parallel \tag{2.25}$$

where A depends on the elastic constants, and has the value A=0.958 for bulk CaF_2 and 0.880 for bulk SrF_2. The detailed derivation of this equation in terms of the crystals' elastic properties is presented in Appendix *A*. The fluoride lattice constants relative to Si may then be expressed as

$$a_\perp = -Aa_\parallel + m(1+A) \tag{2.26}$$

where a=(film lattice constant)/(Si lattice constant) and the lattice mismatch m is 1.006 for CaF_2 and 1.068 for SrF_2 at room temperature. In principle, only a finite range of $a_\parallel$ may be found for a crystal, constrained by the lattice mismatches both at room temperature and at the growth temperature. Between room temperature and all growth temperatures used in this

study, the fluoride lattices are larger than the Si lattice; therefore the smallest possible value of $a_{\|}$ is 1.00 (pseudomorphic growth). Since the fluorides have a larger thermal expansion coefficient than Si, the largest possible value of $a_{\|}$ is given not by the room temperature mismatches but instead by the larger mismatches at growth temperature: 1.025 (1.081) for CaF_2 (SrF_2) [Sch85]. This would be the case for a film fully relaxed to the fluoride lattice constant at the growth temperature. The persistence of the growth temperature mismatch at room temperature has been attributed to interface defects which pin the overlying lattice during cooldown [Has85].

Figure 2.12 illustrates the calculation of $e\Delta\Phi_M$, the difference in the Madelung potential energy between bulk and (a) surface anion and (b) cation sites, as a function of the lattice constants $a_{\|}$ and $a_{\perp}$. These plots indicate the length of the arrows in Fig. 10 as a function of the strain in the overlayer. Curve *H* represents all cubic fluorite lattices hydrostatically distorted between CaF_2 and SrF_2, (i.*e.,* for which $a_{\|}= a_{\perp}$) while curves *C* and *S* represent tetragonally distorted CaF_2 and SrF_2 crystals, respectively, with $a_{\|}$ and $a_{\perp}$ constrained according to (2.26). From (2.2a), $e\Delta\Phi_M$ scales as the inverse lattice constant along curve *H*; the dependence along the other directions is a more complicated function of the strain field and of the exact site being considered.

The tetragonal distortion affects the relaxation energy calculation in two ways. First, the altered atomic coordinates enter directly into the matrix $\ddot{\mathbf{M}}^{ij}$ in (2.15). Second, the calculation of ΔR requres consistency between the polarizabilities α_+, α_- and the dielectric constant ε_∞, which enters the calculation through **P** in (2.09). For bulk ionic crystals, which are not tetragonally distorted, consistent values of α_+, α_- and ε_∞ are compiled in the literature; in the strained films discussed below, these parameters may change due to compression of atomic orbitals. For these calculations, however, we assume that strained layers have the same polarizabilities as unstrained layers, and we estimate the dielectric constant from the Clausius-Mosotti relation [Jac86, p.155]

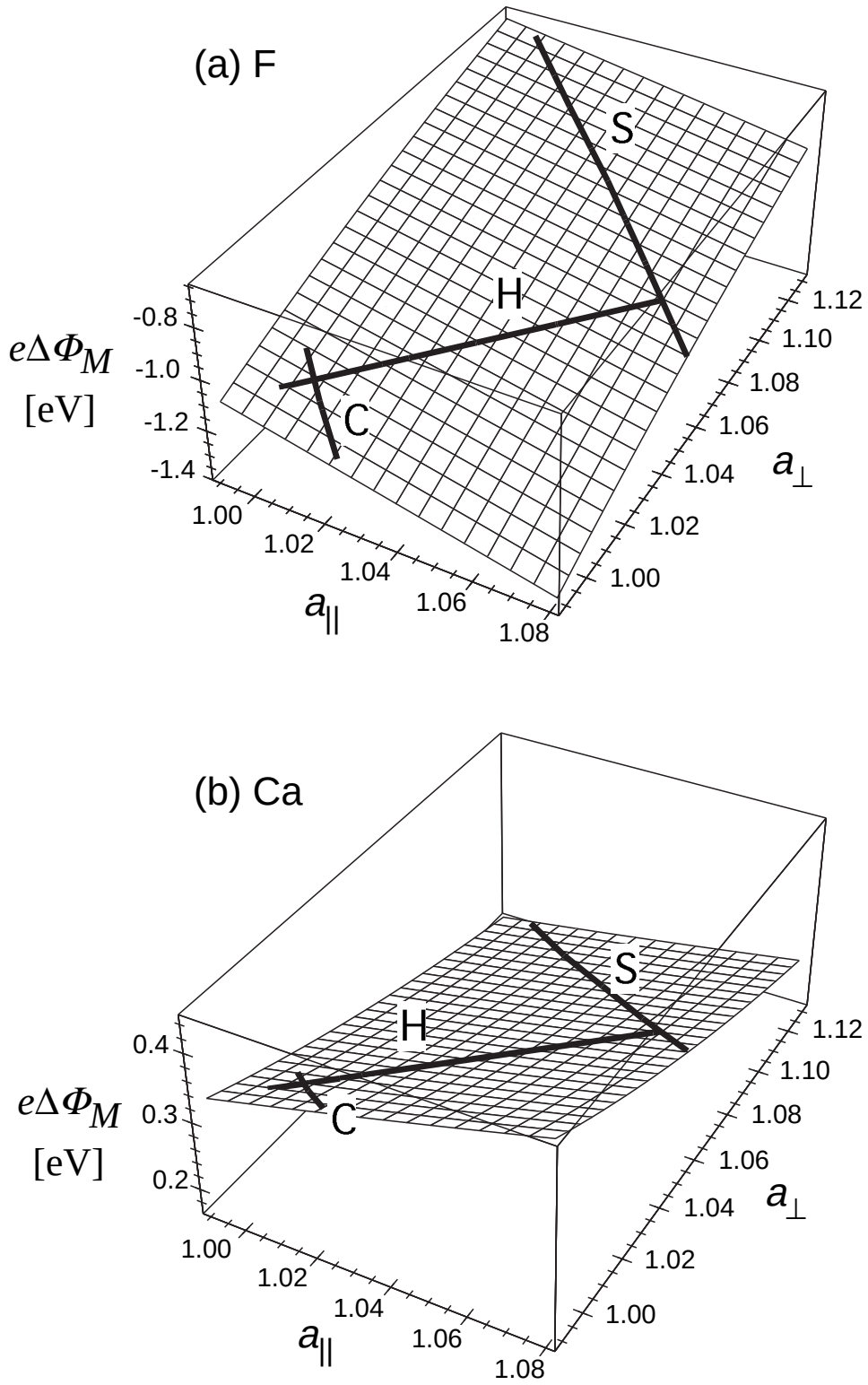

Figure 2.12. Effect of strain on the Madelung shift. Plotted is the difference in Madelung potential between bulk and surface for (a) anions and (b) cations in CaF_2-like crystals as a function of parallel and perpendicular lattice constants relative to Si.

$$\varepsilon_\infty = \frac{1 + 2(4\pi\alpha_{tot}/3v)}{1 - (4\pi\alpha_{tot}/3v)} \tag{2.27}$$

where α_{tot} is the total polarizability of the CaF_2 or SrF_2 molecule, and v is the volume per molecule in the presence of strain.

Figure 2.13 shows the calculation of ΔR, the difference in the relaxation energy between bulk and (a) surface anion and (b) cation sites, as a function of the lateral lattice constant $a_{\|}$. Because of the long calculation times, the calculation was not performed over all values of $a_{\|}$ and $a_{\perp}$ as in the Madelung calculation (Figure 2.12); instead calculations were performed only along the curves "C" and "S" and plotted along the $a_{\|}$ coordinate.

2.3.4 Other Substrate Effects

Madelung Calculation. For real films, the polarizability of the substrate must also be considered for both the Madelung and relaxation calculations. In the Madelung calculation, the substrate polarizes (in the initial state) such that each atom in the ionic overlayer feels the potential of an inverted, "image lattice" composed of image charges of the ionic lattice reflected across the insulator/substrate interface. The charges in the image lattice relative to the real lattice are given by the usual factor $f_M = -(\varepsilon_{sub} - \varepsilon_{film}) / (\varepsilon_{sub} + \varepsilon_{film})$ [Jac86, p.148]. This effect, however, turns out to be negligible for all but the Ca or Sr atoms at the fluoride/silicon interface due to the strong exponential attenuation of the Madelung potential and the large distance between the real and image lattices. At the interface atoms, the image Madelung potential tends to reduce the Madelung potential at a free surface alone, and the magnitude of the reduction is easy to calculate with the formalism developed in §2.1. For reasonable distance between Ca or Sr atoms and Si, the image lattice potential effectively cancels out the Madelung shift caused by truncating the film at the interface if the dynamic dielectric constants are used in computing Φ_M. But the proper dielectric constants to use in computing f_M are at low frequency, not high, since the configuration is in static equilibrium. In this case, $\varepsilon_0(CaF_2)$=6.8, and ε_∞(Si)=11.7 so that $f_M \approx 0.25$. This additional reduction in the

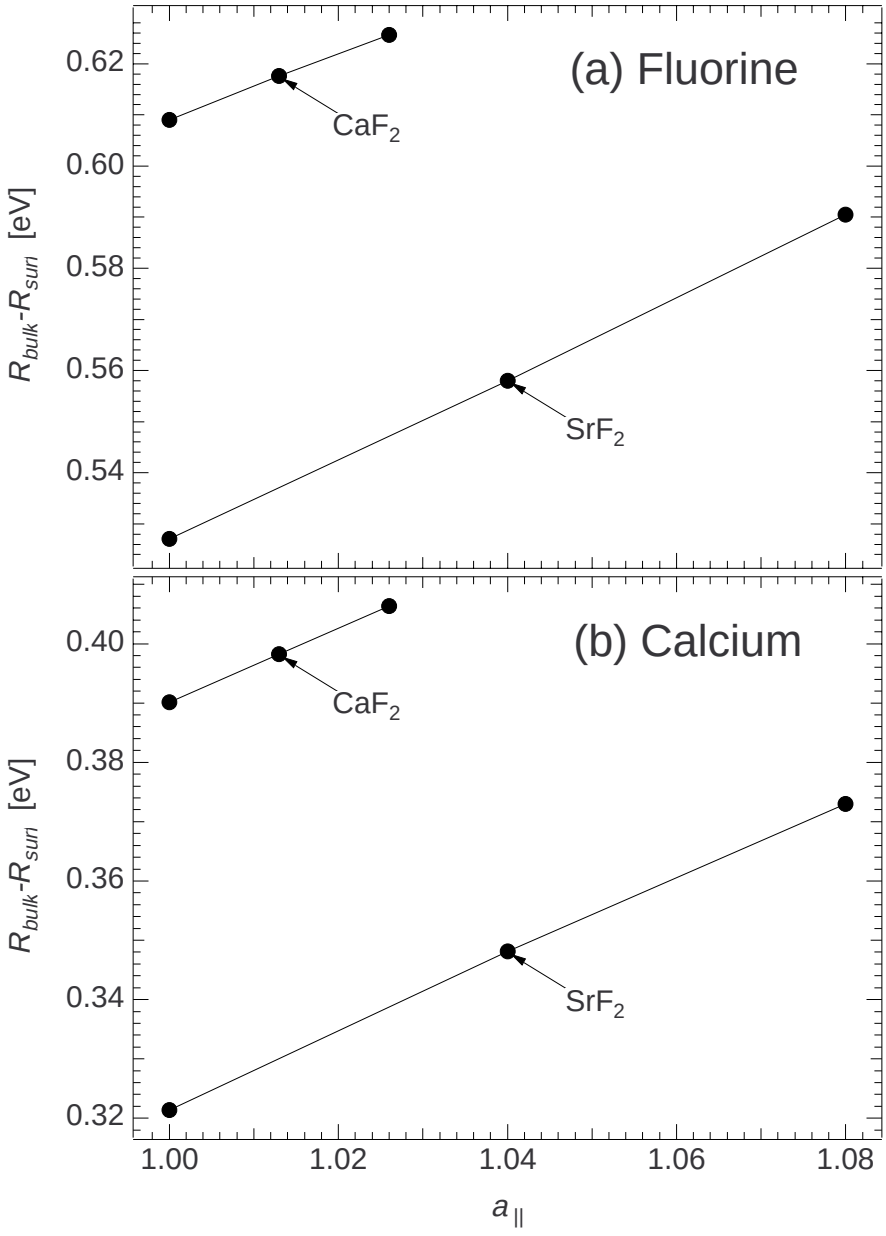

Figure 2.13. Effect of strain on the relaxation energy. Plotted is the difference in relaxation energy between bulk and surface for (a) anions and (b) cations in CaF_2-like crystals as a function of parallel lattice constant relative to Si. The perpendicular lattice constants are constrained as discussed in the text.

image lattice strength makes the effect negligible even for interface Ca and Sr atoms.

Relaxation Calculation. The substrate has a much stronger effect on the final state energy for interface emission. The substrate polarizes dynamically in response to the core hole, and, for metallic or semiconducting substrates (which have essentially infinite polarizability), the substrate polarization can dominate the observed interface core-level shifts. We cannot apply the simple point-polarizable atomic model to these substrates because the polarizable units are not localized to atomic sites, but are diffused throughout the crystal as free electrons or as covalent bonds. To approximate the substrate response, we have modified the relaxation scheme as follows. We consider the final state in the cluster to consist of a core hole Q, an image charge $Q_s = -Q[(\varepsilon_s-1)/(\varepsilon_s+1)]$ located in the substrate, a set of dipoles $\mathbf{p}^i$ in the cluster, and a corresponding set of image dipoles in the substrate. These image dipoles have a magnitude $|Q_s/Q|$ relative to their real counterparts, and a direction which is inverted parallel to the interface. The local field seen by the real dipoles (2.13) is now modified to include the fields of all of the image dipoles as well as that of the image charge Q_s. Also, the total relaxation energy becomes

$$R = R_{r<\rho} + R_{r>\rho} + |QQ_s|/4d_i \tag{2.28}$$

to account for the relaxation energy of the substrate.

This procedure modifies the coefficients of the matrix in (2.15) and (2.19), and necessarily introduces a new parameter to the calculation: the exact position d_i of the interface relative to the cluster. While the non-local relaxation energy (2.23) is not sensitive to this position (for sufficiently large clusters), the local relaxation part is very sensitive to it. For thin films, we allow this parameter to vary to find the best match to experiment.

Intra-atomic effects. Lastly, due to the chemical bond between Ca and Si, there may also be a chemical (intra-atomic) component to the shift at the interface Ca atom. Calculation of this effect is beyond the scope of this thesis. Rather, we ignore chemical effects, and calculate only the extra-atomic terms we have developed. The degree of agreement with the

expermental data will be used to set limits on the size of the chemical shift. This will be discussed further in Chapter 6.

2.3.5 Xe interface: theory vs. experiment

The procedure discussed above for handling polarizable substrates is now shown to give reasonable values for thin (2-4 layer thick) films of solid Xe adsorbed onto metallic substrates. In this system, there has been controversy over whether the substrate work-function shift upon growth is localized to the interface or is distributed over the overlayers. This question is equivalent to whether the initial state or final state effects dominate; the competing arguments are discussed by Jacobi [Jac88]. Our results fully support the final-state model within experimental accuracy.

In Figure 2.14 we show computed results for 1-, 2-, 3-, and 4-monolayer films of Xe on Pd(111), and we compare to the experimental results of CKM [Chi86]. We assumed a bulk-like structure for the film, and fit to a Xe-to-image plane distance of 2.3 Å. For Xe on Al(111) (not shown), we find a best fit to data with a larger distance of 2.8Å, which suggests that the surface electronic structure differs from that of Pd(111). From Figure 2.14, we

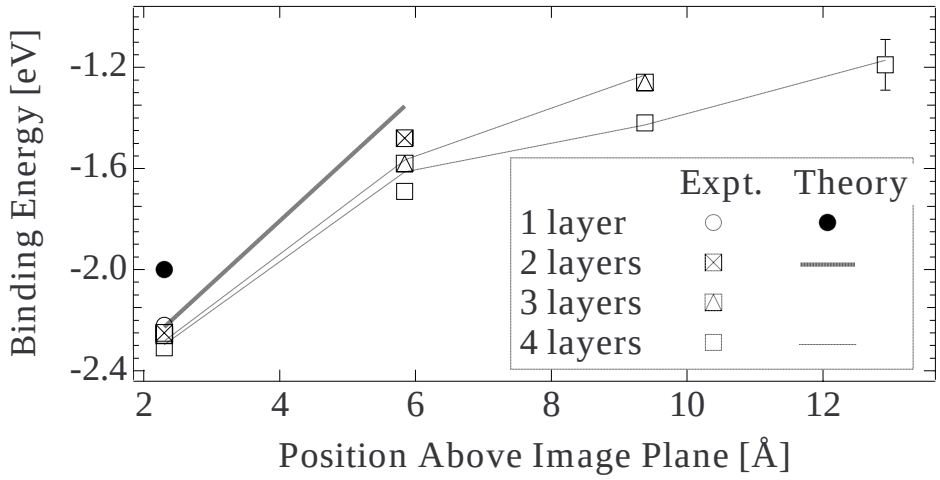

Figure 2.14. Layer-by-layer CLSs in Xe films: experiment *vs* theory. Experimental (open symbols) and theoretical(● and lines) Xe 4d core-level shifts for Xe on Pd(111) relative to gas phase Xe. The error bar indicates the experimental uncertainty in locating the vacuum level.

conclude that the experimentally observed shift is negligible between a monolayer and a monolayer covered by a second layer, while our theory predicts an enhanced binding energy of ~0.2 eV for the uncovered monolayer. For data from Xe on Pd(100) and Al(111) (not shown), the agreement is somewhat better. While this discrepancy may be due to uncertainties in determining the vacuum level (±0.1 eV), the single-monolayer value may also be accounted for if the Xe-Pd distance is contracted by 0.3 Å. This could happen if the Xe settles into hollow sites at submonolayer coverage, but is forced out when the layer becomes buried. This is consistent with observations that at submonolayer coverages Xe is commensurate with the (smaller lattice constant) substrate but becomes incommensurate at greater than one monolayer coverages [Wan84].

2.4 Summary

For the non-ionic solids, we have computed the surface and interface changes in extra-atomic relaxation due to the final-state-induced polarization in insulating films. We have shown that the image-charge approximation has validity in insulators even for surface charges. By testing our model for the case of a van der Waals insulator, we have shown the accuracy and usefulness of our calculation of binding energy shifts due to this mechanism.

For ionic solids, we have shown that this relaxation change can be comparable to the surface Madelung potential previously identified as causing the major surface core-level shifts in such systems, and hence must be considered in interpreting core-level shifts. Moreover, if surface or interface ions have a different ionicity than those in the bulk, then the polarizability can be modified hence further contributing to the relaxation change at surfaces and interfaces. This correction was not considered here, but may be accommodated easily within our model. Finally, these accurate calculations of inter-atomic contributions can be used in combination with experimental data to deduce the intra-atomic chemical shifts in surface and interface XPS. In Chapter 6, we will compare these theoretical calculations to experimental results from CaF_2 and SrF_2 on Si(111) films and find good agreement in these systems as well.

Apparatus 3

3.0 Introduction

The main techniques in this study are x-ray photoelectron spectroscopy (XPS) and x-ray photoelectron diffraction (XPD). Figure 3.01 shows a schematic view of the primary apparatus used for the experiments. The chamber was designed [Den93] to accomplish three goals: sample growth, sample characterization, and mobility (the entire experiment may be transported to available radiation sources). Samples are introduced to ultrahigh vacuum through the load lock (LL) which is separated from the main chamber (MC) by a gate valve. After pumpdown of the load lock, the samples are passed with a magnetically coupled transfer arm (TA) into the main chamber's lowest level. Further transport in the chamber is via the manipulator (M), which serves both to transport and orient the sample with polar (θ) and azimuthal (ϕ) rotation. Samples are cleaned by high temperature annealling and their cleanliness characterized by low energy electron diffraction (LEED, middle level) and photoelectron spectroscopy (upper level); this is followed by deposition of thin films from the Knudsen cells (KC) at the lower level. Samples are finally returned to the upper level where photoelectron spectra may be acquired. The source is an x-ray anode (XRAY) or synchrotron radiation source; spectra are collected with an electrostatic lens (ESL), monochrometized by a hemispherical electron spectrometer (HES) and counted with an electron multiplier tube (EMT). Used samples may be cleaned by repeated cycles of high temperature annealling and ion sputtering using the sputter gun (SG) at the middle level.

The detailed discussion of the apparatus begins with the ultra high vacuum hardware, followed by the electronics.

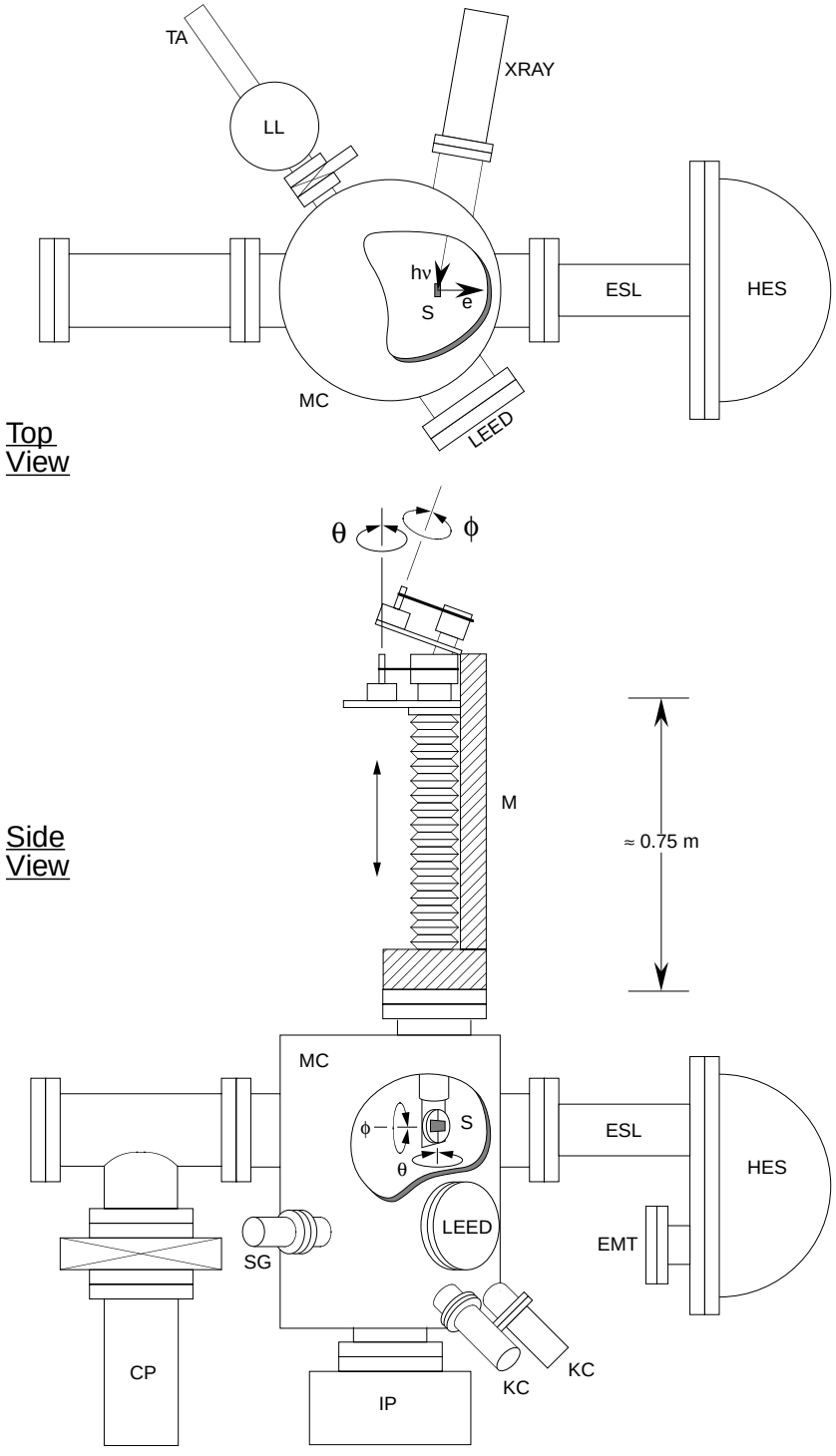

Figure 3.01–Simplified experimental schematic. Major components illustrated: CP=cryopump, ESL=electrostatic lens, HES=hemispherical electron spectrometer, IP=ion pump, KC=Knudsen cell, LEED=low energy electron diffraction, LL=load lock, M=manipulator, MC=main chamber, EMT=electron multiplier tube, S=sample, SG=sputter gun, TA=transfer arm, XRAY=x-ray source

3.1 Ultra High Vacuum

The processes investigated in this thesis are highly susceptible to disruption by contamination. Therefore, experiments are performed in an ultrahigh vacuum (UHV) environment. In this environment, sensitive samples may be safely stored for hours to days while experiments are performed on them. Typical modern UHV systems can achieve pressures as low as ~0.5×10^{-10} Torr (1 Torr = 133 Pa = $^1/_{760}$ atm) with only modest care. Special materials must be used for the chamber and included apparatus; such materials are those which neither excessively outgas their constituents into the vacuum nor otherwise degrade in the extreme conditions (pressure and temperature) used in the experiments. Thus, the materials in the chamber are almost exclusively ceramics, aluminum, low-oxygen-content copper, and non-magnetized stainless steel (type 304). We used ceramic beads to electrically insulate copper conductors except in some special situations where we needed the extra flexibility of Teflon-coated wires.

3.1.1 Pumping

Three main types of pumps are employed: a turbomolecular pump ("*turbo pump*") used for rough pumping, and a helium cryopump and two ion pumps for ultrahigh vacuum (UHV) pressures. Figure 3.02 illustrates the pumping schematic.

Turbopump. The turbopump is the backbone of the system; it rough pumps the main chamber, the load lock, and the cryopump. It also pumps out the gas line between an argon cylinder and the main chamber. The operation of this pump (Leybold TMP-150) is through direct momentum transfer between fast-revolving rotors (45,000 RPM) and the gas molecules. Unlike the other pumps in the system, the turbopump is not very sensitive to which particular atoms and molecules are being pumped. Also, to maintain the high rotational velocity needed, the turbopump is backed up by a rough mechanical pump. To prevent grease contamination (backstreaming) of the system by the latter pump, care must be taken during turn-on. The turbopump must achieve full speed before opening a valve to any

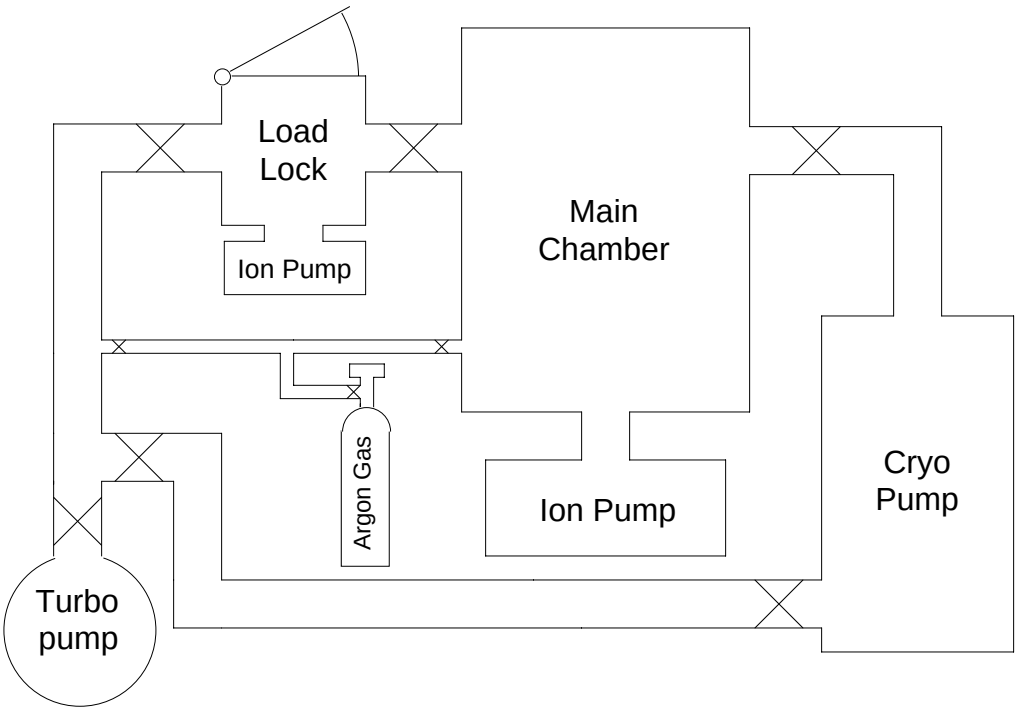

Figure 3.02–Schematic of pumping system. (× = valve)

low-pressure chamber. Using the turbopump, pressures ~10^{-8} Torr may be achieved, depending on the cleanliness of the vacuum chamber.

Ion pumps. The load lock and the main chamber are each equipped with an ion pump to take the system pressure from ~10^{-7} Torr down to ~10^{-10} Torr (In the load lock, our base pressure was limited to ~1×10^{-9} Torr because of the poor seal of the quick-access door). The principle of operation varies with whether the gases being pumped are chemically active or noble gases. In ion pump operation, a high voltage discharge strips electrons from a large Titanium cathode surface; these spiral towards the anode due to an imposed magnetic field. These orbits are desirable to enhance the probability of electron-impact ionization of the ambient gases. The ionized gases are then accelerated into the cathode, ejecting (sputtering) neutral Ti atoms. These Ti atoms continuously coat the anode with a fresh gettering surface, which binds to chemically active gases in order to maintain pumping

action. Noble gases are therefore not pumped by this mechanism; a secondary mechanism (about an order of magnitude less efficient) pumps these atoms. Noble atoms are eventually ionized by the electron current and are accelerated into the cathode. A certain portion are buried in some "shadowed" regions of the cathode and are not resputtered back into the chamber.

To aid in pumpdown of the system before ion pump operation, the main chamber's ion pump is backed up by a Titanium sublimation pump. This pump consists simply of a Titanium filament through which a 50 A current is passed. This heats the filament to a sufficiently high temperature (~1000° C) to sublimate Ti atoms onto the pump's interior surfaces, which we sometimes cooled to liquid nitrogen temperature to avoid excessive outgassing. Because no gas ionization takes place, this pump is primarily effective at pumping chemically active gases. Furthermore, we found that operation of this pump is restricted to pressures in excess of 10^{-8} Torr, due to heating of the pump walls and the excessive outgassing that this heating causes.

To aid in pumping of N_2, H_2O and CO_x gases, we sometimes flowed liquid nitrogen through the Ti sublimation pump even without current passing through the filament. This lowered the best pressure achievable with the ion pump alone from ~ 10^{-10} Torr to 7×10^{-11} Torr simply by condensation of these gases onto the cold surface, or *cryoshield*, inside the pump. After liquid nitrogen flow ceased, the surfaces would warm up and the gases would be rereleased.

Cryopump. The main chamber was eventually upgraded to include a *cryopump* in order to enhance the pumping rate as well as to achieve a lower base pressure. The latter became more important when the duration of data acquisition became on the order of the lifetime of the samples due to contamination by ambient oxygen. The principle of operation is an extension of the simple cryoshield concept. In the first stage, N_2, H_2O, and CO_x gases are adsorbed onto a series of baffles held at ~liquid nitrogen temperature. Lighter gases which

do not condense at these temperatures (He, H, Ne) pass into the second stage of the pump, which consists of a liquid helium-cooled porous graphite element. The baffles perform a dual purpose; in addition to condensing heavier gases, they act as a heat shield to protect the graphite element from ambient infrared radiation. Using the cryopump, we were able to achieve pressures between 6 and 10×10^{-11} Torr.

Although the pressure improvement was dramatic when the cryopump was operating (typically a factor of 2 reduction in gas density), we usually only operated the cryopump during data acquisition. This was because of the loud, incessant thumping sound emanating from the helium compressor.

3.1.2 Pressure Measurement

Two different commercial pressure gauges were employed. The load lock contained a compact, low-maintenance *cold cathode gauge* (Leybold). The principle behind this gauge is similar to the ion pump: an electron discharge is orbited in a modest magnetic field. The current of ionized gases onto the cathode is calibrated to read the pressure; the useful range of the gauge is between 10^{-3} Torr to 10^{-7} Torr. Below this pressure, the discharge cannot be maintained with the modest high voltage (~1 kV) employed. The main purpose of this gauge was to determine when the pressure in the main chamber or load lock was low enough to cross over from the turbo pump to the ion/cryopumps.

The main chamber's ion gauge was in contrast a *hot cathode gauge* (Varian). These gauges achieve electron current flow through thermal emission from a hot filament. Because the gauge does not use a magnetic field (which would disrupt the other experiments in the chamber), the ionization efficiency is reduced so that an expensive amplifier is needed to measure the ion current. Also, the filaments have a short enough lifetime that their failure can occasionally disrupt experiments. But the advantage of this gauge over the cold cathode gauge is that it can be used to much lower pressures, typically 5×10^{-11} Torr.

3.2 Sample Holder

The sample holding system, attached to the bottom of the manipulator arm, was custom-designed and built by our group to serve three purposes: (i) to transport Si wafers between the load lock and manipulator without breaking vacuum, (ii) to accurately orient the wafer in front of the detector system, and (iii) to allow efficient sample heating. In addition, the design had to be as compact as possible to allow the sample to be positioned close to the x-ray source.

3.2.1 Degrees of freedom

The manipulator arm is a commercial (Vacuum Generators, Ltd.) bellows-type transporter with accurate (x, y, z, θ) degrees of freedom (see Figure 3.01). The bottom of the manipulator arm is a stainless steel cylinder; inside this is a stainless steel rod with 2 cm of vertical travel. This linear motion is actuated by a rotating knob, labelled ϕ in Figure 3.01, and was adapted to give an additional azimuthal (ϕ) degree of freedom as discussed below.

Figure 3.03 shows a closer schematic of the manipulator/sample holder system. To effect ϕ motion, the 2 cm vertical travel by the inner rod is connected by a horizontal linkage to a rack-and-pinion. The pinion, or gear, is mounted on a ceramic shaft with small holes drilled down the center to pass current leads to the stainless steel rotation stage. The ceramic shaft rotates in a grease-free bearing for smooth motion. Ceramic spacers keep the two D-shaped halves of the rotation stage from touching each other and the steel backing plate. The two current leads (not shown) complete a circuit only when the molybdenum sample holder is introduced. This sample holder was held in place by spring-steel (type 302) clips (not shown), and contained notches for the transfer arm to securely embrace it for transport onto the rotation stage.

The design employed was simple and compact; more importantly it allowed for unimpeded resistive heating as discussed below. The disadvantage of the system was excessive backlash in the azimuthal rotation, making this motion somewhat irreproducible.

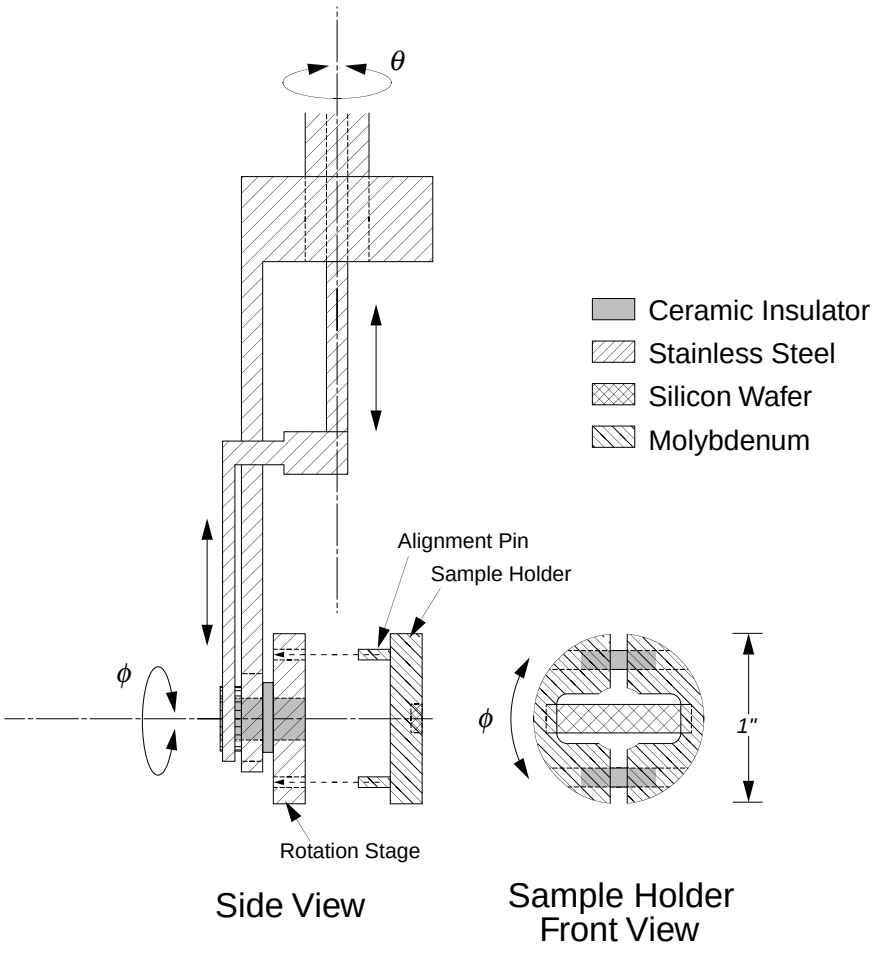

Figure 3.03–Detail of sample holder system. The molybdenum sample holder is transferred *in vacuo* to the stainless steel rotation stage, which has wires for sample heating (not shown), and azimuthal (ϕ) rotation. The entire manipulator has polar (θ) rotation as well.

We eventually adopted the procedure of carefully aligning ϕ once and then scanning θ, which was a much more accurate rotation.

3.2.2 Resistive-heating sample holder

Molybdenum sample holder. As illustrated, the molybdenum "D's" are separated from each other by ceramic spacers. A cavity carved into the D's contains the Si wafer and clips made of tantalum springs to hold the wafer into place. Therefore, the heating circuit is completed directly through the Si wafer so that the samples are resistively heated. A simple calculation which considered the geometry and thermal parameters of Si and Mo showed that modest currents (~8 Amps) would suffice to heat the Si wafers to sufficiently high temperatures (≤1000°C). We used Si wafers of dimensions ~1 cm × 0.5 cm × 1 mm.

Molybdenum and tantalum were chosen as the only metals to contact the Si wafers. The reasons were twofold. First, low thermal conductivity was important to avoid conducting the heat away from the sample. The consequences would be needing too high a current to heat the sample, as well as heating/outgassing of other components. Second, we needed to avoid chemical formation of metal-silicides as might occur at high temperatures. Both metals form silicon compounds ($MoSi_2$, $TaSi_2$, Ta_5Si_3, etc.); the formation temperatures for these metals on silicon are ~750°C and higher [Dol90, Mah91], comparable to temperatures used in this study. However, the metal contacts are at the coolest parts of the sample (due to thermal conduction), so chemical reactions should be minimal. In practice, we found small regions (~1 mm) of Si near the metal/Si contact area with poor LEED patterns, presumably due to Mo diffusion onto these areas. These areas have no effect on our XPS measurements, and only minimal effect on our XPD measurements, due to the small fraction of Si area affected.

Resistive heating takes place in two stages. At low temperatures, (lightly doped) Si has high resistivity, typically a few Ω-cm. Therefore, at turn-on the power supply is voltage-limited. As current passes through the sample, the resistance gradually reduces as the sample

gradually warms. The reduction in resistance is due to the increasing number of electrons thermally excited across the Si bandgap. Eventually the sample suddenly undergoes a transition to metallic-like resistivity (~350-450°C), and the power supply becomes current-limited. We chose a rugged commercial power supply (Hewlett-Packard 6274B) which could handle this transition from constant-voltage to constant-current operation smoothly. Increasing the current to ~3 A brings the sample to 800°C. Beyond this temperature, radiative losses begin to dominate conductive losses, so that it takes a very large current (≥ 8 A) to achieve temperatures on the order of 1000°C. We were limited to this temperature due to the current capacity of the heating wires, the excessive heating of nearby components (which leads to outgassing and poor operating pressures), as well as wear and tear on the sample holder due to mismatched thermal expansion coefficients in its components.

Temperature measurement. The sample temperature was measured with a portable commercial optical pyrometer (IRCON). Similar to a camera with a zoom lens, the pyrometer head was mounted on a tripod and aimed at the Silicon through a window in the vacuum chamber. The head was calibrated using a Si emissivity of 0.65 as per the manufacturer's recommendation. The relative accuracy of the head is very high: within ±5°C. The absolute accuracy is more questionable, however a LEED/pyrometer measurement of the Si 7×7 to 1×1 transition temperature (discussed further below) was ≈820°C, close to the accepted transition temperature (830°C) from the literature [Lat91, Che92].

3.3 Sample preparation

There are two methods we used for sample preparation:

(1) Wet chemical etching

(a) Shiraki-etching of sample wafers to create a protective oxide [Ish86]

(b) Introduction through the load-lock into the main chamber

(c) Thermal annealling treatment to remove the protective oxide

(d) Verify cleanliness with electron spectroscopy and LEED

(2) Sputter/Anneal Cycles

(a) Anneal sample to remove gross contaminants

(b) Ar+ ion bombardment, or *sputtering* to further remove contaminants

(c) Thermal annealling to repair sputter damage

(d) Verify cleanliness with electron spectroscopy and LEED

(e) repeat if needed

Method (1) was always used when new wafers were put into the chamber. Method (2) was used to either reuse a sample which had had a film grown on it, or occasionally when minor contamination had occurred, e.g. when a CaF_2/Si film was briefly exposed to atmosphere. The rest of this section details the two methods.

3.3.1 Wet chemical etching

The chemical etch used was that of Ishizaka and Shiraki [Ish86]. In this procedure, wafers are initially degreased with methanol/water rinses. Special care was taken to use high purity, deionized water to avoid contamination. The smallest traces of contamination produced wafers that were ultimately useless. After degreasing, the sample was alternately dipped in HNO_3/water/HF to remove any native oxide and surface carbon. In the latter step, the test for cleanliness was that water would not "wet" the silicon. The final step was to chemically react onto the wafer a thin (few monolayer) oxide layer in a mixture of HCl and H_2O_2, followed by storage in pure water before introduction into the chamber. This procedure require special consideration for safety due to the corrosive acids handled, the toxic fumes generated, and the somewhat violent reaction in the last step.

After introduction to the chamber, the sample was gradually heated to ~600°C and left for several hours. This would outgas the sample holder, while leaving the protective oxide intact. The minimum temperature required for desorbing the protective oxide was ~710°C; thermal annealling at ~800°C was used in our case. Sample cleanliness was then verified using LEED and electron spectroscopy (discussed below).

3.3.2 Sputtering

The sputtering procedure consists of raising the ambient chamber pressure to ~5×10^{-5} Torr with purified Ar gas using the gas-line arrangement in Figure 3.02. The sputter gun (SG in Figure 3.01) consists of a hot filament; electrons boiled from the filament ionize the Ar gas into Ar^+ ions which are accelerated and focussed through a small einzel lens (see §3.5.2) and accelerated towards the sample, where they impinge at grazing incidence. The ion current on the sample was typically 10 μA, so that many atomic layers are removed in a reasonable time (~30 minutes). The chamber is then evacuated of the remaining Ar atoms.

Under this procedure the sample surfaces are quite damaged with a roughness on the order of 10's of atomic layers. However, the surface mobility of Si atoms is extremely high at temperatures ≥800°C [Bar93] so that thermal treatment at this temperature for a few minutes allows us to recover atomically flat Si surfaces. Sample cleanliness was then verified using LEED and electron spectroscopy (discussed below).

3.3.3 Molecular Beam Epitaxy

Having cleaned and characterized a Si wafer, a film may be grown upon it. In this study, we grew films of CaF_2 and SrF_2, as well as mixed multilayer films. Figure 3.04 illustrates the molecular beam epitaxy (MBE) method. Crystallites of CaF_2 or SrF_2, a few mm across, are placed in separate commercial MBE Knudsen-type cells (WA Technologies Ltd.). This cell consists of either a boron nitride or graphite crucible surrounded by a filament and held within Ta heat shields nested in a water-cooled jacket. The assembly also includes an integral shutter for ease of use. In contact with the crucible there is also a tungsten-rhenium thermocouple (the original manufacturer's thermocouple was platinum-rhodium; however we found that the K-cell temperature was high enough to melt this thermocouple, so we had to replace it). The current and thermocouple wires are fed to a temperature controller; the overall system was designed to maintain a steady temperature up to ~1400 ± 1°C.

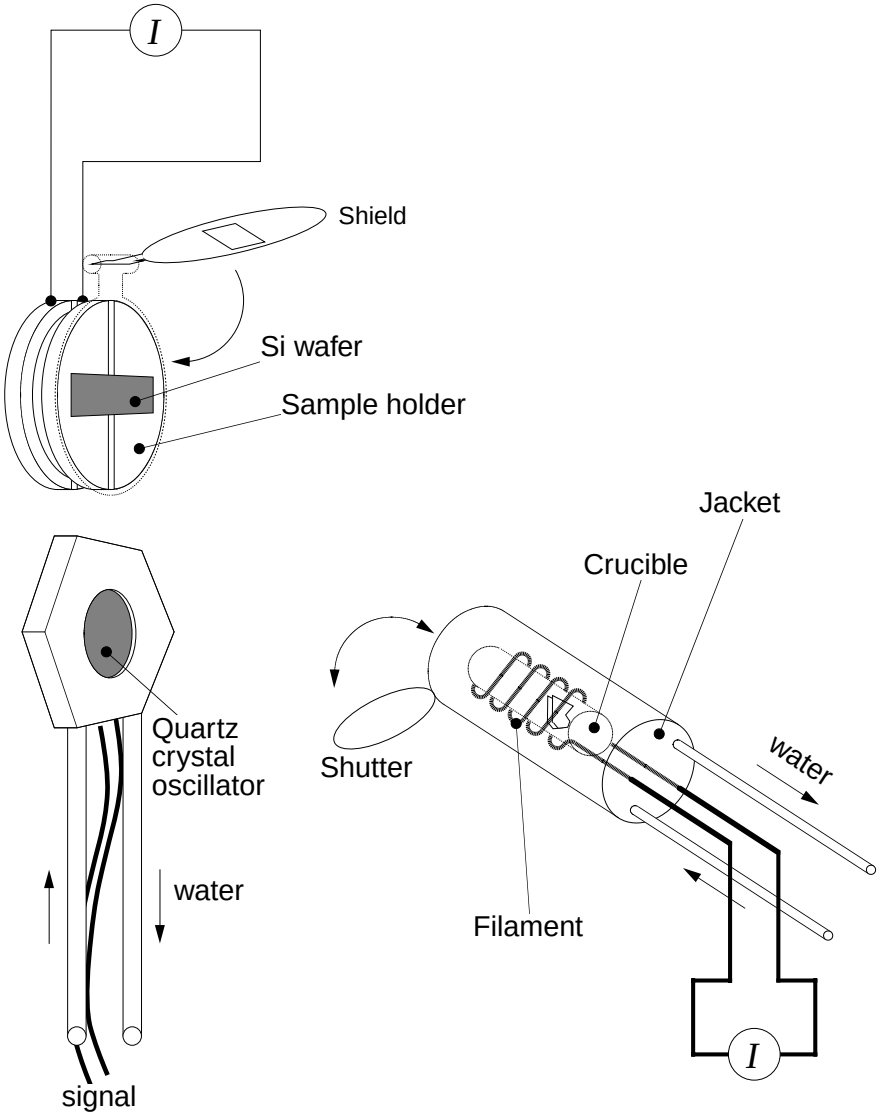

Figure 3.04–Molecular Beam Epitaxy Components. Upper left, the resistively heated sample holder with integral shutter. Lower left, quartz crystal oscillator used to measure calibrated molecular flux. Lower right, Knudsen cell consisting of a crucible, filament, water-cooled jacket, and integral shutter.

At temperatures of ~1000-1200° (the exact temperature measurements are inaccurate because of the proximity of the K-cell filament to the thermocouple), CaF_2 and SrF_2 sublimate from the bulk crystals as molecules [Blu63]. To calibrate the flux rate, we placed a moveable quartz-crystal oscillator head (Leybold) in the sample position and exposed it to a flux of molecules. This device is a simple RF oscillator (≥ 6 MHz) with a frequency counter/ digital readout. The electronics are sensitive enough to detect small changes in the oscillation frequency as impinging molecules stick to the quartz crystal, which increases its mass. In fact, the slowest rate detectable is better than 0.1 Å/sec. The electronics are programmable for the exact material being grown and allows an arbitrary tooling factor to compensate for any geometry. Our flux calibration was based on the experimental thickness unambiguously obtained in this study. The flux range in this study is from 5 to 110 Å/minute.

Once the K-cell has stabilized so that the measured flux is steady, the flux meter is removed, and the sample is moved into position (with the K-cell shutter closed). The sample has had a moveable shutter lowered (see Figure 3.04) so that no film is grown on the Mo surface. This shutter is then removed during data collection later, so that the electron spectrometer sees only CaF_2 on Si and not CaF_2 on Mo. The sample has also been raised to a stable temperature between room temperature and 800°C. The K-cell shutter is opened for a specified period, and then closed. Usually, we followed the sample growth with a short (~30 sec) thermal anneal at various temperatures from 400-700°C. This is to prevent contaminants from sticking to the film, since activating the K-cells raises the ambient pressure to ~3×10^{-8} Torr. Within ~30 sec of deactivating the K-cell, the pressure lowers to acceptable levels to stop the resistive heating current.

3.4 Low energy electron diffraction

The commercial LEED apparatus (Perkin Elmer/Princeton) is shown schematically in Figure 3.05. The basic LEED apparatus is reviewed by Pendry [Pen74]. Electrons are thermally emitted from a hot thoriated tungsten filament. The thorium lowers the tungsten

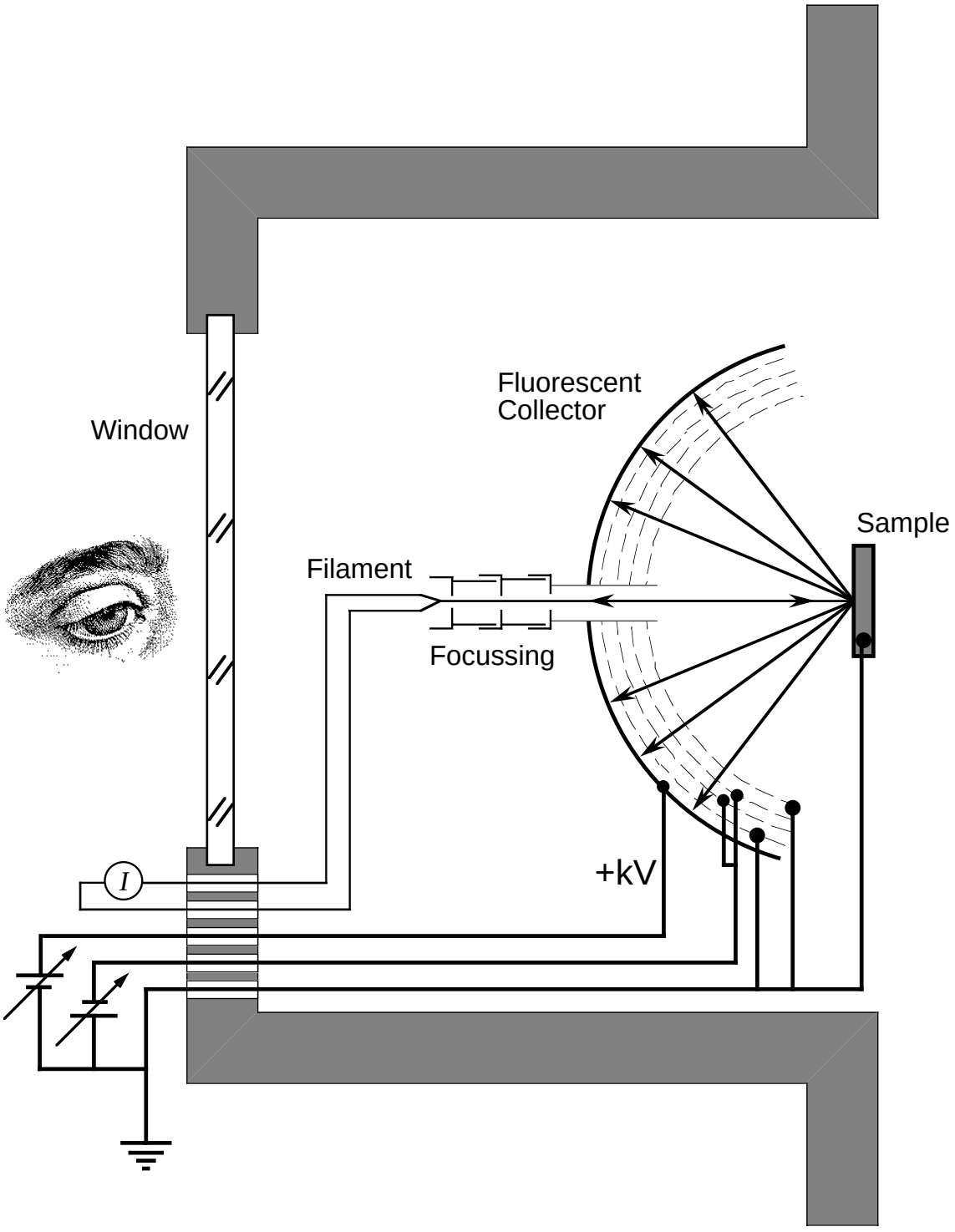

Figure 3.05–Low Energy Electron Diffraction (LEED) apparatus. Electrons thermally emitted from the filamant are focussed onto the sample. Elastically scattered electrons are passed by the grids and accelerated onto the fluorescent collector grid.

work function so that lower temperatures (~1000°C) are required to excite electron emission. The electrons are focussed by a small einzel lens (discussed below in connection with the electron spectrometer) onto the sample surface, which is at the center of several concentric hemispherical grids. Diffracted electrons are scattered back towards the grids. The first two grids are used to reverse the paths of electrons which have scattered inelastically at the sample surface. Elastically scattered electrons, on the other hand, continue past the third grid, and are accelerated via a high potential (~2 keV) onto the final grid, which acts as a fluorescent screen. The diffraction pattern is viewed through the window shown in Figure 3.05.

Figure 3.06 illustrates the simple kinematic scattering model for LEED. Any two dimensional lattice, such as occurs at a crystal surface, has a two-dimensional reciprocal lattice in the surface plane. The reciprocal lattice "points" in the normal direction are distributed along finite rods, called *crystal truncation rods*. Given this reciprocal-space distribution, the standard Ewald-sphere model describes the diffraction scattering (Figure 3.06(a)). Since the electron energy is ≤ 50 eV, the Ewald sphere radius is on the order of the reciprocal lattice dimensions. Intersections between the sphere and the crystal truncation rods give the scattered vectors as shown. Although the LEED *patterns* observed are determined by this construction, the *intensities* are not easily predicted; multiple scattering between the incident electrons and the solid surface preclude a simple structure-factor analysis. Dynamic electron scattering theory must be employed to find the correct intensities.

For the case of Si(111) surfaces in this study, the diffraction pattern of the simple bulk-terminated surface appears hexagonal (Figure 3.06(b)). The relative intensities of the spots is energy-dependent, and in general at most a 3-fold symmetry is observed. When Si(111) is thermally treated in the cleaning process, the surface takes on a characteristic reconstruction with a unit cell 7×7 fundamental unit cells large [Tak85]. This complicated reconstruction leads to a characteristic LEED pattern (3.06(c)), which can be used to determine the wafer orientation. In particular, for kinetic energies between 40 and 45 eV, we

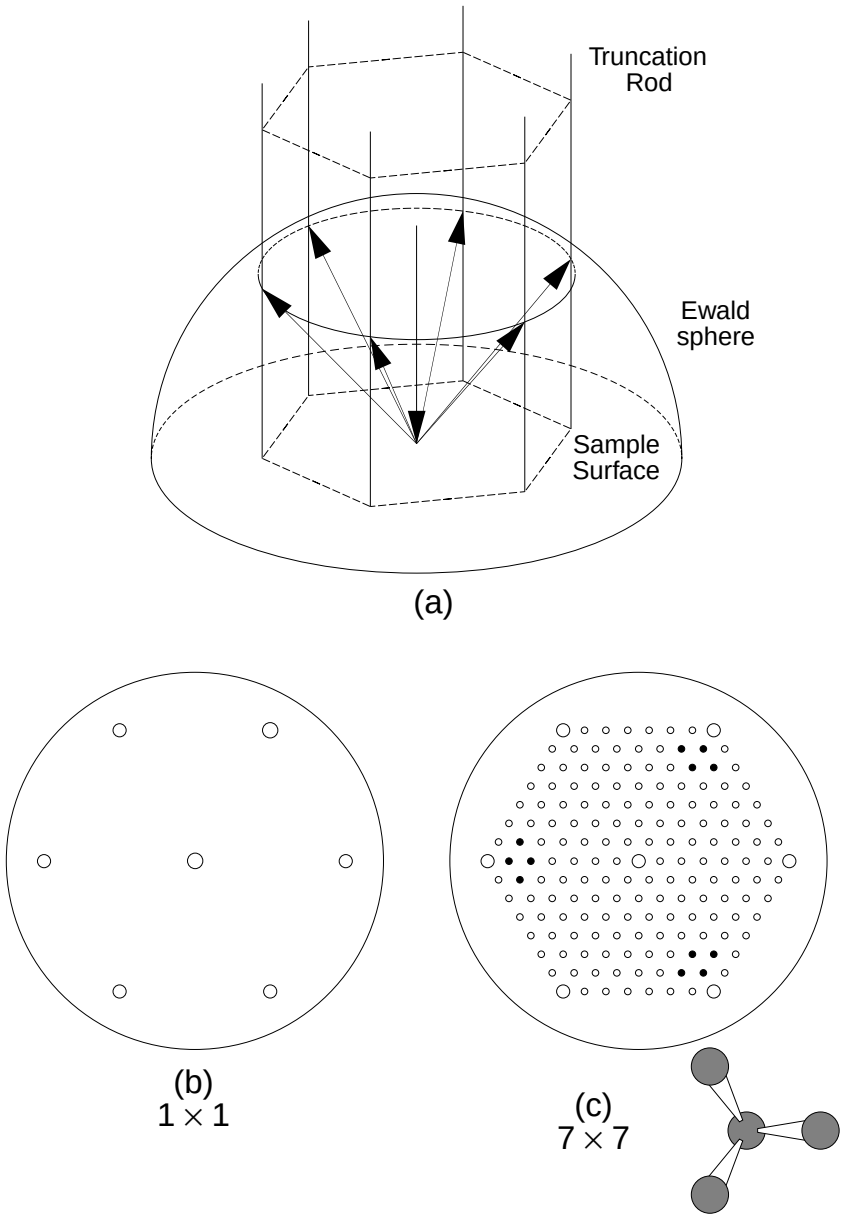

Figure 3.06–LEED patterns. (a) Surface crystal truncation rods intersect the Ewald sphere to determine scattered electron vectors. (b) hexagonal pattern obtained in principle from bulk-terminated Si(111) surfaces. (c) actual pattern obtained from clean 7×7-reconstructed Si(111) surfaces. The black spots have a weaker intensity, and their angles are correlated with the orientation of the bulk tetrahedra (see inset).

reproducibly observe some weak spots (illustrated as black in Figure 3.06(c)). This indicates that the bulk tetrahedra in the sample are oriented as in the small inset in the figure, as determined by XPD studies (Chapter 4).

There are three ways to characterize samples using LEED. First, we observe the amount of diffuse scattering. This scattering is manifested as a uniform background glow, and is minimized for the cleanest (i.e. best-ordered) samples. Large diffuse scattering is correllated with surface contaminants such as carbon. Second, we look for the characteristic 7×7 diffraction pattern of the clean Si(111) surface and verify its sharpness. Third, the LEED pattern is obtained during thermal treatment.. At ~830° the Silicon (111) exhibits a phase transition from 7×7 to 1×1 [Lat91], a transition whose mechanisms are still unclear. In our system, the transition consistently occurred at 820°C for clean samples; otherwise the transition was lowered by several degrees (This discrepancy with the literature value represents our slight temperature miscalibration). This is because the transition is governed by the strain near step edges [Lat91, Che92], which is modified by the presence of contaminants.

3.5 Electron Spectroscopy System

In this section we describe the electron spectroscopy system with which the main experimental results are obtained. Figure 3.07 shows the spectroscopy setup. X-ray radiation from a Mg or Al anode broadly illuminates the samples. Photo- and secondary electrons are emitted from the sample; the electrostatic lens accepts a limited solid angle of this emission and passes this current to the hemispherical spectrometer. The electron spectrometer is controlled externally through a microcomputer interface so that spectra are acquired digitally.

3.5.1 X-ray Anode

As indicated in Figure 3.07, the x-ray lamp is a dual anode type; two separate tungsten filaments direct thermally emitted electrons towards either a Mg or an Al anode. The emission of electrons is aided by the accelerating voltage (typically 11-12 kV) between

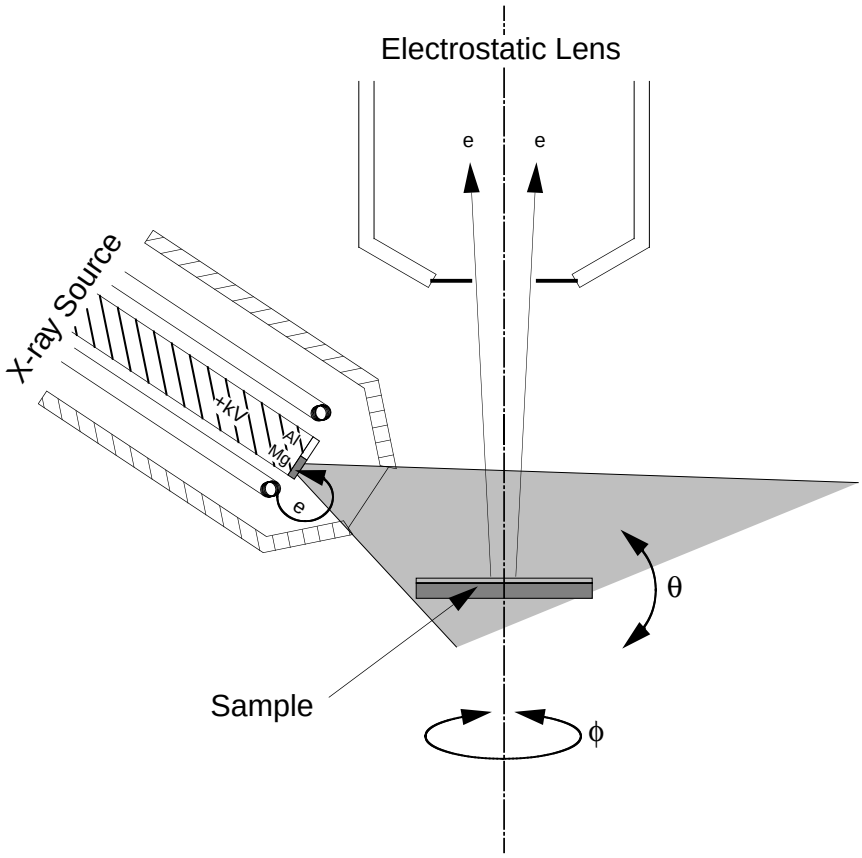

Figure 3.07–Electron spectroscopy schematic. X-rays emitted from the Mg or Al anodes broadly illuminates the sample; primary and seconday electron emission are collected by the electrostatic lens for transmission to the spectrometer.

the cathode filaments and the anodes. The regulated current supply can only operate one filament/anode combination at a time. The radiation consists of two parts: broad-band weak bremsstrahlung radiation and sharp, intense line radiation. In addition, there is also a flux of unwanted, stray electrons directed towards the sample. Only the sharp line radiation is useful; therefore a thin (0.8 μm) Al window is suspended between the anode assembly and the sample to filter the bremsstrahlung and stray electron radiation.

The strongest useful emission lines correspond to the following transitions:

$$\begin{aligned} K_{\alpha 1}&: 1s^1 2p^6 \rightarrow 1s^2 (2p^5)_{1/2} \\ K_{\alpha 2}&: 1s^1 2p^6 \rightarrow 1s^2 (2p^5)_{3/2} \end{aligned}, \tag{1}$$

where the final states are p holes with spin 1/2 or 3/2. The difference in energy between these transitions reflects the spin-orbit splitting in the $2p$ level and is much smaller than the combination of the remaining instrumental linewidth plus the natural linewidths of the spectra measured. The composite lineshape of this spin-orbit doublet is often referred to as $K_{\alpha 1,2}$. Other, weaker transitions occur for double-hole initial states:

$$\left.\begin{matrix} K_{\alpha'} \\ K_{\alpha 3} \\ K_{\alpha 4} \end{matrix}\right\} : 1s^1 2p^5 \rightarrow 1s^2 2p^4 \tag{2}$$

where the final states are complicated by multiplet splittings. Experimentally, the multiple lines are convoluted with the experimental spectra; Figure 3.08 illustrates typical results for Silicon $2p$ core-level spectra. The spectrum of interest is a spin-orbit doublet with 0.605 eV splitting convoluted with the $K_{\alpha 1,2}$ x-ray line; the additional peaks to lower binding energy originate from satellite x-ray emission. Analysis of these spectra allow us to derive relative x-ray satellite splittings and amplitudes which in turn may be used to deconvolve the satellite contribution from these and other spectra. Table 3.01 summarizes the splittings, linewidths, and satellite splittings for the Mg and Al radiation employed in this thesis. The acquisition of core-level spectra is discussed further below; the deconvolution technique is discussed in

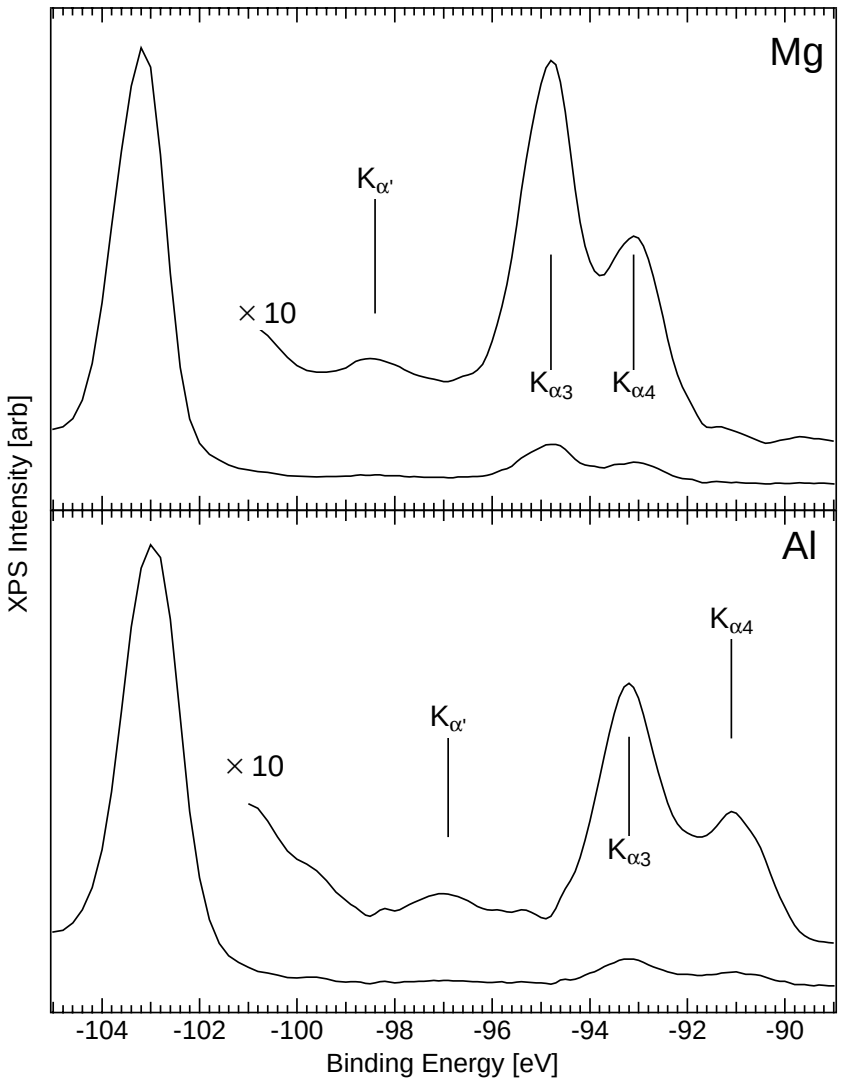

Figure 3.08–Characteristic x-ray satellites. Typical Si 2p core-level photoemission spectrum illustrating the satellite shifts and intensities due to Mg (upper panel) and Al (lower panel) radiation.

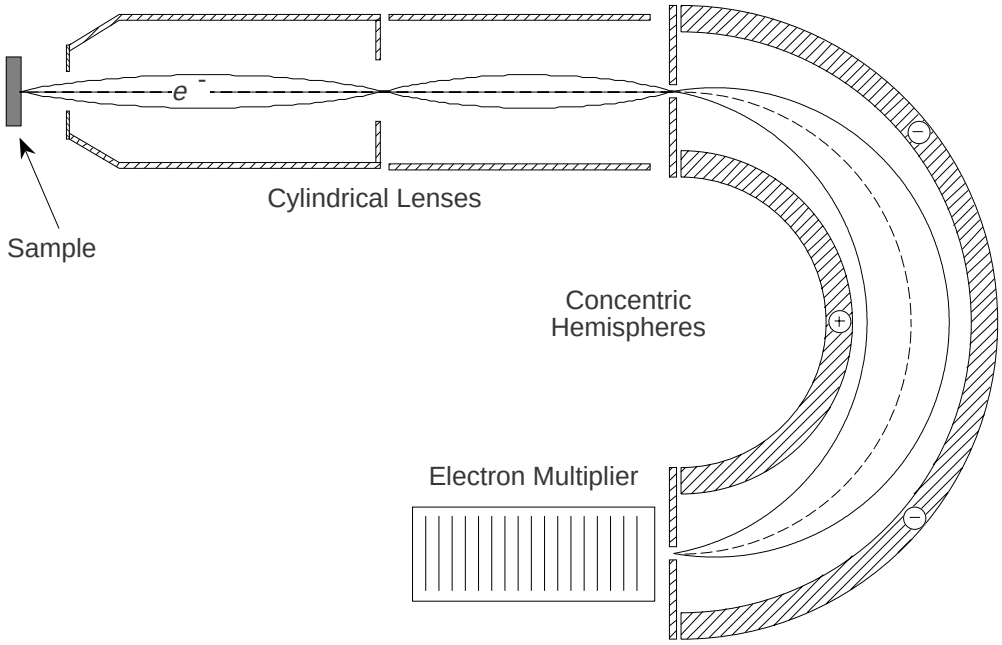

Figure 3.09–Electron spectrometer schematic. Shown are the two-stage lens, the hemispherical spectrometer, and the electron multiplier.

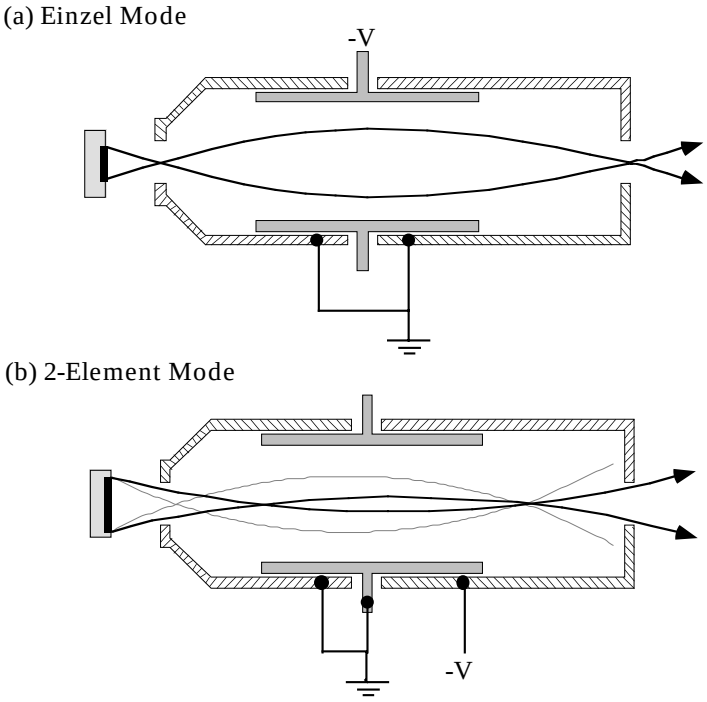

Figure 3.10–First stage lens modes. (a) Einzel mode (small sample area and large acceptance cone). (b) Two-element mode (large sample area and small acceptance cone)

Table 3.01–X-ray satellite properties. The energies and splittings of the main and satellite x-ray emission lines for the anode materials used in this study.

Element	Main line[a]			Satellite relative positions[b] [eV] and amplitudes[b] (%)		
	$K\alpha_1$ energy [eV]	$K\alpha_2$ relative energy [eV]	Linewidth [eV]	$K\alpha'$	$K\alpha_3$	$K\alpha_4$
Mg	1253.6	0.250	0.353	4.5 eV (1%)	8.4 eV (9%)	10 eV (5%)
Al	1486.6	0.416	0.413	5.6 (1%)	9.6 (8%)	11.5 (3%)

[a][Kal75, Ric90]
[b]Measurements obtained from this work

chapter 4.

3.5.2 Electrostatic lens and spectrometer

Figure 3.09 shows a schematic of the electrostatic lens and hemispherical spectrometer. The system is a commercial one (Leybold EA-11). The electrostatic lens is divided into two stages: (i) the first lens collects electrons and transmits them to the second stage; the particular potential settings combined with the opening adjustable aperture define the sample collection area and acceptance cone. (ii) The second lens transmits the electrons to the spectrometer entrance slit; it also decelerates the electrons to the pass energy of the hemispheres. The hemispheres select the electron kinetic energy of interest and passes these electrons through the exit slit to the electron multiplier tube. Pulses are collected here and amplified using commercial electronics.

Stage 1 lens. Operation of the first stage lens is illustrated in Figure 3.10. Two different modes of operation are indicated: (a) Einzel mode, in which only the middle electrode bears an applied potential, and (b) Two-element mode, in which only the third electrode bears an applied potential. As indicated in the figure, the modes are designed to complement each other. Einzel mode integrates electron flux from a smaller source area, but over a larger acceptance cone, while the two-element mode detects from a larger area but over

a smaller acceptance cone. An adjustable aperture at the opening of the lens can be used to further restrict the angular acceptance.

Figure 3.11 illustrates the progressive improvement in angular resolutions available with the Einzel mode, the Einzel mode + input aperture, and with the two-element mode + input aperture (Figure 3.11(a-c)). The scans shown are angular variations of electron emission; the variations in (a-c), due to the x-ray photoelectron diffraction effect, are discussed in detail in chapters 4-5. From these curves, we have estimated the angular resolution to be ~10° in Einzel mode (+aperture) and ~4° in two-element lens mode. The background electron counts (due largely to inelastically scattered electrons) is seen to rise at large emission angle, mainly due to the amorphous molybdenum in the sample holder. The rise occurs at more grazing emission in the Einzel mode (Figure 3.11(d)) compared to the two-element mode (Figure 3.11(e)); this is due to the larger sample area "seen" in the latter mode.

Stage 2 lens and hemispheres. The remaining lens transmits and decelerates the electrons towards the entrance slit to the hemispheres. The purpose of decelerating the electrons is to increase the resolution. The resolution ΔE is proportional to the hemispherical pass energy E_o; however the transmission decreases quadratically as the pass energy decreases. Therefore, the pass energy E_o should be set no smaller than the combined x-ray and electron linewidth under study. Typically this crossover energy was $E_o \approx 35$ eV, although we usually collected electrons with $E_o = 50$ eV in order to improve count rate.

Computer control. Figure 3.12 shows how the electron spectrometer is controlled by computer. The central intelligence is provided by a DECstation II MicroVAX, which is interfaced to the experiment via a standard CAMAC bus. The digital to analog converter (DAC) transmits a 0-10 Volt signal to the spectrometer electronics; this signal sets the spectrometer kinetic energy from 0-100% of full scale (1600 eV kinetic energy). The measured count rate is transmitted from the electron multiplier to a scalar, which is gated by

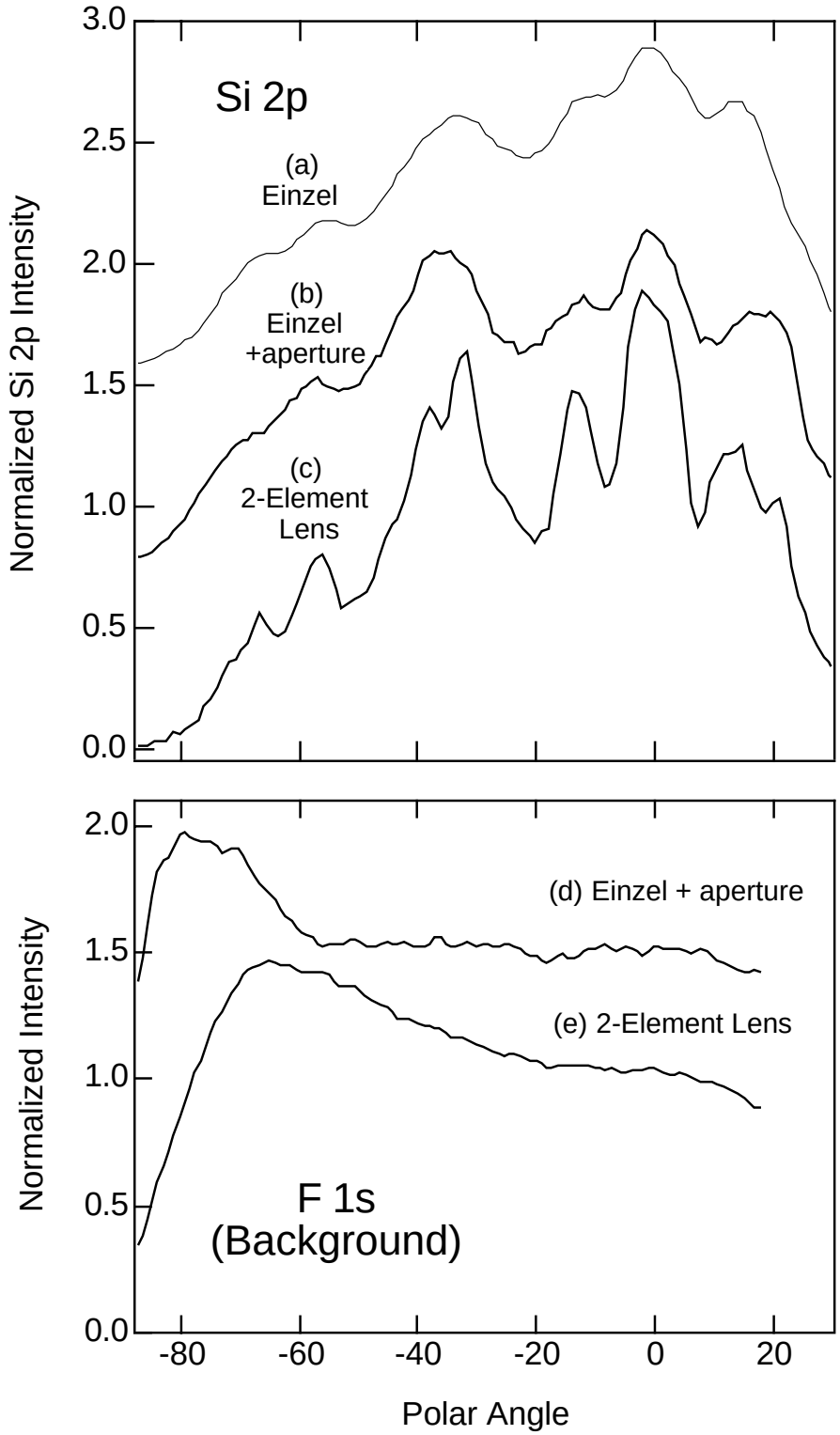

Figure 3.11–Typical angular resolution. Si 2p emission amplitude for (a) Einzel mode only, (b) Einzel mode plus the additional entrance aperture, (c) Two-element lens mode. F1s background emission for (d) Einzel + aperture, and (e) Two-element lens mode.

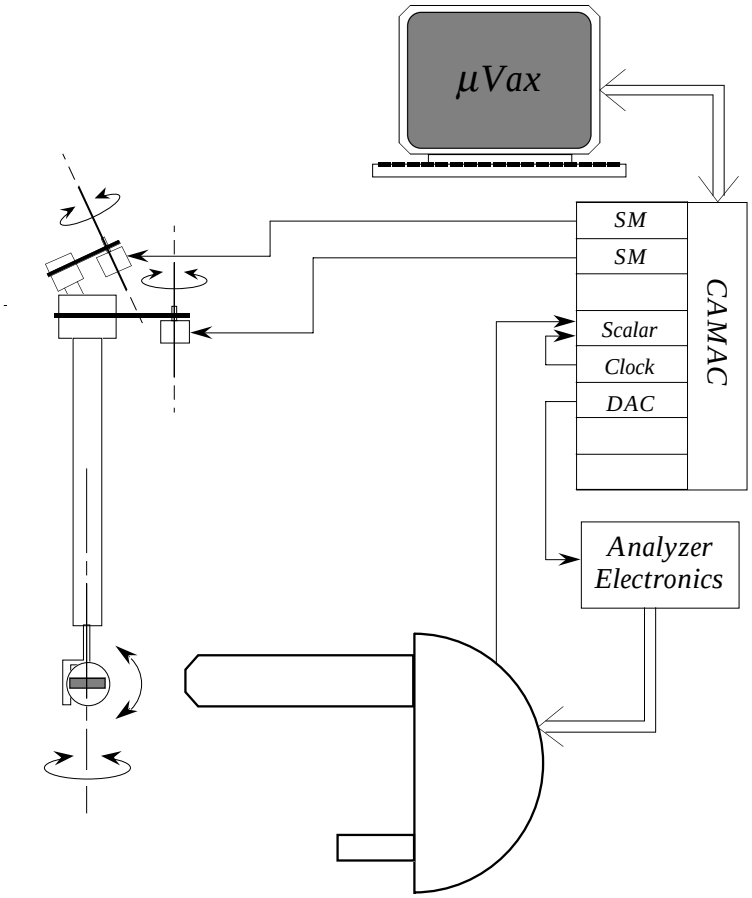

Figure 3.12–Computer control schematic. Shown are the main microprocessor elements (Microvax workstation + CAMAC bus crate) and the connection to the experimental apparatus (stepping motors and electron spectrometer).

a clock in order to normalize the count rate per time precisely. Simultaneously, the sample angles (θ, ϕ) may be varied through stepping motors controlled by the computer. After spectra are acquired, the data are transferred to a Macintosh personal computer, where analysis takes place.

3.5.3 Synchrotron radiation

For some work, the entire apparatus (Figure 3.01) was transported to the Stanford Synchrotron Radiation Laboratory (SSRL) in Palo Alto, California. The purpose was to perform experiments not with the fixed photon energy x-ray lamp but with the tunable radiation available at beamline 1-1. Although synchrotron instrumentation is beyond the scope of this thesis, a brief description is given here.

The source of broad band x-ray emission is the orbit of a relativistic (~2 GeV) electron current (~60 mA) through a bending magnet; a small portion of the cone of emission is

collected by a "grasshopper" monochrometer [Bro78] controlled by the MicroVAX workstation. Although the radiation provided from this monochrometer is from 25-1000 eV, we found the useful range (defined by resolution and intensity requirements) to be limited to 100-200 eV. The intensity was focussed to a spot size on the sample ~2 mm in diameter. This is unlike the broad illumination provided by the x-ray anodes so that the spectrometer was very sensitive to electrostatic lens settings and sample positioning.

3.5.4 Lawrence Berkeley Laboratory Setup

Some of the experimental results in this thesis were also verified at the Advanced Materials Laboratory at the Lawrence Berkeley Laboratory [Won93]. The commercial UHV chamber used in this experiment is schematically listed in Figure 3.13. It is functionally similar to the main chamber discussed in this chapter. The growth and analysis is carried out in separate chambers separated by gate valves. Sample characterization is by reflection high energy electron diffraction (RHEED), which, like LEED, probes the long range surface

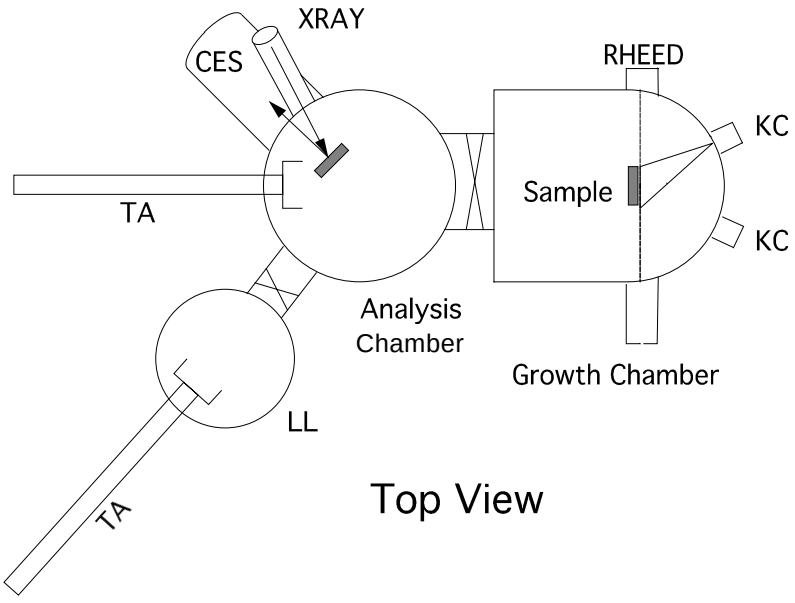

Figure 3.13–Lawrence Berkeley Laboratory experimental schematic. Major components illustrated: CES=cylidrical electrostatic lens, KC=Knudsen cell, LL=load lock, RHEED=reflection high energy electron diffraction, TA=transfer arm, XRAY=x-ray source

order. XPS and AES are carried out with Al K_α illumination and detected with a cylindrical electron spectrometer (CES). The CES differs from the hemispherical electron spectrometer because it accepts electron paths on the *surface* of an ~60° cone (as opposed to the interior of an ~10° cone). In our system, the CES is tilted ~45° to the sample holder. Therefore, the CES detects a wide range of emission angles (θ, ϕ) and the setup precludes angular-resolved measurements.

XPS & XPD Techniques 4

4.0 Overview

The main techniques used in this thesis are x-ray photoelectron spectroscopy (XPS) and x-ray photoelectron diffraction (XPD). In XPS, the energy spectrum of the emitted electrons is recorded by integrating electrons over a large angular acceptance. The term XPS includes both core-level and Auger electrons emitted from the solid, although when speaking strictly about the latter, the term Auger electron spectroscopy (AES) is used. In XPD, the angular acceptance is reduced so as to measure the angular distribution of elastically scattered electrons. If the kinetic energies are a few hundred or more eV, photoelectrons are preferentially scattered along axes between the source atom and other atoms between the source and the detector, an effect termed *forward focussing*. In addition to forward focussing peaks, there are also diffraction peaks originating from the interference between scattered and unscattered electrons. If no atoms lie between the source atom and the detector, then the angular distribution of photoelectrons will be uniform, insofar as one can neglect backscattering from underlying atoms, as happens in the energy regime considered here. An important application of this effect is the ability to distinguish surface from bulk atoms apart from any differences in their core-level energy. For the purposes of this thesis, the signature we use for surface atoms is that their photoelectrons have a uniform angular distribution in the near-normal direction.

4.1 X-ray Photoelectron Spectroscopy

The XPS apparatus was discussed in detail in Chapter 3. In this section, we discuss how spectra are analyzed. This analysis involves background subtraction, deconvolution, smoothing, and curve-fitting. In addition the spectral energies are calibrated to the Fermi

level of the particular solid being considered.

4.1.1 Overview spectra

Figure 4.01 illustrates XPS spectra for a variety of samples: (a) a chemically-etched Si wafer (§3.3.1), with an amorphous oxide layer as inserted into the chamber, (b) a similar wafer after annealling to remove the oxide layer, and (c) after growth of a CaF_2 film. The spectra were all acquired with Mg K_α illumination ($h\nu$ = 1253.6 eV), so that the binding energy scale was determined by the approximate relation, (binding energy) = (kinetic energy) - $h\nu$. In this thesis, the term *high binding energy* always means towards the left side of the binding energy plot, i.e., to lower electron kinetic energy.

There are several common features among these spectra. Each spectrum allows identification of the chemical compounds present on the surface by comparing the characteristic binding energies to tabulated values. The characteristic background rise to high binding energy at each peak is due to inelastic scattering (discussed in the next section). Inelastic scattering leads to a cascade effect whereby the background level increases monotonically towards higher binding energies. Close to zero kinetic energy (not shown) the background rises dramatically until there is a sharp cutoff at the work function of the material. Electrons with energies smaller than the work function reflect from the surface potential barrier and remain bound to the solid.

4.1.2 Inelastic scattering: Peak Heights

We now look more closely at the inelastic scattering process and its implications. The first major effect is on the peak heights in Figure 4.01 and will be discussed here. The second effect is the background shape and will be discussed in §4.1.3.

The escape depth of electrons in Si 2*p* as a function of kinetic energy is illustrated in Figure 4.02. The data were taken from the literature, except for one data point which came from this study. Data for *all* materials (metals, insulators, etc.) closely follow the result for Si within about a factor of two. When referring to this general property of all materials, the

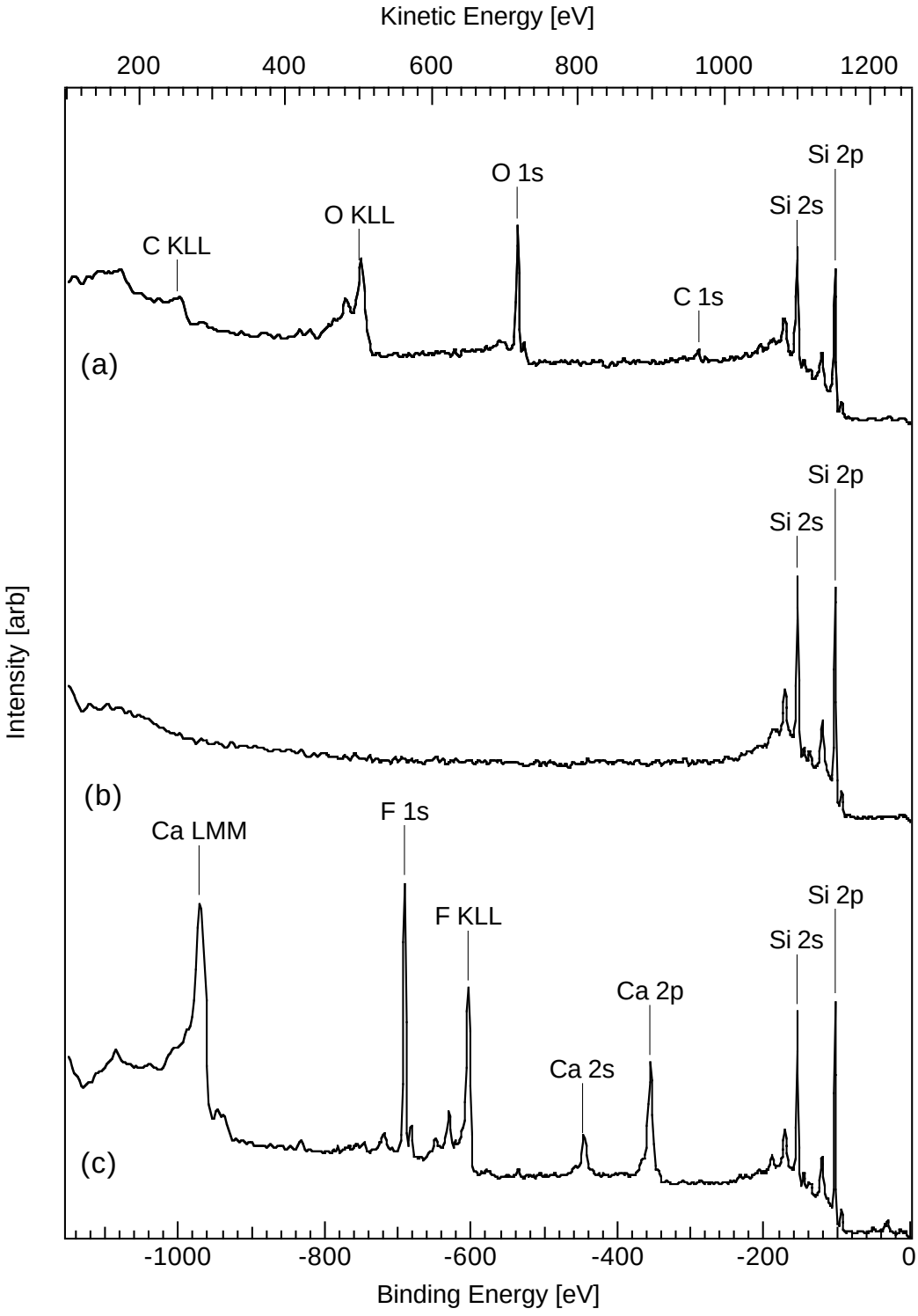

Figure 4.01. Overview XPS spectra for (a) Si(111) substrate as inserted into the chamber following a wet chemical etch, (b) the same substrate after thermal treatment to remove the passivating oxide layer, and (c) after growth of a CaF_2 film.

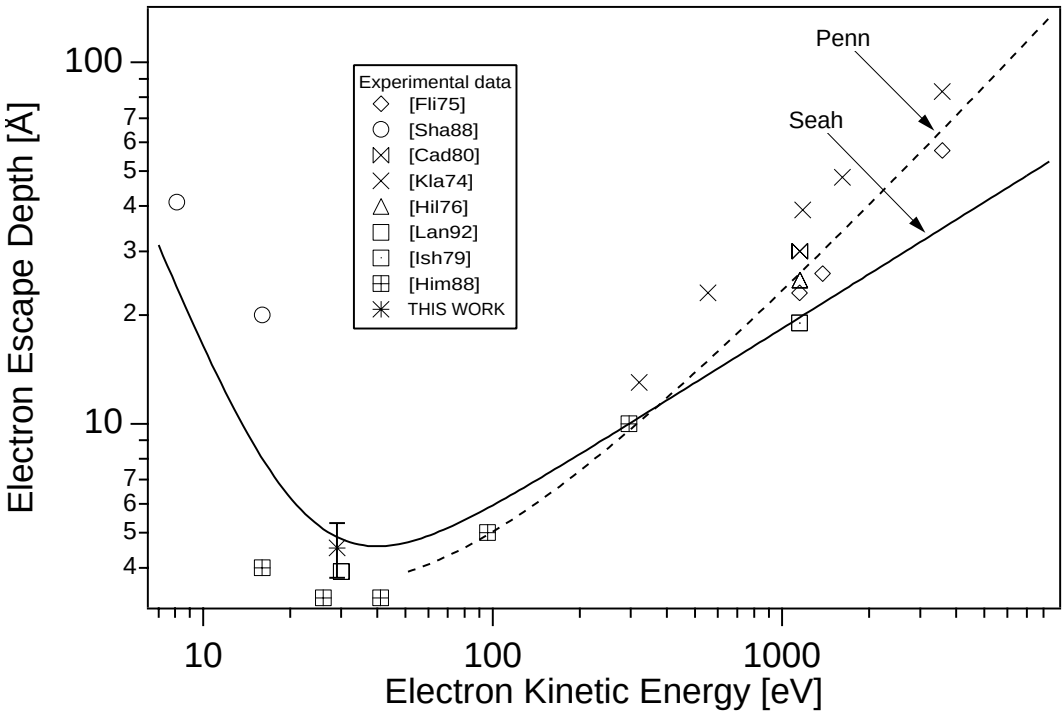

Figure 4.02. Experimental (symbols) and theoretical (curves) values for the Si escape depth as a function of electron kinetic energy. The dashed (solid) curve corresponds to the model by Penn [Pen76] (Seah [Sea79]).

curve through the data points in Figure 4.02 is called the *universal curve*.

It should be noted that inconsistencies in terminology abound in the literature. The *escape depth* as used here means the travel distance normal to the material surface for which the fraction of unscattered electrons is reduced to $1/e$. The *attenuation length* is defined as the escape depth corrected for geometric factors, e.g. the angle of electron emission from the surface. Finally, the *inelastic mean free path* is the average distance of travel before an electron is scattered and is normally computed theoretically. In principle the attenuation length and inelastic mean free paths should be equal, however, Monte Carlo simulations of total scattering (inelastic + elastic) show that the inelastic mean free path can be as much as 30% larger than the attenuation length [Jab90]. Presumably all the data in Figure 4.02 reports the escape depth; the inaccuracies in correcting for the geometric factors is probably responsible for the scatter in the values.

The shape of the universal curve may be understood as follows. At infinite kinetic energy the cross section for scattering necessarily drops to zero, so that the escape depth approaches infinity. At intermediate kinetic energies, plasmon scattering—from free and bound electrons—dominates the inelastic losses. Below the plasmon energy for a material, electrons have insufficient kinetic energy to excite losses, so that the escape depth again rises. Therefore, the universal curve is seen to go through a minimum; for most materials this minimum is from 30 to 100 eV kinetic energy.

Several theories have been proposed to account for the shape of the universal curve. They fall into the categories of first-principle and empirical, and the best-known of these two are plotted in Fig. 4.02. The mean free path is given by

$$\lambda(E_k) = v(E_k)\tau(E_k) \tag{4.1}$$

where v is the group velocity and τ is the collision lifetime in a solid with band structure E_k. The collision lifetime can be related to the electron self-energy $\Sigma_k(E_k)$ through [Pen76, Bec81]

$$\tau(E_k) = \hbar / 2\,\mathrm{Im}\,\Sigma_k(E_k) \tag{4.2}$$

where the electron self-energy can in turn be related to the energy loss function -Im $\varepsilon(\mathbf{q}, \omega)^{-1}$:

$$\Sigma_k(E_k) = \int \frac{4\pi e^2 d\mathbf{q}}{(2\pi)^3 q^2} \int_{-\infty}^{\infty} \mathrm{Im}\,\varepsilon(\mathbf{q},\omega)^{-1} \int_{-\infty}^{\infty} dE'\,\delta(E'-E_k)^{-1}\,. \tag{4.3}$$

It then becomes a matter of determining the inverse dielectric function. Penn's solution [Pen76] for the free-electron gas is shown in Figure 4.02. The agreement is good for Si, where the valence-band plasmon excitation dominates the inelastic scattering process. For materials like transition metals where electronic excitations are an important energy loss process, the density of states for such excitations must also be considered [Pen87, Tan90].

Semiempirical models attempt to estimate the inverse dielectric function from optical data. However, since optical measurements only measure the frequency-dependent part of the dielectric response, a method must be found to connect the optical response $\varepsilon(\omega, 0)$ to

$\varepsilon(\omega, \mathbf{k})$. A sum-rule based method was presented by Ashley [Ash81].

Finally, some authors [Tan90, Sea79, Tok85] have compiled large bibliographies on many materials from which they derive empirical laws for the escape depth. The goal is to characterize materials by as few physical parameters as possible; these parameters are entered into an equation for the universal curve to specialize to a particular material. A commonly used empirical rule is due to Seah [Sea79]:

$$\lambda[\mathrm{nm}] = \begin{cases} a(538 / E^2 + 0.41(aE)^{1/2}) & \textit{elemental solids} \\ a(2170 / E^2 + 0.72(aE)^{1/2}) & \textit{inorganic solids} \end{cases}, \tag{4.4}$$

where a[nm] is the monolayer thickness and E [eV] is the kinetic energy. For Si (with a averaged over all directions), the Seah formula has been added to Figure 4.02, where it is in reasonable agreement with experiment.

The energy dependence of the electron escape depth for Si 2*p* electrons in Si is vividly illustrated in Figure 4.03 for a clean Si(111) substrate. In (a) the photon energy is 111 eV (the data were acquired at beamline I-1 at the Stanford Synchrotron Radiation Lab), so that for the Si 2*p* electrons of interest, the kinetic energy ~5 eV. From Figure 4.02 we see that the measurement is sensitive to >30Å of material, so that a single sharp doublet is observed which is representative of the spin-orbit split $2p_{3/2,\,1/2}$ core level at the bulk Si atoms. In (b), the photon energy was 135 eV, so that the kinetic energy at the 2*p* peak is ~29 eV. This "surface-sensitive" spectrum is sensitive mainly to electrons in the top 6Å of the solid; we see the sharp doublet has smeared into a broader feature. This spreading is accounted for by the various core-level shifted species present at the 7×7-reconstructed Si(111) surface (discussed in Chapter 3) [Him81]. In (c) we see the effects of the growth of ~1 ML CaF on this surface, with the structure as shown in the inset (the structure determination of this and similar films is a major result of this thesis and will be elaborated upon). First, the overall height reduction compared to the spectrum in (b) is due to the inelastic scattering through the CaF layer. Second, the overall shift of the spectrum is due to a Fermi-level shift (discussed further below)

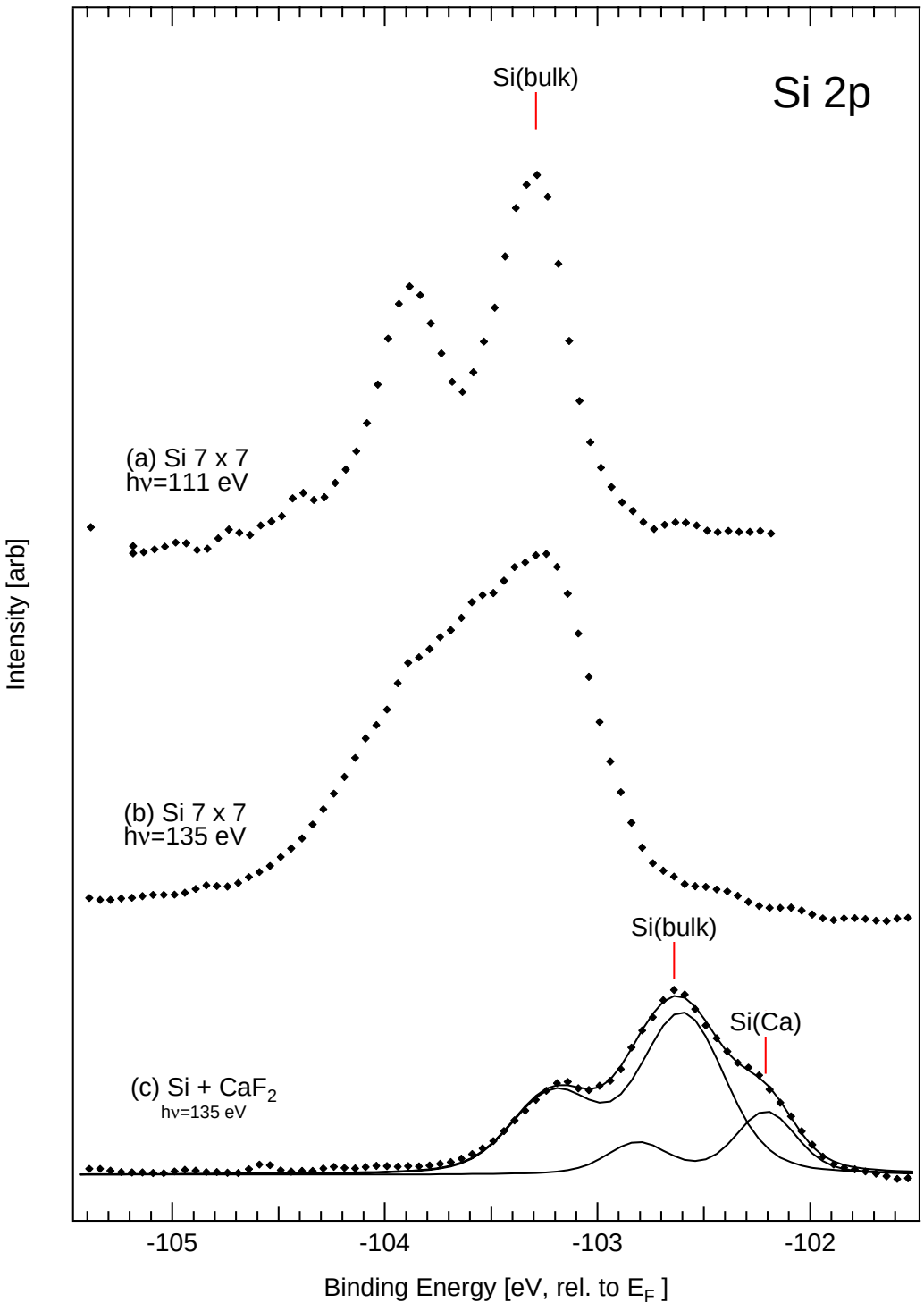

Figure 4.03. Surface sensitivity using synchrotron radiation. XPS data acquired with synchrotron radiation for (a) Si 7×7 at bulk-sensitive $h\nu$=111 eV, (b) Si 7×7 at surface-sensitive $h\nu$=135 eV, and (c) CaF_2 on Si (7/2/91) at surface-sensitive $h\nu$=135 eV.

and is unrelated to inelastic scattering. Third, the smeared-out spectrum in (b) has sharpened to two resolved doublets of separation ~0.4 eV. This is due to the single chemically reacted Si atom at the Si-CaF interface, which contributes the smaller component in (c) [Rie86, Olm87].

This chemically shifted component was used to estimate the electron escape depth in Si 2*p* at 29 eV. Curvefit results (indicated in Figure 4.03(c)) show the shifted component's area was $f = 0.5$ times the area of the bulk component. For a variety of similar samples, we found a range $0.33 < f < 0.50$. This fraction is given by the simple relation (for a continuum solid)

$$f = \frac{1 - e^{-a/\lambda}}{e^{-a/\lambda}}, \tag{4.5}$$

where a is the thickness of a single Si atomic layer. We approximate a as one half the average interlayer spacing normal to the surface ($a = \frac{1}{2}3.13$ Å) [Lan92, Him88]. Solution of Equation (4.5) for the range of f measured yields the experimental point in Figure 4.02.

Another use for the inelastic scattering effect is the estimation of island morphology of CaF_2 or SrF_2 films. As discussed in Chapter 5, the islanding mode in CaF_2 or SrF_2 films consists of a single CaF bilayer which completely covers the substrate, and which in turn is partially covered by islands, as determined by XPD and XPS. The structure is illustrated in Figure C.01. A quick way to determine the fractional coverage and island heights is illustrated in Figure 4.04. We grew a (nominally) 15 triple layer (TL) thick CaF_2 film on Si wafer which was intentionally miscut 4° away from the (111) surface. Two spectra were acquired: one at θ=-26.1° and one at θ=-70°, both at ϕ=-18°. The particular value of ϕ was chosen to avoid any low-index directions in the crystal that would lead to forward focussing. The fitted spectra are shown in Figure 4.04(a), in which the partially buried interface Ca atoms and the Ca atoms in the islands each contribute a peak to this spectrum. It is immediately evident that the film is islanded because the relative height of the interface peak

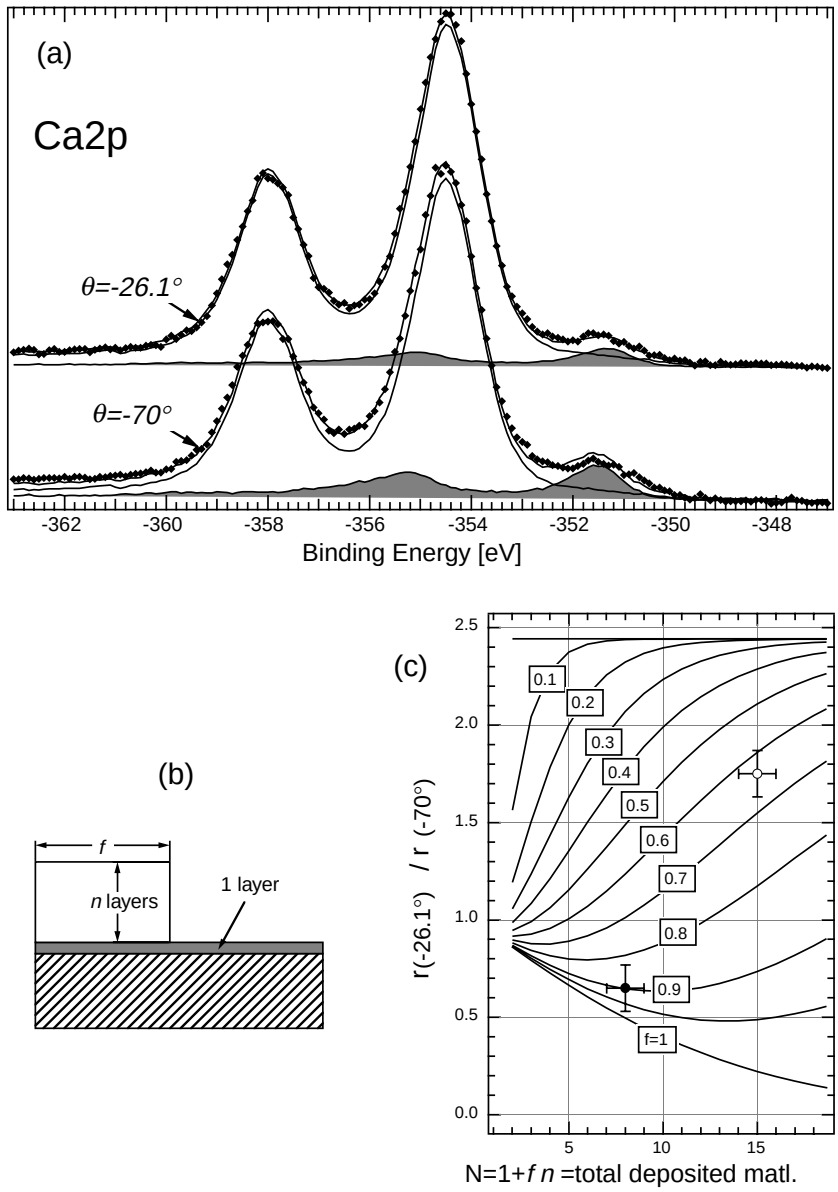

Figure 4.04. Morphology determination using inelastic scattering for an islanded film grpwn upon a misoriented substrate. (a) Ca 2p spectra for a nominally 15 triple layer CaF_2 on Si(111) film (2/2/93) at two different emission angles, (b) the Stranski-Krastanov islanding model as discussed in the text, and (c) the bulk/interface ratio plot used to infer the islanding parameters *n* and *f* from the XPS data. The hollow circle indicates the deduced morphology parameters. Shown for comparison is the result from a flat film (10/2/92) grown on a well-oriented substrate (filled circle).

is not reduced at the more grazing emission angle. This can be quantified as follows. For simple exponential attenuation, the ratio (island Ca signal) divided by (interface Ca signal) is

$$r(\theta) = \frac{f(1-e^{-n/\lambda\cos\theta})\Big/(1-e^{-1/\lambda\cos\theta})}{fe^{-n/\lambda\cos\theta}+(1-f)}, \tag{4.6}$$

where f is the fractional coverage of the islands, θ is the emission angle, λ [TL] is the escape depth, and n is the island thickness (see Figure 4.04(b)). In Figure 4.04(c) contours of $r(26.1°)/r(70°)$ for constant f are plotted. We used a value of λ=12 TLs which derives from Seah's formula (4.4) for CaF_2. The open-circle data in Figure 4.04(c) represents the known total amount of deposited material and the measured value of $r(26.1°)/r(70°)$. By comparison to the contours, we can conclude that the islands in this film cover ~65±5% of the exposed interface layer. This result can be compared to the result for an 8 TL film grown on a wafer oriented to better than 0.25° of the Si(111) surface (filled circle in Figure 4.04(c)). This film was uniformly covered according to the XPD measurements, and is nearly so according to this measurement. The measurement on this film is more difficult because at large θ the interface signal is very small and hence its amplitude is difficult to quantify. In addition to the statistical error bars in the figure, there is a systematic error as well. It arises from the residual XPD modulations that are present at the emission angles chosen for the spectra. In principle we would have to average the peak heights over all angles ϕ to get a better estimate of the ratios. But the usefulness of this measurement (as compared to the XPD measurements below) is the relative speed at which the data can be acquired compared to the XPD experiment. A film grown can be judged as uniform or islanded qualitatively in a relatively short time after growth; it can be judged by eye using Figure 4.04(c) as reference.

4.1.3 Inelastic Scattering: Peak Shapes

The second major effect of inelastic scattering is on the peak and background shapes. A certain fraction of scattering events results in *inelastically scattered* electrons which are seen by the detector. Thus we can identify two different contributions to the background shape

which can affect the peak shape: (i) inelastically scattered electrons excited from the main-peak electrons, and (ii) *secondary* electrons excited by electrons of higher kinetic energy. Some of these secondary electrons are also scattered before collection. These effects are the cause of the background's monotonic increase towards zero kinetic energy. We can also distinguish between discrete and continuous energy losses. For example, there can be discrete losses to quantized collective modes such as plasmons or phonons (the latter being rarely if ever resolved from the main peak). In metals there can also be a continuum of losses due to electron excitations near the Fermi level; since these losses can be infinitesimally small, they result in a loss tail that starts at the main peak and extends towards higher binding energy. This sort of inelastic scattering will distort the peak shape from the pure Lorentzian (convoluted with the Gaussian instrument response) one would expect theoretically.

We now discuss some particular cases of inelastic contributions to the peak/background shapes. Figure 4.05 highlights the two types of inelastic scattering events that affect the observed peak heights: discrete loss peaks and infinitesimal losses. In (a) we show the loss region near the Si 2*s* peak for a clean Si(111) 7×7 surface. Observed are regularly spaced loss peaks ~17 eV apart. These discrete losses are due to valence band plasmons in bulk Si. An exact treatment of the plasmon losses in Si using a self-consistent estimate of the dielectric loss function was performed by Bechstedt [Bec82]. A more pedestrian calculation using the plasma frequency formula

$$\omega_p = (ne^2 / \varepsilon_0 m)^{1/2} \tag{4.7}$$

and solving for the electron density with $\hbar\omega_p$ = 17 eV shows a similar result: that there are 4.2 electrons per Si atom participating in the plasmon excitation; this reflects the fact that the valence electrons (4 electrons/atom) dominate the plasmon density, with only a small amount of participation by deeper core-electrons [Ash81, Bec81]. In addition to the discrete losses, there is also an overall rise in the background that occurs through the Si 2*s* peak; this corresponds to electronic excitations across the bandgap of the silicon (although a certain part

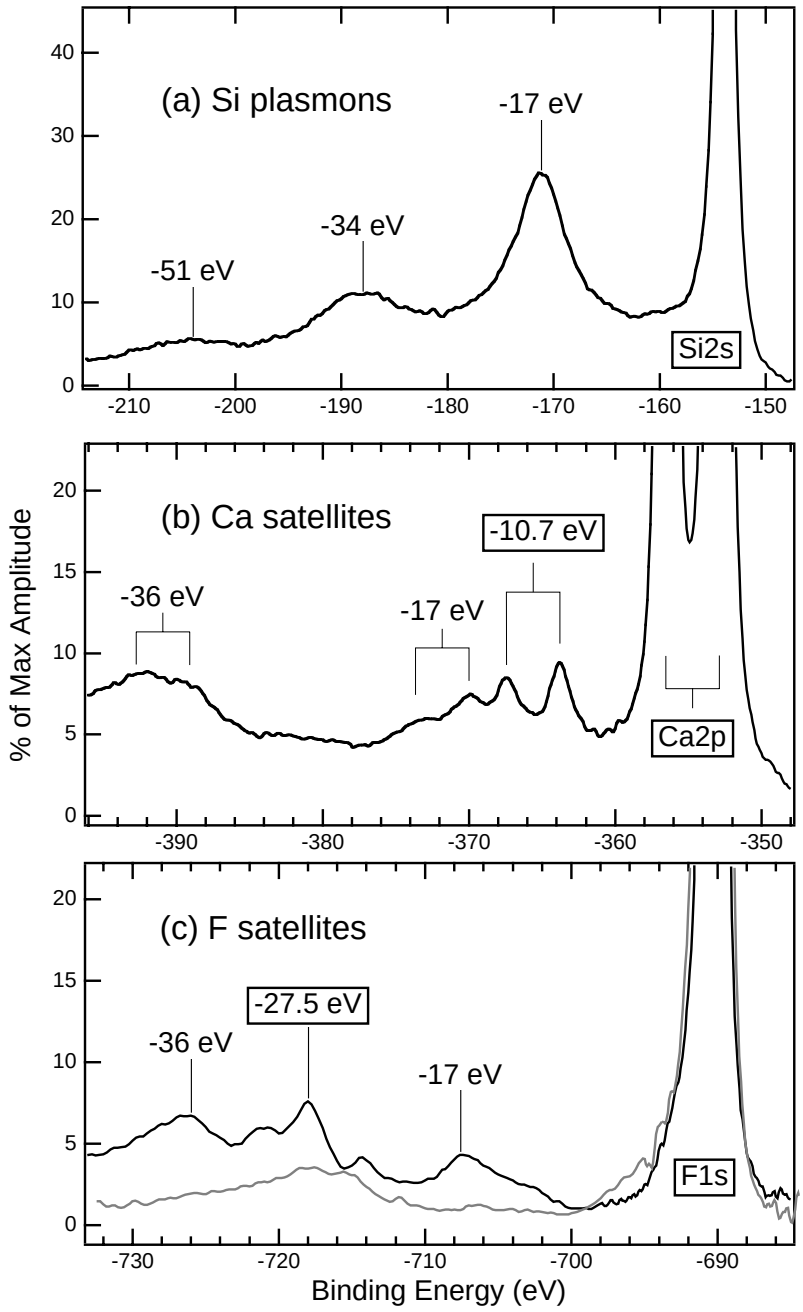

Figure 4.05. Discrete inelastic loss features for (a) Si 2s (substrate) electrons, (b) Ca 2p, and (c) F 1s electrons in thick CaF_2 (10/1/92). Intrinsic loss features are shown boxed. Also shown for comparison in (c) is the spectrum from a single CaF bilayer (10/6/92, grey).

of this can be attributed to detector response). This is similar to the metallic case except that the minimum energy that can be lost is the bandgap of silicon (1.1 eV). This background, which is present for Si 2*p* peaks as well, may be removed by assuming that it is proportional to the integral of the peak, shifted by the bandgap of the semiconductor (~1.1 eV). We have used an iterative algorithm to remove this background from Si 2*p* spectra before curve-fitting.

Similarly, for Ca and F atoms in CaF_2 crystals, there are discrete excitations apparent in Figure 4.05(b, c) (Recall that the Ca 2*p* spectrum consists of a spin-orbit-split doublet of separation ~3.5 eV). By comparing the two spectra, it is possible to classify the discrete excitation losses into two categories: (i) extrinsic losses, which are those that occur for any electron on its way through the solid (hence appearing as losses for both Ca and F emission), and (ii) intrinsic losses, which depend on a core-hole being created at a particular atom. The extrinsic losses at -17 eV and -36 eV have been assigned as electronic excitations (F 2*p* and Ca 3*p* $\rightarrow$ conduction bands, respectively) [Sai87]. Further evidence for the extrinsic nature of these losses comes from the loss spectrum of a single Ca-F bilayer deposited on Si (dotted curve, Figure 4.05(c)), in which the extrinsic excitations have been removed simply by removing the overlying bulk material between the F atom and the detector. The intrinsic band at ~-27.5 eV (attributed to an electronic excitation from F 2*p* $\rightarrow$ conduction bands [Ike77]) remains in this film. The intrinsic Ca excitation at -10.7 eV is assigned to the exciton transition (F 2*p* $\rightarrow$ Ca (4*s*,3*d*)) which is also seen in UV optical absorption. It arises as an alternate final state, or *shake-up* peak to the fully relaxed final state which was discussed theoretically in Chapter 2. The polarization of the fluorine ligands in the presence of the core hole can cause sufficient spatial overlap with the Ca 4*s*-like conduction band state to induce electronic excitations simultaneous with the photoemission process.

Unlike for Si 2*s* and 2*p* electrons, the smooth inelastic background contributions to Ca and F atoms are not removed from the spectra for analysis; instead they are incorporated into the empirical lineshapes used for curve fitting. This was because the inelastic scattering

backgrounds were unique to each chemically shifted species (e.g. interface Ca atoms *vs.* bulk Ca atoms) and furthermore, in the case of the interface Ca atoms, the inelastic background was too complicated to subtract in a direct fashion. Further details of the lineshapes used for fitting are discussed in the next section.

A special situation where care was required for background subtraction is shown in Figure 4.06. In (a), we show the Si 2*s* and Si 2*p* substrate peaks before growth; in (b) we show the same spectral range after a SrF_2 film is grown on Si(111). The binding energy of the Sr 3*d* peak places it between the Si 2*s* and Si 2*p* substrate peaks; therefore the Sr 3*d* peak is subject to interference from both Si 2*s* and Si 2*p* satellites. The former is caused by the Mg K_α satellites (§ 3.5.1) and the latter are caused by multiple-plasmon creation. Figure 4.06(b) shows the Sr 3*d* spectrum after growth, and 4.06(c) shows the corrected Sr 3*d* spectrum after subtraction of the Si 2*s*, 2*p* contributions. The subtraction was to a small degree arbitrary because the Sr 3*d* spectrum in turn distorts the Si 2*s* spectrum due to an exciton loss at ~10 eV, similar to the CaF_2 exciton loss discussed above. Finally, Figure 4.06(d) illustrates the final Sr 3*d* spectrum after deconvolution of its own x-ray satellites, using the Fourier deconvolution method discussed below (§4.1.7).

4.1.4 Curve-fitting: Functional Lineshapes

For some XPS peaks, the background subtraction discussed above is sufficient to allow accurate curve-fitting of the remaining peak using a mathematical lineshape. We have used the Voigt lineshape, which is a convolution of a Lorentzian (the intrinsic lineshapes of the core level and x-ray spectra) and a Gaussian (which includes all other instrumental broadening). We used a fast algorithm for generating numerical approximations to this function [Arm67, Whi68, Dra76]. Figure 4.07 shows a family of Voigt curves with constant full-width for various mixtures of Lorentzian and Gaussian widths.

We applied such analytic-lineshape fitting to Si 2*p* and F 1*s* peaks. From the fitted heights of Si 2*p* core-level peaks before and after growth, we can estimate the thickness of the

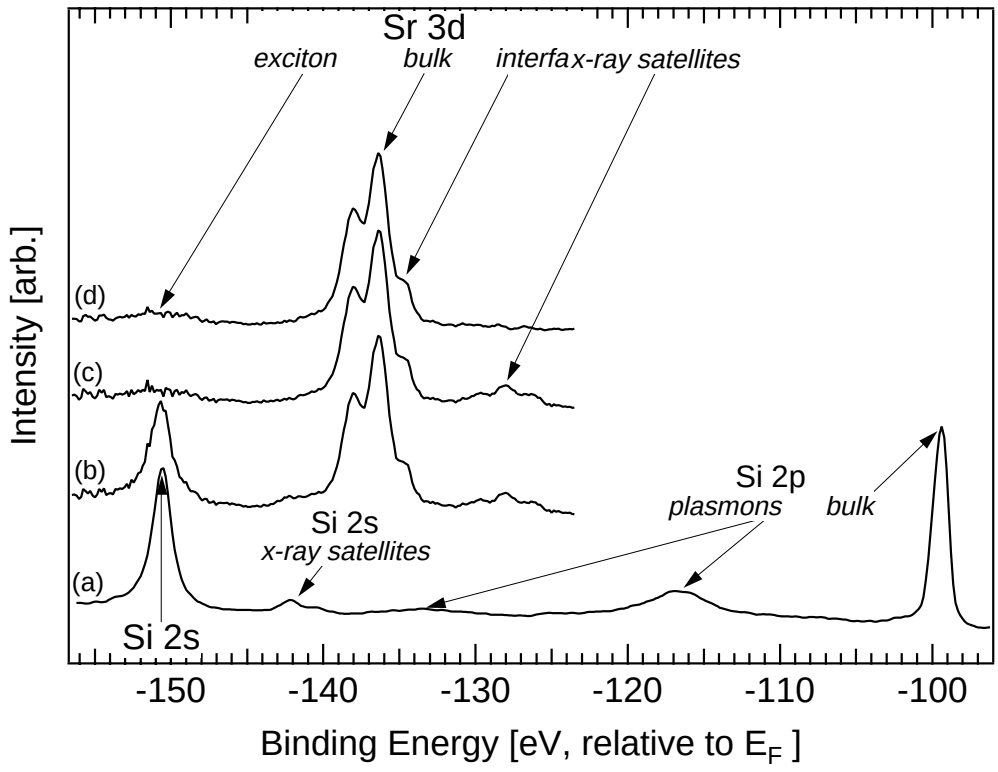

Figure 4.06. Background subtraction for Sr 3d electrons. Shown are XPS spectra for (a) clean Si 2s and 2p electrons, (b) the same region following SrF_2 deposition (3/2/93: 15s, 52 Å/min, 700°C), (c) corrected for Si 2s x-ray satellite removal, and (d) corrected for Sr 3d x-ray satellite removal.

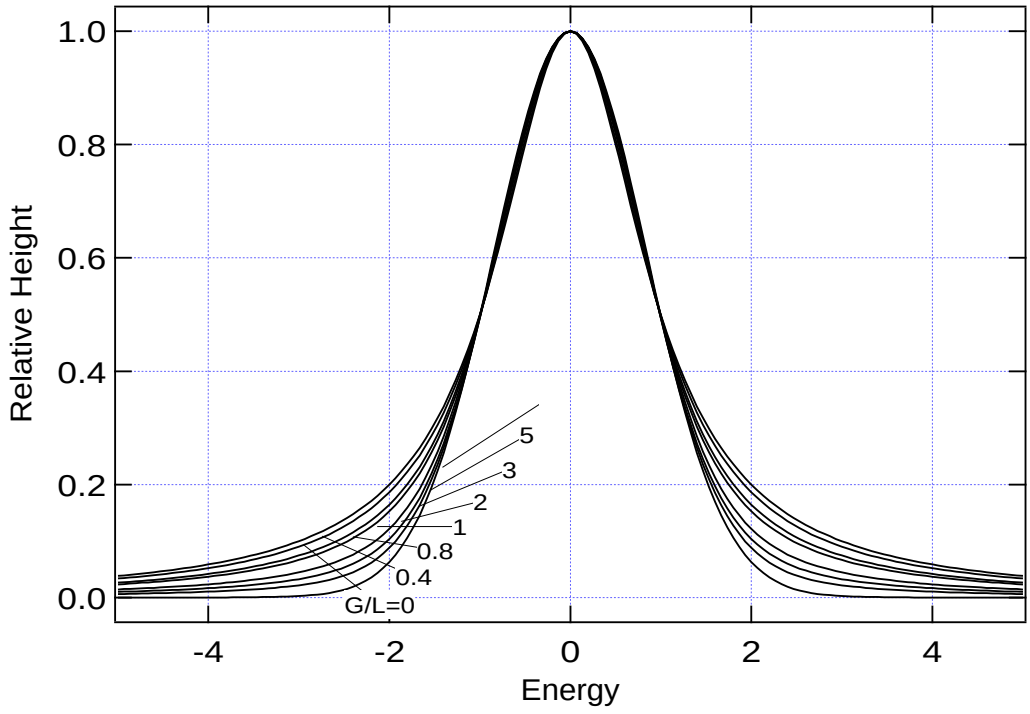

Figure 4.07. Voigt lineshape profile for a variety of mixtures of Gaussian and Lorentzian peak widths. The curves shown have constant FWHM; the parameter G/L indicates the ratio of Gaussian to Lorentzian FWHM in the convolution.

overlayers on it, and in some cases estimate the islanding morphology (flat *vs.* islanded). We also use the heights to normalize our detector response from sample to sample; this was necessary because of the gradual degradation of the electron multiplier's sensitivity with time. It is also useful to monitor the interface electronic properties by measuring the Si 2*p* peak position before and after overlayer growth. Since the energy between the Si 2*p* and Si valence band is constant, motion of the Si 2*p* peak directly gives the motion of the Fermi level. Before growth, the Fermi level is pinned to a metallic surface state located ~0.63 eV above the valence band [Him83]. It was established that for completely reacted interface layers that Si 2*p* shifts 0.4 eV [Olm87] to 0.6 eV [Rie86] to lower binding energy after CaF_2 or SrF_2 growths, so that after growth the Fermi-level is pinned at or just above the Si valence band. The cause of this pinning has not been established, but it has been attributed to a defect density of states at the interface [Rie86].

4.1.5 Curve-fitting: Empirical Lineshapes

For many Ca, Sr, and F overlayer peaks, we have used empirical lineshapes for curve-fitting. The main conclusions of this paper depend on accurate measured values of the peak heights and energies, and so we have tried to make as few assumptions as possible in the fitting procedure in an attempt to avoid any bias. The general method is to identify bulk-like and interface core-level lineshapes, usually from extremely thick and from single-layer films, respectively. For intermediate thicknesses, the overall spectrum is to be least-squares fitted to a linear combination of bulk and interface lineshapes. Peaks from surface atoms were always found to be well-described by bulk-like lineshapes. The free parameters in such a fit are simply the amplitude and position of the peaks; the peak widths are held fixed from the empirical lineshape. In the following paragraphs, we will discuss the CaF_2, SrF_2 lineshapes, how they were measured, and their peculiarities.

$\underline{CaF_2}$. (*a) Ca 2p.* Figure 4.08 compares the inelastic loss region from a thin film (a single Ca-F bilayer adsorbed on Si); to reduce the noise, we averaged the signals from four

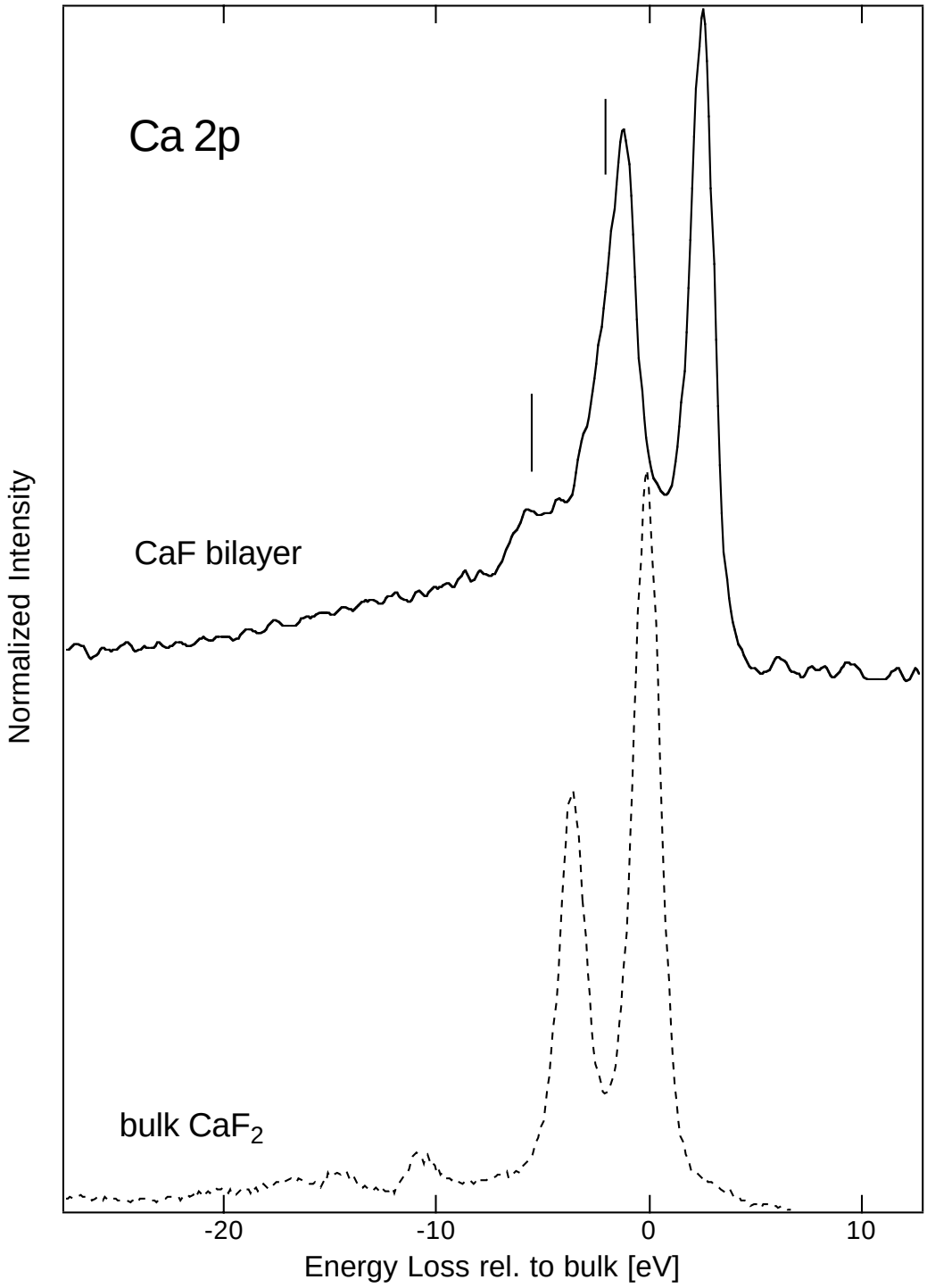

Figure 4.08. Ca 2p bulk and interface lineshapes for the Ca 2p spin-orbit-split doublet. The lineshapes are taken from the spectra of a thick film (10/7/91) and a single exposed Ca-F bilayer (avg. of 10/2/91, 3/3/92, 4/1/92, 6/2/92), respectively. The vertical lines indicate a satellite doublet in the case of the interface emission only.

nearly identical films) to a thick CaF_2 film . Intermediate-thickness films appeared to be linear combinations of these two spectra, except that the interface Ca linewidth appears to sharpen somewhat upon being covered, as discussed below. There are two main differences between the inelastic loss spectra. First, the 10.7 eV exciton doublet in the bulk CaF_2 spectrum is absent in the bilayer spectrum; instead there appears a new doublet (indicated by the vertical lines) at ~-4.5 eV loss from the main doublet. We have proposed two possible models for this doublet, and they are discussed in Appendix B. The second difference observed is the much larger continuous loss tail observed for the bilayer. This tail resembles that observed for metal atoms, in which the large density of empty states at the Fermi edge creates a large transition probability starting at zero loss energy. For this reason, the tail in Figure 4.08 is referred to as the "metallic-like" tail. Work on its origins is still under progress and will be discussed in §4.1.6 and in future work [Les94].

One assumption being made is that the *buried* interface lineshape is the same as the *exposed* interface lineshape which was discussed in that section. Although this turns out to be a reasonable approximation, the buried lineshape is found to be sharper than the exposed one. We take this as partial evidence that there is some fluorine disorder in the exposed CaF bilayer, and that this fluorine becomes ordered upon being covered by more CaF_2. Further evidence for this comes from two observations: First, the same effect is present for F atoms, and to a much greater degree. Second, the Ca $\rightarrow$ F forward scattering peak in this layer (discussed further in the XPD section below) becomes less diffuse upon being covered; this scattering is also more diffuse in the CaF bilayer than in the surface triple layer of a thick CaF_2 film.

(b) Ca $L_{2,3}MM$. Figure 4.09(a) shows Ca LMM Auger lineshapes for bulk-like and interface signals, derived from thick-film and single bilayer films, respectively. The assignments of each group are derived from the Ca 2*p*, Ca 3*p*, and F 2*p* (valence band, V) core level energies and are corroborated by a study for the insulating solid CaO [Väy90].

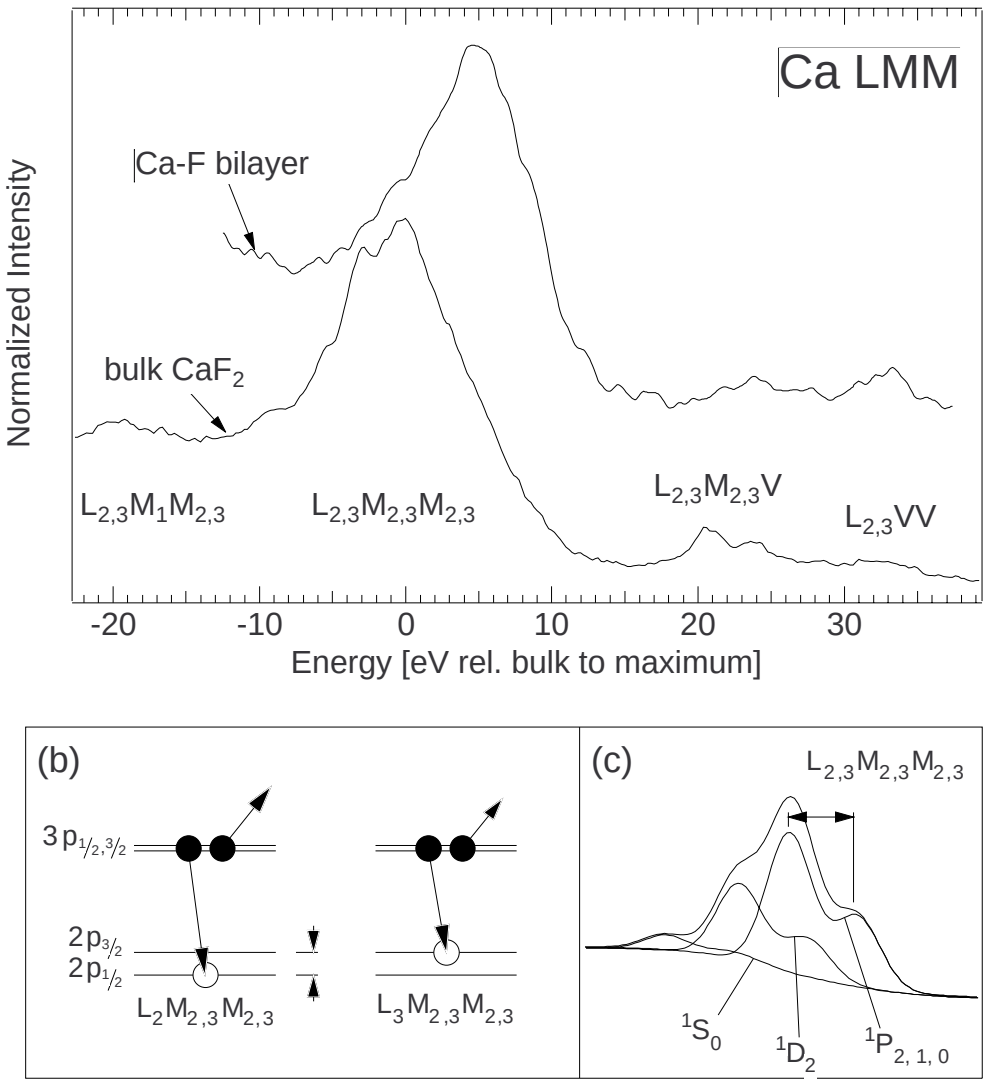

Figure 4.09. (a) Ca LMM bulk and interface lineshapes, taken from the spectra of a thick film (2/2/92) and a single exposed Ca-F bilayer (2/2/91), (b) the energy levels involved for the $L_{2,3}M_{2,3}M_{2,3}$ transition, and (c) a simplified theoretical model for the lineshape, using the multiplet analysis discussed in the text.

We concentrate on the largest feature in the figure, which is due to $L_{2,3}M_{2,3}M_{2,3}$ transitions (Figure 4.09(b)). The general shape can be understood from a straightforward argument. The final state consists of two identical $3p$ holes. According to the standard LS-coupling scheme [Con51, Sob79], the interaction of two identical p electrons leads to three approximately degenerate configurations: ^{1}S, ^{1}D, and ^{3}P, with relative degeneracies 1, 5, and 9, respectively. These represent the possible final states that are observed in the Auger transition. The 3.55 eV spin-orbit splitting Δ of the initial $2p$ core hole (Figure 4.09(b)) further splits each of these configurations; therefore the $L_{2,3}M_{2,3}M_{2,3}$ group is comprised of three spin-orbit pairs, with relative strengths given by the "statistical" relative occupancy of the $2p$ levels, i.e. 2:1. Figure 4.09(c) shows a simulated spectrum using these relative transition probabilities (1:5:9) and spin-orbit ratio (2:1). The simulation uses artificial broadening and includes the observed inelastic electron background observed in CaF_2. The simulation crudely reproduces the observed transition; the main discrepancy is due to deviations from the simple 1:5:9 transition probabilities. A proper calculation for CaO (whose spectrum is nearly identical with that of CaF_2) including the appropriate Slater integrals [Väy90] gives transition probabilities ~1.8 : 6.2 : 7.0 as well as the correct energy splittings to account for the observed Auger peak.

(c) *F KVV*. Figure 4.10(a) shows F KVV Auger spectra for bulk-like and exposed interface films, acquired from thick and single bilayer films, respectively. As in the case of Ca LMM, the Auger lineshape for F KVV derives from ^{1}S, ^{1}D, and ^{3}P final-state configurations. Since the initial state core hole was in the K shell, there is no spin-orbit splitting, and the overall F KVV lineshape consequently is much narrower than the Ca LMM lineshape.

Comparing the signals from the thick and thin (exposed bilayer) samples, it is evident that the lineshapes differ. The bulk F signal appears to be a sharp peak with a smaller shoulder ~3 eV to lower kinetic energy. We assign these features as being the ^{1}D and ^{3}P final state configurations discussed above; their relative amplitudes are consistent with the ex-

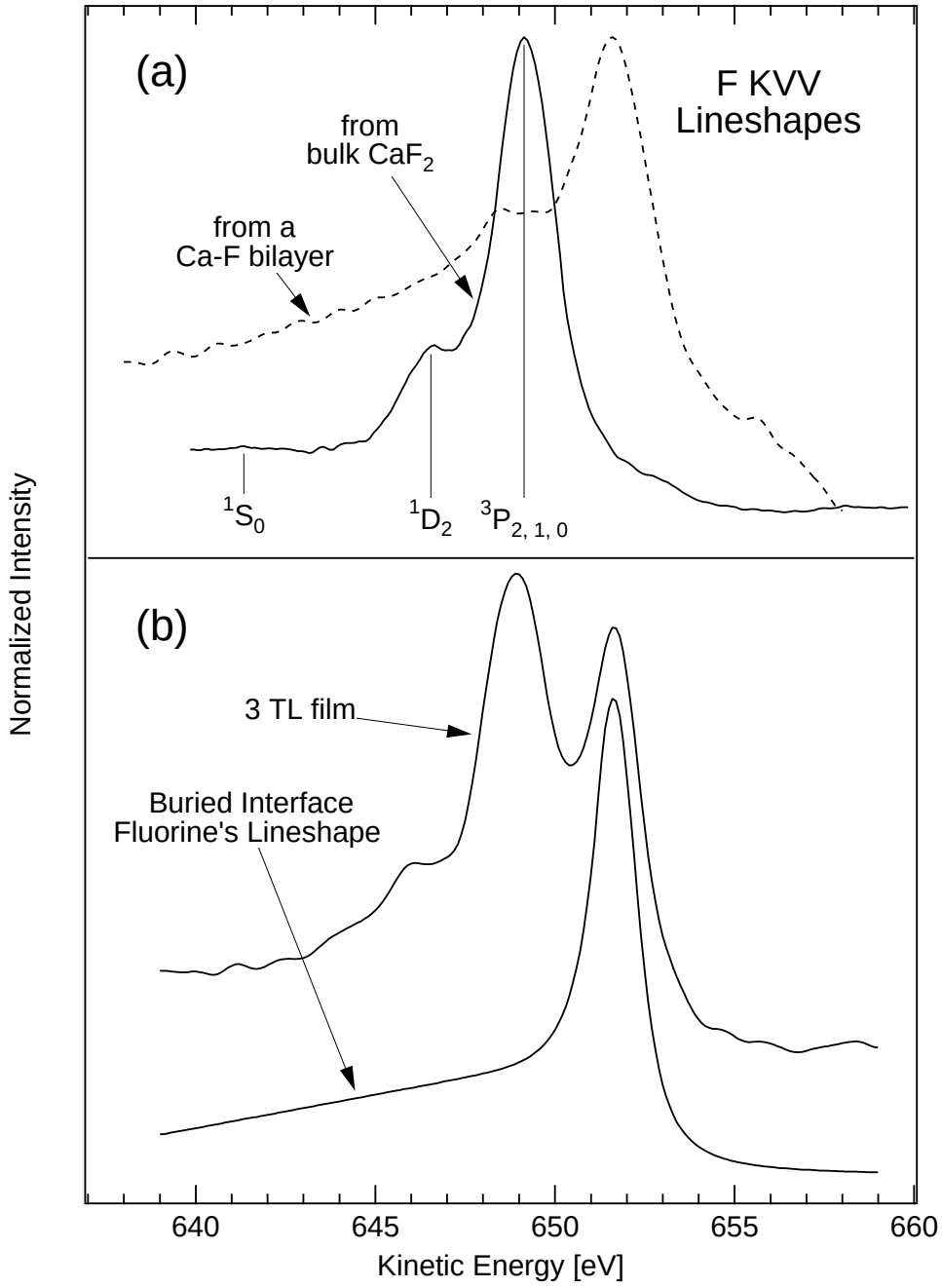

Figure 4.10. (a) F KVV bulk and (disordered) interface lineshapes, taken from the spectra of a thick film (4/7/92) and a single exposed Ca-F bilayer (4/1/92), and (b) Self-consistently derived (ordered) interface lineshape taken from an intermediate thickness film (10/1/92).

pected transition probabilities, and their splitting is consistent with that of elemental F, as reported by Siegbahn [Sie67]. The exposed F atoms' signal is much broader, with a long "metallic-like" tail extending to low kinetic energy.

Figure 4.10(b) shows a typical spectrum from an intermediate thickness film (solid), in this case 3 triple layers (TL) thick. The spectrum is an example of the $\mathscr{S}_{on\text{-}off}$ spectra (described in §5.1) so that it only represents the buried interface and buried bulk-like F signals. While to lowest order this spectrum appears to be a linear combination of the lineshapes in (a), we are unable to derive a satisfactory fit using these spectra as lineshapes. The interface F atom's peak in (b) is much too narrow, and the "metallic-like tail" is reduced in magnitude. Therefore, we found it necessary to derive an acceptable interface lineshape. We did this as follows: We first used the lineshapes from (a) to curve-fit the best values of position and amplitude for the bulk and interface atoms. We subtracted the bulk part of the fit from the experimental spectrum, and used the residual as a new interface lineshape. After iterating this procedure, the interface lineshape quickly converged to the shaded curve in (b) (shown after smoothing). Obviously the converged lineshape is not unique, and one potential problem is that the derived lineshape lacks any remnant ^{1}D peak. This is because of the close alignment of this peak and the bulk ^{3}P peak. It is impossible to determine whether the interface has this peak or not; on the other hand, because of this close alignment, the only affect this has on curve-fits is a slight alteration of the relative bulk/interface heights. Having the correct linewidth for the interface atoms was of much more importance in order to get accurate energy splittings, so we were satisfied with the derived lineshape.

$\underline{SrF_2}$. *(a) Strontium.* Figure 4.11 shows the (a) Sr 3*p* and (b) Sr 3*d* lineshapes used in this study, both for bulk and for interface Sr atoms' peaks. As was usual, the lineshapes were taken from very thick and from very thin (single Sr-F bilayer) samples' spectra. Similar to the Ca 2*p* case, the bulk loss spectra show exciton loss peaks at ~11 eV loss (not shown in the figure); these exciton losses are replaced by less shifted loss features in the interface loss

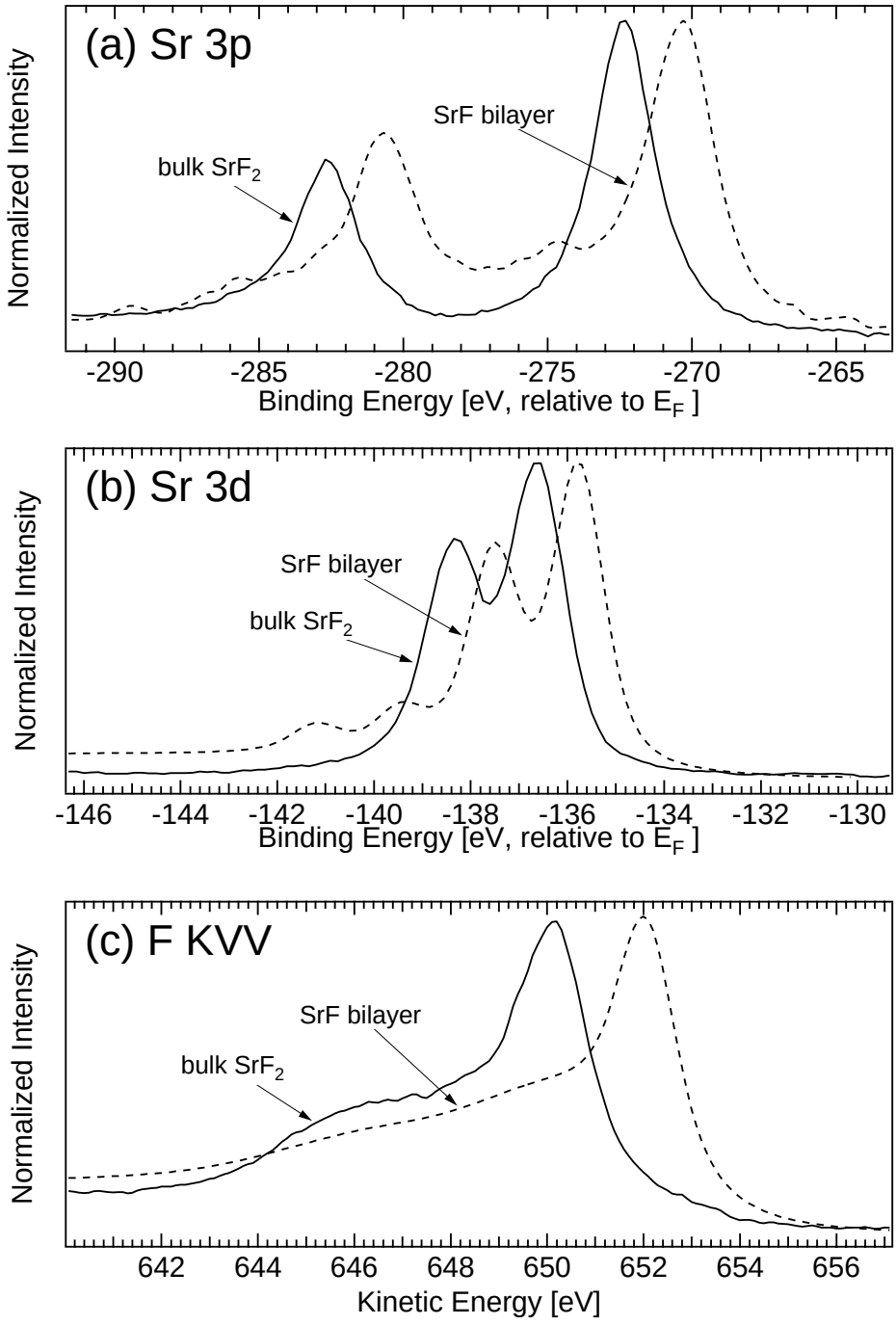

Figure 4.11. SrF_2 bulk (solid, 3/1/92) and interface (grey, 10/3/92) lineshapes for (a) Sr 3p electrons, (b) Sr 3d electrons, and (c) F KVV electrons.

spectra. The magnitudes and shifts of the loss peaks are not, however, the same for both Sr 3*p* and Sr 3*d* (or for that matter, Ca 2*p*). This has implications for any model which tries to explain the origin of these loss peaks (see Appendix B). The interface lineshapes also have the metallic-like tail that was characteristic of the interface Ca 2*p* spectrum.

(b) F KVV. Figure 4.11(c) shows F KVV bulk and interface lineshapes. The bulk lineshape was taken from a thick film spectrum, while the interface lineshape was derived self-consistently using a similar procedure to that for CaF_2 (discussed above). It is interesting to compare the bulk F KVV lineshapes for CaF_2 and SrF_2 (Figures 4.10 and 4.11(c), resp.). The main difference is that SrF_2 has a larger ratio ^1D:^3P than CaF_2. The ^1D peak also appears to be wider for SrF_2. Clearly the nature of the Auger transition makes it highly sensitive to the valence-band structure, so that the observed difference must somehow reflect the electronic states in the crystal. There is very little experimental work on this issue; we have performed a literature search and have not found similar reports for other ionic crystal families. The lack of data is probably due to the difficulty in performing this measurement on insulators due to sample charging, and from the relative rarity of epitaxial insulating thin film systems.

4.1.6 Inelastic Scattering: Comments

Throughout the previous sections, we did not discuss the physical implications of the different smooth backgrounds observed. We determined the following rules for smooth backgrounds, which can be observed in Figure 4.01 and other figures in this chapter. (i) All bulk Auger peaks have large step-like backgrounds, i.e. the background on the low kinetic energy side is considerably higher than on the high kinetic energy side. These step like backgrounds do eventually decay ~60 eV from the primary peaks. Bulk photoemission peaks, on the other hand, have relatively little of this effect. This also holds for Si substrate emission, although there is some step-like background on the Si 2*p* core level. (ii) Interface Ca and F core-level peaks, on the other hand, have large metallic-like tails, for both Auger and core-level peaks.

First we discuss observation (i). Currently, the accepted model is that the inelastic scattering tail is due to extrinsic losses, i.e. scattering between the emitting atom and the detector. Commonly quoted sources are Tougaard [Tou88] and Tofterup [Tof88], who have considered Auger/XPS peaks in metals. It could very well be true that the inelastic losses are completely extrinsic in metals, for there the backgrounds are similar for Auger and XPS peaks. For semiconductors [Ros91] and insulators [Ben90, Väy90], the Auger peaks look very similar to metallic ones, so that the Tougaard and Tofterup models adequately describe the peak shapes. To our knowledge, however, there are no studies which compare Auger and core-level peaks in the same insulator; in CaF_2 and SrF_2 we determined that the extrinsic explanation is not consistent with observation (i). Also, at first glance, the Auger peaks in these insulators should not have such inelastic losses starting at the primary peak because they violate the fact that the minimum energy for electronic excitations is equal to the bandgap, or ~12 eV.

If the Auger and core-level emission have different inelastic losses, there are several possible explanations. The first is that inelastic scattering could be energy-dependent. This is ruled out dramatically by the case of F 1*s* *vs.* F KVV electrons. For Mg K_α radiation, the F 1*s* kinetic energy is only ~100 eV less than the F KVV kinetic energy, yet the F 1*s* has no observable step-like tail, while the F KVV has a significant one. For Al K_α radiation, the F 1*s* kinetic energy is ~100 eV greater than the F KVV energy, yet the same observation still holds. Another possible explanation is the final state angular momentum difference; however, this effect should be short-range and also weak for the high kinetic energies for the fluorine emissions. The only remaining explanation is that the loss structure observed for Auger electrons is due to an intrinsic process. The main difference between the Auger and XPS final states is the presence of two versus one core holes, respectively. We speculate that in insulators, the presence of the second core hole affects the local electronic structure around the atom of interest so that very locally the solid becomes "metallic." A mechanism for this is

that the presence of so much localized positive charge can lower the binding energy of the unoccupied conduction band to let it overlap with the occupied valence band. The outgoing Auger electron can then create infinitesimal excitations between the valence and conduction bands. Evidently, the single core-hole present in XPS is insufficient to close the band gap in this fashion.

Observation (ii) says that both the Auger and XPS peaks appear metallic for the interface atoms. This would make sense because it is known that the interface bond between Ca/Sr and Si is the basis for a two-dimensional, semiconducting bandgap [Him89]. In this case the presence of a single core hole must be sufficient to close the bandgap. The interpretation is further complicated by the possibility of creating excitations both in the silicon and in the overlayer, although it would appear the excitations must be in the overlayer, since bulk Si does not show such a strong metallic tail.

4.1.7 Fourier Transform Techniques

Analysis and presentation of XPS data poses several requirements. It is often important to deconvolve the x-ray satellites (§3.5.1) from the spectrum. Because of our empirical lineshape approach, we have preferred to do this deconvolution before curve-fitting. Additionally, after curve fitting it is convenient to deconvolve the spin-orbit splittings observed for non-s electrons (e.g. Figures 4.03 and 4.04). Finally, it is desirable that statistical noise be removed from the data before presentation, i.e. that the data be *smoothed*. We developed a single, simple algorithm based on the fast Fourier transform (FFT) which can optionally perform one, two, or all of these operations on an spectrum. In our method, we rely on the convolution theorem,

$$F[s * f] = F[s]F[f], \tag{4.7}$$

where the raw data $s * f$ is comprised of a desired signal s convoluted with some function f, and $\mathcal{F}[]$ is the Fourier transform operator. We can easily solve numerically for s as

$$s = F^{-1}\left[F[s*f]/F[f]\right]. \tag{4.8}$$

The x-ray satellites were discussed in Chapter 3. We can approximate the effect of the satellite convolution by (refer to Table 3.01):

$$f_{Mg} = \delta(0) + 0.01\delta(4.5\ eV) + 0.09\delta(8.4\ eV) + 0.05\delta(10\ eV) \tag{4.9}$$

with a similar result applying for Al. This approximation assumes that the widths of the satellite peaks are each equal to the combined width of the $K_{\alpha 1,2}$ peak (In principle one could replace the delta functions with Gaussian functions to represent wider satellite peaks, although (4.9) gave satisfactory results). The Fourier transform of (4.9) is simply (in general form):

$$F[f] = 1 + \sum (ratio) e^{2\pi i (splitting)}. \tag{4.10}$$

Eqs. (4.8) and (4.10) are used together to deconvolve the satellite spectrum. They are equally applicable to spin-orbit deconvolution, where now the ratio used is given by the quantum mechanical degeneracies as:

$$ratio = \begin{cases} \dfrac{2(3/2)+1}{2(1/2)+1} & p\ electrons \\ \\ \dfrac{2(5/2)+1}{2(3/2)+1} & d\ electrons \end{cases}, \tag{4.11}$$

etc., and the splitting may be determined for any particular atom by analyzing the spectrum from a thick material. Spin-orbit splittings and ratios used in this study are tabulated in Table

Table 4.01. Spin-orbit splittings and ratios used in this study.

Core-level	Splitting [eV]	Ratio
Ca 2p (1/2, 3/2)	3.55	0.53
Sr 3p (1/2, 3/2)	10.3	0.55
Sr 3d (3/2, 5/2)	1.75	0.67
Si 2p (1/2, 3/2)	0.605	0.50

4.01.

Data smoothing may also be performed using the FFT method. We rely on the fact that the observed noise is comprised largely of higher frequencies than the data and use a standard optimal filtering algorithm [Pre86].

4.1.8 Fermi Edge Determination

This section discusses how we established the energy scale calibration for our spectrometer. The basic principle for XPS calibration is that samples are always in contact with a metallic (in our case Molybdenum) sample holder, so that the Fermi level is the same across our sample and overlayer. In this condition, the sample and the electrostatic analyzer's potentials are referenced to a common ground. Therefore, it is common practice to calibrate the energy scale against the sample holder's Fermi level.

Constant Fermi level across an overlayer requires the free flow of charge which in principle is inhibited in insulating overlayers. If this is violated, then sample charging may be a problem as photoelectrons leaving the sample are not replaced by conduction from ground. This is manifested as a gradual increase in binding energy of peaks as the degree of charging increases with time. Nonuniform charging leads to a broadening of peaks as well, which can impede the measurement of small CLSs. We have not observed this to be a problem, for three possible reasons: (i) Our overlayers are thin enough so that electron conduction via tunnelling may occur, (ii) Defects in the insulating overlayer may improve the electric conductivity of the overlayers, and (iii) CaF_2 and SrF_2 have high ionic conductivity (via F ion motion) which may also act to compensate charging.

The Fermi level is easy to determine by moving the sample holder into the spectrometer's focus and acquiring the electron density of states (DOS) for the Mo conduction band. Figure 4.12(a) shows a theoretical DOS profile for crystalline Mo [Koe74, Jan89]. Figure 4.12(b) shows the same theoretical DOS convoluted with a Voigt profile to simulate an experimental spectrum; the experimental data acquired with monochrometized Al K_α

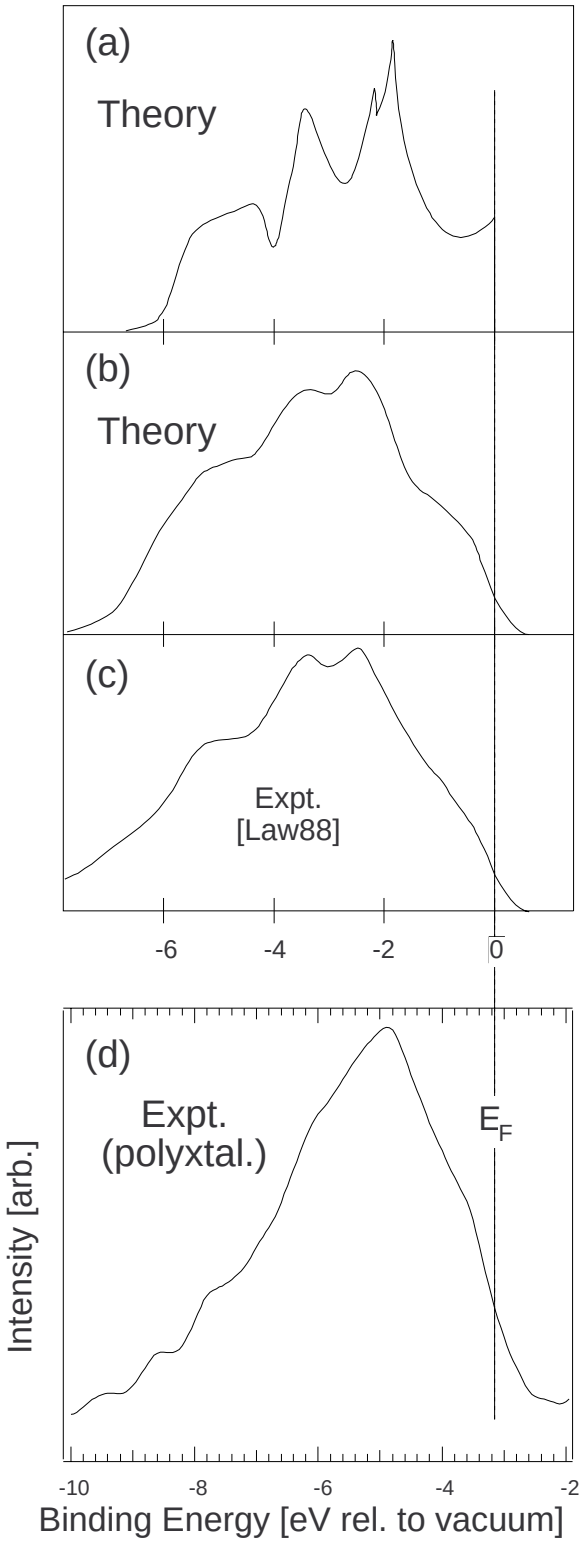

Figure 4.12. Fermi edge determination using Molybdenum DOS. (a) Theoretical Molybdenum DOS [Koe74], (b) the theoretical DOS convolved with a Voigt profile to simulate experiment, (c) the experimental profile of crystalline Mo [Law88], and (d) the experimental profile in this study of polycrystalline Mo.

radiation is shown in (c) [Law88]. We show the same Mo DOS acquired from our polycrystalline Mo sample holder in Figure 4.12(d). Comparing (c) to (d) we are able to establish the Fermi level E_F to within about $\pm$ 0.3 eV. In practice we need only measure the DOS once in conjunction with the much stronger and sharper Mo 3*d* peak; later recalibrations need only measure the Mo 3*d* peak to infer the Fermi level.

An alternate method sometimes used was to rely on the published binding energy of Au 4*f* electrons relative to the Au Fermi level (-84.0 eV [Bri83]). In this case, a sputtered gold foil was brought into the spectrometer. This method has the advantage that the Au 4f levels are very sharp compared to the Mo 3d levels; the disadvantage was that a special gold sample had to be introduced into the chamber. It was sometimes more convenient to rely on the Mo sample holder which could quickly be placed in the spectrometer's focus.

4.2 X-ray Photoelectron Diffraction

In the previous discussion, we evaluated the effect of inelastic scattering on the XPS peaks measured. The inelastic scattering lead to both useful and burdensome effects. In this section, we discuss elastic scattering, or the x-ray photoelectron diffraction (XPD) technique. The exact theoretical treatment has been adequately reviewed [Cha91, Den93] and is beyond the scope of this thesis. The purpose here is to highlight the important features and how they will be used to interpret angle-resolved data. Figure 4.13 shows a schematic of the XPD experiment. An x-ray excites a photoelectron from a buried atom; electrons scattered from this atom are emitted into a torus characteristic of dipole radiation. A photo- or Auger electron can elastically scatter from a neighboring atom, which then emits a spherical electron wave. The detector, which is located at angles (θ, ϕ) relative to the sample surface, sees an interference pattern between the unscattered and scattered electrons; this interference leads to a characteristic diffraction pattern.

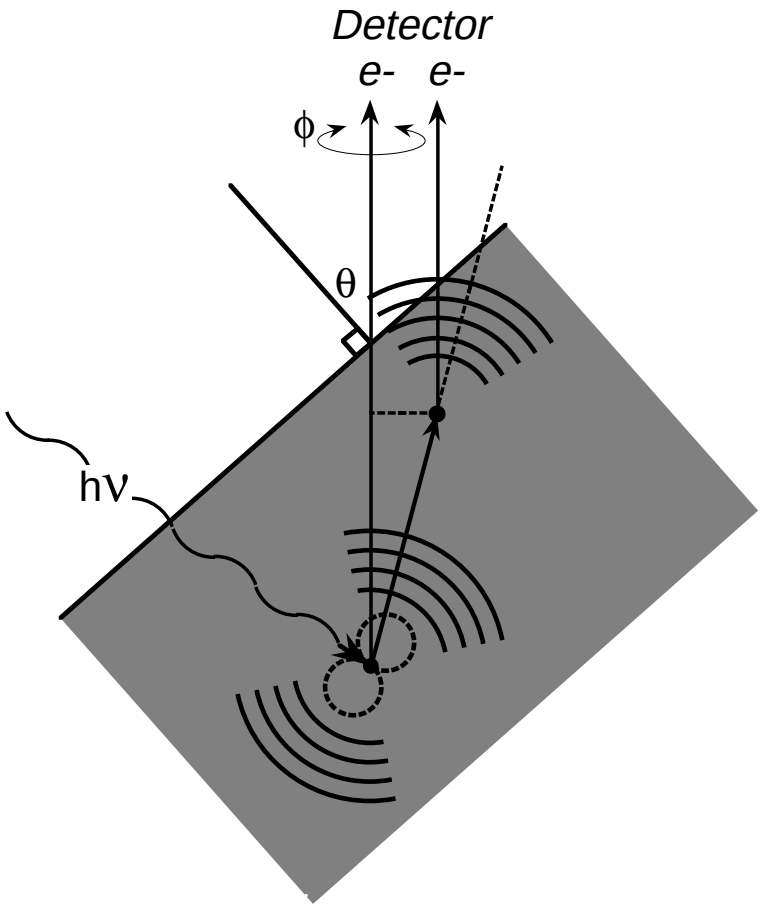

Figure 4.13. XPD experiment schematic. An incident x-ray induces electron emission from a buried atom. Interference between this electron wave and a scattered wave is determined at the detector.

4.2.1 XPD Theory

The theory follows the development by Chambers [Cha91]. The unscattered electron wave function is a modulated spherical wave given by

$$\Psi_0(\mathbf{r}) \propto Y_{L_f}(\hat{k}) \times \frac{e^{ikr}}{r}, \tag{4.12}$$

where the prefactor Y, which depends on the initial x-ray polarization, is the matrix element for the ionization event. The prefactor depends on L_f, the angular momentum of the final state, e.g. for s core electrons, Y reflects a p-wave amplitude according to the dipole selection rule. Auger transitions, on the other hand, do not follow a simple selection rule (since the

interaction is a multiple electron-electron coulomb interaction [Cha76]), so that the emission consists of many angular momenta components. For Auger electrons with high kinetic energy, then, we can substitute $Y \sim 1$.

The scattered wave at the j^{th} atom is expressed as a spherical wave in terms of the unscattered wavefunction:

$$\Psi_j(\mathbf{r}_j) = \Psi_0(\mathbf{r}_j) \times \left| f(\theta_j) \right| e^{i\delta(\theta_j)} \times \frac{e^{ik|\mathbf{r}-\mathbf{r}_j|}}{|\mathbf{r}-\mathbf{r}_j|}, \tag{4.13}$$

where θ_j is the angle the scattered wave makes with the unscattered wave. The important physics of the scattering is contained in the complex phase factor with amplitude $|f|$ and phase shift δ. The total intensity observed at the detector in direction $\mathbf{k}$ is

$$I(\mathbf{k}) \propto \left| \Psi_0(\mathbf{r}) + \sum_j \Psi_j(\mathbf{r}_j) \right|^2 \tag{4.14}$$

Several modifications are added to this simple picture in order to model real samples:

(1) Thermal corrections. These are modelled by multiplying the outgoing spherical wave (4.13) with an appropriate Debye-Waller factor. The Debye-Waller factor can also be used to simulate disorder due to lack of crystallinity in the film.

(2) Inelastic scattering. A simple exponential factor is added to each of the unscattered (4.12) and scattered waves (4.13) to account for beam attenuation due to inelastic scattering.

(3) Multiple scattering. In general multiple scattering can be neglected, since the scattering amplitude is weak for large θ_j. For small θ_j, as occurs along chains of atoms, multiple scattering becomes important, so that more scattered wavefunctions need to be added to (4.14).

(4) Electron wave refraction. As the electron wave departs through the sample surface, a potential barrier is encountered. Similar to Snell's law for optical waves, the electrons with angle θ in the solid have a rotated angle θ' outside the solid. For a potential

barrier V_0 this change in angle is determined by

$$E_{out}{}^{-1/2}\cos\theta' = E_{in}{}^{-1/2}\cos\theta, \tag{4.15}$$

where E_{in} is the kinetic energy in the sample, and $E_{out} = E_{in} - V_0$ is the kinetic energy outside of the sample.

(5) Detector angular acceptance. Because of the finite angular acceptance of the detector, equation (4.14) is averaged over a finite range of angles. In our experiment the angular acceptance was ≈ 4°.

Calculation of the complex scattering factor $f(\theta)$ is accomplished using the FEFF code written by Rehr and coworkers [Reh91] based on the theory by Mustre de Leon *et al.* [Mus89]. From elementary scattering theory, the complex scattering factor is broken into partial waves (for infinitely small scatterer radius) as

$$f(\theta) = \frac{1}{k}\sum_l (2l+1)\left(e^{i\delta_l}\sin\delta_l\right)P_l(\cos(\theta)), \tag{4.16}$$

where P_l is a Legendre polynomial. The FEFF code gave the partial phase shifts δ_l for each scatterer in a finite cluster supplied to the program. This program, originally developed for EXAFS modelling, is a complete muffin-tin potential LDA calculation which determines the charge densities on each atom. From these charge densities the required phase shifts are calculated and reported.

For smallest emitter-scatterer distances, the finite size of the scatterer must be taken into account. Equation (4.16) neglected the curvature of the unscattered wave in comparison to the size of the scatterer. To lowest order, inclusion of *spherical wave corrections* transforms (4.16) to

$$f(\theta) = \frac{1}{k}\sum_l G(l, L_f)\left(e^{i\delta_l}\sin\delta_l\right)P_l(\cos(\theta)), \tag{4.17}$$

where the coefficients G depend on the angular momentum state of the unscattered wave and are given by Mustre de Leon [Mus89].

Typical Ca → Ca electron scattering factor (ESF) amplitudes for various scattering distances are shown in Figure 4.14. Plotted are $|f(\theta)|$ according to (4.17) for three interatomic distances: 2.37, 3.86, and 5.46 Å. They were calculated for Ca 2*p* *d*-wave scattering from another Ca atom (The dipole selection rules specify *p*-states are emitted into s and d waves; because the degeneracy of d-waves is 5 times that of *s*-waves, we assume that the s-wave component is negligible). These ESFs converge in shape to the plane-wave approximation (4.16), also plotted in the figure. The important feature in Figure 4.14 is the strong peak in the scattering amplitude at zero scattering angle. This is called the forward-focussing effect, since the scattering factor moves intensity from large angles to the forward direction parallel to the interatomic axis.

The interference between unscattered and scattered waves imposes additional interference oscillations upon the observed signal, which are called *first and higher order diffraction peaks*. This effect, is demonstrated in Figure 4.15, where the total intensity $I(\mathbf{k})$ from (4.14)

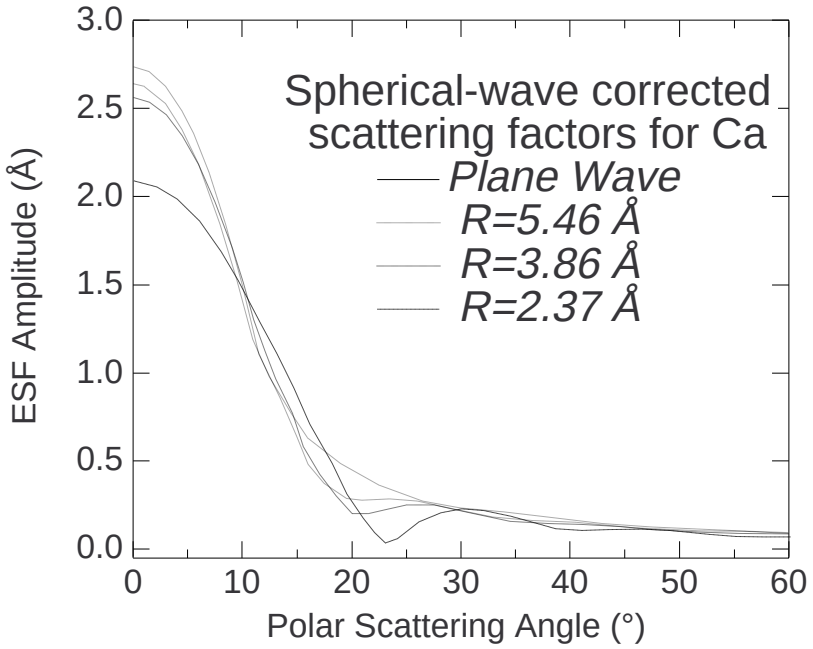

Figure 4.14. Electron scattering factor amplitude for Ca in CaF_2. Shown are computations for Ca→Ca scattering with various interatomic distances. The computed shapes converge to the plane-wave approximated curve (bold). The Ca *d* electrons have 905 eV kinetic energy.

for the chain of Ca atoms in the [110] direction of CaF_2. The figure illustrates how the forward-focussing peak is convoluted with the interference pattern, and it also serves to show the effect of multiple scattering. Scatterings from atoms $1 \rightarrow 2$ plus $1 \rightarrow 3$ calculated with (4.14) as-is results in an artificially large forward scattering peak. But inclusion of the extra scattering event $1 \rightarrow 2 \rightarrow 3$ introduces an extra cancellation which reduces the forward focussing effect. A further observation is the narrowing of the central peak as multiple scattering is introduced. This narrowing will be easily observable in the data for progressively thicker films.

Application of XPD theory to a real solid surface ($CaF_2(111)$) is shown in Figure 4.16. We show the complete XPD modulations for electrons emitted from each of the three Ca atoms closest to the surface, acquired for scattering confined to the $(1\bar{1}0)$ plane. The surface Ca atom (a) shows forward focussing and interference structure corresponding to F atoms at large angles; the emission is almost isotropic near the normal [111] direction. In (b,

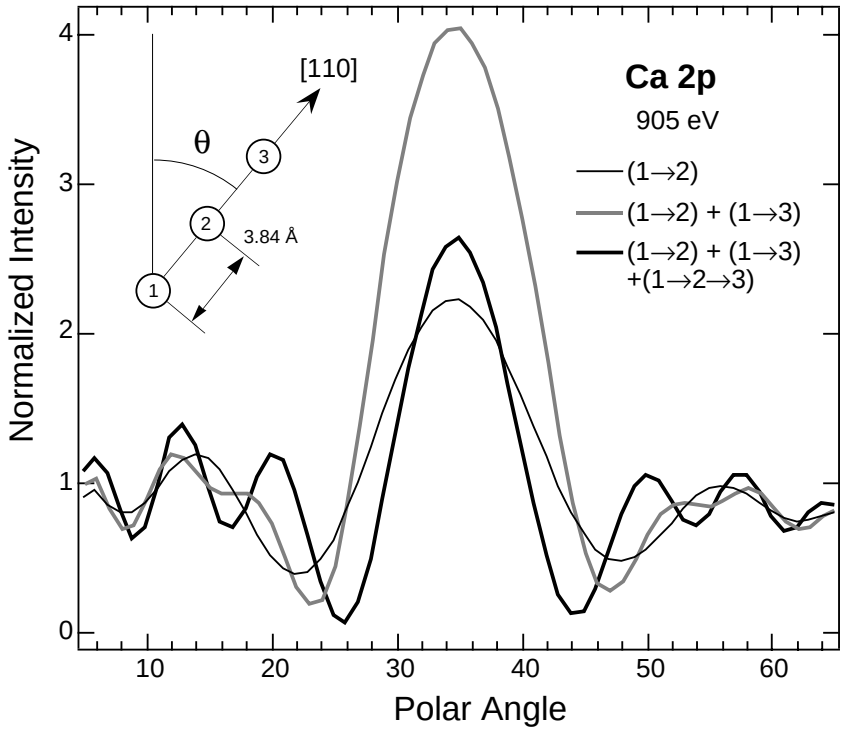

Figure 4.15. Simulated XPD scattering for a chain of Ca atoms. The included scattering for each calculation is described in the legend [Den93].

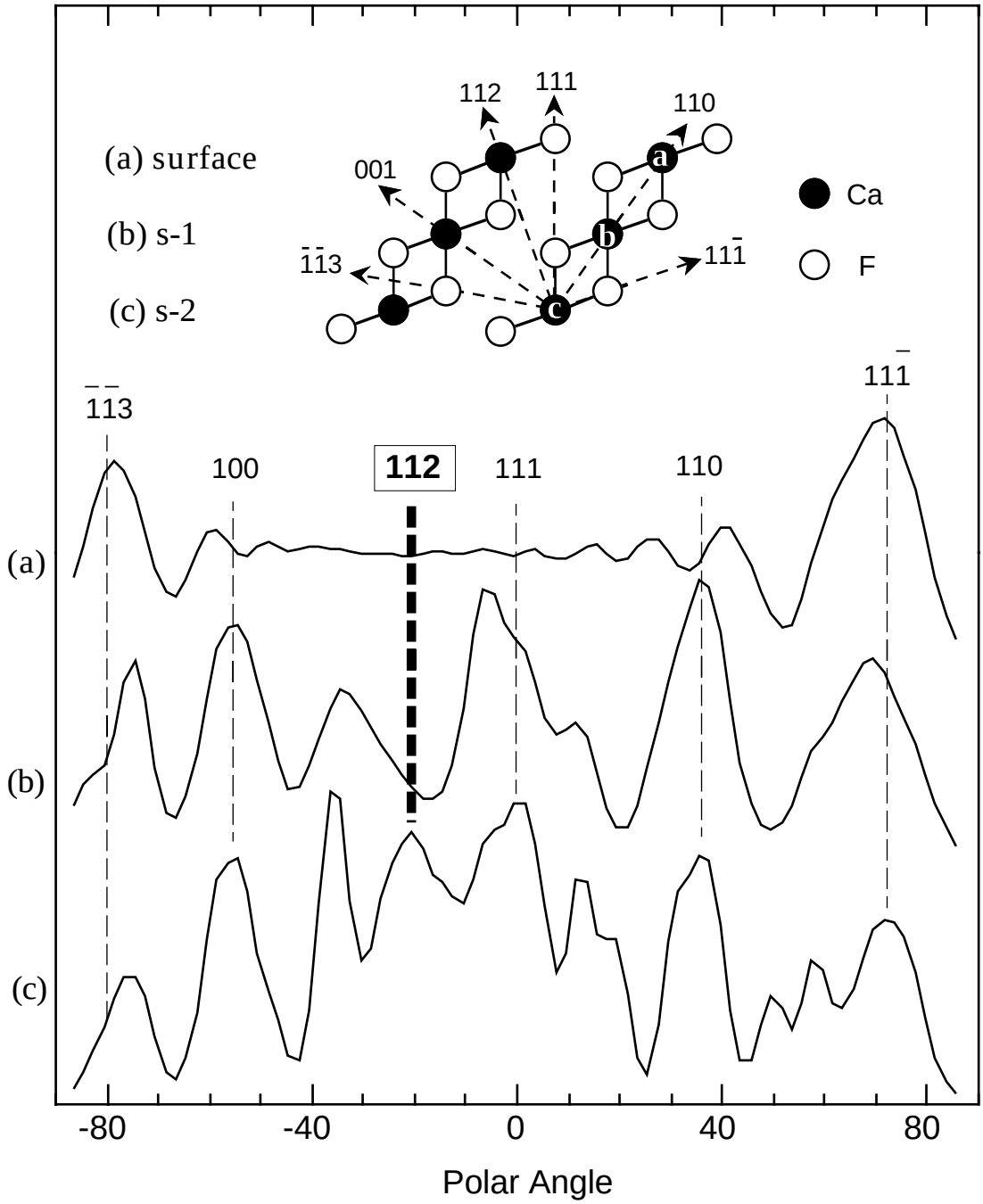

Figure 4.16. Theoretical XPD profiles for 3 triple layers of CaF_2. (a) Surface Ca emission, (b) Second layer Ca emission profile, and (c) Third layer Ca emission profile. The [112] peak, which uniquely identifies the third layer Ca site, is shown boxed.

c), we see the development of additional scattering features due to the overlying atoms. We have singled out a particular feature in (c): the Ca → Ca scattering in the [112] direction. We will later rely on this peak as a "signature"—any XPD profile with forward focussing in this direction comes from a Ca atom with at least two overlying F-Ca-F triple layers above it. Other unlabelled features in the figure are assigned to first or higher order diffraction features. Because of constructive interference, these spurious diffraction features can be as strong as the forward-focussing peaks we are concerned with. They can be identified either by comparison with theoretical models such as in the figure, or by comparing XPD profiles acquired with electrons of different wavevectors–Ca 2*p* *vs.* Ca LMM, for example–in which case the diffraction features will be observed to appear at different angles while the forward-focussing peaks remain fixed at the low-index directions of the crystal.

The next chapter unifies the XPS and XPD techniques and shows how powerful the combination can be both for measuring small core-level shifts as well for discerning film morphology.

Sample Growth & Characterization 5

5.0 Introduction

Chapter 4 introduced the XPS and XPD techniques. In this chapter we discuss how the combination gives valuable information on film structure and morphology. We also discuss the microscopic mechanisms behind the formation of different film morphologies. Once the film morphologies are known, we will be in a position to correlate the observed core-level shifts with the known film morphologies (Chapter 6).

Thin (0.5 to 8 triple layer) CaF_2-on-Si(111) films were grown using molecular beam epitaxy (MBE) and characterized using an *in situ* combination of x-ray photoelectron spectroscopy (XPS) and component-resolved x-ray photoelectron diffraction (XPD). We identify three distinct regimes: (i) for high temperatures and flux we find a complete, reacted Si-Ca-F layer, overlaid by 2 layer high islands which coalesce, followed by layer-by-layer growth, (ii) for high temperature and low flux, we find the reacted Si-Ca-F layer to be partially covered with thick islands, and (iii) for low temperatures we find an incompletely occupied Si-Ca-F layer followed by layer-by-layer growth. In all cases we find the buried interface to be structurally identical to the unburied Si-Ca-F layer, apart from an increased ordering as discussed in Chapter 4.

Tables C.01 and C.02 in appendix C summarize the film growths in this thesis. Table C.01 shows CaF_2 growth conditions and morphologies determined using the XPS/XPD methods detailed in the coming sections. The samples are indexed as (month/sample #/year). Samples grown at the Lawrence Berkeley Laboratory are similarly indexed as (month/day/year). For CaF_2 films, we will show that the morphology ranges from uniformly flat to islands atop an exposed interface layer. The parameters n and f characterize this range and are illustrated in Figure C.01: n is the average island thickness, and f is the fraction of the

interface layer covered by islands. The naming convention for particular atoms used throughout this Chapter and Chapter 6 is illustrated in Figure C.02. Surface, bulk, and interface atoms are abbreviated *S*, *B*, and *I*, with numerical subscripts when more than one type is present at once.

Table C.02 summarizes the SrF_2 growths. We find that all the films display the islanded morphology seen sometimes for CaF_2. We additionally find differences in the film orientation and interface reconstruction, which are summarized in the table.

The technique of deriving CLSs from XPS/XPD measurements (§5.1) has been published by Rotenberg *et al.* [Rot93]. The quantitative model for morphology from XPS/XPD data (§§5.2.1-5.2.4) has been published by Denlinger [Den93 (thesis)], as well as Denlinger *et al.* [Den93b, c]. The determination of morphology from XPS/TEM data (§5.2.5) has been outlined by Wong *et al.* [Won93]. Some of the SrF_2 results (§5.4) have been published by Denlinger [Den93 (thesis)].

5.1 Combined XPD/XPS Analysis

In this section, we show how the XPD effect can be used to identify small XPS core-level shifts. Figure 5.01 shows how the two techniques are coupled. The diagram shows a generic three-layer thick film. Curve (a) shows a possible XPS spectrum in which the three types of atoms (surface *S*, bulk *B*, and interface *I*) each contribute a peak. The spectrum is acquired away from any low-index directions so that none of the peaks are forward-focussed. This direction is called the *off-axis* direction. Curve (b) represents a spectrum acquired along a low-index direction, which will usually be normal to the film ($\theta = 0°$); this direction is called the *on-axis* direction. Atoms *B* and *I* have their signals forward-focussed in this direction, with fractional enhancements β and ι, respectively. These enhancements are only approximately equal because of the different multiple scattering paths and also because the signal from *I* suffers more attenuation due to inelastic losses than *B*. These two spectra are designated as $\mathscr{S}_{off}$ and $\mathscr{S}_{on}$:

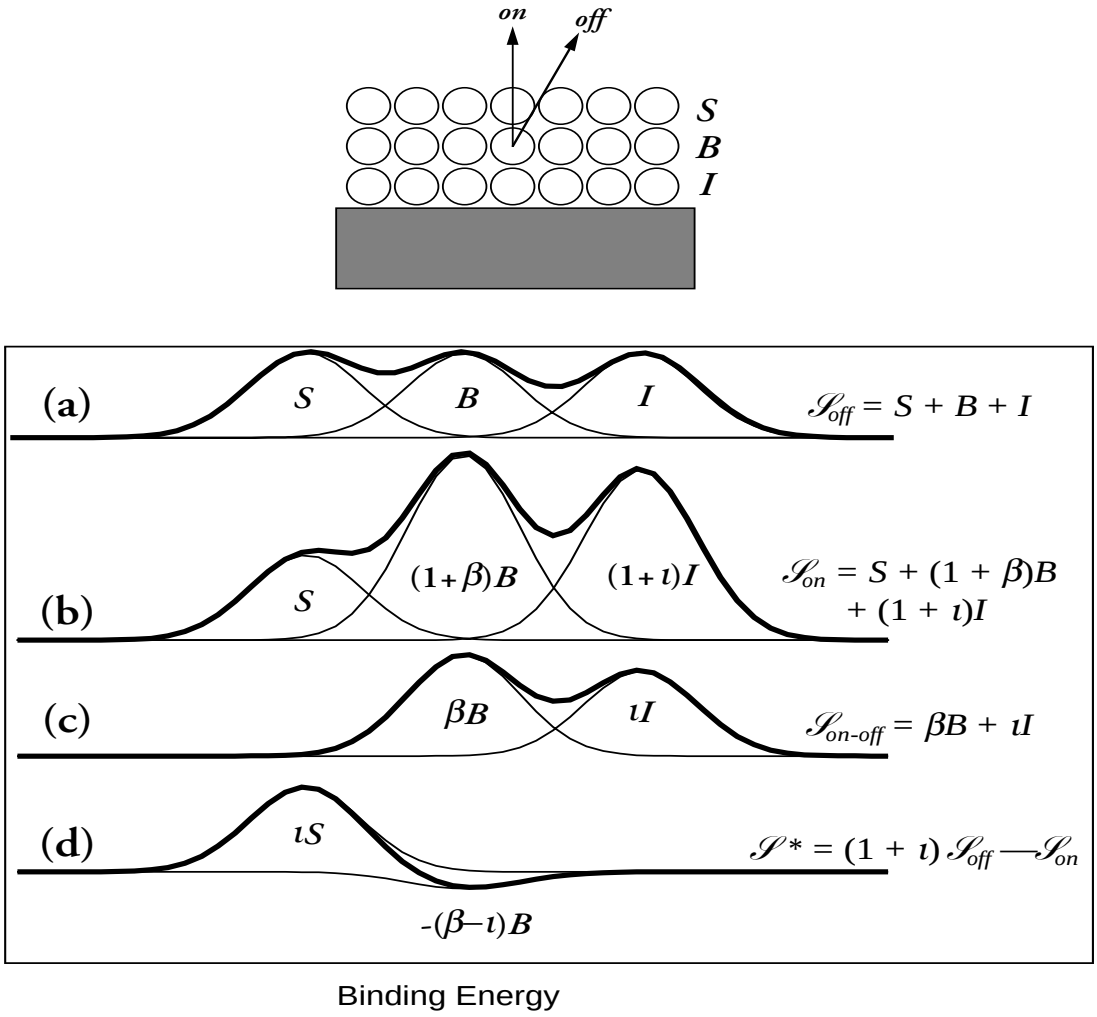

Figure 5.01. Schematic of coupling between XPS spectra and XPD modulations. (a) off-axis spectrum $\mathscr{S}_{off}$, which approximates unmodulated signals from bulk, surface, and interface atoms, (b) on-axis spectrum $\mathscr{S}_{on}$, in which the bulk and interface emissions are forward focussed as they leave the sample, (c) the difference curve $\mathscr{S}_{on-off}$, which is only sensitive to atoms which forward scatter in the normal direction, and (d) the linear combination $\mathscr{S}^*$, which is mostly sensitive to atoms which do not forward scatter in the normal direction.

$$\mathcal{S}_{off} = S + B + I \tag{5.1a}$$

$$\mathcal{S}_{on} = S + (1+\beta)B + (1+\iota)I. \tag{5.1b}$$

Curves (c) and (d) are linear combinations of the measured spectra $\mathcal{S}_{on}$ and $\mathcal{S}_{off}$:

$$\mathcal{S}_{on-off} = \beta B + \iota I \tag{5.1c}$$

$$\begin{aligned}\mathcal{S}^* &= (1+\iota)\mathcal{S}_{off} - \mathcal{S}_{on} \\ &= \iota S - (\beta - \iota)B\end{aligned}. \tag{5.1d}$$

It is clear the $\mathcal{S}_{on\text{-}off}$ unambiguously represents only contributions from atoms *B* and *I*. The other curve $\mathcal{S}^*$ is mostly comprised of surface emission, although it is impossible to completely remove both *B* and *I* by taking a linear combination of $\mathcal{S}_{on}$ and $\mathcal{S}_{off}$ since $\beta \neq \iota$. For the case shown, there is a small negative contribution from the *B* peak.

We will encounter the situation where the *B*-*S* energy splitting is very small, but the *B*-*I* splitting is reasonably large. When this is true, we are able to easily determine the enhancement factor ι (but not β) by inspection of the $\mathcal{S}_{on}$ and $\mathcal{S}_{off}$ spectra. Under these conditions, Figure 5.01 suggests a method of fitting the spectra to accurately measure the *B*-*S* splitting. First, curve (c) is fitted as shown to two peaks only. Then curves (a) and (b) are fit simultaneously, subject to the restrictions that *S* has the same height in both fits, and that the energy positions of *B* and *I* are fixed from the first fit. In principle, this fit gives us the desired positions and height of the *S* peak. We found, however, that for very small splittings *S*-*B* that our least-squares fitting algorithm always underestimated the *S*-*B* splitting and overestimated the height of *S*. Therefore, this fit only gives us a lower limit on the *S*-*B* splitting.

To get an upper limit on the *S*-*B* splitting, we fit curve (d) to a single peak *S*. We construct $\mathcal{S}^*$ using the <u>smallest</u> value of ι consistent with $\mathcal{S}_{on}$ and $\mathcal{S}_{off}$. This always results in an <u>upper</u> limit on the *S*-*B* splitting. The final splitting may then be reported as the average splitting ± one-half of the difference.

An alternate method was sometimes used to get upper and lower limits to the splitting *S*-*B*. Single peak fits to curve (d) were performed for the largest and smallest possible values of

ι consistent with the data. This method was not as accurate as the method described above, but was most useful for cases of extremely small shifts when the least-squares algorithm could not fit to $\mathscr{S}_{on}$ and $\mathscr{S}_{off}$ directly.

5.2 Characterization of Sample Growths using XPD

In this section, we show how the techniques developed in Chapter 4 were used to determine the morphologies of CaF_2 and SrF_2 grown on Si(111).

5.2.1 Growth

CaF_2 was deposited from a graphite crucible at rates from 5 to 110 Å/min onto resistively heated, p-type, 7×7-reconstructed Si wafers oriented within 0.25° of the (111) surface. The growth temperature T was varied from room temperature (RT) to 800°C. Base pressure during analysis was below 10^{-10} Torr; during growth the pressure was $\leq 10^{-8}$ Torr, consisting mainly of nitrogen gas. XPS and XPD spectra were acquired using Mg K_α illumination. XPD scans were obtained in a fixed x-ray/analyzer geometry with polar (θ) and azimuthal (ϕ) sample rotations as discussed in Chapter 3.

5.2.2 Crystallography by XPD

Figures 5.02 and 5.03 show XPD results for a clean Si(111) substrate and for an 8 TL film (6/1/93). In these figures, we show the angle-resolved Si 2*p*, Ca 2*p*, Ca LMM, F 1*s*, and F KVV electron yields. The film was grown with an incident CaF_2 flux of 50Å/min at 650°C. The diagram in Figure 5.02 shows the angular range of (θ, ϕ) over which data were acquired (the definition of ϕ used in the diagram is the same throughout this thesis). The index directions given are relative to the CaF_2 lattice, and data were taken over the shaded sector shown, and then symmetrized according to the substrate's C_{3v} symmetry (we have verified this symmetry over a limited range of polar scans). This procedure is not completely equivalent to acquiring the data over the complete 2π solid angle since the asymmetric placement of the x-ray lamp relative to the sample removes the C_{3v} symmetry. This effect

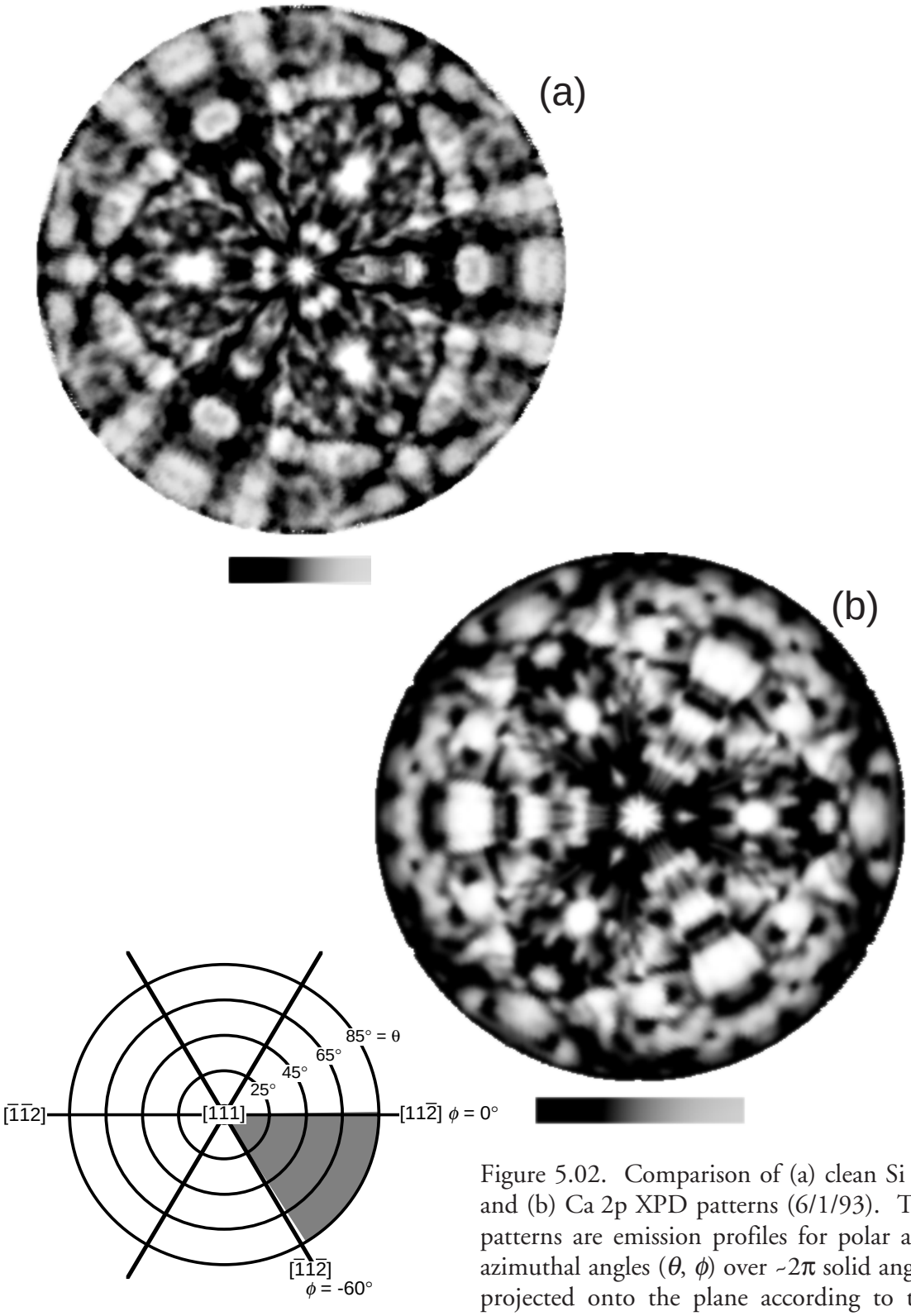

Figure 5.02. Comparison of (a) clean Si 2p and (b) Ca 2p XPD patterns (6/1/93). The patterns are emission profiles for polar and azimuthal angles (θ, ϕ) over ~2π solid angle, projected onto the plane according to the inset. It is evident that the forward focussing peaks in (b) are rotated 180° relative to those in (a), confirming the type-*B* orientation.

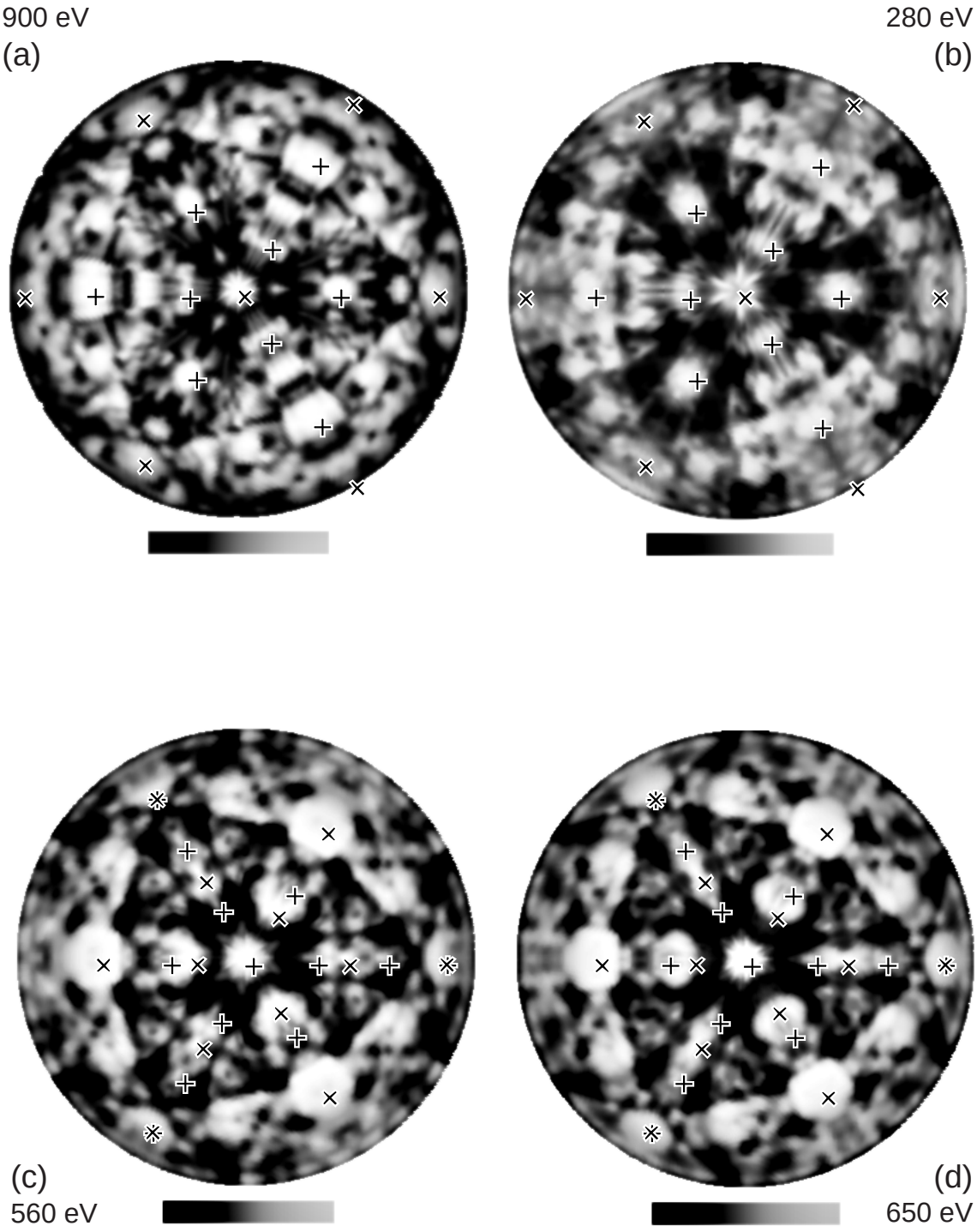

Figure 5.03. Comparison of (a) Ca 2p, (b) Ca LMM, (c) F 1s, and (d) F KVV XPD patterns (6/1/93). Comparison of (a) and (b) illustrates the differences that occur between low and high kinetic-energy electrons in the XPD technique.

arises from the orientation of the x-ray polarization plane relative to the sample and was manifested as differences in the XPD peak shapes taken along symmetry-equivalent crystal directions. The differences were slight (affecting mainly peak amplitudes and not positions) and do not change any of the conclusions presented. The ~cos θ background due to both penetration depth effects and our detector geometry has been subtracted. The background was removed by cylindrically averaging the raw XPD plots and by using the resulting featureless smooth function for subtraction. The image contrast was smoothed and edge-enhanced using a commercial program on a personal computer.

The resulting modulations shown are quite strong (~100%) as predicted by the theory (Figure 4.16), and we have used either theoretical modelling or studied the kinetic energy dependence (see below) to assign all the features as either forward scattering peaks or higher-order diffraction peaks. The plus signs in Figure 5.03 indicate forward focussing directions through neighboring Ca atoms, and the diagonal crosses indicate forward focussing directions through F atoms. Several conclusions may be drawn upon examining the data.

Orientation. For all CaF_2 films we have examined (even down to submonolayer depositions), the overlayer orientation is type-*B*, in which the overlayer is rotated 180° about the [111] direction relative to the Si substrate; this confirms a known result from the literature [Pon86, Tro88, Bat88, Kat91]. This may be readily determined by comparison with substrate XPD modulations in Figure 5.02(a)-(b). The bright forward focussing spots of Si(111) in (a) are a mirror-reflection of CaF_2's in (b). (The overlayer orientation for SrF_2 films is discussed in §5.5.)

Kinetic Energy Dependence. Comparison of Figure 5.03(a) and (b) shows the dependence of the XPD pattern on the kinetic energy of the scattered electron. In (a), we are able to identify forward scattering of 905 eV Ca 2*p* electrons passing through Ca and F atoms as indicated. Confirmation of these features as forward scattering peaks comes from compari-

son with (b), where we show the XPD pattern of 280 eV Ca LMM electrons. The Ca LMM pattern shows features at the same angles, while very few of the remaining features remain constant. The remaining features, then, are due to diffraction peaks arising from the interference between the scattered and unscattered electron waves. As in elementary diffraction experiments, the diffraction peaks for the lower kinetic energy (longer wavelength) electrons (Ca LMM) are dispersed further from the interatomic axes than for the higher kinetic energy electrons (Ca 2*p*), although the many overlapping interference peaks makes this difficult to verify visually. In (b), the strongest forward-focussing peaks are due to Ca → Ca (+ symbols), while the Ca → F peaks (× symbols) are weakened and distorted.

In general, when comparing Auger diffraction patterns to photoelectron diffraction patterns, distortions in peak shapes may be caused by the altered kinetic energy, the altered angular momentum of the electron, or a combination of the two [Fri90, Bar92, Gre92, Sal92, Ter93]. Weissman and Müller [Wei81] give the following selection rules for the final-state angular momentum for *ijk* Auger transitions:

$$\begin{aligned} &\left| l_i - \left| l_j - l_k \right| \right| \le l_f \le l_i + l_j + l_k \\ &l_i + l_j + l_k + l_f = even \end{aligned} \tag{5.0}$$

where $l_{i,j,k}$ are the angular momenta of the participating core levels, and l_f are the possible angular momentum characters of the outgoing electron waves. For the main Ca $L_{23}M_{23}M_{23}$ electrons used here, $l_i = l_j = l_k = 1$, so that we conclude $l_{f,LMM} = 1$ or 3. For the Ca 2*p* electron, the simple optical transition rule applies ($\Delta l = \pm 1$), so that $l_{f,2p} = 0$ or 2. The relative weights of these channels is ~1:5, so that the outgoing electron wave has mostly *d*-character, or $l_{f,2p} \approx 2$. Since both the Auger and photoelectron have different angular momentum character, the distortion of the Ca → F peaks in Figure 5.03(b) may be due to a combination of kinetic energy and angular momentum differences between the electrons.

In contrast, comparing F 1*s* to F KVV Auger XPD patterns (Figure 5.03(c) and (d)), we find very little difference between the two. Because the electron kinetic energies are very

similar, we can conclude that something about the angular momentum final states from this observation. The F 1*s* final state from optical selection rules is $l_{f,1s} = 1$ (*p*-wave). For F KVV=$KL_{2,3}L_{2,3}$, the selection rules indicate that $l_{f,KVV} = 0$ (*s*-wave) or 2 (*d*-wave). A simple rule does not exist for determining the dominant character of the outgoing Auger electron, other than directly computing matrix elements from a complete atomic calculation [Wei81].

Saldin *et al.* [Sal92] calculated the dependence of Cu → Cu XPD for fixed kinetic energy and variable angular momentum. They showed that the XPD patterns are qualitatively almost identical for $l_f = 0$ and $l_f = 1$ waves but begin to show significant deviations for $l_f \geq 2$. If we can generalize these results to F→ Ca and F → F scattering at lower energy, then we can preliminarily conclude from the XPD patterns that $l_{f,KVV} = 0$ dominates the Auger transition final state.

Atomic Structure. There are two distinct pieces of structural information presented in the XPD patterns in Figures 5.02-3. First, the forward scattering peaks as discussed above give direct information on bond angles. We rely on the rich forward-scattering information apparent in the line scans at the boundary of the sector shown in the inset of Figure 5.02: ϕ=0° and ϕ=-60°. Since by symmetry the XPD profile between [111] and $[\bar{1}\,\bar{1}2]$ is equivalent to the profile between [111] and $[\bar{1}1\,\bar{2}]$, we will later (§5.2.3) for convenience report data from the ϕ=-60° azimuth as though it were for ($\theta < 0°$, ϕ=0°).

Because the CaF_2 XPD data shown were acquired from a relatively thick sample, the bond angles which can be obtained from Figure 5.03 are characteristic only of bulk Ca and F sites. Additional information may be acquired for thinner films, in which the individual Ca and F XPS peaks from each triple layer may be separately resolved. For each distinct XPS peak, XPD data such as in Figures 5.02-3 were separately acquired, and the interpretation of these in terms of the interface atomic structure is discussed in §5.2.3.

The second source of structural information comes from the remaining interference peaks, which contain both bond angle and bond length information, similar to the way an

optical hologram of an object preserves distance relationships along an object's surface. This is because, similar to optical holography, a reference wave (unscattered photoelectron from the source atom) interferes with an object wave (the elastically scattered electron from the neighboring atom) such that the phase difference between the waves encodes the bond length information in an interference pattern. Therefore, this remaining part of the XPD pattern forms a hologram which may be numerically inverted to yield the local structure around each Ca, or F atom [Bar88].

The maximum structural information may be obtained by acquiring full XPD patterns for each of the individual Ca and F atoms in a thin film, and by holographically inverting the data for each layer. Currently, the experiment is only marginally feasible with our apparatus due to the large amount of data required and due to the long counting times involved. The experimental apparatus will be upgraded in the future to achieve at least an order of magnitude improvement in counting rate so that this experiment can be routinely performed.

5.2.3 Thin film XPD results

Figure 5.04(a) shows deconvolved Ca $2p_{3/2}$ spectra for a four triple-layer film (9/1/92) at two different emission angles. The spin-orbit splitting and x-ray satellites were deconvolved using the Fourier method discussed in §4.1.7. The growth conditions were 15 s, 52 Å/min at 700°C. Shown are the on-axis emission spectrum $\mathcal{S}_{on}$, the off-axis emission spectrum $\mathcal{S}_{off}$, and the difference curve $\mathcal{S}_{on\text{-}off}$. The off-axis spectrum corresponds to the signal measured at (θ=-26.1°, ϕ=-18°). The angles θ and ϕ for these spectra were carefully chosen from the XPD measurements in Figure 5.03 to be along and just away from the Ca → F forward-scattering enhancement along the [111] axis. The assignments of surface *S*, bulk *B*, and interface *I* peaks are as shown in Figure C.02. The surface assignment is justified because this peak, close in energy to *B*, is absent from the difference spectrum $\mathcal{S}_{on\text{-}off}$, similar to Figure 5.01(c). The assignments *B*, *I* conform to those in previous studies [Rie86,

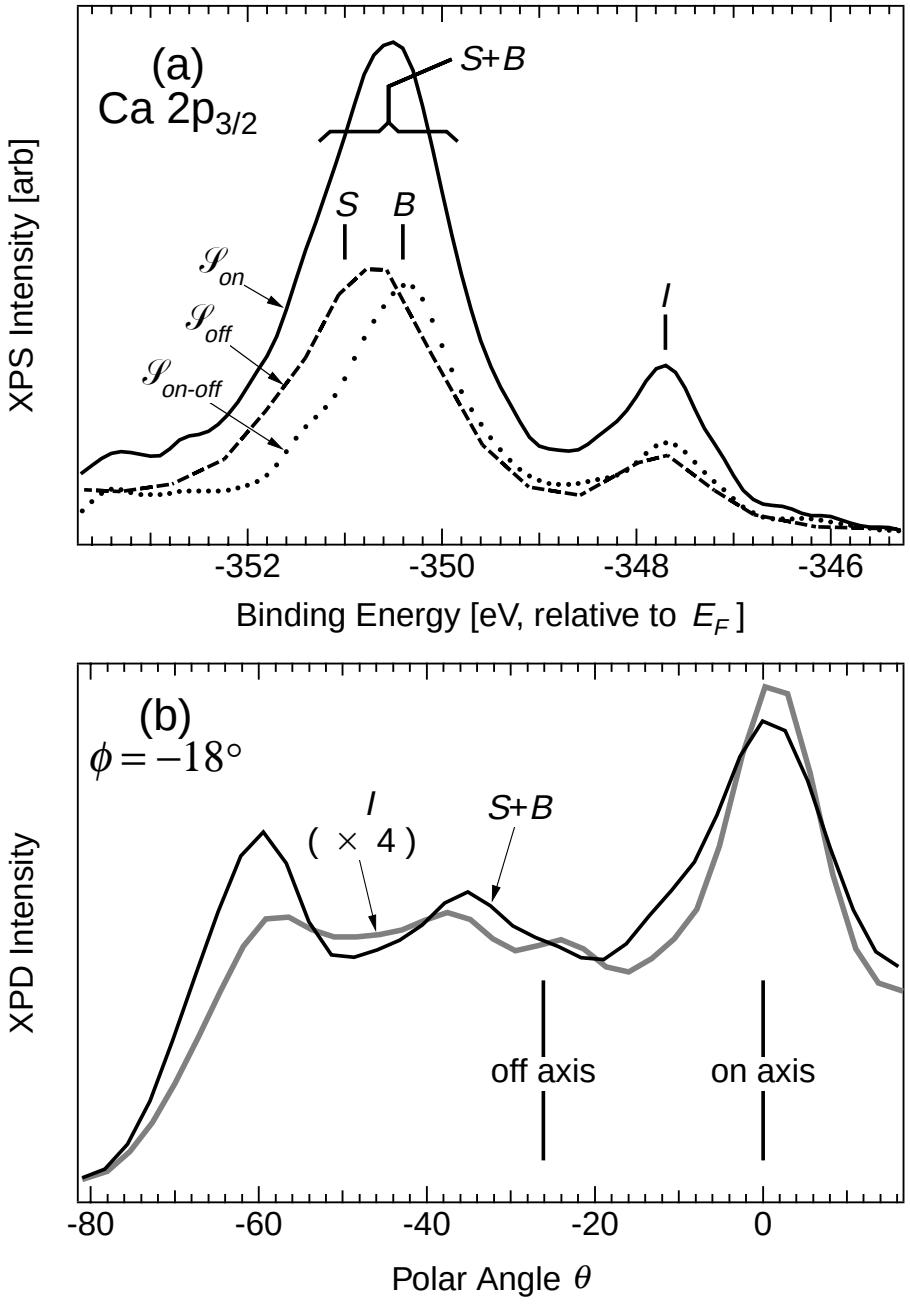

Figure 5.04. XPS and XPD results for a 4 TL CaF_2/Si(111) film (9/1/92). (a) Ca $2p_{3/2}$ core level spectra acquired at normal, on-axis emission ($\mathcal{S}_{on}$, θ=ϕ=0°, solid), at off-axis emission ($\mathcal{S}_{off}$, θ=-26°, ϕ=-18° dotted), and the difference spectrum ($\mathcal{S}_{on\text{-}off}$, dashed). The assignment of surface *S*, bulk *B* and interface *I* peaks is indicated by the vertical lines. (The atomic structure and location of the atoms is indicated in Figure C.02.) (b) XPD profiles taken in the ϕ=-18° plane, showing the interface and combined surface+bulk peak heights as a function of emission angle θ. The on- and off-axis angles are indicated by vertical lines.

Olm87]; all the assignments are verified in the XPD data discussed below, as well as in the comparison to theoretical binding energy in Chapter 6.

Figure 5.04(b) shows *component-resolved* XPD results for these peaks. These profiles were acquired by repeatedly taking data such as in Figure 5.04(a) at all polar angles θ along ϕ = -18°. These data were then fitted to two peaks; the resulting peak heights as a function of angle are reported in (b). The plot verifies that the XPD modulations are minimal in the vicinity of the off-axis direction for all atoms in the film. Also, the plot shows that the off-axis direction yields spectra which approximate completely isotropic emission, since there are no strong features at this angle.

Figure 5.05 shows the linear combinations $\mathscr{S}_{on}$ and $\mathscr{S}^*$, along with the optimal fits for *S*, *B*, and *I*. The fitting method was that described in §5.1; the lineshapes used were discussed in §4.1. Bulk lineshapes were used for both *S* and *B*, while the interface lineshape was used for *I*.

Figure 5.06 shows similar results for F KVV emission. Part (a) shows the $\mathscr{S}_{on}$, $\mathscr{S}_{off}$, $\mathscr{S}_{on\text{-}off}$, and $\mathscr{S}^*$ spectra, while (b) shows final fitting results. Comparison of $\mathscr{S}_{on}$, $\mathscr{S}_{off}$, $\mathscr{S}_{on\text{-}off}$ clearly indicates surface *S*, bulk-like *B* and interface I_1 fluorine atoms (see Figure C.02). The feature *S* comprises unresolved peaks S_1 and S_2 from the two surface F atoms. Further interpretation of F KVV data is complicated by the fact that, unlike Ca atoms, F atoms have two unique sites relative to the on-axis [111] direction. One site has a nearest-neighbor Ca atom along [111] and thus is strongly focussed in this direction. The other site has a fifth near neighbor fluorine atom in this direction and hence is expected to have negligible [111] forward focussing. The electrons emitted from interface atoms I_1 have a much stronger forward scattering amplitude than those emitted from bulk atoms *B*, which are an average of two strongly and one weakly scattered electron. This means that for fluorine atoms, $\beta << \iota$ (From Figure 5.06, we estimate $\beta \approx 1.1$ and $\iota \approx 2.5$). This affects the appearance of both the $\mathscr{S}_{on\text{-}off}$ and $\mathscr{S}^*$ spectra as follows: the $\mathscr{S}_{on\text{-}off}$ spectrum has a reduction in the amount of *B*

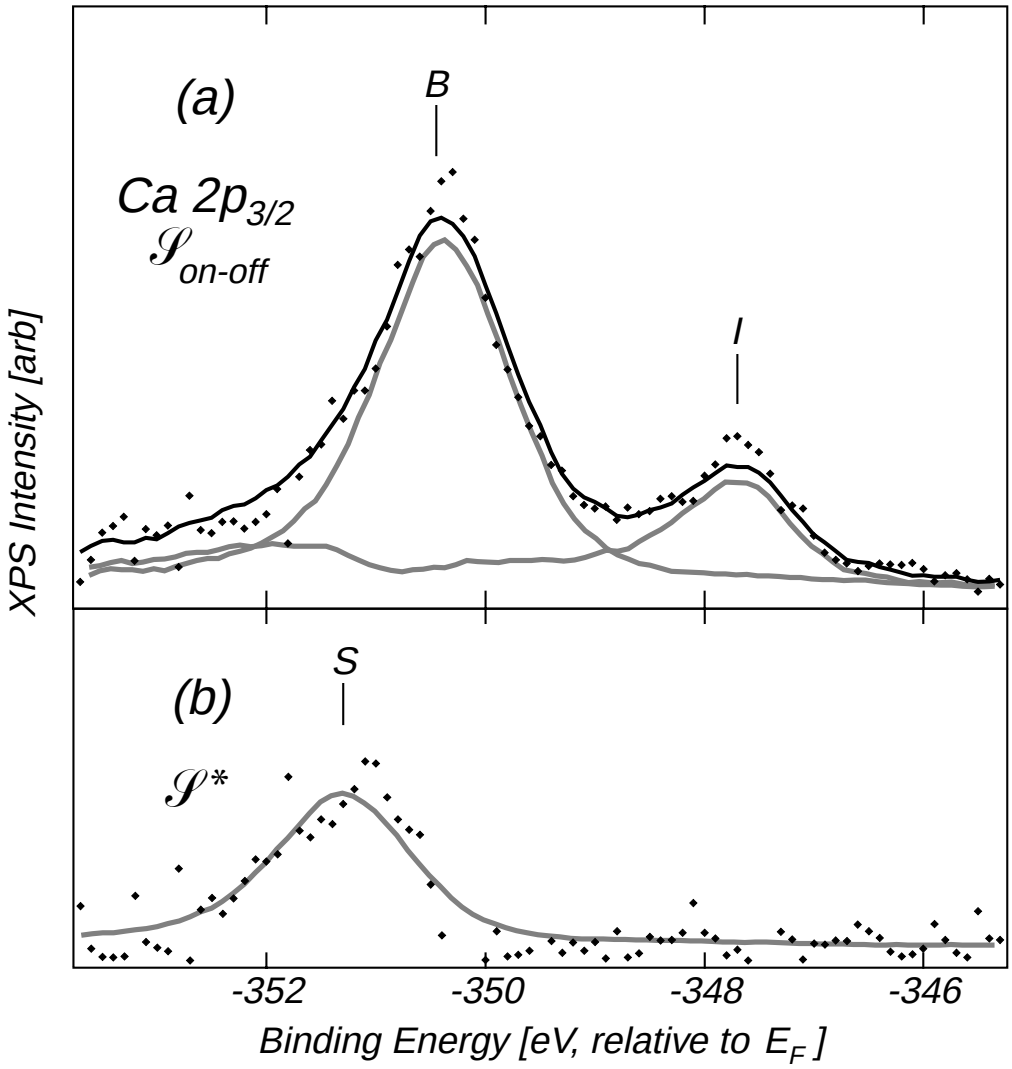

Figure 5.05. Curve fits for the 4 TL CaF_2 film (9/1/92) in Figure 5.04. (a) Difference spectrum $\mathcal{S}_{on\text{-}off}$, which is only sensitive to bulk and interface Ca atoms. (b) Linear combination $\mathcal{S}^* = 2.1\,\mathcal{S}_{off} - \mathcal{S}_{on}$, which is primarily sensitive to surface Ca atoms.

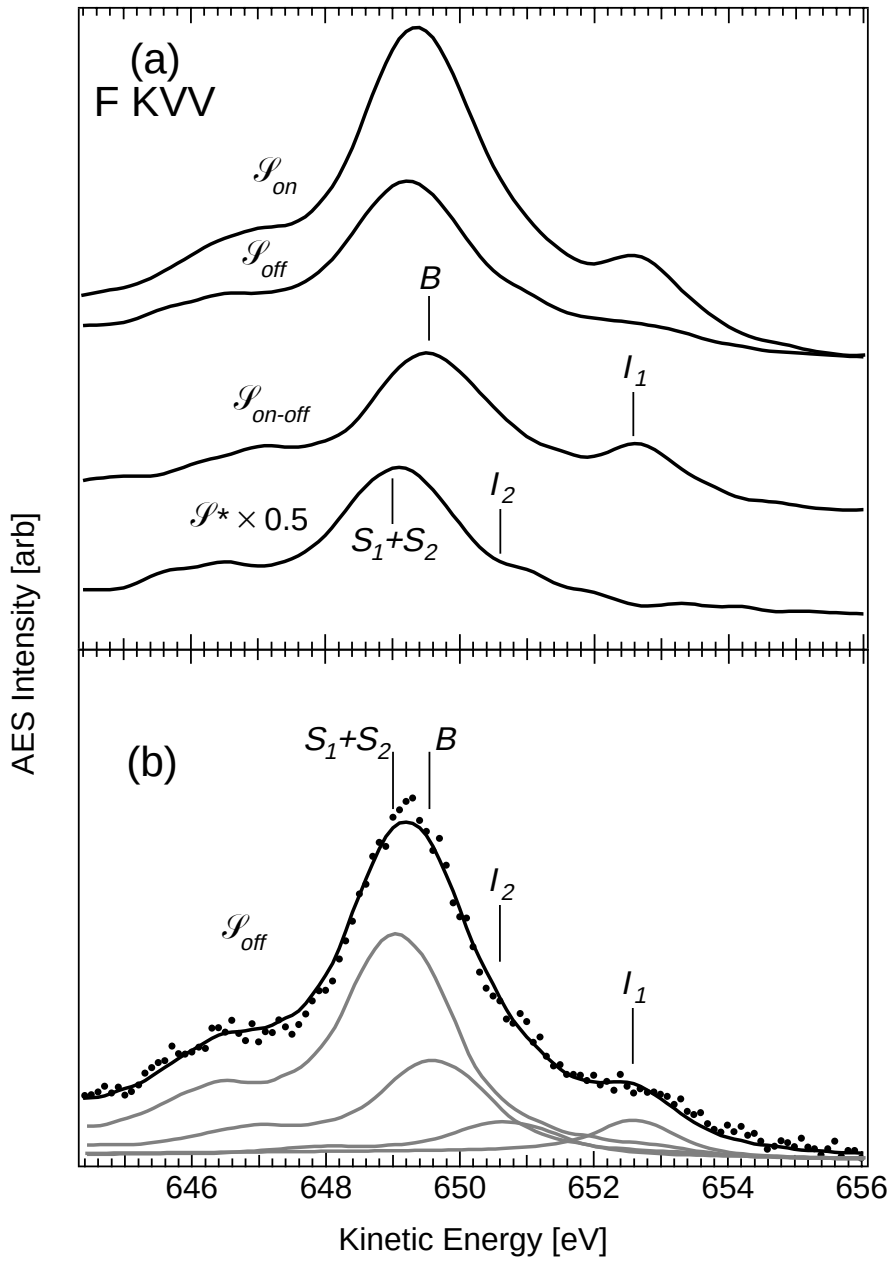

Figure 5.06. F KVV AES results for a 4 TL CaF_2/Si(111) film (9/1/92). F KVV Auger spectra for (a) on-axis emission $\mathscr{S}_{on}$ (θ=ϕ=0°) off-axis emission $\mathscr{S}_{off}$ (θ=-26°, ϕ=-18°), the difference spectrum $\mathscr{S}_{on-off}$, which is sensitive to bulk and surface F atoms, and the spectrum $\mathscr{S}^*$=3.5 $\mathscr{S}_{off}$- $\mathscr{S}_{on}$, which is sensitive to fluorine atoms without scattering centers in the on-axis direction. Figure C.02 indicates the position of F atoms in the film. (b) The final fit to the $\mathscr{S}_{off}$ spectrum, showing all four components (surface atoms S_1 + S_2, bulk B, interface I_1 and I_2).

component because one of the bulk atoms has no Ca atom directly above it. This unmodulated component instead appears in the $\mathscr{S}^*$ spectrum, distorting the S_1+S_2 peak slightly. Additionally, the $\mathscr{S}^*$ spectrum displays an additional peak between I_1 and B. We assign this intensity to a second interface atom I_2 (see Figure C.02), which, being of the second type of site, also has negligible forward scattering in the [111] direction. We have taken special care to verify the existence and nature of this peak, as will be discussed below.

The final off-axis F KVV fit, which used the buried interface lineshape (Figure 4.10(b)) only for the I_1 peak, is shown in Figure 5.06(b). The second interface fluorine atom I_2 appears to have a bulk-like lineshape, which is not surprising since this atom is fully coordinated. We observe this atom's signal to be somewhat weaker than expected. This may be an artifact of the fitting procedure, or due to uncertainty in the I_1 lineshape, although it cannot be ruled out that this I_2 site has a diminished occupation.

The identification of surface, bulk, and interface peak positions for Ca and F species enables full component-resolved XPD profiles to be measured. We acquired Ca 2*p* and F KVV spectra such as in Figures 5.04 and 5.06 repeatedly for all θ values for scattering along ϕ=0° and ϕ = -60°. We performed curve-fits on these spectra at each angle, using the known positions derived from the XPS fits. The fitted peak heights as a function of angle for a 3 TL thick CaF_2 on Si(111) film (11/3/92) are shown in Figure 5.07 for Ca 2*p* electrons, and in Figure 5.08 for F KVV Auger electrons. We immediately reach three qualitative conclusions: (i) The identification of surface, bulk, and interface signals is correct, since as we progress from the surface downwards each XPD profile acquires successively more modulations. Moreover, the theoretical Ca 2p modulations from Figure 4.16 (lines) have been superimposed on the data in Figure 5.06 and the agreement is excellent. (ii) The atomic structure is the simple one illustrated in the insets, in which the Ca-F bilayer is covered by bulk-like F-Ca-F TLs. (iii) We conclude that the film is everywhere 3 TLs thick, due to the presence or absence of the second-layer scattering features in the different profiles (e.g. the [112] peak in

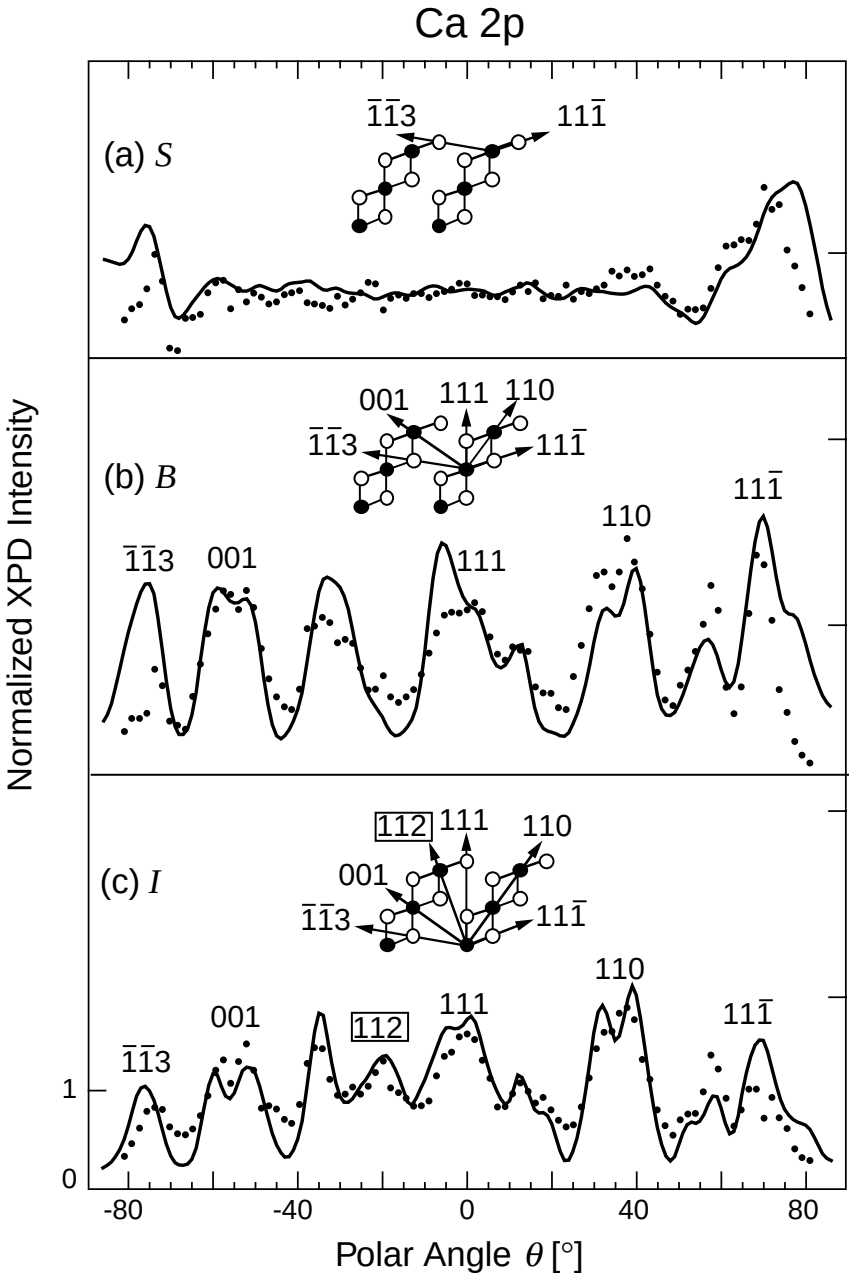

Figure 5.07. Component-resolved XPD profiles (solid lines, theoretical; dots, experimental) for Ca 2p electrons in a 3 TL CaF_2 on Si(111) film (11/3/92). (a) surface Ca atoms *S*. (b) bulk-like Ca atoms *B*. (c) interface Ca atoms *I*. The insets show the corresponding in-plane scattering angles responsible for the forward-scattering peaks in the XPD profiles.

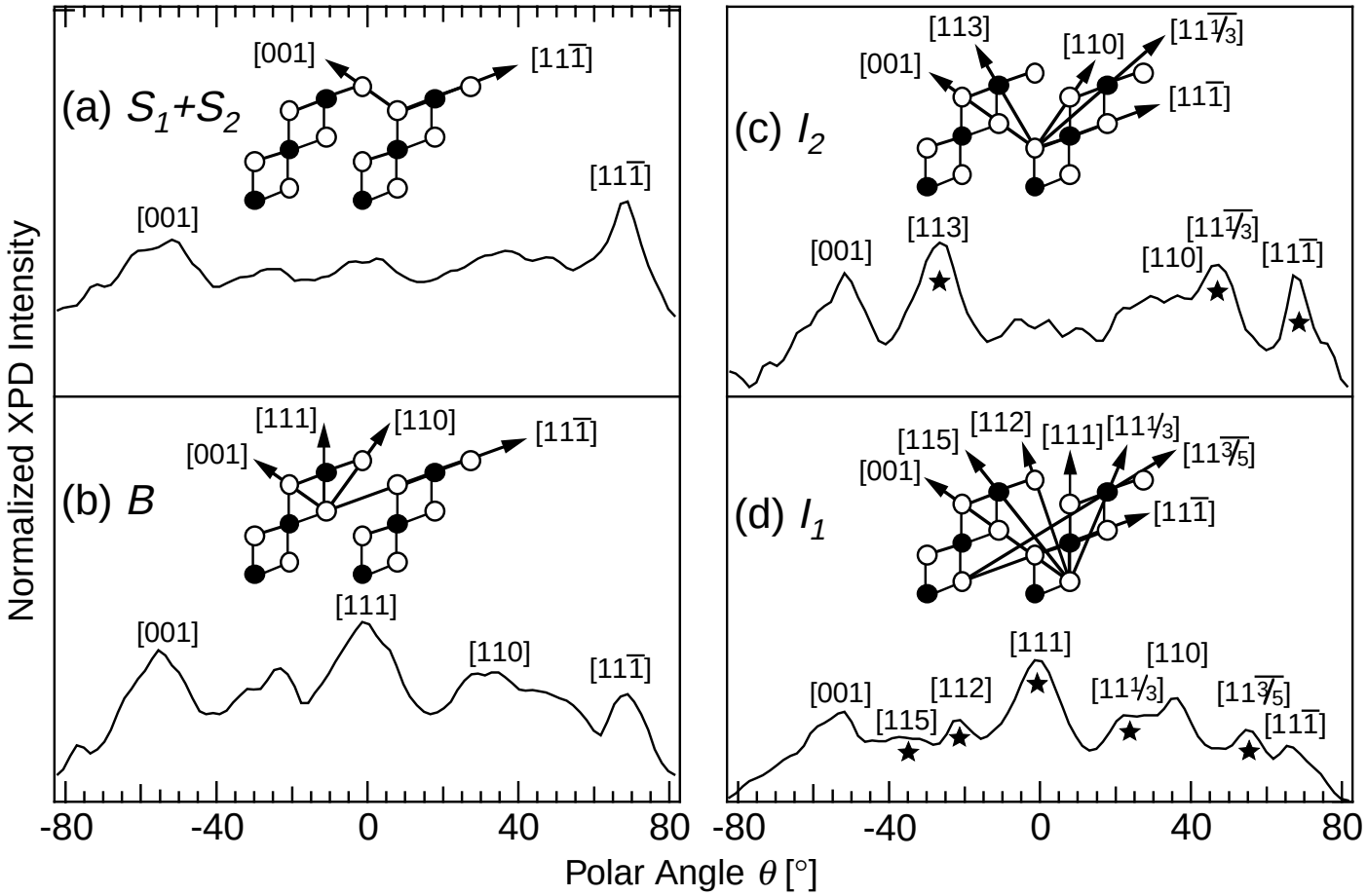

Figure 5.08. Experimental component-resolved XPD profiles for F KVV Auger electrons in a 3 TL CaF_2 on Si(111) film(11/3/92). (a) surface F atoms S_1+S_2, (b) bulk-like F atoms B, (c) interface F atoms I_2, and (d) interface F atoms I_1. The insets show the corresponding in-plane scattering angles responsible for the forward-scattering peaks in the XPD profiles. Scattering directions which uniquely distinguish I_1 from I_2 atoms are shown starred.

the interface Ca XPD signal). Further indication that the films are flat comes from analyzing the XPS spectra (not shown), in which we see an absence of additional core-level shifted species associated with an exposed Si-Ca-F layer in islanded films, as well as from the quantitative analysis described next.

We paid special attention to fitting the F KVV spectra in order to confirm the identities of the I_1 and I_2 sites since these XPS peaks were difficult to resolve. As indicated in Figure 5.08, only the I_2 atomic site should display forward scattering along [113]. We anticipated this before XPD data were taken and acquired a high-resolution XPS spectrum along this [113] direction. This is plotted along with the off-axis spectrum and their difference in Figure 5.09. The difference clearly shows the I_2 peak located between I_1 and B in energy; we fitted this spectrum to a single peak. The energy of the I_2 peak in the component-resolved XPD (Figure 5.08) was fixed to this energy. The final results in Figure 5.08 quite dramatically show the different character of the I_1 and I_2 sites in accord with the atomic structures in the insets.

We now consider why the I_2 atom is not located between the Si and Ca atoms at the interface. Such might be the case if the interface reaction is not complete, thus leaving some unreacted F-Ca-F triple layers at the interface. This site is also compatible with the XPD modulations observed. There are several observations that rule out this site assignment: (i) the ML samples have no F in a coherent site between Si and Ca. It is not likely that F would insert itself there after covering the first layer, since there is no source of extra F. Furthermore, x-ray scattering studies [Luc93b] and x-ray standing wave studies [Zeg90] which measure the Ca-Si bond length for multiple-TL films are not consistent with F in such a site. (ii) High-resolution measurements of Si 2*p* spectra we acquired at SSRL (similar to Figure 4.03) show no characteristic core-level shifted Si species which is known to occur for Si interacting with F [Rie86, Olm87]. (iii) According to the relaxation calculation (Chapters 2 and 6), F located close to the Si would have a very large (4-5 eV) CLS in the F KVV spectrum relative to bulk,

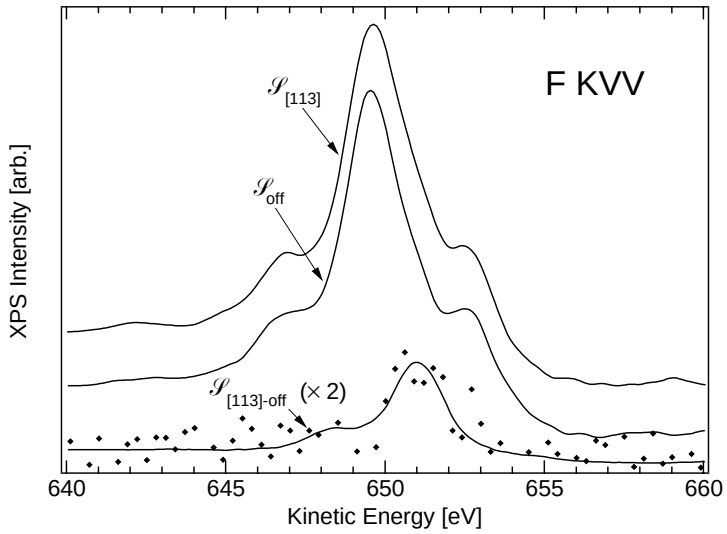

Figure 5.09. Determination of I_2 energy from selective XPS spectra (11/3/92). Shown are F KVV spectra acquired for emission along [113] ($\mathscr{S}_{[113]}$), off-axis emission $\mathscr{S}_{off}$, and the difference spectrum $\mathscr{S}_{on-off}$. The difference spectrum is curvefitted to a single component representing the I_2 atoms' signal.

which we do not observe.

5.2.4 Temperature and Flux studies: Crystalline Films

Crystal growth by molecular beam epitaxy is inherently a non-equilibrium process. For example, there is a flux of incident particles onto the surface which is much greater than the (insignificant) reevaporation rate. Similarly, a "sea" of mobile molecules diffuses along the sample surface causing the growth of islands with little "reevaporation" back into the diffusing state. The microscopic processes underlying nucleation and diffusion govern the final film's growth morphology; the development of the morphology with time is called the *growth kinetics*. The experimental *kinetic parameters* on which nucleation and diffusion depend are incident flux and substrate temperature. An additional kinetic parameter is the substrate misorientation, which we have already seen can lead to islanded films, all other things being equal (§4.1.2, Figure 4.04(c)). Variation of all of these parameters can lead to different observed growth modes.

In this and the next section, we explore the dependence of film morphology on the

kinetic parameters of CaF_2 flux and Si substrate temperature. All the data here were acquired on highly oriented Si(111) wafers; future studies [Les94, Hes94] will explore the dependence on wafer misorientation further. In particular, we will find a range of behaviours from completely flat to highly islanded, and we quantitatively characterize these using a combination of the XPS and XPD techniques to estimate island coverage and heights. In particular, these two measurements can be used together with the known CaF_2 electron escape depths to solve for the two quantities of average island height n and island coverage f within a simple Stranski-Krastanov-like morphology, in which a reacted Si-Ca-F layer is covered by bulk-like islands.

Using XPS, we measure the ratio of the (bulk + surface) to (interface) Ca $2p$ emission. Equation (4.6) relates this measured quantity to the islanding parameters n and f:

$$\left(\frac{B+S}{I}\right)_{XPS} = \frac{f(1-e^{-n/\lambda\cos\theta})\big/(1-e^{-1/\lambda\cos\theta})}{f\,e^{-n/\lambda\cos\theta}+(1-f)}, \tag{5.2a}$$

where θ is the angle of emission relative to the surface and $\lambda \approx 12$ TL is the escape depth for Ca $2p$ electrons in CaF_2. Similarly, we can derive an expression for the relative XPD oscillation strength for bulk and interface signals [Den93]:

$$\left(\frac{B+S}{I}\right)_{XPD} = \left(\frac{e^{-1/\lambda\cos\theta}-e^{-n/\lambda\cos\theta}}{1-e^{-n/\lambda\cos\theta}}\right)\Bigg/\left(\frac{fe^{-n/\lambda\cos\theta}}{1-f+fe^{-n/\lambda\cos\theta}}\right). \tag{5.2b}$$

After measuring the two ratios in (5.2a, b), we can solve for the two parameters (n, f) on the right hand sides. The results of this procedure are used below.

XPS/XPD Results. Figure 5.10 shows Ca $2p$ XPD results for a sequence of growths for (a) high temperature, low flux (HT/LF), (b) high temperature, high flux (HT/HF), and (c) low temperature (LT) growth conditions. The side panels illustrate the average island heights and coverages as obtained from our quantitative analysis using the XPS peak heights. For simplicity, we show only Ca $2p$ interface (I) and surface+bulk (S+B) XPD profiles. In our notation, HT means $T \geq 600$°C, LT means $T \leq 600$°C, HF means flux ≈ 50Å/min, and LF

means flux ≈ 5Å/min.

The HT/LF films (Figure 5.10(a)) displayed island formation after the interface was formed; with greater deposition, the island thickness increased faster than the island coverage, leading ultimately to severely islanded films. The islanding may be determined not only from the quantitative analysis outlined above but also from the presence of the bulk atoms' [112] forward scattering peaks in the 3 TL sample.

The HT/HF films (Figure 5.10(b)) start out islanded but become uniform by the completion of the second bulk TL (the middle scan is for the same film as in Figure 5.07), and the XPD results for thicker films are consistent with subsequent layer-by-layer growth. Examination of the [112] peaks in the sequence shows that the development of flat films proceeds through the formation of 2 TL thick islands, which coalesce before true layer-by-layer growth can begin. The [112] forward-scattering peak is present only for the interface Ca atoms until after the 2 TL high bulk islands have coalesced. Recently, the observation of the 2 TL islands has been indicated by low energy electron microscopy [Tro93], although the development of these islands for thinner coverages than we studied may be more complicated than the simple picture shown here.

The LT films (Fig. 5.10(c)) show a different behavior. For submonolayer films (0.5 to 0.8 ML) we can identify disorder in the interface layer, and nucleation of bulk TLs before the reacted Si-Ca-F layer is complete, as further evidenced by weak 7x7 LEED spots. For thicker films, the interface becomes ordered, and analysis of XPS intensities (acquired before LEED) shows that the F:Ca stoichiometry of the interface layer is 2:1 rather than 1:1 as for HT films. This difference is due to both an enhanced presence of F atoms as well as an absence of ~1/3 of the interface Ca atoms. The relatively weak XPD modulations of the bulk Ca signal at 2-3 TL suggests the growth to be essentially layer-by-layer immediately.

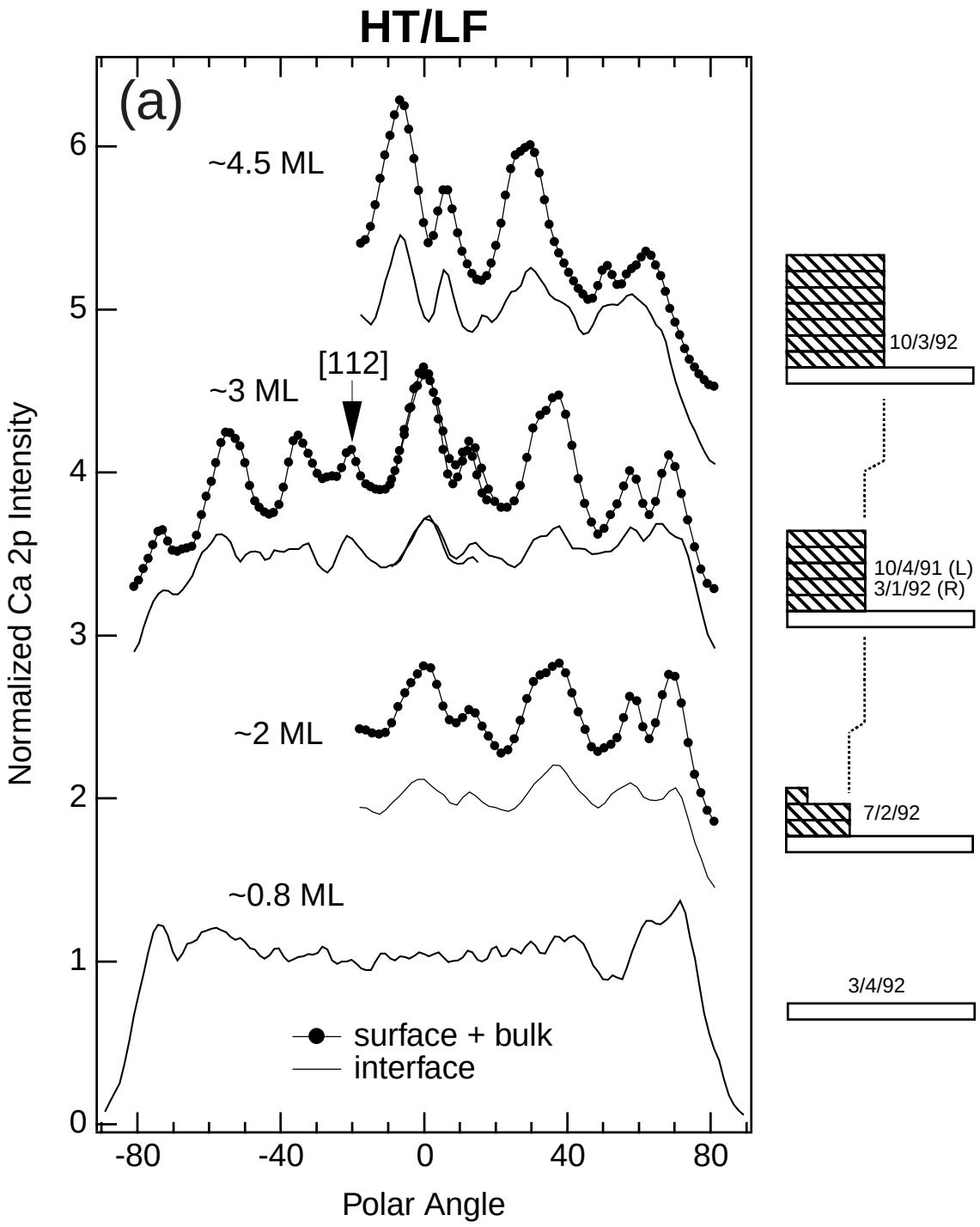

Figure 5.10. Component-resolved XPD for various depositions (indicated) for (a) high temperature/low flux (HT/LF), (b) high temperature/high flux (HT/HF), and (c) low temperature (LT). The temperature and flux regimes are defined in the text and in Figure 5.13. The side panels indicate the morphology determined for each film, where ▭ = a reacted F-Ca-Si interface layer, and ▬ = bulk-like F-Ca-F triple layers.

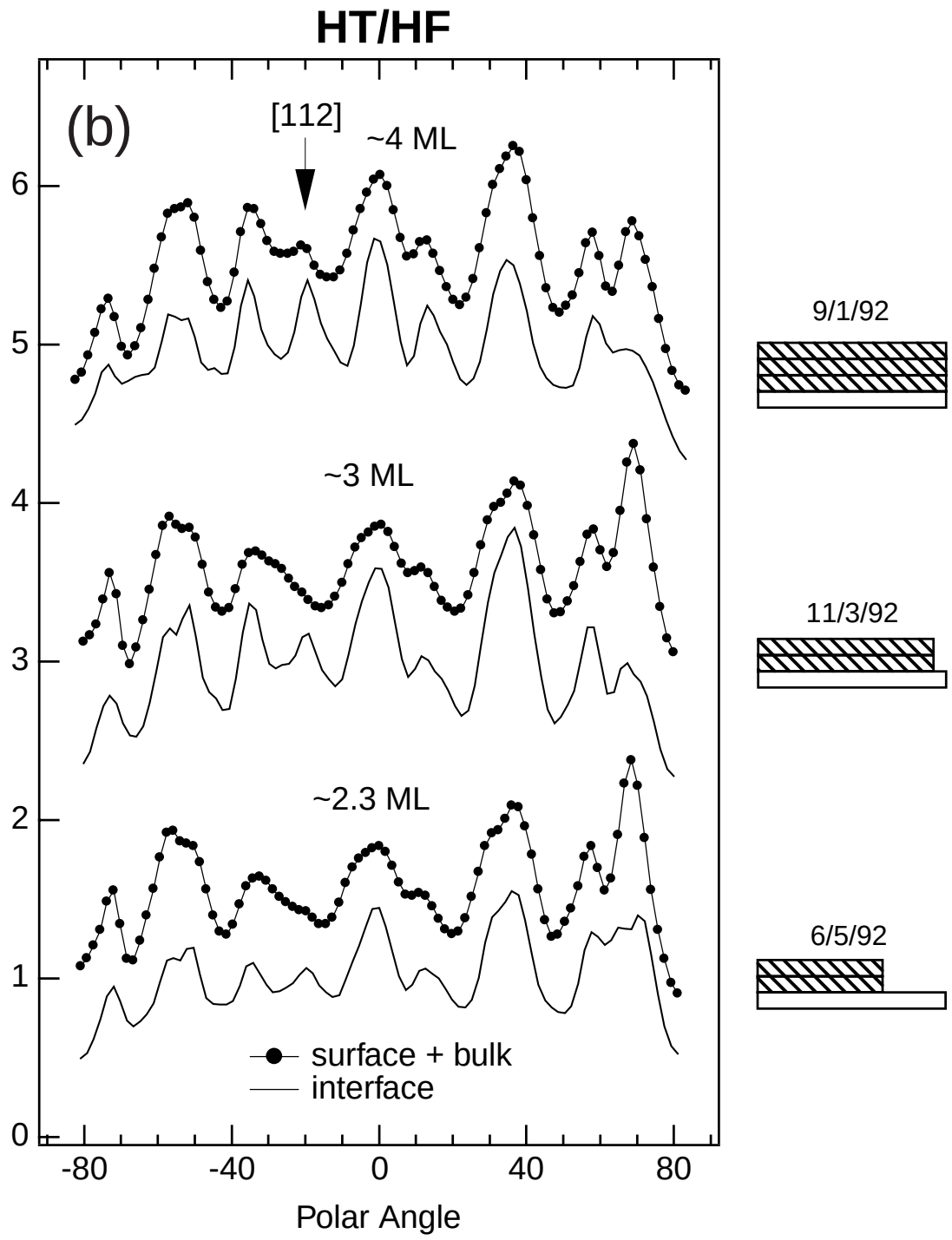

Figure 5.10(b). HT/HF results. The absence of [112] scattering peaks (arrow indicates the angle) in the bulk XPD profiles indicates 2 TL thick islands (lower films), which coalesce before a third TL forms (upper film).

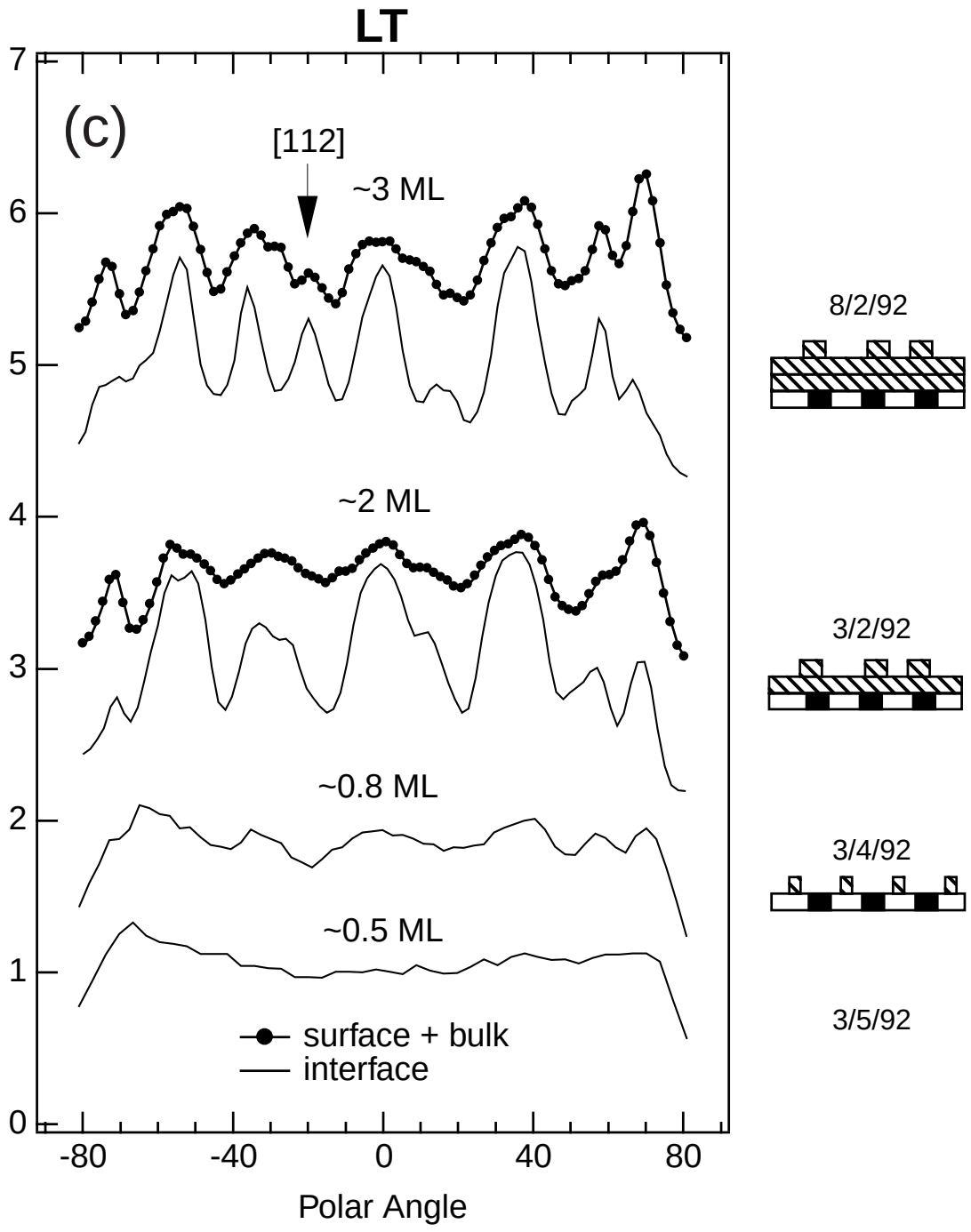

Figure 5.10(c). LT results. The thinnest films show early nucleation of bulk layers before the interface layer is complete. The weak modulation in the bulk profile (middle film) confirms ~layer-by-layer growth.

5.2.5 Lawrence Berkeley Laboratory Results

We also studied the HT regime using samples grown by G. C. L. Wong at the Lawrence Berkeley Laboratory (LBL) [Won93]. In the previous section, we used two measured quantities (Ca 2*p* (*B*+*S*)/*I* XPS and XPD ratios) to determine the two quantities *n*=island height and *f*=island coverage. At LBL only the Ca 2*p* XPS ratio was measured; we did not have the apparatus available for the XPD measurement. However, samples were also characterized *ex situ* by transmission electron microscopy (TEM) by D. Loretto to directly determine island coverage *f*. The two measured quantities are directly related through Equation (5.2a). Inverting this equation numerically determined *n*=island thickness.

Figure 5.11 shows LBL XPS results acquired for three progressively thicker depositions. The samples were grown in a similar fashion to those throughout the rest of the thesis. The growth temperature was 720°C and the flux rate was ~30Å/m, which was calibrated against x-ray scattering measurements by G. C. L. Wong and C. A. Lucas at LBL. The temperature calibration is somewhat uncertain relative to the other measurements in the thesis, since absolute temperature measurements are certain only within ± 20°. XPS spectra were acquired with Al K_α radiation; following XPS measurements the samples were capped with ~100 Å of amorphous Si (deposited at room temperature) to protect the films for *ex situ* TEM measurements. TEM micrographs were then imaged and analyzed in order to determine island coverages *f* [Won93].

There are several uncertainties in this procedure: (i) the value of theta used in (5.2) is only an effective value since the electron analyzer used at LBL detected a wide range of angles, (ii) it was assumed that a large enough solid angle of electrons were detected such that the XPD peaks were averaged out, (iii) the capping procedure may disrupt the film structure, thus giving unreliable values of *f*, (iv) the spectrometer response distorted the peak shapes to the point where the curvefits became ambiguous. The spectra in Figure 5.11 have had the response function deconvolved using a Fourier transform approach (§4.1.7) before curve-

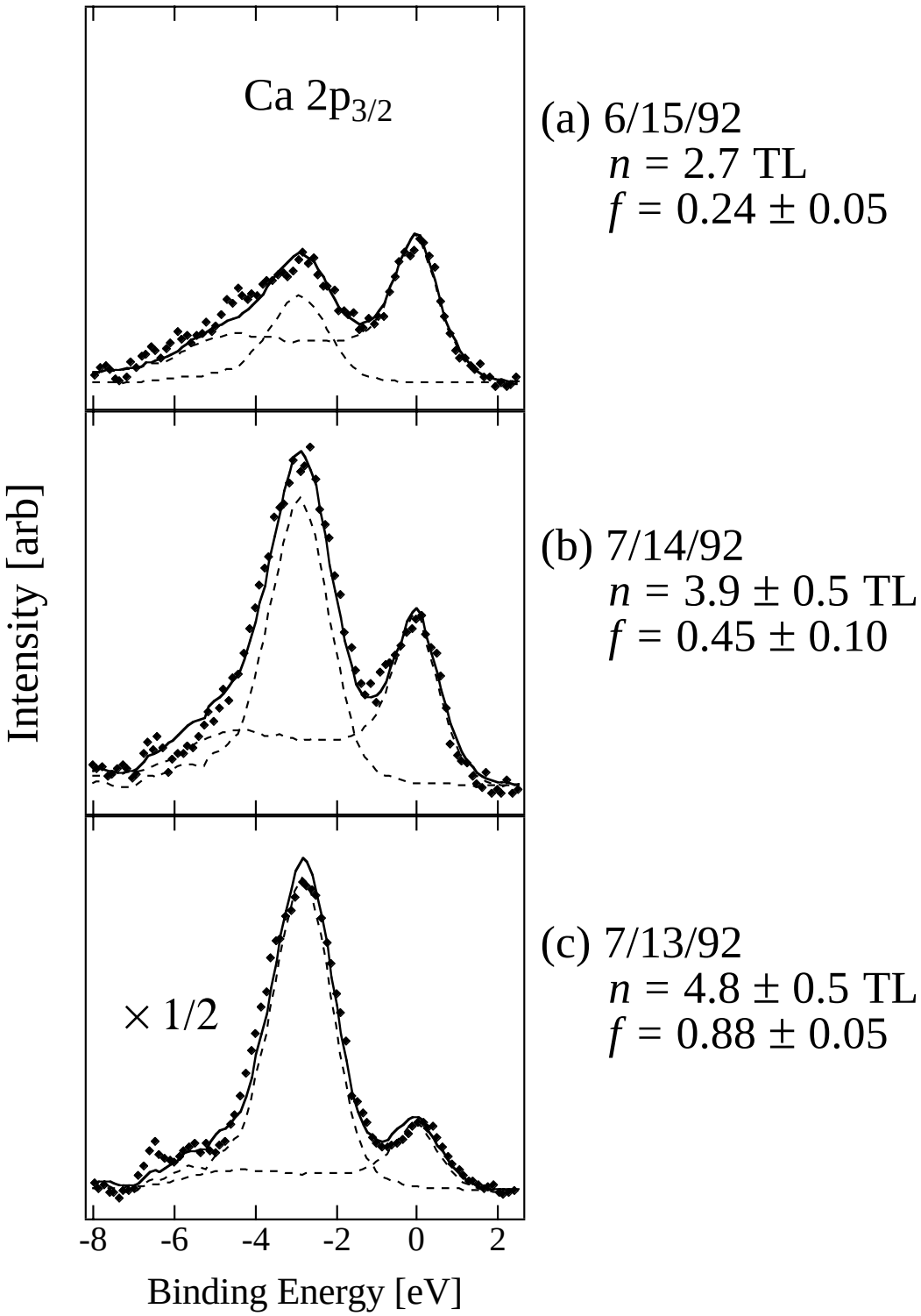

Figure 5.11. XPS fits for samples grown at Lawrence Berkeley Laboratory. Spin-orbit deconvolved Ca 2p for films grown at 720°C on Si(111): (a) 12 s, (b) 16 s, and (c) 32 s depositions. Also indicated are island thickness *n* and coverage *f*.

fitting took place.

The curvefits in Figure 5.11 are very similar to those in the rest of the thesis. It is evident that the films have exposed Si-Ca-F layers since the interface signal does not diminish upon going from (a) ~ 1 ML to (b) ~ 2 TL deposition, as would occur if the interface were being uniformly buried. Only when ~4 TLs have been deposited (c) does the interface amplitude significantly drop. The TEM values of *f* and the derived values of *n* for these films are included alongside the XPS data.

Figure 5.12 summarizes the HT morphology. Plotted are experimental contours of *n vs. f* for constant flux rate at high temperature. In this plot, curves with large slope are very rough, while curves with low slope are flatter. The 5 Å/min contour represents the roughest films, while the 50Å/min contour represents the flattest. The LBL data (30Å/m), determined with XPS/TEM, is completely consistent with the other data, which was determined using XPS/XPD.

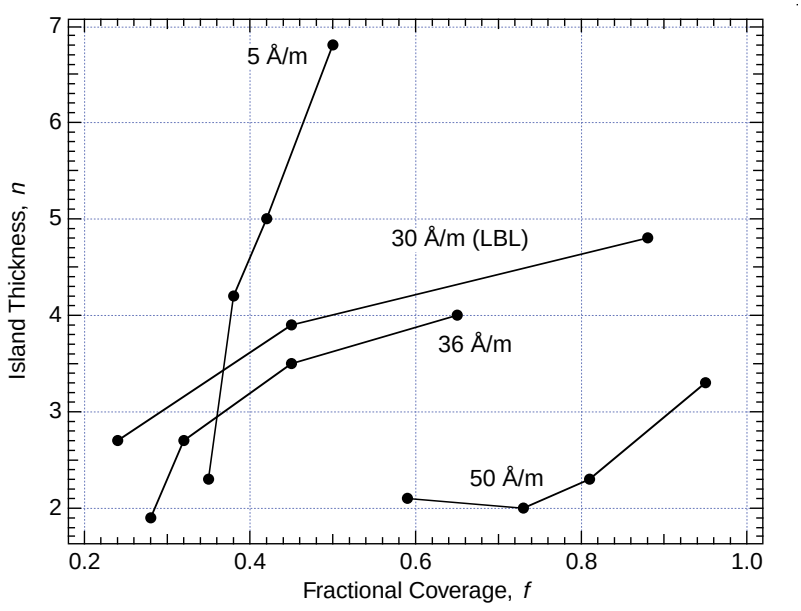

Figure 5.12. High Temperature growth kinetics. Island thickness *n* vs fractional coverage *f* for fluxes of 5, 30, 36, and 50 Å/min at temperatures 750, 720, 750, 700°C, resp.

5.3 Discussion: Growth Kinetics

5.3.1. Structure.

Having classified the growth morphologies for different regimes, we are now in a position to discuss the possible origins. First, we discuss the atomic structure of the films. We have shown that the atomic structure of the buried interface is identical to the unburied interface, namely that there exists a Ca-F bilayer upon which F-Ca-F triple layers are stacked with bulk spacings and angles. This is seen both for flat films and for the buried regions in Stranski-Krastanov-like films. This is contrary to the recent publication by Lucas *et al.* [Luc93], who proposed (using transmission electron microscopy and x-ray scattering) that the buried interface has a more complicated, less dense structure with a two-layer thick $\sqrt{3}\times\sqrt{3}$ buried reconstruction. We suggest the different structure they observed originates from the *ex situ* (in air) study of Si-capped samples. Either contamination or some other effect associated with capping the films might explain their results, although similarly capped films studied by Alvarez *et al.* failed to show this reconstruction [Alv93]. We have observed a $\sqrt{3}\times\sqrt{3}$ reconstruction, but only upon annealling ~ML CaF_2 films in the presence of adsorbed oxygen. Furthermore, the interface model of Lucas *et al.* is inconsistent with the XPS shifts we have observed, which we have been able to model successfully in this thesis by taking into account initial and final state effects for the geometry shown (Chapters 2, 6).

5.3.2. Growth Kinetics

In this section, we qualitatively discuss the observed dependence of growth mode on the kinetic parameters we varied. In the next section, we apply the model of Myers-Beaghton and Vvedensky [Mye90] to our system in order to understand the division between HT/LF and HT/HF modes and derive quantitative parameters.

Figure 5.13 summarizes the dependence of the growth modes on the kinetic parameters of flux and temperature. The upper left portion of the diagram represents the approach to thermodynamic equilibrium, in which the incident species have sufficient energy to

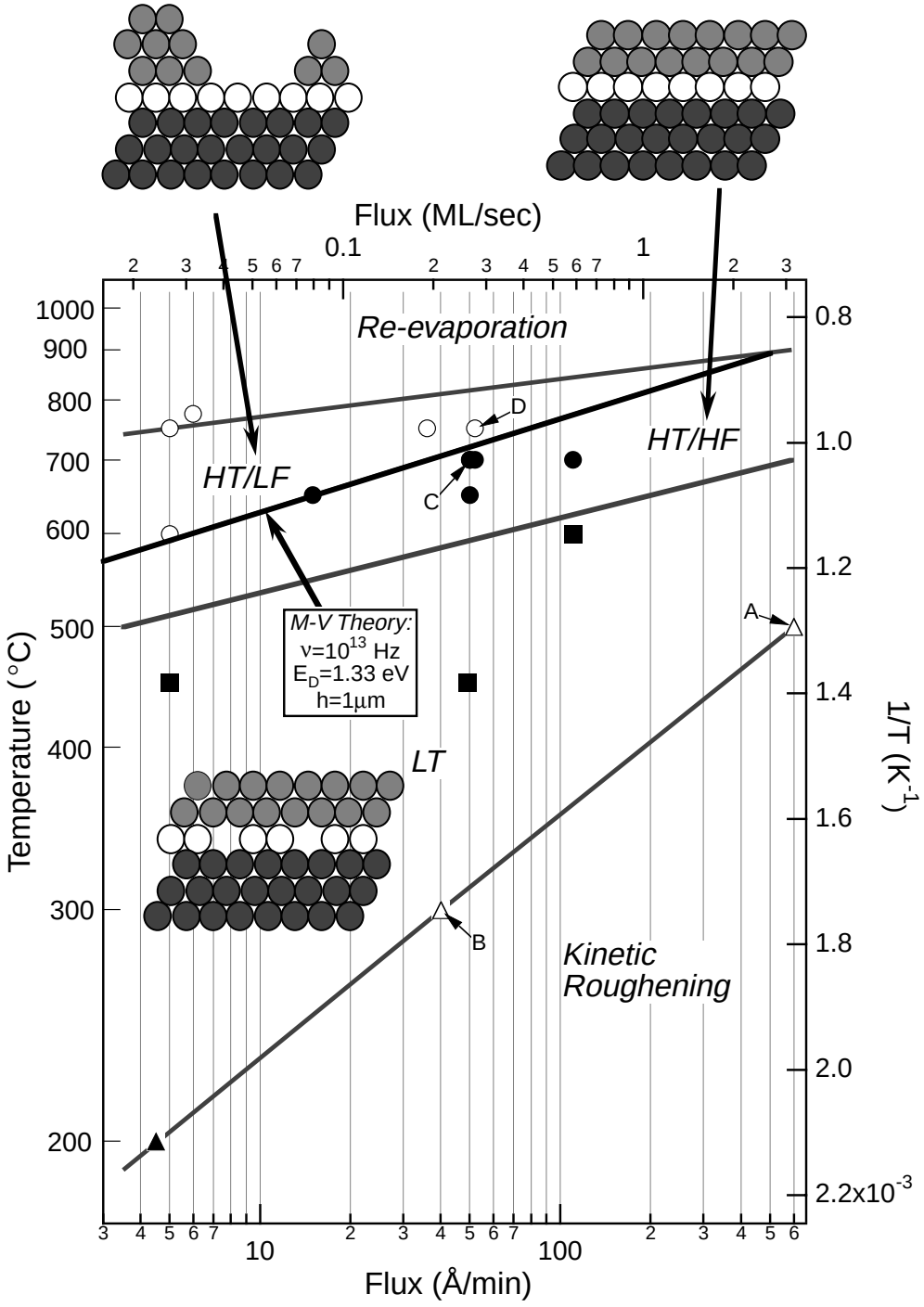

Figure 5.13. Kinetics phase diagram for growth of CaF_2 on Si(111), where H=high, L=low, T=temperature, and F=flux. The symbols (●, ○ , ▲, ■) indicate different morphologies (see side illustrations) observed in this study. The symbols △, labelled A and B, were taken from the literature ([Cho92] and [Asa93], resp.). See text for a description of the lines separating the different regions.

overcome barriers and sufficient time to diffuse to their low-energy sites. Islanding in the HT/LF films shows that the usual thermodynamic surface energy argument (which predicts laminar growth) is incomplete. The early formation of the reacted Si-Ca-F layer creates a new surface for subsequent growth whose surface energy must also be taken into account; the reduced Ca charge state (1+ *vs.* 2+) [Him86] in the interface layer can lead to a moderate (~20%) reduction in electrostatic binding energy between CaF_2 on Si-Ca-F relative to CaF_2 on CaF_2. This was calculated via the Madelung potential discussed in Chapter 2 (see §5.3.3 below). An alternative contribution may come from the favorable energy gain from forming islands [Rat93]; this may be driven by the lattice mismatch present at HT (2.5% at 700°C; see appendix A).

The HT/HF films are much flatter than the HT/LF films, and illustrate how kinetics can influence growth. In these films, increased flux leads to an altered growth mode, perhaps by altering the surface diffusion length as follows: at lower flux, samples exhibit step nucleation, while at higher flux, the probability of terrace nucleation increases, leading to more uniform coverage (this will be expanded upon in the next section). The observed minimum film thickness of interface + 2 bulk TLs may be accounted for by the lowered binding energy of CaF_2 to the interface layer as compared to the bulk. This would lead to a net flux of CaF_2 molecules jumping up from the interface layer to form a second bulk layer.

Plan-view TEM images of thick films (~15 TL nominally deposited) support this picture of terrace nucleation competing against step-edge nucleation. Figure 5.14 shows bright-field TEM images acquired by U. Hessinger [Hes94] for two CaF_2 films: (a) HT/LF and (b) HT/HF. In these images, CaF_2 regions which are beyond their critical thickness (*i.e.*, regions which have been driven by lattice-mismatch to their own lattice constant) appear as areas containing Moiré fringes, which result from the interference between the CaF_2 and underlying Si lattice constants. For our growth temperatures, the critical thickness is t_c~12 TL [Luc92].

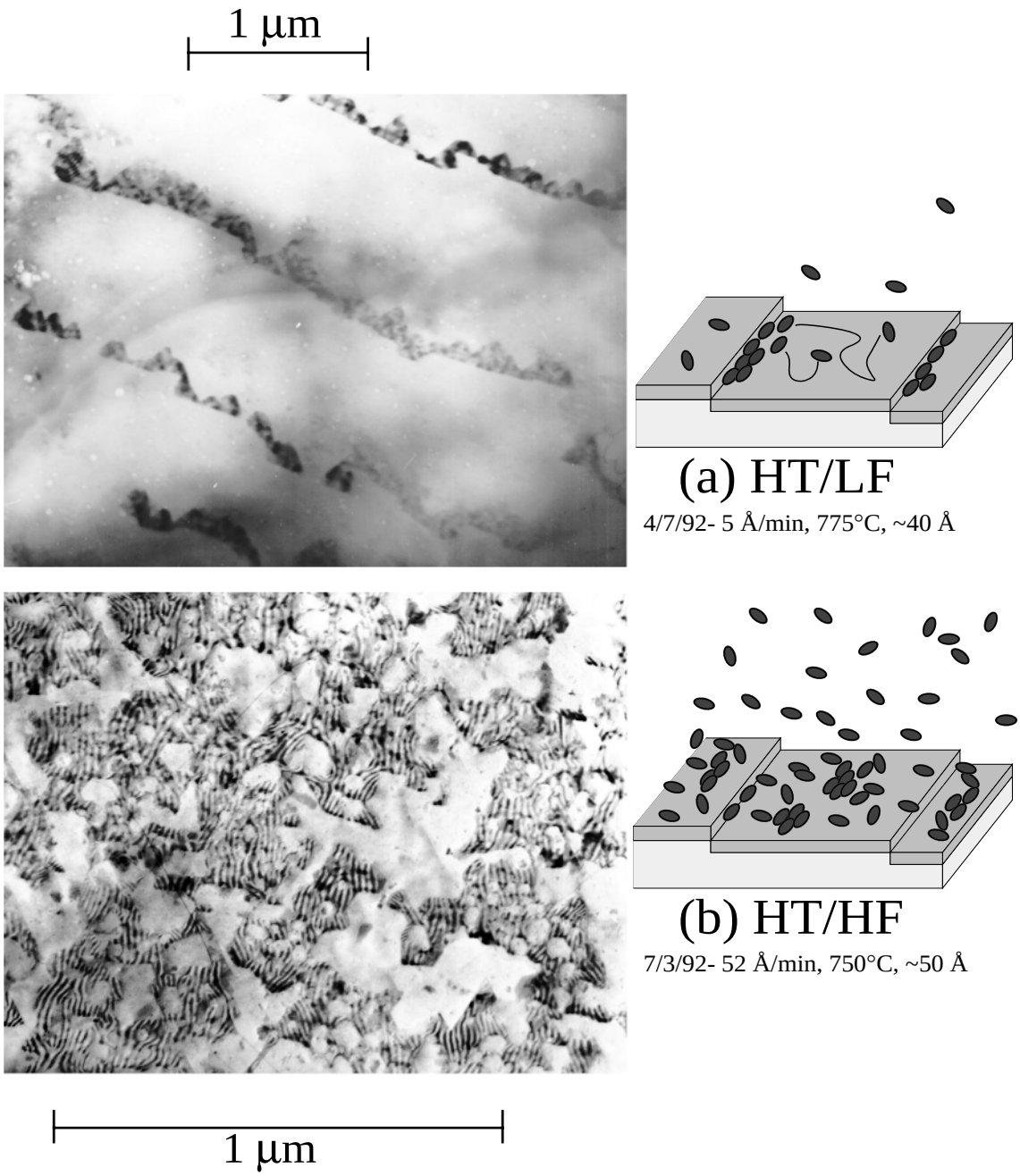

Figure 5.14. TEM images for HT films (a) 5 Å/min and (b) 52 Å/min. The right panels indicate models for diffusion/nucleation kinetics in the early stages of film growth.

For HT/LF (Figure 5.14(a)), triangular relaxed regions $\geq t_c$ TL thick are arranged along narrow lines spaced ~1 μm apart. The remaining featureless regions are composed of CaF_2 with thickness $\leq t_c$ TL thick. This distance between thick regions is comparable to the expected terrace width (≥ 0.8 μm) between steps in the Si substrate, which we expect from the known miscut of the wafers ($\leq 0.25°$). From this thick film, we infer the picture of early deposition illustrated in the side panel: uninhibited diffusion of molecules until adsorption at the step edge.

For HT/HF (Figure 5.14(b)), the relaxed regions are uniformly distributed along the sample surface. We are unable to detect any relationship between the relaxed regions and the underlying step structure (on this or larger length scales). This suggests the early stages of deposition illustrated at the right hand panel: diffusion towards step edges is limited by nucleation of islands upon terraces.

The LT films displayed an altogether different behavior. We found increased F and reduced Ca concentrations in the first layer of the film, accompanied by early nucleation of bulk layers. We propose this is due to an incomplete dissociation of the first incident CaF_2 molecules, leading to the excess F seen. This excess F blocks some of the CaF_2 molecules from chemisorbing, leading to the disorder and reduced Ca occupation seen at the interface. Furthermore, if the defects associated with excess F increase the sticking coefficient or reduce the diffusion coefficient of CaF_2 to the interface layer, it would explain both the observed early nucleation of bulk-like layers on the incomplete interface layer, as well as the ability to form a single complete bulk layer at LT (in contrast to the 2 TL minimum bulk thickness seen at HT/HF).

5.3.3 Myers-Beaghton/Vvedensky quantitative model of diffusion and nucleation

Myers-Beaghton and Vvedensky (MV) [Mye90] modelled how terrace nucleation impedes diffusion of molecules on terraces in MBE growth. They derived a one-dimensional effective-diffusion equation:

$$\frac{\partial n(x,t)}{\partial t} = D\frac{\partial^2 n(x,t)}{\partial x^2} + J - R(n), \tag{5.3}$$

which relates the density n of moving molecules to the incident flux rate J and the diffusion coefficient (in the absence of collisions) D. The coordinate x ranges from one step edge, across a terrace, to the next step edge. The term $R(n)$ represents the island creation rate on the terraces:

$$R(n) = \frac{2m}{n_0} Jn(x,t) + 2Dn^2(x,t), \tag{5.4}$$

where the first term describes incident molecules landing directly alongside mobile molecules to form islands, and the second term describes the collision of mobile molecules and subsequent nucleation of islands. The parameters in (5.4) are n_0=density of adsorption sites and m=number of ways one adatom can combine with another to nucleate an island.

The dimensionless parameter α is defined as

$$\alpha = \frac{\textit{diffusion time for an adatom to reach a step}}{\textit{inter - arrival time for incident atoms to land on a site}} = \frac{h^2 / D}{n_0 / J}, \tag{5.5}$$

where h is the width of a terrace. By numerically integrating (5.3), MV found a simple criterion for the crossover between terrace nucleation and step-edge nucleation. They found that for $\alpha > 1$, terrace nucleation reduces the effective diffusion of particles to step edges, while for $\alpha < 1$, step-edge nucleation becomes competitive with terrace nucleation. This simple model, then, gives a criterion for the boundary between the HT/HF and HT/LF regimes in Figure 5.13. The diffusion coefficient D in a simple hopping model is given by:

$$D = \frac{\nu}{n_0} \exp(-E_D / k_B T), \tag{5.6}$$

where ν is the "attempt" frequency for hopping, and E_D is the energy barrier for site-site hopping. Typically, ν is given by the optical phonon frequency ~10^{13} Hz. Combining (5.5) and (5.6) for $\alpha = 1$ and inserting geometrical parameters for CaF_2 on Si, we arrive at the

condition

$$T_c^{-1} = \frac{8.62 \times 10^{-5}}{E_D} \ln\left(\frac{\nu / Jh^2}{3.59 \times 10^{12}} \right), \tag{5.7}$$

where T_c [°K] is the critical transition temperature, E_D is measured in eV, ν is measured in s^{-1}, J is measured in Å/min, and h is measured in cm. Equation (5.7) was plotted in Figure 5.13 as the line separating the HT/HF and HT/LF regions for the parameters indicated in the plot.

The physical parameters in (5.7) are constrained by the experimental data. The points labelled C and D in Figure 5.13 straddle the critical temperature line, so that this line must pass through the point (T_c, J)≈(1000 K, 52 Å/m). Furthermore, from the TEM image (Figure 5.12), h≈1 μm; and the phonon frequency is $\nu \approx 10^{13}$ Hz. Therefore, the experimentally determined hopping barrier within the MV model is E_D^{Expt} =1.33±0.06 eV.

This value of the hopping barrier may be directly compared to the theoretical prediction in §2.1.3 using the Madelung potential. For the surface of CaF_2(111), we computed E_D^{Theory} ≈1.75 eV which is of the same magnitude as E_D^{Expt}. But for HT growths, we always observe the immediate formation of a Si-Ca-F composite layer, which becomes the surface upon which further layer-by-layer or islanding growth occurs. We can approximate this layer's ionicity as $Si^0Ca^{1+}F^{1-}$. By computing the attractive interaction of a mobile CaF_2 molecule on such a layer in the same manner as in §2.1.3, we arrive at an upper limit for the hopping barrier E_D=1.41 eV, which is closer to E_D^{Expt}. We conclude that the MV model correctly predicts the transition between HT/LF and HT/HF behaviours, and predicts a physically reasonable value for the hopping barrier E_D.

Furthermore, the MV model is also in agreement with the result (§4.1.2) that growth on 4°-miscut wafers results in islanded films. From (5.7) we see that for a particular growth temperature, the critical flux required for flat films $J \propto h^{-2}$. On 4°-miscut wafers, the terrace width $h \approx 45$ Å as compared to $h \approx 1$ μm for oriented wafers. Therefore the flux required for flat films at 700° becomes unphysically large over the flux required for 0.25° wafers. This

would predict that no flat films are possible at HT for 4°-miscut wafers.

5.4 Temperature Studies: Miscellaneous

5.4.1. Amorphous Films

Conditions for growth of amorphous films were previously reported in the literature [Cho92, Asa83]. In general, amorphous film growth by molecular beam epitaxy occurs at low substrate temperatures (so that atoms have insufficient kinetic energy to surmount barriers) and at high incident fluxes (so that atoms are buried before they have the time to migrate to optimal sites). This regime is labelled "kinetic roughening" in Figure 5.13. In this section we characterize this extreme regime and show that indeed we find significant non-crystallinity of films grown at very low (room) temperature; however we find that the simple kinetic argument does not completely explain the observed non-crystallinity. We will show that in CaF_2 on Si(111), the limitation is the complete formation of the reacted Si-Ca-F layer; once this layer is created, crystalline growth can proceed at room temperature. This was observed by the creation of a "template" layer, discussed in the next section.

Figures 5.15 to 5.17 show comparison Ca 2*p*, F 1*s*, and Si 2*p* XPD plots for 3 films all grown at identical high flux rates (50Å/min) and identical thickness (8 triple layers) but with different substrate temperature histories. The first film was our standard for high crystallinity and was grown at HT/HF; it shows strong XPD modulations in Ca 2*p* and F 1*s* profiles (Figure 5.15(a) and 5.16(a)). We also show the Si 2*p* modulations from the substrate after growth (Figure 5.17(a)).

We grew another film with the substrate fixed at room temperature. Both the Ca 2*p* and F 1*s* XPD scans (Figures 5.15-16(b)) show only weak modulation, which indicates a high degree of randomness in atomic position. One measure of the randomness is to consider these profiles to be an average of completely crystalline (film in (a)) and completely amorphous (isotropic emission) patterns. Fitting to a superposition of the two profiles, we find

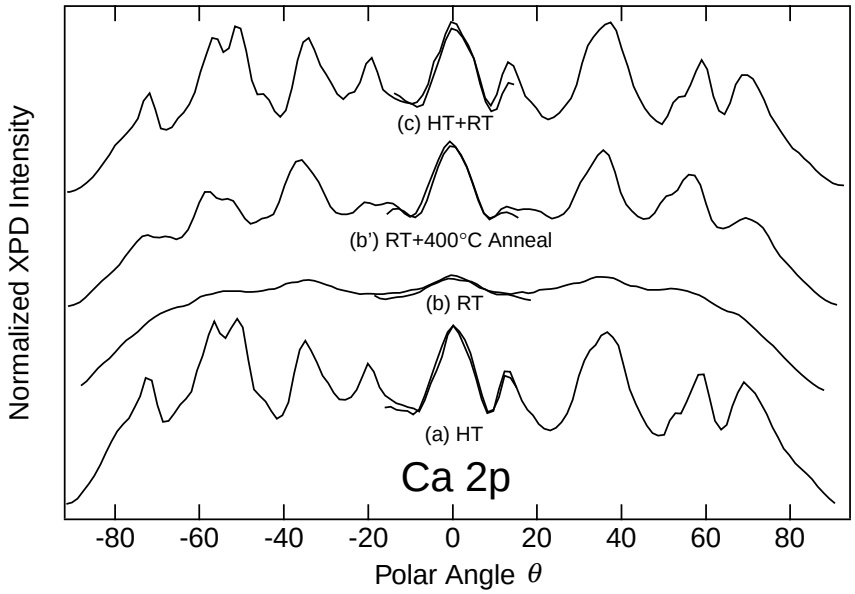

Figure 5.15. XPD profiles for 8 layer films grown at various temperatures: Ca 2p. (a) HT film (11/3/93), (b) RT film(5/1/93), (b') RT film + 400°C anneal, (c) "template" film, 4 layers at HT + 4 layers at RT (6/2/93).

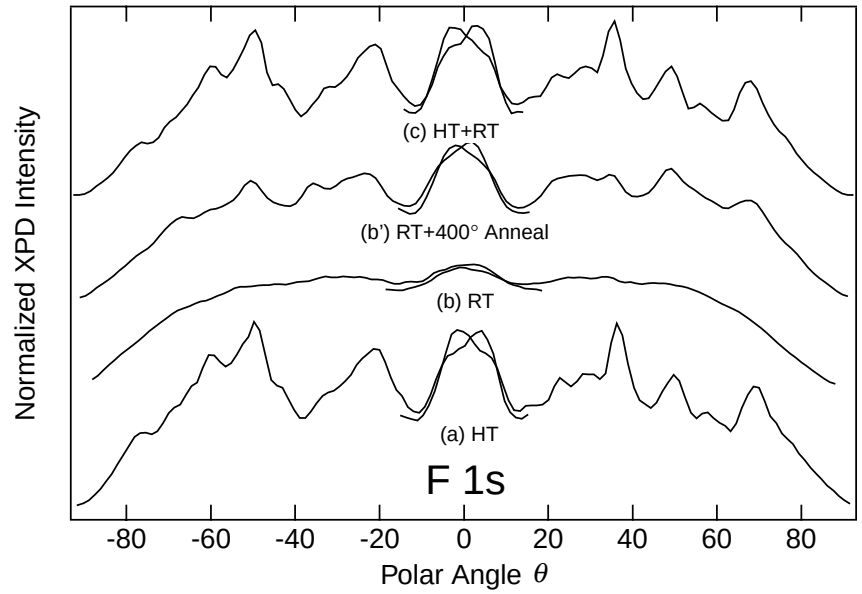

Figure 5.16. XPD profiles for 8 layer films grown at various temperatures: F 1s. (a) HT film (11/3/93), (b) RT film(5/1/93), (b') RT film + 400°C anneal, (c) "template" film, 4 layers at HT + 4 layers at RT (6/2/93).

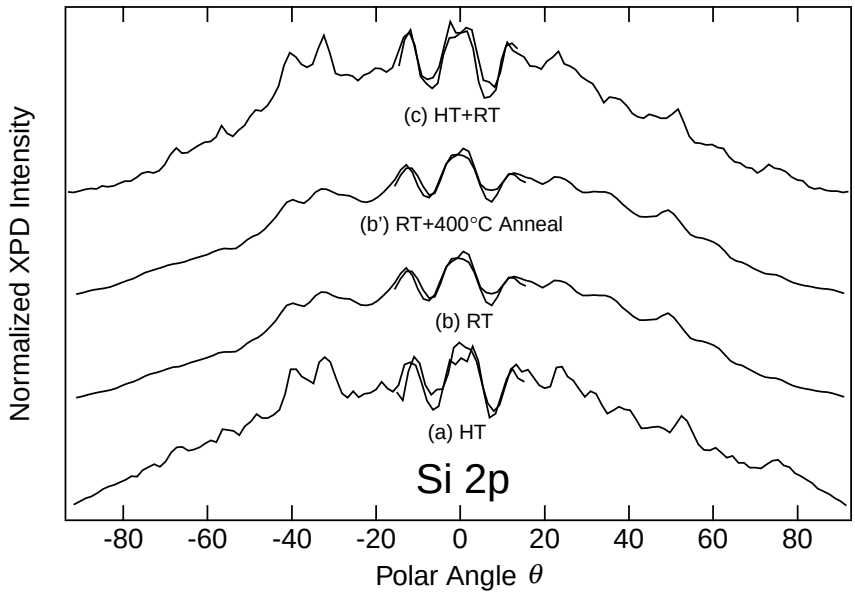

Figure 5.17. XPD profiles for 8 layer films grown at various temperatures: Si 2p. (a) HT film (11/3/93), (b) RT film(5/1/93), (b') RT film + 400°C anneal, (c) "template" film, 4 layers at HT + 4 layers at RT (6/2/93).

that the film is ~20% crystalline + 80% amorphous. Other effects of the disorder are apparent in the Si 2p data (Figure 5.17(b)) at large angles. Crystal defects in the film cause random elastic scattering (which reduces the modulation amplitude) as well as inelastic scattering (which reduces the absolute intensity).

We attempted to anneal out the disorder at 400°C for 60 sec. We found significant improvement in the order (Figures 5.15-16(b')), yet annealling at higher temperatures failed to improve the crystallinity further. Only annealling to ~800°C, which is just past the sublimation temperature of CaF_2, brought about a further marginal improvement in crystallinity. Interestingly, the XPD for the annealled film is symmetric about θ=0°. This indicates that the film consists of approximately equal domains of type B (rotated 180° about [111] relative to the substrate) and type A (not rotated). Although type-B interface formation was shown to be energetically favorable [Sat89], apparently the low temperature and altered

kinetics of this growth prevented its formation. We will discuss this further in connection with SrF_2 results below (§5.5)

5.4.2 "Template" Growth Method

A third film was grown with a 4 triple layer "template" with the sample at HT; the sample was then cooled to RT and an additional 4 triple layers were deposited. This method is of technological interest because at RT, the lattice mismatch between CaF_2 and Si is smaller (~0.6%) than at HT (~2.1%). Hence thicker films may be grown free of strain-relieving defects at RT than at HT [Alv92, Won93]. The resulting film (Figures 5.15-17(c)) retains full crystallinity in comparison to the film grown completely at HT. Therefore we can conclude that RT growth is possible as long as the initial chemically reacted layer is completely ordered before further layers are grown. This result was also shown by x-ray standing wave studies [Alv92, Zeg93] and TEM/x-ray scattering studies [Luc92]. Future studies will attempt to minimize the template thickness for crystalline growth [Hes94, Les94].

It is surprising that RT growth is possible, considering that the barrier for a CaF_2 molecule to hop from one surface unit cell to the next is >1.3 eV as discussed above. This may be understood because the incident CaF_2 molecules are accelerated towards the surface by the electrostatic attraction and can acquire enough kinetic energy to cause local lattice heating upon impact with the lattice. This mechanism was shown to be effective and further augmented by ionizing the CaF_2 beam and accelerating it with an imposed potential by Watanabe *et al.* [Wat92].

5.5 SrF_2 Results

In this section we summarize the growth morphologies of SrF_2 on Si(111) films (summarized in Table C.02). Because the chemistry of Ca and Sr fluorides are so similar, the main effect on the morphology is due to the relative sizes of these atoms and the resultant

lattice mismatches to the substrate. Although the growth parameters have not been studied as systematically for SrF_2 as for CaF_2, we have been able to determine the following general characteristics:

(i) Islanding. For all temperatures and fluxes for which crystalline SrF_2 films resulted, we found the morphology to consist of SrF_2 islands atop a partially exposed Si-Sr-F reacted layer. This morphology is similar to that of the CaF_2 HT/LF case above. This suggests that either (i) the HT/HF parameters for layer-by-layer growth cover a much stricter range for SrF_2 than for CaF_2 (and which we did not probe), or (ii) we did not grow at high enough flux, or else (iii) there is no regime for SrF_2 layer by layer growth. Qualitative morphology was determined in two ways: by LEED or by XPD.

The LEED results are illustrated in Figure 5.18. First, it was observed that for all SrF_2 layers past the first reacted Si-Sr-F layer, the film lattice constant had relaxed to its bulk value. The interface lattice constant was always observed to be commensurate with the Si substrate. For films in which both relaxed islands and exposed interface layers were present, then, the LEED pattern contained a sum of these two patterns. The LEED pattern for the exposed interface layer varied, because for submonolayer films, SrF_2 growth proceeds through a progression of LEED patterns $4\times1 \rightarrow 5\times1 \rightarrow 1\times1$. However, early growth of SrF_2 bulk layers began for some growth conditions before the transition to 1x1 was completed.

The XPD results are illustrated for a typical film in Figure 5.19(a). This film (3/2/93) was grown under identical conditions as the HT/HF CaF_2 films, yet the interface Sr 3*d* signal is less modulated than that of the bulk atoms. Analysis of the XPS heights at off-axis and grazing emission (the method of §4.1.2) suggests that ~35% of the interface layer was exposed.

(ii) Overlayer orientation. Except for the annealled RT growth above, CaF_2 films consistently exhibited type-*B* orientation (in which the overlayer is rotated 180° about the [111] axis relative to the substrate); in contrast, we found that SrF_2 films exhibited either

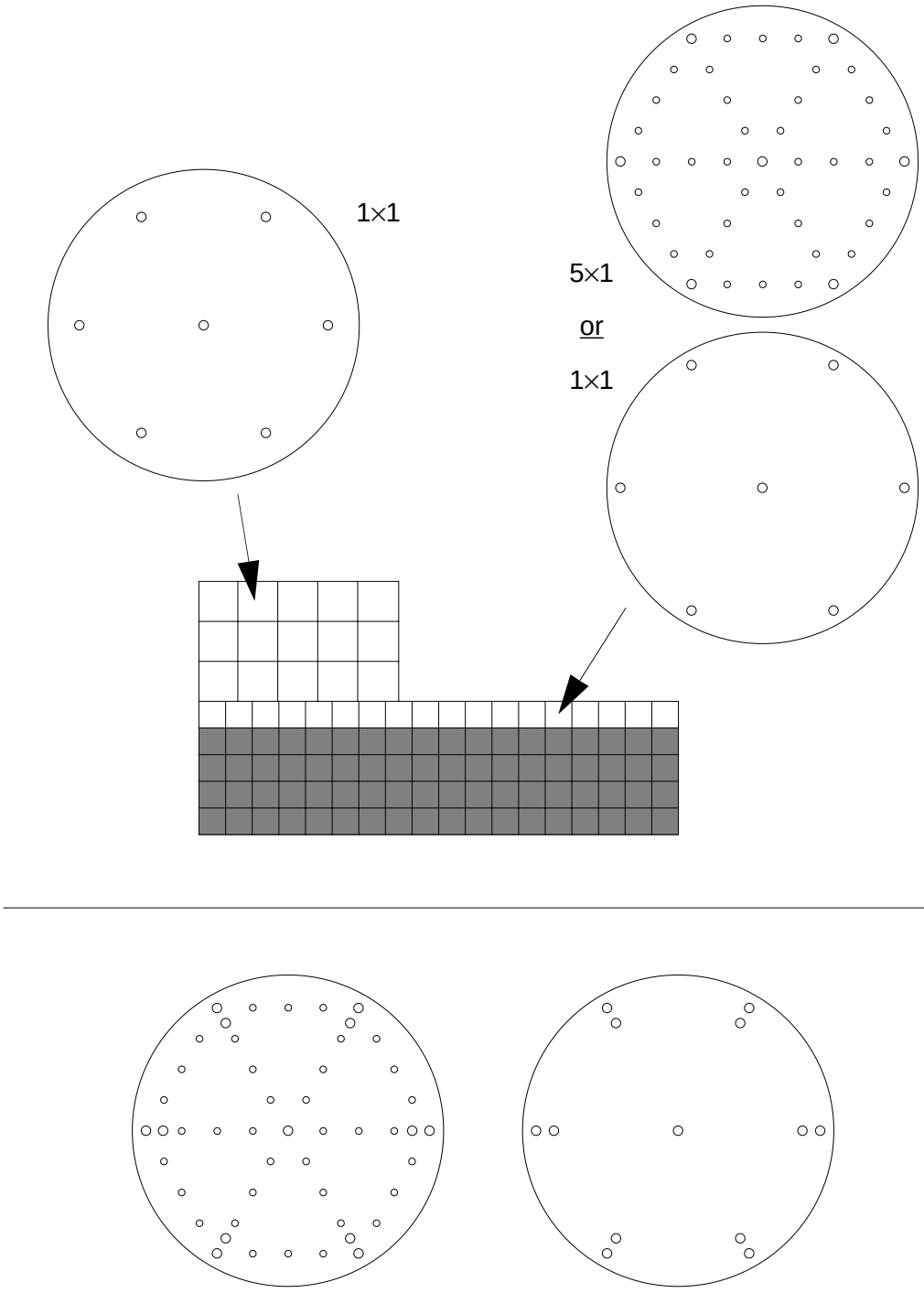

Figure 5.18. Mixed LEED patterns from islanded SrF_2 films. (upper) relaxed SrF_2 islands have a larger lattice constant and hence a contracted LEED pattern relative to the exposed interface layer. (lower) the mixed LEED patter observed for such films.

~equal mixtures of type-*A* and type-*B* overlayer orientations or purely type-*B*. Figure 5.19(b) illustrates determination of type-*A*/*B* mixtures: the XPD pattern for this film (11/5/91) is symmetrical, indicating mixed-domains. This is to be contrasted to the film in Figure 5.19(a), which is asymmetrical due to the pure type-*B* arrangement of atoms.

A calculation [Sat89] showed that the type-*B* orientation was favored over the type-*A* orientation of CaF_2 by a very large amount (~3 eV/molecule at the interface), presumably due to repulsive F-Si interactions in the type-*A* case. One would expect a similar interaction for

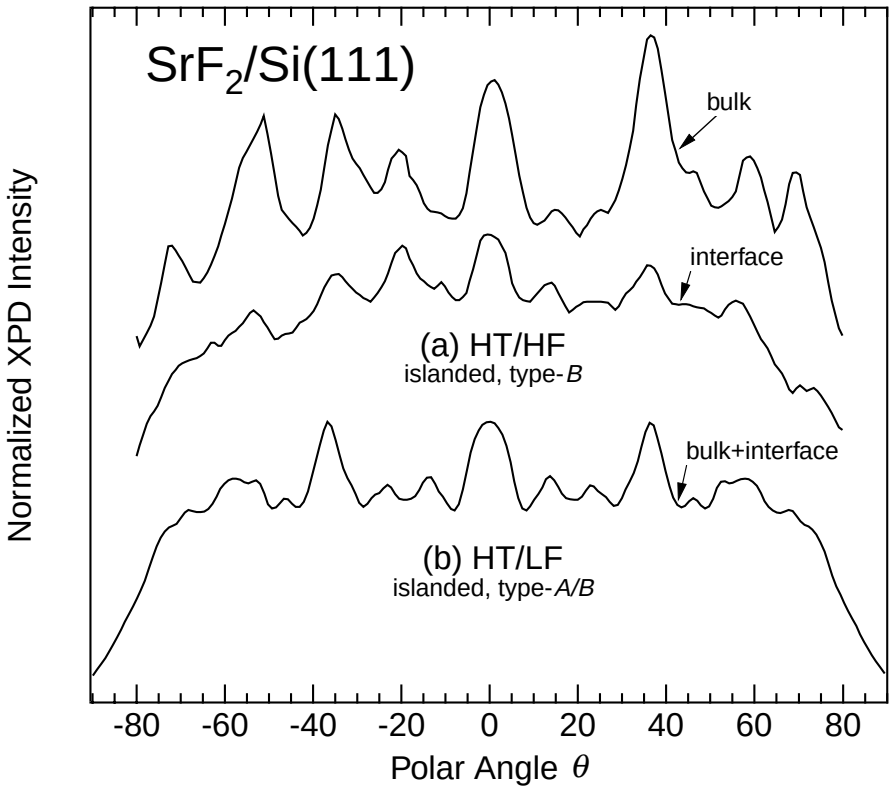

Figure 5.19. Overlayer orientation of SrF_2 on Si(111) films as a function of flux. (a) a HT/HF film (3/2/93) showed distinct asymmetry characteristic of type-*B* orientation. (b) a film grown at HT/LF (11/5/91) is symmetrical, indicating mixed type-*A*/*B* orientations.

SrF_2 on Si(111) (The calculation [Sat89] assumed a relatively small interface bond length b=2.35 Å, so that the barrier would be expected to be less than 3 eV in CaF_2 (b=3.1 Å), and even lower when the larger size of the Sr atom pushes that F out further). But we found that for longer growth times and lower fluxes (i.e. conditions which approach thermodynamic equilibrium) that type-*A*/*B* mixtures resulted, while for faster depositions and higher flux, pure type-*B* resulted. This is an unusual kinetic dependence of the bond orientation on growth conditions which will be explored in future studies.

The ultimate origin of the mixed *A*/*B* orientation in SrF_2 on Si(111) is the increased strain in the films compared to CaF_2 on Si(111). Strain relief is normally obtained by the creation of dislocations; a simple way to create dislocations in fluoride on Si films is to shift the interface Sr from the 4-fold coordinated (*T4*) site to the three-fold coordinated hollow (*H3*) site. This provides a mechanism for the mixed *A*/*B* domains: since the low energy position for the first F atom (I_1) is always above a hollow site, the *H3* domains are forced to be type-*A* oriented, and the *T4* domains are forced to be type-*B* oriented. The presence of mixed domains of *H3*/*T4* has been indicated by x-ray standing wave experiments [Den91, Den93]. This model predicts that the presence of type *A*/*B* domains should be correlated with *H3*/*T4* domains; the search for such correlations has not been carried out.

In contrast, the transition from type-*A* to type-*B* seems to be thermally activated for CaF_2, since we saw mixed A/B domains for CaF_2 grown at RT. The thermal activation energy is only high in the interface layers, since a pure type-*B* template grown at HT was able to sustain further pure type-*B* growth at RT. In fact, it has been shown that pure type-*A* growth is possible if the temperature is ramped from RT to LT during initial growth of the film [Cho91, Cho92].

Core Level Shifts: Expt. vs. Theory 6

6.0 Introduction

In previous chapters, we described the experimental techniques used to measure core-level shifts (CLSs). In this chapter, we apply these techniques, x-ray photoelectron spectroscopy (XPS) and Auger electron spectroscopy (AES), to CaF_2 and SrF_2 films. We have resolved surface, bulk, and interface Ca and F core level emission in thin films (3-8 triple layers) of CaF_2 and SrF_2 on Si(111) and have confirmed these assignments using x-ray photoelectron diffraction (XPD). We have also confirmed these assignments using surface modification by oxidation, and, for CaF_2 films, by Si and SrF_2 overgrowth. The surface and interface CLSs (SCLSs and ICLSs) obtained are in good agreement with the theoretical predictions presented in Chapter 2; from this agreement, we conclude that the interface and surface chemical states do not differ significantly from the bulk states.

In Chapter 5, we showed how XPD was used to identify the growth modes of the films as being laminar or layer plus islands; in the latter case we have resolved buried and uncovered interface F and Ca/Sr atoms. We compare these shifts to theoretical estimates using extra-atomic Madelung potentials for the initial-state shifts and extra-atomic relaxation for the final-state shifts and find reasonable agreement.

The remainder of this chapter is adapted from the publication [Rot93b]. Some of the data here has also been presented in Chapters 4-5; this data is furnished again here for convenience. For reference, the growth conditions for particular samples are summarized in Tables C.01 (CaF_2) and C.02 (SrF_2); the atomic structure and labelling convention for atoms in particular films are summarized in Figures C.01-02.

6.1 Experimental CLSs

In this section, we detail the experimental measurements of the CLSs in CaF_2 and SrF_2 films on Si(111). The resulting CLSs and comparison with theoretical calculations are presented in Tables 6.01 and 6.02 for CaF_2 and SrF_2, respectively. Section 6.4 will discuss the results and assess the agreement with theory.

6.1.1 Growth Conditions

CaF_2 and SrF_2 were deposited from separate graphite crucibles onto resistively heated, p-type (≈1 Ω-cm), on-axis (miscut < 0.25°) Si(111) wafers in an ultra-high vacuum chamber. Unless otherwise indicated, the substrate temperatures were 700°C and the incident flux was 50Å/minute, calibrated with a quartz crystal oscillator. According to Figure 5.13, these conditions (for CaF_2) lead to uniform films for thicknesses greater than 3 TL. The base pressure was better than 10^{-10} Torr, and the growth pressure was typically 10^{-8} Torr. The substrates were prepared using either Shiraki-etching and annealling, or repeated sputter/anneal cycles until the substrates exhibited sharp 7×7 low energy electron diffraction (LEED) patterns and no measurable oxygen XPS signal. Sample temperature was measured by an optical pyrometer and is expected to be accurate relatively to within a few degrees; the temperature was calibrated to the Si substrate $7\times7 \rightarrow 1\times1$, which we observed with LEED to occur at ~ 820°C. After the samples were grown, electron spectra were acquired without removing the samples from ultrahigh vacuum. Once a film was grown, LEED was not performed until all spectra were acquired; this was to avoid damaging our films by electron beam exposure.

We also allowed our samples to remain exposed to the residual gases of our chamber for several days. The main feature we observe is several species of adsorbed oxygen, possibly in the form of H_2O or OH compounds. These species have different desorption energies as determined by annealling studies and may be due to first and higher layers of adsorbed species. The appearance of these species are correlated with our Ca and F observations to

confirm our assignments of Ca and F surface atoms.

XPS spectra were acquired with Mg K_α illumination ($h\nu$ =1253.6 eV) of the samples. Chapter 4 discussed the deconvolution and fitting procedures in detail. Spectra were mathematically deconvolved using the Fourier-transform technique to remove satellite $K_{\alpha'}$ and $K_{\alpha_{3,4}}$ x-ray lines. This was the only deconvolution used before fitting the spectra. For display purposes, a similar deconvolution was performed to remove the Ca $2p_{1/2}$ and Sr $3d_{3/2}$ spin-orbit-split replicas, using splittings and ratios determined from thick films. Background subtraction in all cases was restricted to a constant offset fit to the low binding energy side of our spectra; the background shape was incorporated into our fitting lineshapes.

The electron spectrometer used was a 126 mm hemispherical analyzer (Leybold EA-11), with fixed angle between the x-ray source and the electronic analyzer of 55°. All binding energies are reported relative to the Fermi Level E_F. For XPS spectra, the angular acceptance cone was approximately 10°; to acquire XPD data, the input lens voltages are altered to enhance the spectrometer's angular resolution to ~4°. The sample holder rotates both in the polar angle θ and azimuthal angle ϕ, where θ=0 means electron emission is normal to the sample surface. Full -90° to +90° polar spectra were taken in the $[\bar{1}10]$ plane in two separate scans from -90° to 0° at azimuthal angles of ϕ = 0° (towards substrate $[\bar{1}\,\bar{1}2]$) and ϕ = -60° (towards substrate $[1\,\bar{1}2]$). Because the overlayer has type-*B* orientation (rotated 180° about [111]), these direction indices are inverted relative to the overlayer's indices. For each angle in a scan, a complete XPS or Auger spectrum is taken and stored for later automated curve fitting.

We have measured the surface and interface core-level shifts relative to bulk for CaF_2 (Ca 2*p*, F 1*s*, Ca LMM, and F KVV electrons) and SrF_2 (Sr 3*d*, F 1*s*, F KVV electrons) films; the results are presented in the following subsections and summarized in Tables 6.01 and 6.02. In general, we acquire "off-" and "on-axis" spectra $\mathcal{S}$at angles (θ, ϕ)=(-26.1°, -18°) and θ=0°, respectively:

$$\mathcal{S}_{off} = S + B + I \tag{6.1a}$$

$$\mathcal{S}_{on} = S + (1+\beta)B + (1+\iota)I, \tag{6.1b}$$

where S, B, and I represent peaks from surface, bulk, and interface atoms, and β and ι are forward-scattering enhancements in the [111] direction. We then compute the linear combinations

$$\mathcal{S}_{on-off} = \beta B + \iota I \tag{6.1c}$$

$$\begin{aligned}\mathcal{S}^* &= (1+\iota)\mathcal{S}_{off} - \mathcal{S}_{on} \\ &= \iota S - (\beta - \iota)B\end{aligned}, \tag{6.1d}$$

where the difference curve $\mathcal{S}_{on-off}$ is only sensitive to signals from buried atoms (which have neighbors in the [111] direction), while $\mathcal{S}^*$ is sensitive mainly to the remaining atoms. Further details were discussed in Chapter 5.

6.1.2 CaF_2 SCLSs

Typical XPS and XPD results are shown in Figure 6.01 for a 4 layer CaF_2 film (9/1/92) consisting of a reacted Si-Ca-F bilayer at the interface and three F-Ca-F triple layers. We show in Figure 6.01(a) Ca $2p_{3/2}$ core-level spectra $\mathcal{S}_{on}$, $\mathcal{S}_{off}$ and the resulting difference spectrum $\mathcal{S}_{on-off}$. We measured the emission over the full sector $-60° < \phi < 0°$ and found that the off-axis emission approximates the isotropic emission amplitude in the absence of all elastic scattering.

The coarse features in the spectra in Figure 6.01(a) are two peaks of separation ~2.7 eV. The smaller-intensity peak I to lower binding energy has been previously identified as the interface Ca atom bonded to the Si substrate [Rie86, Olm87], while the remaining peak S+B is further resolved as discussed in Chapter 5 into two closely-spaced components due to surface S and bulk-like B atoms.

We illustrate the effect of forward focussing in Figure 6.01(b), in which surface+bulk and interface Ca $2p$ XPD scans are presented as a function of θ in the plane formed by the on-

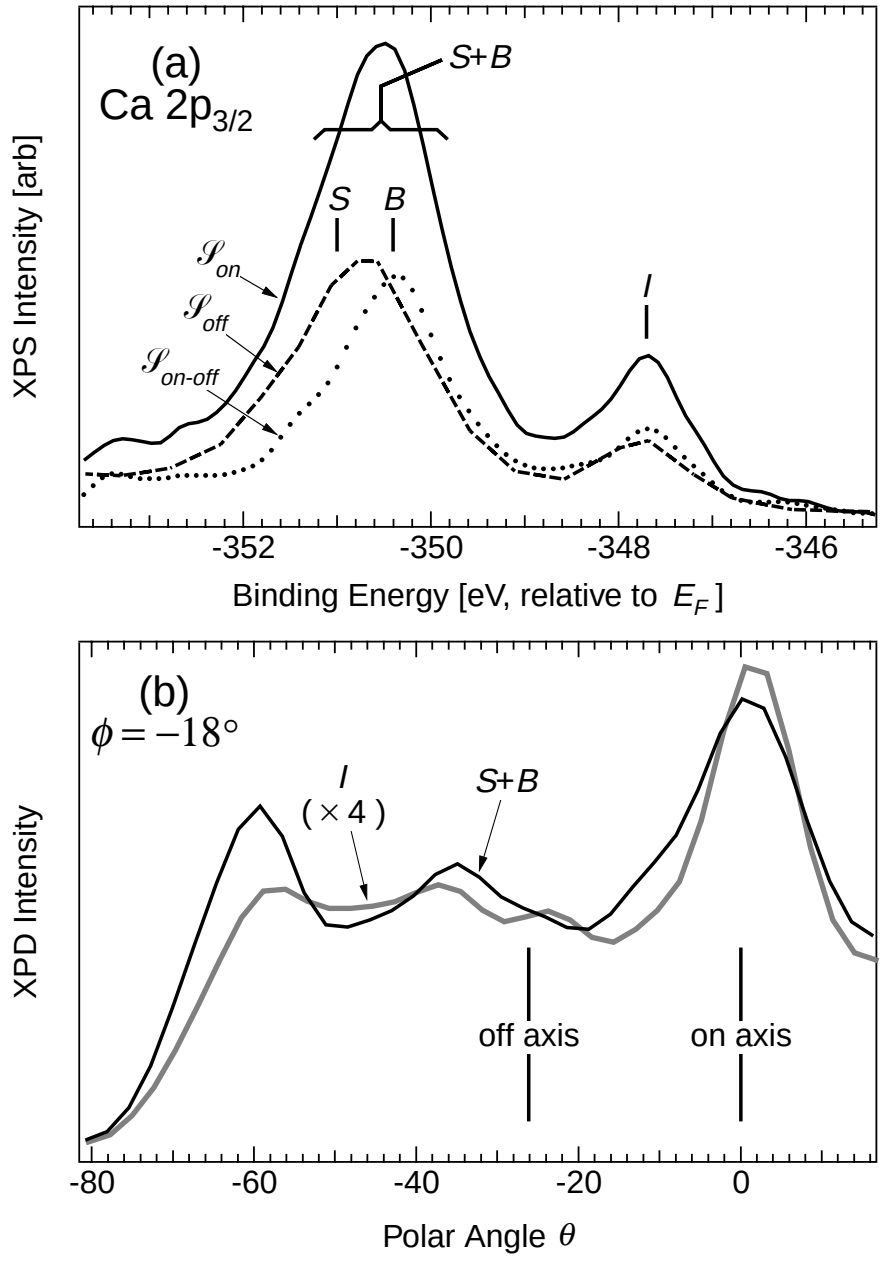

Figure 6.01. XPS and XPD results for a 4 TL CaF_2/Si(111) film (9/1/92). (a) Ca $2p_{3/2}$ core level spectra acquired at normal, on-axis emission ($\mathcal{S}_{on}$, θ=ϕ=0°, solid), at off-axis emission ($\mathcal{S}_{off}$, θ=-26°, ϕ=-18° dotted), and the difference spectrum ($\mathcal{S}_{on\text{-}off}$, dashed). The assignment of surface *S*, bulk *B* and interface *I* peaks is indicated by the vertical lines. (The atomic structure and location of the atoms is indicated in Figure C.02.) (b) XPD profiles taken in the ϕ=-18° plane, showing the interface and combined surface+bulk peak heights as a function of emission angle θ. The on- and off-axis angles are indicated by vertical lines.

and off-axes (ϕ = *-18°)*. These data were obtained by repeatedly acquiring spectra similar to those in Figure 6.01(a) at each angle, performing a least-squares fit to two peaks, and storing the peak heights. Both scans exhibit a strong forward scattering feature at θ=0° (on-axis) compared to the emission level observed near θ=26° (off-axis).

Chapter 5 showed how this forward-scattering effect is exploited to resolve the *S*+*B* peak into separate surface and bulk components. The difference spectrum in Figure 6.01(a) reflects emission only from *B* and *I* atoms, which have scattering centers located directly above them in the [111] direction. In the difference spectrum, it is evident that the Ca peak labelled *S*+*B* has narrowed and its center has shifted towards lower binding energy. This was explained by having subtracted an unmodulated surface peak *S* at higher binding energy which we assign to be the surface-shifted Ca contribution. The two bulk-like layers of Ca between the surface and interface layers contribute a single unresolved peak *B* to the difference spectrum.

Figure 6.02 shows the fitting results. First we fit the difference spectrum $\mathscr{S}_{on\text{-}off}$ to locate the core-level energies of the interface and buried atoms using a least-squares method (Figure 6.02(a)). The energy difference between bulk and interface atoms can be estimated in this procedure to within ~±0.05 eV. Figure 6.02(b) shows the $\mathscr{S}^*$ spectrum for t=1.1; the fit shown indicates an upper limit to the *S*/*B* energy shift. Having accurately fixed the positions of the interface and bulk peaks, we used them to obtain an upper and lower limit to the bulk-surface splitting by simultaneously fitting the $\mathscr{S}_{on}$ and $\mathscr{S}_{off}$ spectra to three peaks *S*, *B*, and *I*. Using this procedure, we determine the Ca SCLS to be 0.71 ± 0.09 eV and the ICLS to be 2.65 ± 0.05 eV. The SCLS is observed to be the same in films 3-8 layers thick within the experimental uncertainties; the ICLS was found to be somewhat variable from growth to growth and was especially sensitive to the growth temperature [Won93]; furthermore, the splitting sometimes widened slightly (with the interface position remaining fixed) in the first hour after growth. All of the spectra discussed in this paper were acquired after this

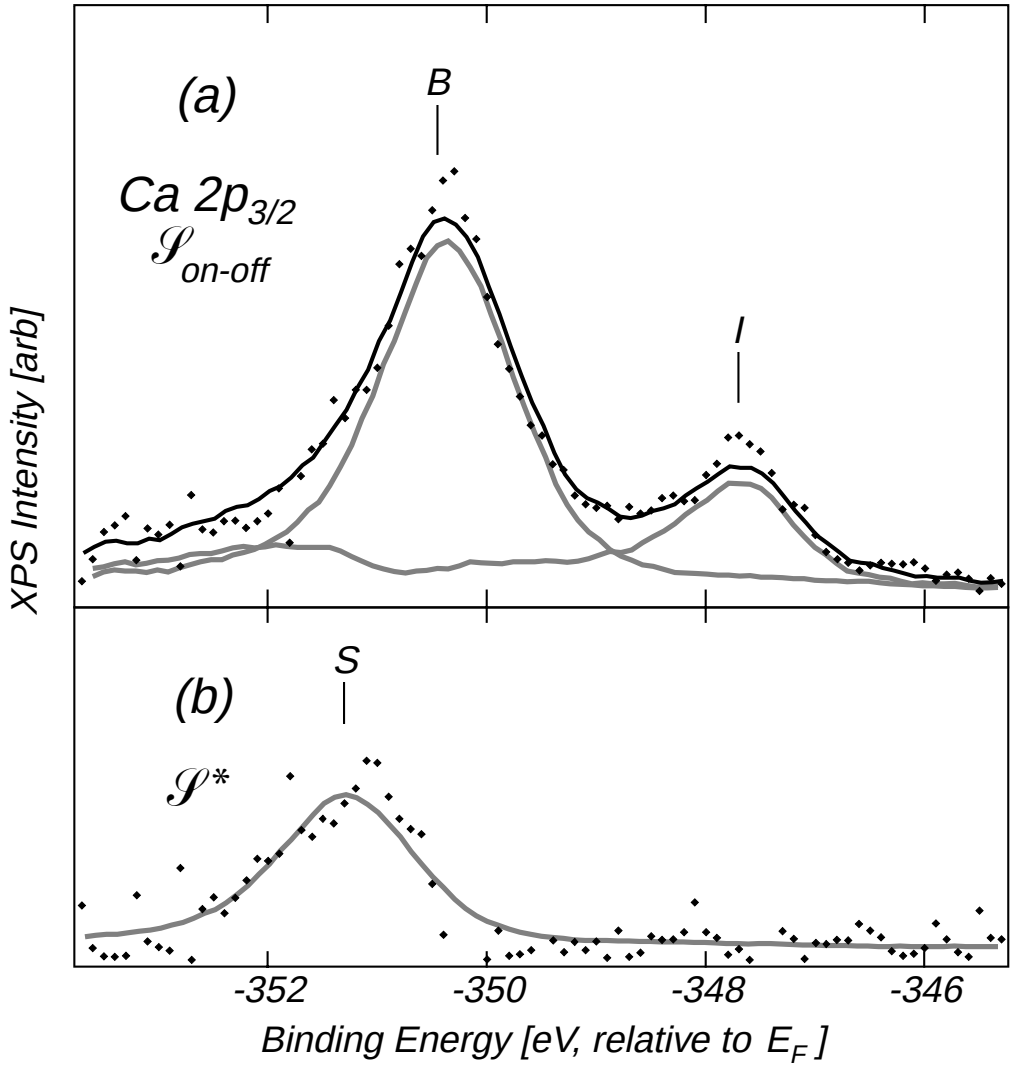

Figure 6.02. Curve fits for the 4 TL CaF_2 film (9/1/92) in Figure 6.01. (a) Difference spectrum $\mathcal{S}_{on\text{-}off}$, which is only sensitive to bulk and interface Ca atoms. (b) Linear combination $\mathcal{S}^* = 2.1\,\mathcal{S}_{off} - \mathcal{S}_{on}$, which is primarily sensitive to surface Ca atoms.

widening (if any) was complete.

Close examination of Figure 6.02(a) shows that the Ca lineshape from the unburied interface used in the fit is somewhat broader than the actual signal from the buried interface Ca atoms; an even larger width difference is observed for interface F atoms. This was discussed in §4.1.5 as partial evidence that in the bare Si-Ca-F layer there is some disorder in the position of the F atoms and that these F atoms become ordered upon being covered. The atomic structures near the Ca *S*, *B*, and *I* atoms were observed for a 3 TL film (11/3/93) with component-resolved XPD (CR-XPD). The separate diffraction patterns for a three layer film are shown in Figure 6.03 (dots). These curves were obtained by recording a Ca 2*p* spectrum $\mathscr{S}_\theta$ for each polar angle θ and fitting it with three peaks whose energies are fixed from prior fits to $\mathscr{S}_{on}$ and $\mathscr{S}_{off}$ XPS spectra. The normalized peak amplitudes are then reported in Figure 6.03. There are three qualitative conclusions established from this data. First, we confirm the assignment of the *S* component as the surface Ca atom. This is because while the *S* component has little modulation near θ=0°, it shows significant forward scattering in the $[11\bar{1}]$ and $[\bar{1}\bar{1}3]$ directions, which would be expected for Ca $\rightarrow$ F scattering (see upper inset). This rules out the possibility that *S* results from randomly located Ca atoms, since such atoms have isotropic emission in all directions, not just near θ=0°. Second, we verify the simple structural model illustrated in the insets, since theoretical multiple-scattering calculations (solid lines) agree with the XPD profiles indicated. (Recently, it was proposed [Luc93] that the buried Si-Ca-F interface layer undergoes a strain-driven reconstruction to a $\sqrt{3}\times\sqrt{3}$ structure which would have drastically different XPD behavior . Our results for films at least 8 TL thick contradict this proposed interface structure.) Third, we confirm the film thickness as not being more than 3 TL thick (Si-Ca-F + 2 bulk TLs). This is because of the presence of the [112] scattering from second-layer atoms in the interface XPD profile and the absence of this scattering peak for the bulk-like atom *B*.

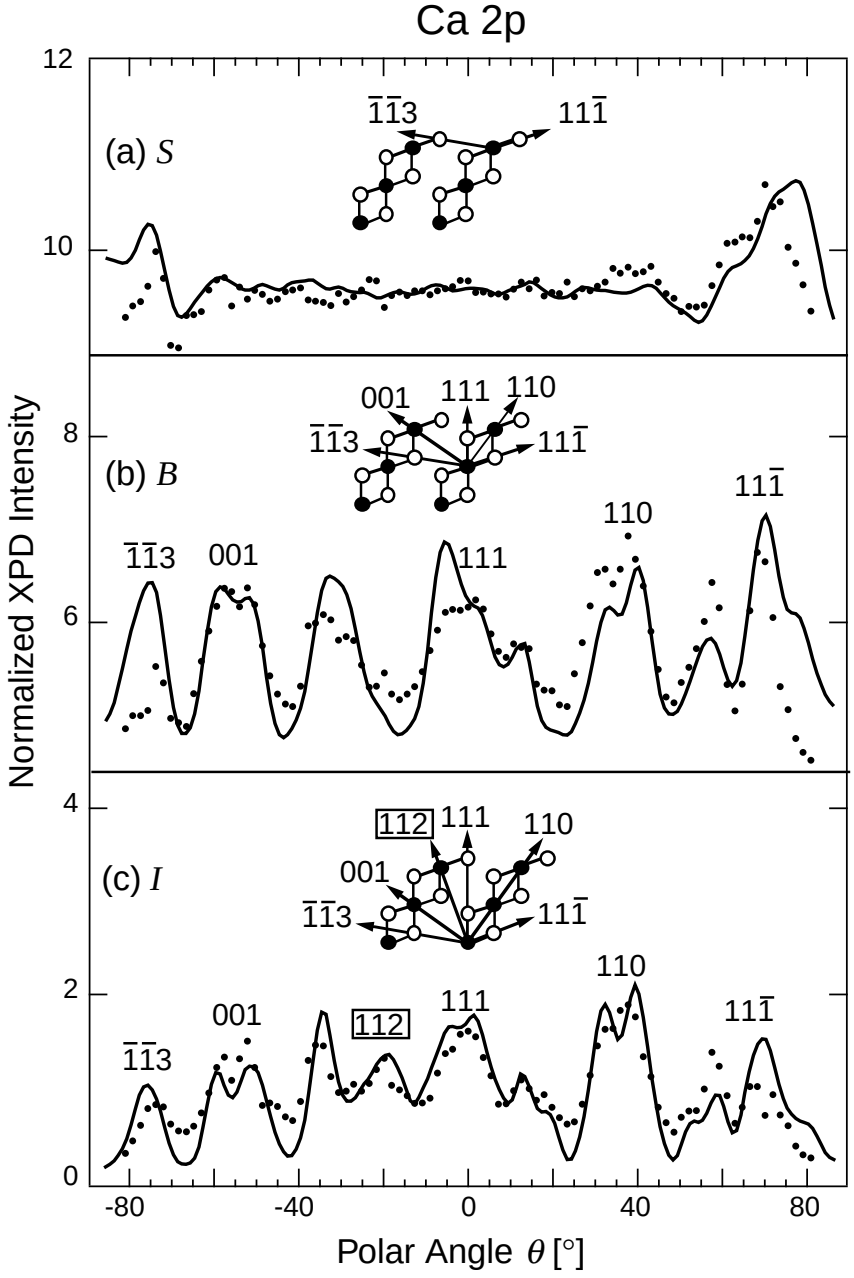

Figure 6.03. Component-resolved XPD profiles (solid lines, theoretical; dots, experimental) for Ca 2*p* electrons in a 3 TL CaF_2 on Si(111) film (11/3/92). (a) surface Ca atoms *S*, (b) bulk-like Ca atoms *B*, (c) interface Ca atoms *I*. The insets show the corresponding in-plane scattering angles responsible for the forward-scattering peaks in the XPD profiles.

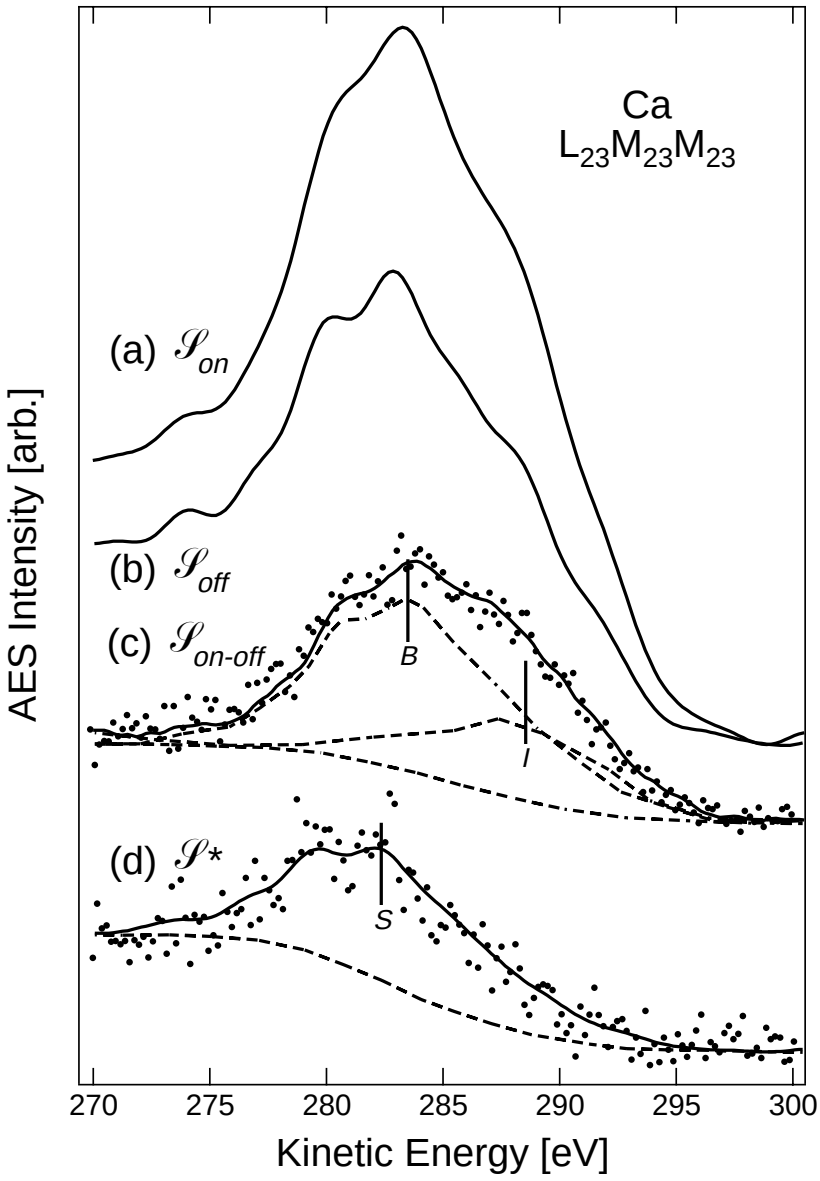

Figure 6.04. Ca LMM AES spectra for a 4 TL CaF_2/Si(111) film. (a) on-axis emission (θ=0°), (b) off-axis emission (θ=0°, ϕ=-18°), (c) difference spectrum $\mathscr{S}_{on-off}$, which is sensitive to bulk and surface Ca atoms, and (d) the spectrum $\mathscr{S}^*$=1.95 $\mathscr{S}_{off}$ - $\mathscr{S}_{on}$, which is sensitive to surface Ca atoms.

6.1.3 Ca LMM Auger

Figure 6.04 illustrates the results for Ca $L_{23}M_{23}M_{23}$ Auger electrons for the same 4 TL film (9/1/92) in Figures 6.01-02. Spectra (a) through (d) show the on-axis data $\mathscr{S}_{on}$, the off-axis data $\mathscr{S}_{off}$, and the linear combinations $\mathscr{S}_{on-off}$ and $\mathscr{S}^* = 1.95\,\mathscr{S}_{off} - \mathscr{S}_{on}$. The smaller value of ι compared to that of Ca 2*p* is due to the reduced forward scattering at lower kinetic energy (~280 *vs.* ~900 eV). The fit to the interface and bulk core-levels is indicated in Figure 6.04(c), using appropriate lineshapes obtained from ML and thick films. For Ca LMM electrons, the situation is complicated by the extremely wide (~10 eV) and complicated shape, as well as the large inelastic scattering background which is different for each of the components. To compensate for the inelastic background, we subtracted the background using the Shirley method from both the spectra to be fit as well as from the empirical lineshapes. After fitting, the inelastic backgrounds were restored to the spectra $\mathscr{S}$. The ICLS was found to be -5.0 ± 0.4 eV, while the SCLS was 1.2 ± 0.3 eV.

6.1.4 F KVV Auger

Figure 6.05 shows AES results for F KVV Auger electrons for the 4 TL film. Figure 6.05(a) shows the $\mathscr{S}_{on}$, $\mathscr{S}_{off}$, $\mathscr{S}_{on-off}$, and $\mathscr{S}^*=3.5\,\mathscr{S}_{off} - \mathscr{S}_{on}$ spectra, while Figure 6.05(b) shows final fitting results. Examination of $\mathscr{S}_{on}$, $\mathscr{S}_{off}$, and $\mathscr{S}_{on-off}$ clearly indicates surface *S*, bulk-like *B* and interface I_1 fluorine atoms (see Figure C.01). The feature *S* is comprised of two unresolved peaks S_1 and S_2 from the two fluorine atoms in the surface TL.

Analysis of these spectra is complicated by the fact that, unlike Ca atoms, fluorine atoms have two unique sites relative to the on-axis [111] direction. The upper site of a TL has a first near neighbor Ca atom along [111] and thus its emission is strongly focussed in this direction. The lower site of a TL has a fifth near neighbor fluorine atom in this direction and hence its emission has negligible [111] forward focussing (since the forward focussing amplitude is proportional to the inverse spacing between emitter and scatterer atoms). Because of this, the electrons emitted from interface atoms I_1 have a much stronger forward

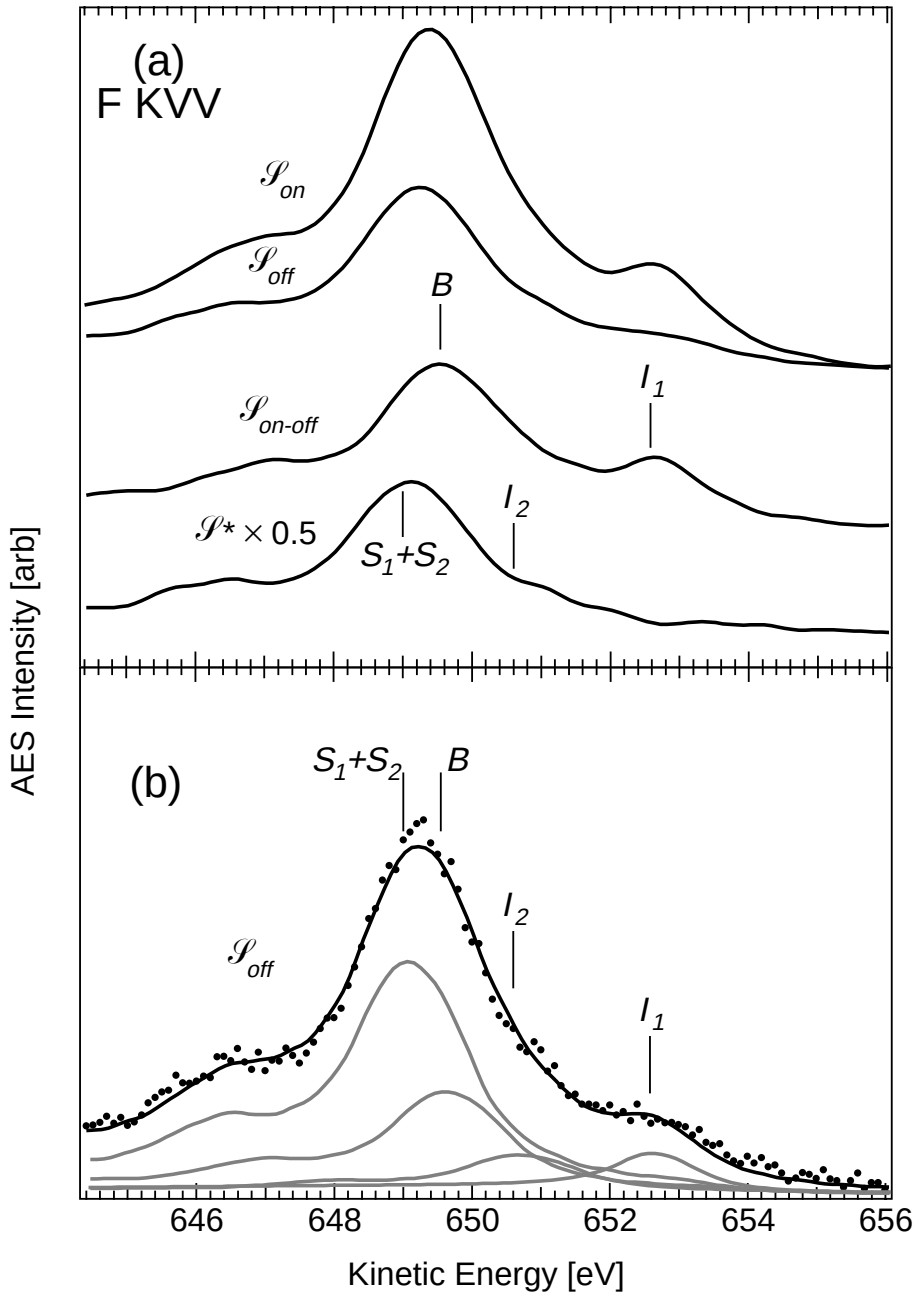

Figure 6.05. F KVV AES results for a 4 TL CaF_2/Si(111) film (9/1/92). F KVV Auger spectra for (a) on-axis emission $\mathscr{S}_{on}$ (θ=0°) off-axis emission $\mathscr{S}_{off}$ (θ=-26°, ϕ=-18°), the difference spectrum $\mathscr{S}_{on-off}$, which is sensitive to bulk and surface F atoms, and the spectrum $\mathscr{S}^*$=3.5 $\mathscr{S}_{off}$- $\mathscr{S}_{on}$, which is sensitive to fluorine atoms without scattering centers in the on-axis direction. Figure C.02 indicates the position of F atoms in the film. (b) The final fit to the $\mathscr{S}_{off}$ spectrum, showing all four components (surface atoms S_1 + S_2, bulk B, interface I_1 and I_2).

scattering amplitude than those emitted from bulk atoms *B*, which, in this 4 layer film, are an average of one weakly scattered and two strongly scattered components. This means that for fluorine atoms in a 4 TL film, $\beta << \iota$. (From Figure 6.05, we estimate $\beta \approx 1.1$ and $\iota \approx 2.5$). This affects the appearance of both the $\mathscr{S}_{on\text{-}off}$ and $\mathscr{S}^*$ spectra as follows: the $\mathscr{S}_{on\text{-}off}$ spectrum has a reduction in the amount of *B* component because one of the bulk atoms has no Ca atom directly above it. This only affects the relative amplitudes of *B* and *I*, and not the fitted energies. This unmodulated component instead appears in the $\mathscr{S}^*$ spectrum, distorting the S_1+S_2 peak slightly. Additionally, the $\mathscr{S}^*$ spectrum displays additional intensity between I_1 and *B*. We assign this intensity to the second interface peak I_2, which, being of the second type of site, also has negligible forward scattering in the [111] direction. The assignment of this peak is evident in Figure 6.06 below; the detailed interpretation was presented in §5.2.3.

The final off-axis fluorine KVV fit is shown in Figure 6.05(b). The SCLSs and ICLSs were found to be 0.7±0.2 eV (S_1+S_2), -1.5 ± 0.5 eV (I_1) and -3.03 ± 0.03 eV (I_2),. The I_1 component sharpens considerably upon being buried; this is further evidence for some fluorine disorder in the unexposed Si-Ca-F layer which is removed upon further growth. The lineshapes used in the fit were discussed in Chapter 4.

The I_2 CLS is difficult to determine from the data presented since this peak has no forward-scattering enhancement in the [111] direction and hence does not appear in $\mathscr{S}_{on\text{-}off}$. The most accurate measurement of its energy is for the 3 TL film (discussed below), in which this peak was highlighted using the XPD effect. The lineshape of I_2 appears to be bulk-like, which is not surprising since this atom is fully coordinated.

Similar to the case of Ca, we were able to confirm the F KVV assignments and thickness using CR-AED as shown in Figure 6.06 for a 3 TL film. The results for F KVV furnished here (Figures 6.06-07) will be used to interpret F 1*s* data presented in §6.1.5. The peak positions I_1, I_2, *B*, and *S* were first determined (the values are summarized in Table 6.01) and these energies were then used for fitting the CR-AED data. As mentioned above, there

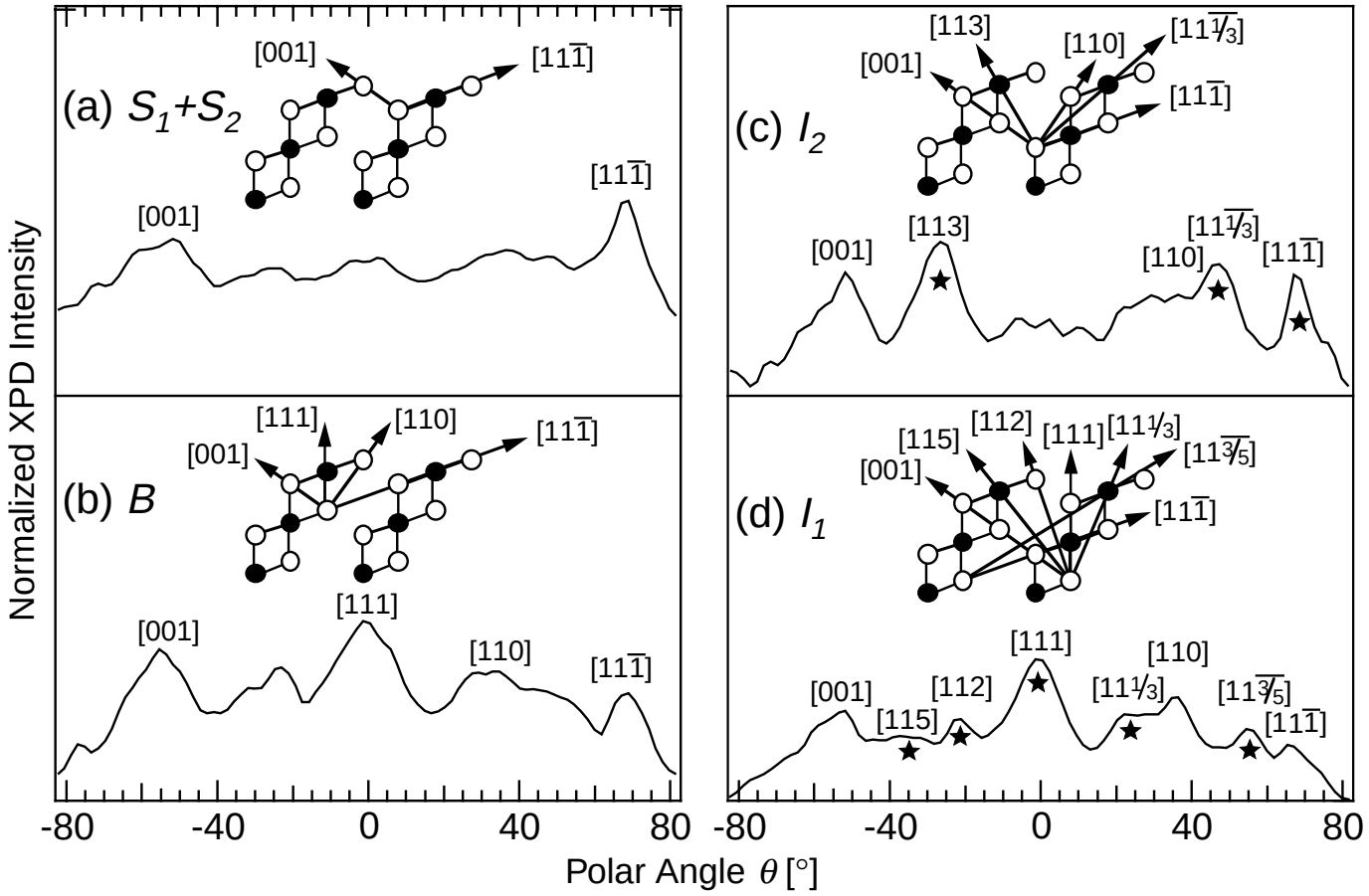

Figure 6.06. F KVV AED results for a 3 TL CaF_2 on Si(111) film (11/3/92). (a) surface F atoms S_1+S_2, (b) bulk-like F atoms B, (c) interface F atoms I_2, and (d) interface F atoms I_1. The insets show the corresponding in-plane scattering angles responsible for the forward-scattering peaks in the XPD profiles. Scattering directions which uniquely distinguish I_1 from I_2 atoms are shown starred.

are two inequivalent F sites with respect to the [111] direction. I_1 and B are of the first type, which has a first-near-neighbor Ca in the [111] direction and hence have strong scattering into θ=0°; I_2 is of the second type and therefore should have weak scattering into this direction. The CR-AED verifies this; in addition other scattering angles which distinguish I_1 and I_2 are indicated in the figure by stars (★). Finally, the assignment of the unresolved surface atoms S is confirmed upon comparison with the theoretical calculation indicated, which is an incoherent addition of the expected signals for the two surface atoms.

The I_2 CLS was determined as follows. From Figure 5.06 (c), the I_2 peak has a unique forward-scattering peak in the [113] direction. After acquiring a spectrum $\mathcal{S}_{[113]}$ along this direction and subtracting the spectrum $\mathcal{S}_{off}$, the resulting spectrum $\mathcal{S}_{[113]\text{-}off}$ displayed a single peak I_2 whose energy could be easily determined. This fit is illustrated in Figure 6.07.

6.1.5 F 1s

The F 1*s* XPS data also showed CLSs, although they were small enough to preclude easy assignment. We discussed in Chapter 5 that the XPD modulations (amplitude and position) are virtually identical for F 1*s* and F KVV electrons from thick films (Figure 5.03(c) and (d)). In the analysis that follows, then, we assume that the observed F 1*s* peaks have the same XPD modulations as the corresponding AED modulations (Figure 6.06). Figure 6.08(a) illustrates the $\mathcal{S}_{on}$, $\mathcal{S}_{off}$, and $\mathcal{S}_{on\text{-}off}$ F 1*s* spectra for the same 3 TL film as in Figures 6.03 and 6.06. From the F KVV results above, we know that the $\mathcal{S}_{on\text{-}off}$ spectrum is comprised of two peaks due to the I_1 and B atoms. Accordingly, the F 1*s* $\mathcal{S}_{on\text{-}off}$ spectrum appears to be composed of two peaks of separation ~0.75 eV. From the XPD results presented below, we assign the larger component in $\mathcal{S}_{on\text{-}off}$ to be due to the interface atom I_1, while the smaller component is due to the bulk atom B. This is in spite of the fact that attenuation should make B larger than I_1 in an ideal film. A possible reason for this is that the forward scattering is greater for I_1 than for B; a further contribution is that the electrons from bulk atoms have

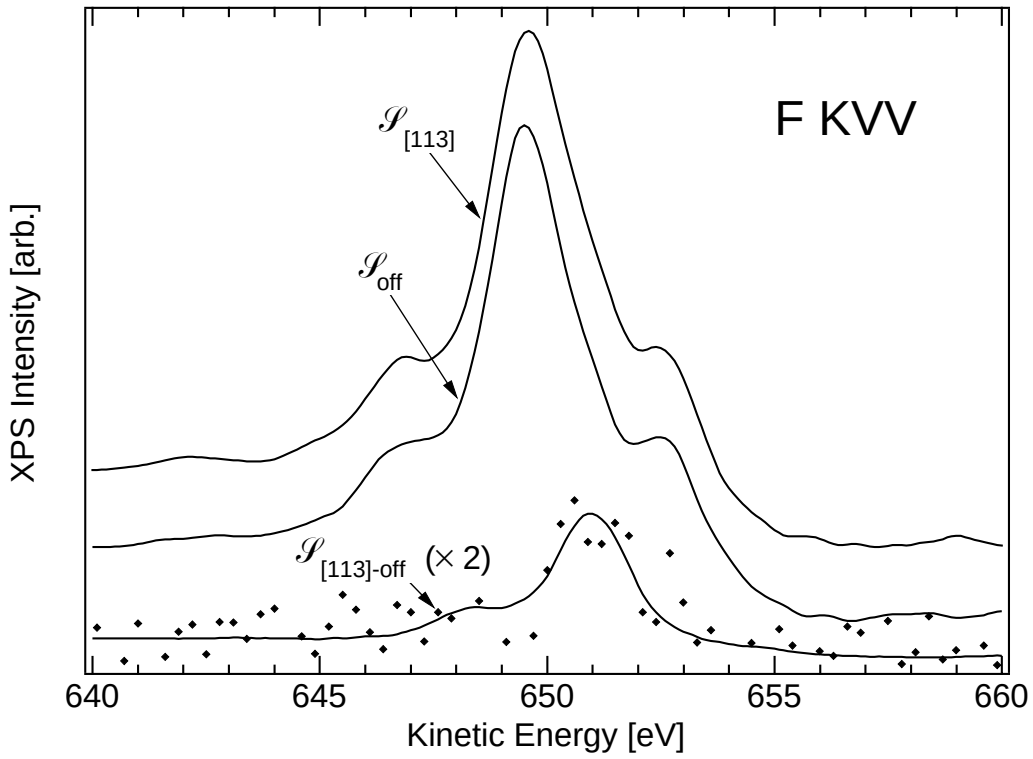

Figure 6.07. Determination of I_2 energy from selective XPS spectra (11/3/92). Shown are F KVV spectra acquired for emission along [113] ($\mathscr{S}_{[113]}$), off-axis emission $\mathscr{S}_{off}$, and the difference spectrum $\mathscr{S}_{on\text{-}off}$. The difference spectrum is curvefitted to a single component representing the I_2 atoms' signal.

an additional intrinsic loss channel (see Figure 4.05) that is unavailable to electrons from the interface.

The assignments of B, I_1 and I_2 F 1s peaks are facilitated by CR-AED as suggested by the F KVV results in Figures 6.06-07. This is because the F 1s XPD and F KVV AED modulations from bulk sites was observed to be the same (see Figure 5.03). We assume here that the F 1s CR-XPD and F KVV CR-AED results should also be similar for all film atoms. We observe that the I_1 atom has a unique forward-scattering peak at the angle θ=+58° (labelled [11$\overline{3/5}$] in Figure 6.06), while similarly, the I_2 atom has a unique forward scattering peak along θ=-39° ([113]). Therefore, we acquired XPS spectra $\mathscr{S}_{[11\overline{3/5}]}$ and $\mathscr{S}_{[113]}$ at these two angles. Relative to the off-axis spectrum $\mathscr{S}_{off}$, these spectra showed enhancements at the energies of the I_1 and I_2 peaks; the difference spectra $\mathscr{S}_{[11\overline{3/5}]\text{-}off}$ and $\mathscr{S}_{[113]\text{-}off}$ which show this enhancement are presented in Figure 6.08(b). The $\mathscr{S}_{[11\overline{3/5}]\text{-}off}$ spectrum is similar to $\mathscr{S}_{on\text{-}off}$, except that the component to low binding energy is more dominant. This confirms the assignment of this peak to the I_1 atom. The $\mathscr{S}_{[11\overline{3/5}]\text{-}off}$ spectrum shows a single peak, shifted 0.35 eV to lower binding energy relative to B, which we have assigned to the I_2 atom.

Finally, we consider the position of the surface F 1s signals. In Figure 6.08(a), $\mathscr{S}_{on\text{-}off}$ is slightly displaced to higher binding energy compared to $\mathscr{S}_{on}$. As before, this indicates that the unmodulated surface signal has energy to higher binding energy than the remaining atoms. However, we cannot rule out the presence of additional surface intensity to lower binding energy in approximately the same position as I_1. This is because the relative forward scattering enhancements β and ι of B and I_1 are unknown; the observed displacement of $\mathscr{S}_{on\text{-}off}$ may be accounted for if ι is just slightly greater than β. For this reason, we have not presented $\mathscr{S}^*$ data for F 1s, nor have we determined SCLSs for F 1s.

6.2 Surface Modification Experiments

The previous sections report the use of CR-XPD and CR-AED to identify surface core-level shifts. We have also studied the CaF_2 SCLSs after modifying the film surfaces in

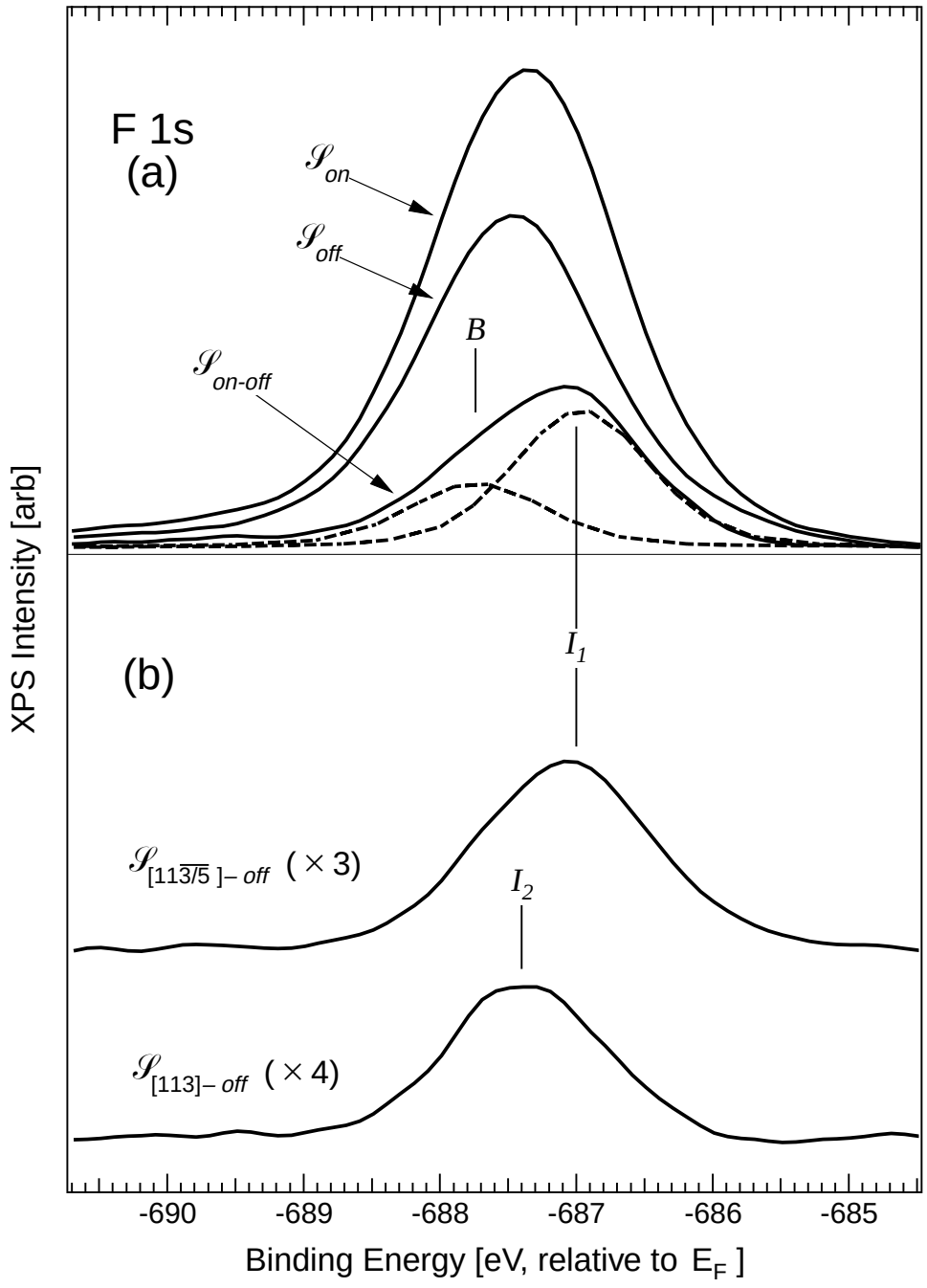

Figure 6.08. F 1*s* XPS results for a 3 TL CaF_2 on Si(111) film (11/3/92). (a) $\mathscr{S}_{on}$, $\mathscr{S}_{off}$, and the difference spectrum $\mathscr{S}_{on\text{-}off}$, which shows an asymmetric peak consisting of bulk *B* and interface I_1 components (see Figure C.02), (b) difference spectra $\mathscr{S}_{[11\overline{3/5}]\text{-}off}$ and $\mathscr{S}_{[113]\text{-}off}$, which are mainly sensitive to I_1 and I_2 interface atoms, respectively.

three different ways: by SrF_2 deposition on CaF_2, by exposure of CaF_2 and SrF_2 to oxygen species, and by Si deposition on CaF_2.

6.2.1 SrF_2 on CaF_2 on Si(111)

The surface Ca atoms may be converted to a bulk-like environment by adding an overlayer of SrF_2. We first prepared and characterized a 4 TL CaF_2 film as above, and then covered it with ~1.5 TLs of SrF_2 grown at 400°C. In this structure, the surface Ca atom's site becomes essentially bulk-like and hence its emission *S* overlaps the signal of the *B* atom. This is illustrated in Figure 6.09, where we compare off-axis Ca $2p_{3/2}$ spectra acquired from the as-grown and SrF_2-exposed films (the latter has been scaled so that the interface Ca signal has the same height; this is to compensate for the signal attenuation caused by the overlayer). The difference spectrum shown indicates that the surface peak to high binding energy has shifted approximately to the bulk binding energy. A similar result was observed in Ca LMM spectra (not shown). Furthermore, we demonstrated that the 1.5 TL SrF_2 cap is crystalline and maintains the same orientation ("type-*B*") as the underlying CaF_2 lattice. This was established by analysis of CR-XPD of the two Sr 3*d* components observed from the first and second SrF_2 TLs.

6.2.2. Oxygen Exposure

Second, we studied SCLSs after oxygen adsorption onto our CaF_2 and SrF_2 surfaces (possibly in the form of H_2O or OH); the source of oxygen was the residual gases present in the vacuum chamber. Changes in the surface features were accompanied by a gradual buildup of oxygen 1*s* photoemission intensity. This adsorption reaction is quite efficient, since a significant coverage may be observed after 10-20 hours in a cryopumped system at pressures of 8×10^{-11} Torr.

Off-axis spectra for Ca 2*p* immediately after growth, and after two weeks in the UHV chamber, are compared in Figure 6.10(a). (Two weeks was more than sufficient to observe the effect of oxidation, which could occur within a day of the original growth.) The

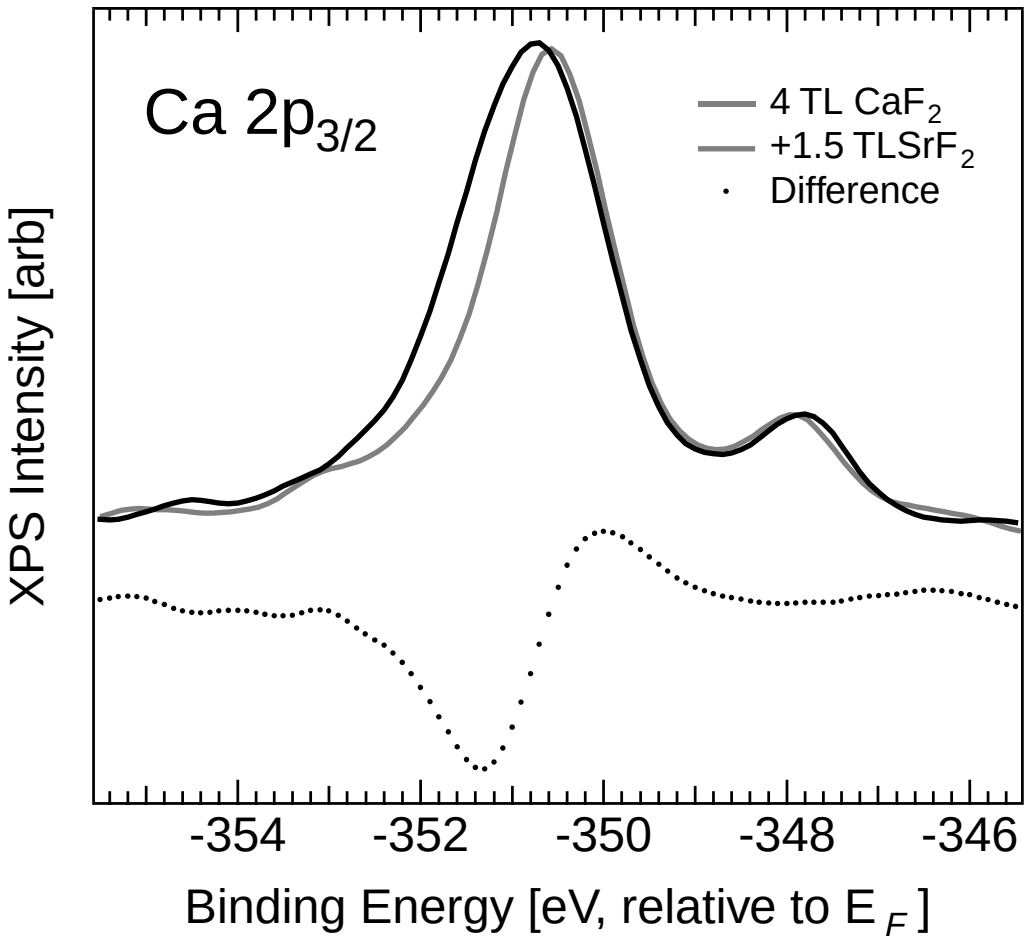

Figure 6.09. XPS results for SrF_2 on CaF_2 on Si(111) (5/4/92). Shown are Ca $2p_{3/2}$ spectra for an as-grown 4 TL CaF_2 film, after ~1.5 TL SrF_2 deposition and the difference spectrum. The difference spectrum shows the removal of surface Ca and the increase in the bulk Ca components.

corresponding F KVV spectra are presented in Figure 6.10(b). We observe a reduction of the surface Ca 2*p* and F KVV signals (evidenced by a dip in difference curves); simultaneously, both Ca 2*p* and F KVV spectra acquire broad chemically-shifted components *S'* (indicated by the arrows in Figure 6.10). For Ca 2*p*, the new component is distinctly seen between the bulk and interface peaks, but for F KVV, it overlaps with the I_2 component. The net intensity before and after oxygen adsorption in both cases is about the same, implying that the oxygen species adsorbs to the surface rather than reacting to replace surface fluorine atoms.

A similar effect was seen for SrF_2 on Si films; a Sr 3d spectrum is shown in Figure 6.10(c). We show a nominally 4 TL film obtained immediately after growth, and after one day of exposure to the residual gases. After exposure, a new component (indicated by the arrow) has replaced the surface peak. As will be discussed below, this film has an islanded morphology, where the interface peak is primarily due to an exposed Si-Sr-F layer in between ~6 TL thick SrF_2 islands. Because the interface peak appears unchanged after oxidation, we conclude that the SrF_2 surface is attacked by oxygen more readily than the Si-Sr-F layer, although for similarly islanded CaF_2 surfaces, the opposite seemed to hold.

6.2.3 Si on CaF_2 on Si(111)

Figure 6.11 compares the spectra before and after room-temperature deposition of Si on top of a 4 TL CaF_2/Si(111) film. Because of the complicated behaviour, it is not easy to interpret the difference curve (after-before $\mathcal{S}_{off}$) as was done in the previous two figures. Instead, we show $\mathcal{S}_{on}$, $\mathcal{S}_{off}$, and $\mathcal{S}_{on\text{-}off}$ for (a) before Si growth and (b) after Si growth. From the attenuation of the curves in (b), we can estimate that the Si thickness is ~3-4 bilayers (~11 Å). We will discuss two observations: (i) the removal of the surface peak, and (ii) the Fermi-level shifts. To interpret the data completely, we need to establish the detailed structure of the new, second CaF_2-Si interface, as well as to understand the crystallinity of the Si cap; both of these will be approached using the XPD technique in the future [Les94].

Removal of the surface peak. First, we can see that the before-growth spectra in

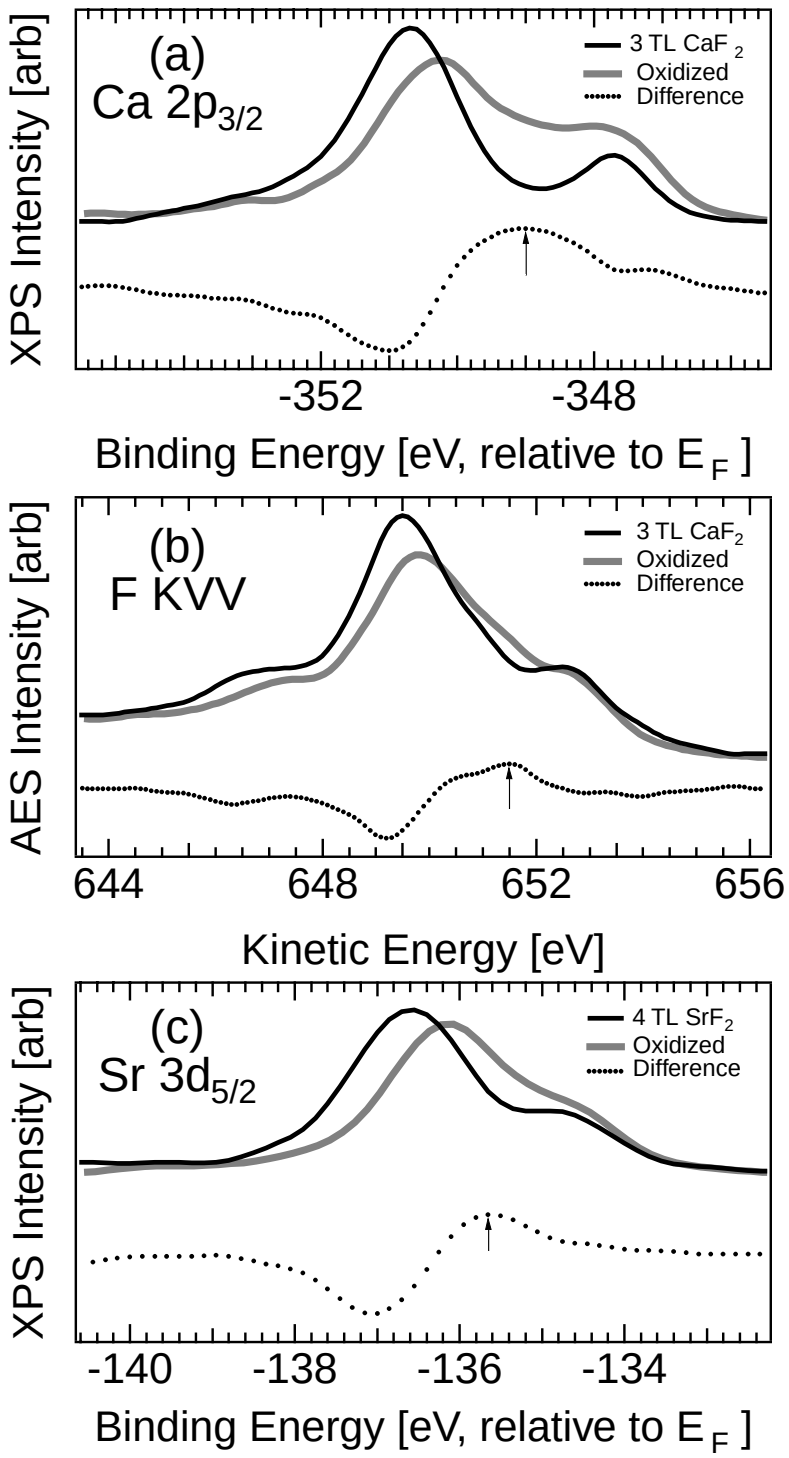

Figure 6.10. XPS results for clean and oxygenated CaF_2 (11/3/92) and SrF_2 (3/2/93) films. As-grown, after oxygen exposure, and the difference spectrum for (a) Ca $2p_{3/2}$, 3 TL film, (b) F KVV, 3 TL CaF_2 film, and (c) Sr $3d_{5/2}$, islanded film with 4 TL nominal deposition. The difference spectra show the removal of surface components and the appearance of new components indicated by the vertical arrows.

Figure 6.11(a) are very similar to Figure 6.01, which indicates the usual presence of a surface peak to higher binding energy than the bulk peak. After growth, however, the off- and on-axis bulk peaks are aligned. This shows that upon Si coverage, the Ca surface peak has been removed. Unlike the oxygenated surface, it is difficult to determine if any new peaks appear associated with the new interface; instead, diffuse intensity appears from ~0.5 to 4 eV to lower binding energy relative to bulk Ca, indicating several different interface Ca species present (Similar effects were also observed for F KVV spectra). This is not surprising since the second CaF_2-Si interface might not be very well ordered. This is consistent with the observation that the Si cap's forward-scattering modulation in the [111] direction is reduced compared to the bulk, suggesting that the cap was somewhat amorphous.

Fermi-level shifts. Comparing the two $\mathscr{S}_{on\text{-}off}$ in Figure 6.11, we observe that the interface peak has shifted ~0.20 eV to lower binding energy upon Si coverage; simultaneously, the bulk peak has shifted ~0.58 eV to lower binding energy. Of these shifts, the slight interface peak shift is less convincing since an apparent shift might be caused by creating new components at the second CaF_2/Si interface; also, transmission of the Ca 2p electrons through the Si layer creates an additional inelastic background which distorts the spectrum. However, the larger bulk Ca shift is significant, and indicates that the structure at the CaF_2/substrate interface has been altered. (Similar shifts were also seen for metal/CaF_2/Si [Xu89, Vos89] and Ge/CaF_2/Si [Olm90].) Large structural or chemical changes at one interface are unlikely to be due to the creation of a second interface several TLs away. Instead, a more likely explanation is due to the removal of some F atoms between the first interface Ca atom and the remaining bulk atoms [Olm90]. These defects would alter the dipole moment of the interface layer, and since photoemission measurements are referenced to the substrate Fermi level, this would alter the bulk/interface Ca splitting. One possible driving force for this defect formation is the strong electrostatic field across the film after deposition of the Si layer. This field is due to the combined dipole moments at the two CaF_2/Si interfaces, which

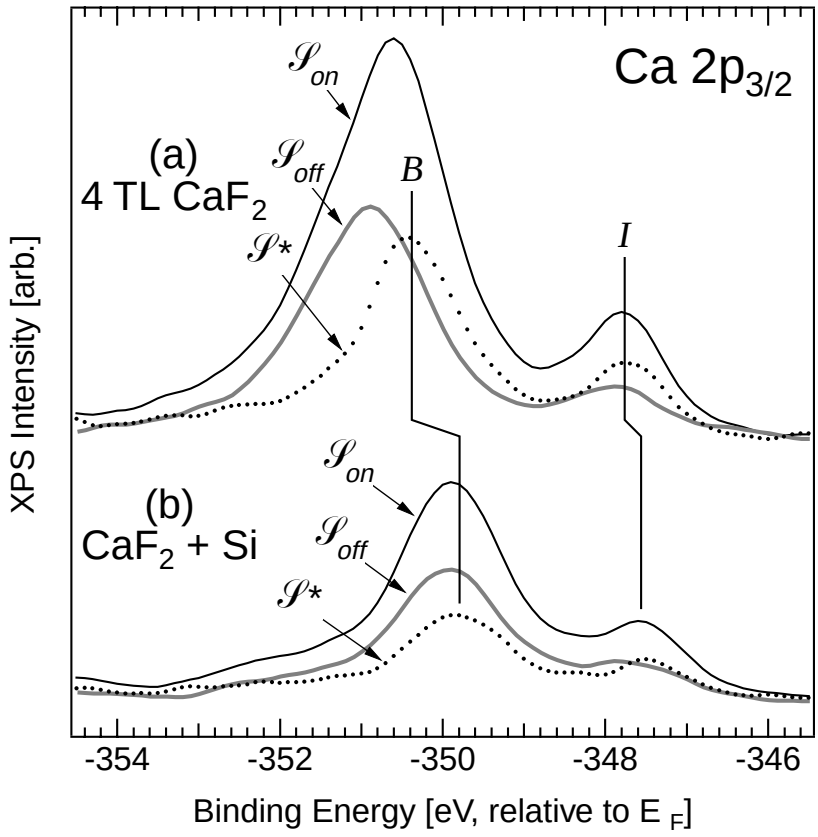

Figure 6.11. XPS results for a clean and Si-covered CaF2 film (7/2/93). $\mathcal{S}_{on}$, $\mathcal{S}_{off}$, and $\mathcal{S}_{on\text{-}off}$ Ca $2p_{3/2}$ spectra for (a) as-grown 4 TL CaF_2/Si(111) film and (b) after burial with ~4 bilayers of Si. The as-grown film shows indications of a surface peak, which has been removed after Si deposition.

induces a strong field across the film, of the order 5×10^6 V/cm (~0.6 V across ~13 Å of film). This field is strong enough to induce ionic conduction of F ions away from the interface, so that the entire field drop is across the interface layer instead of the entire film. This is plausible, since the threshold for ionic conduction in CaF_2 is ~1 eV [Rea77].

6.3 Buried *vs.* Exposed Interface CLSs

6.3.1 Islanded CaF_2

In Chapter 5, we discussed the unusual growth mode of CaF_2 on Si. We showed that growth proceeds by nucleation of 2 TL thick islands atop the reacted interface layer; these 2 TL islands merge to completely cover the solid, after which layer-by-layer growth begins. Before the islands completely cover the reacted interface, both buried and unburied ICLSs are present, and we have been able to measure the relative shifts. Additional mechanisms also lead to simultaneous buried and exposed interfaces: for lower flux rates, higher substrate temperatures, or higher substrate step densities, we observe that islanded growth atop the Si-Ca-F layer. For all of these conditions, we were able to distinguish CLSs from exposed and buried interface atoms, with similar results. The structures are very similar to the one illustrated in Figures C.01-02.

Figure 6.12(a) presents $\mathscr{S}_{on\text{-}off}$ and $\mathscr{S}^*$ spectra for Ca 2*p* in such an islanded layer. A nominally 2.5 TL CaF_2 film was deposited at the relatively slow growth rate of 5 Å/min. The resulting structure consisted of ~4 TL islands covering ~35% of the surface, as determined by XPD and XPS. Similar to the flat film (Figures 6.01-6.02), the $\mathscr{S}^*$ spectrum displays a surface signal *S*, but in contrast to the flat film, the $\mathscr{S}^*$ spectrum also displays a peak due to exposed interface Ca atoms I_0 in addition to the surface signal *S*. We determined the I_0/I splitting to be 0.2 ± 0.05 eV, which was an average value obtained for several films of similar morphology.

Figure 6.12(b, c) shows similar results for F KVV and F 1*s* atoms for the same film.

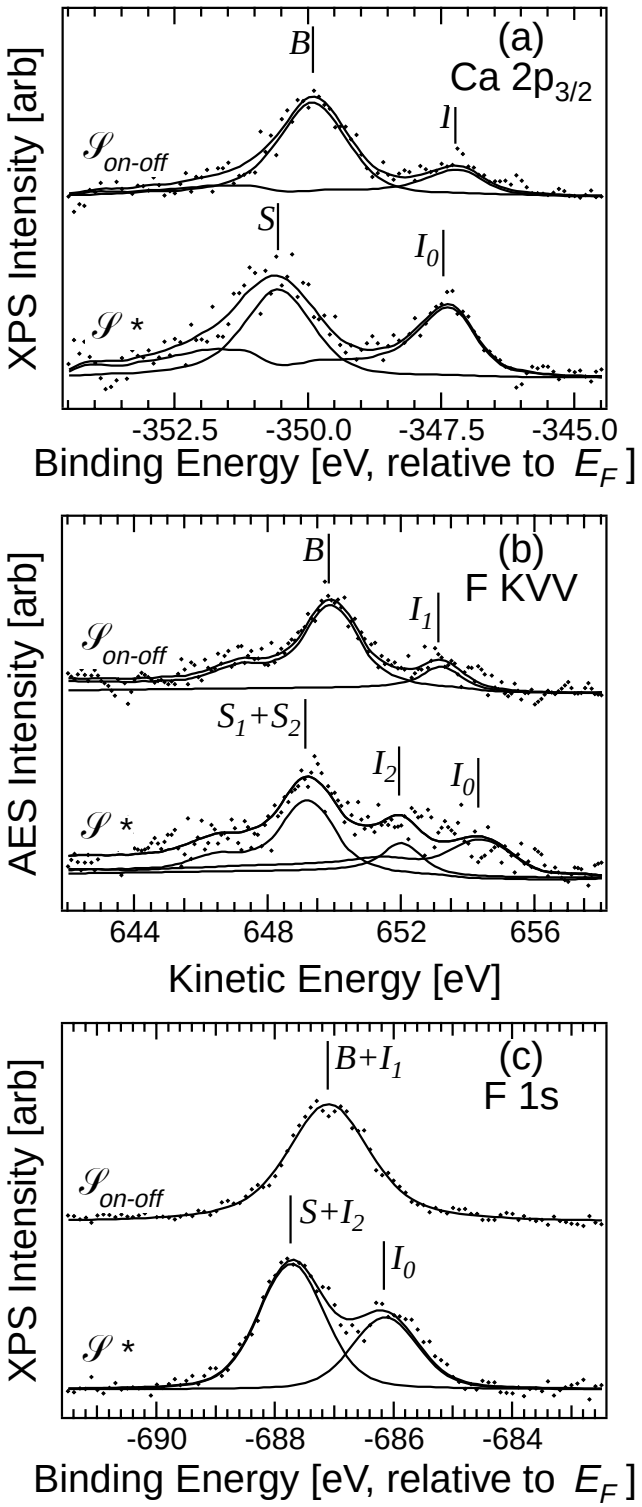

Figure 6.12. XPS spectra from a CaF_2 film (9/3/92) consisting of islands ~4 TL average height covering ~35% of the Si-Ca-F layer. Spectra $\mathscr{S}_{on\text{-}off}$ and $\mathscr{S}^*$ (sensitive to buried and exposed atoms, resp.) and fitted peaks are shown for (a) Ca $2p_{3/2}$, (b) F KVV, and (c) F 1*s*. The peak assignments correspond to the buried and exposed atomic sites illustrated in Figure C.02.

Both of these spectra also show new interface components I_0 corresponding to the uncovered interface F atoms. The I_0/I splittings were determined to be 0.84 ± 0.3 eV and 1.30 ± 0.25 eV for F KVV and F 1*s*, respectively (averaged over a variety of samples).

6.3.2 Islanded SrF_2

Similar surface and interface core-level shifts to those observed in CaF_2/Si films are also present in SrF_2/Si films. The extra-atomic contributions to these shifts depend strongly on the interatomic distances in the film. To investigate this dependence, we measured SCLSs in SrF_2 films on Si(111). While the chemical bond between SrF_2 and Si(111) is similar to that of CaF_2 and Si, the increased lattice constant creates strain in the films, so that strain should play the dominant role in any differences between CaF_2 and SrF_2 films.

Figure 6.13 shows the identification of surface, bulk, and interface Sr 3*d* and F KVV peaks (Figure 6.13(a) and (b), resp.). The film was grown under the same conditions as the 4 TL CaF_2 film (15 s, 52 Å/m, 700 °C). By combined the XPS/XPD, we determined the reacted Si-Sr-F layer to be covered ~50% by islands of average thickness ~6 TL.

The SCLSs were found to be 0.63 ± 0.04 eV (for Sr 3*d*) and 0.64 ± 0.08 eV (for F KVV). The peak assignments were confirmed using CR-XPD and also by surface oxidation. The measurement of the interface positions is difficult for this particular film, since the unburied interface peaks I_0 dominate the observed interface signal. This makes it difficult to measure splittings between buried and unburied interface components; therefore, the fits were performed with a single peak representing both buried and unburied atoms. Preliminary measurements, though, indicate very similar buried/exposed splittings as were obtained for CaF_2.

6.4 Discussion

To test the theory of CLSs, it is important to measure both Auger electron (AE) and photoelectron (PE) shifts, since these are linearly independent combinations of the initial and

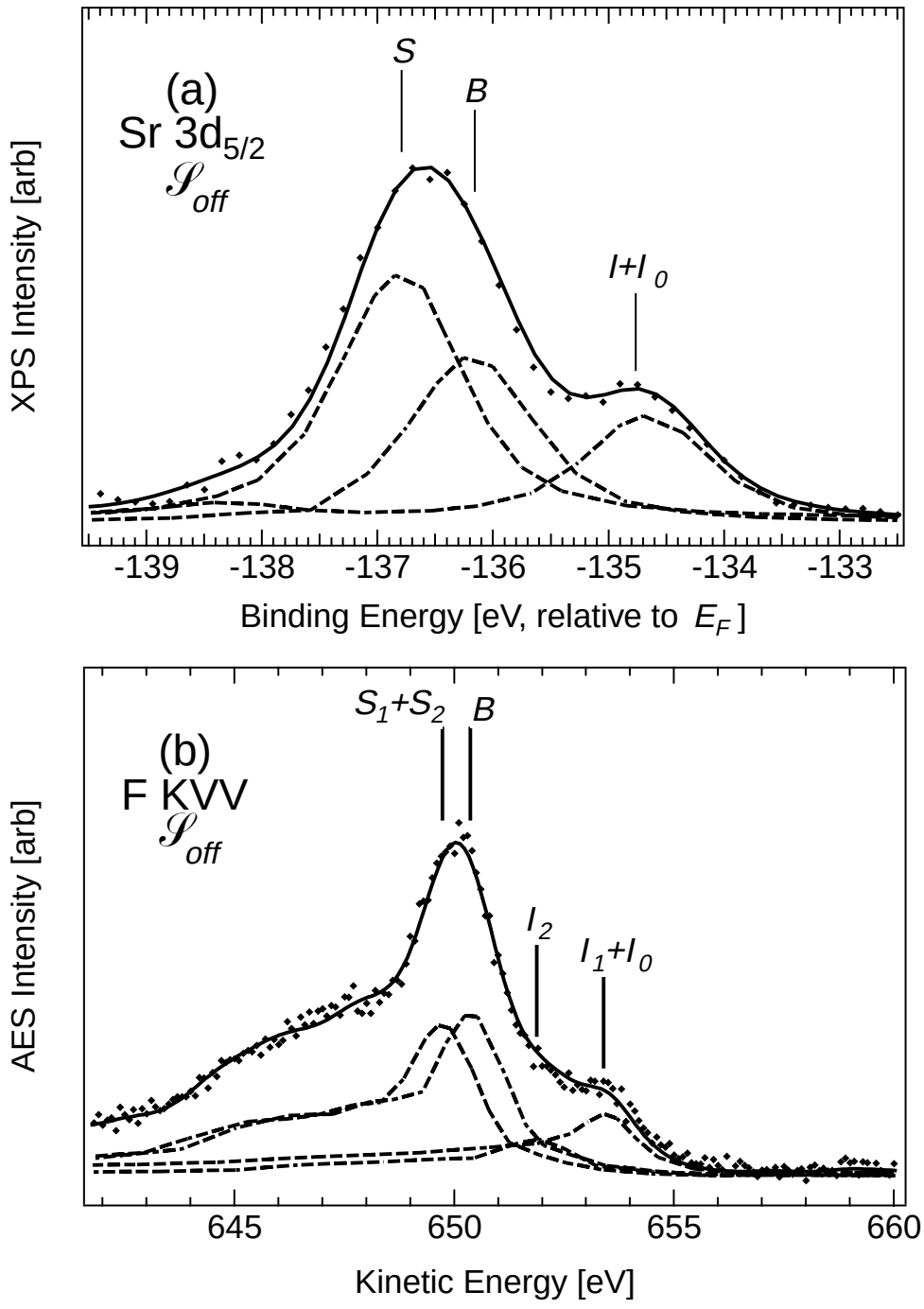

Figure 6.13. XPS spectra from a SrF_2 film (3/2/93) consisting of islands ~6 TL average height covering ~50% of the Si-Sr-F layer. Off-axis spectra $\mathscr{S}_{off}$ and curvefits for (a) Sr $3d_{5/2}$ showing surface S, bulk B, and interface I_0 and I components (see Figure C.02), and (b) F KVV showing surface S_1+S_2, bulk B, and interface I_2 and I_1+I_0 components.

final state effects (Chapter 2):

$$\Delta E_{\mathrm{PE}} = e\Delta\Phi_{\mathrm{M}} + \Delta R \tag{6.2a}$$

$$\Delta E_{\mathrm{AE}} = e\Delta\Phi_{\mathrm{M}} + 3\Delta R \tag{6.2b}$$

Therefore agreement between theory and experiment for both ΔE_{PE} and ΔE_{AE} implies agreement for both $\Delta\Phi_{\mathrm{M}}$ and ΔR. We have therefore acquired both Auger and photoelectron shifts wherever possible; in general good agreement between theory and experiment is obtained. In cases where theory disagrees with experiment, we use the measured CLSs, ΔE_{PE} and ΔE_{AE}, to invert (6.2a, b); this yields experimental measurements of ΔR and $e\Delta\Phi_{\mathrm{M}}$, which give insight into the nature of the observed shifts.

Throughout the following, theoretical and experimental CLSs are summarized in Tables 6.01 (CaF_2) and 6.02 (SrF_2). In order to compare theoretical values to experiment, the theory must be corrected to include the effect of finite electron escape depth [Chi86]. Because the bulk atoms in a film have slightly different relaxation energies, and because these atoms have different weights according to each's distance to the surface, the bulk theoretical relaxation energy becomes a weighted average over the bulk atoms in the film:

$$R_{bulk} \longrightarrow \sum_{i=1}^{N_b} R_i \exp(-z_i / \lambda) \Big/ \sum_{i=1}^{N_b} \exp(-z_i / \lambda) \tag{6.3}$$

where N_b is the number of bulk atoms, z_i and R_i are the position and calculated "bulk" relaxation energy of the ith atom, and λ is the electron escape depth, taken from Equation (4.4). Equation (6.3) leads to about a 10% reduction in the ΔR computed relative to that for an infinitely thick film.

6.4.1 CaF_2 CLSs

Experimental and theoretical CLSs for CaF_2 on Si(111) films are presented in Table 6.01. First we discuss the 8 TL film (10/2/92), which was sufficiently thick to neglect the substrate relaxation. The theoretical calculations are the same as the total shifts in Figure

Table 6.01. Summary of CaF_2 CLSs for various geometries. Experimental and theoretical values are reported in eV, where positive shifts correspond to higher binding energy (lower kinetic energy) than a reference peak. Theoretical calculations assumed $a_{||}$=1.

Geometry	Atom	Photoelectrons		Auger Electrons	
		Theory	Expt.	Theory	Expt.
8 TL Film	F (S_1)	-0.54	?	0.54	0.53 ± 0.1
	Ca (S)	0.64	0.63 ± 0.13	1.32	?
	F (S_2)	0.16	?	0.50	0.53 ± 0.1[a]
4 TL Film	F (S_1)[b]	-0.45	?	0.75	0.7 ± 0.2
	Ca (S)[b]	0.74	0.71 ± 0.09	1.61	1.2 ± 0.4
	F (S_2)[b]	0.20	?	0.63	0.7 ± 0.2[a]
	F (I_2)[b]	-0.33	?	-0.99	1.5 ± 0.5
	F (I_1)[b]	-0.98	?	-2.92	-3.04 ± 0.03
	Ca (I)[b]	-2.05	-2.65 ± 0.05	-6.78	-5.05 ± 0.5
3 TL Film	F (S_1)[b]	-0.46	?	0.71	0.51 ± 0.05
	Ca (S)[b]	0.75	0.63 ± 0.1	1.63	1.5 ± 0.5
	F (S_2)[b]	0.16	?	0.50	0.51 ± 0.05[a]
	F (I_2)[b]	-0.25	-0.35 ± .1	-0.75	-1.1 ± 0.3
	F (I_1)[b]	-0.92	-0.75 ± .1	-2.72	-2.74 ±0.04
	Ca (I)[b]	-1.96	-2.42 ± 0.05	-6.51	-4.3 ± 0.5
3 TL Film	F (S_1)[d]	···	-0.35 ± 0.35	···	-2.4 ± 0.1
+ Oxide	Ca (S)[d]	···	-2.0 ± 0.1	···	-3.9 ± 0.5
Islands	F (I_0)[e]	-0.55	-1.30 ± 0.2	0.54	-0.84 ± 0.3
w / Exposed	Ca (I_0)[e]	0.64	0.20 ± 0.05	1.32	≥ 0
Interface					

[a]Not resolved from S_1
[b]Shifts relative to remaining bulk atoms
[c]Data averaged over 4 samples
[d]Shifts relative to uncovered surface atoms
[e]Shifts relative to buried interface atoms

2.11, except that here the calculation was for a strained film with lattice constants ($a_{\|}$=1.000, $a_{\perp}$=1.012) relative to Si. Also, the bulk relaxation energies were corrected for the penetration depth using Equation (6.3). For the 8 TL film, only the Ca 2*p* and F KVV SCLSs are large enough (compared to the linewidths) to give quantitative measurements. The predicted shifts are in good agreement with experiment, including the prediction that the surface F KVV atoms S_1 and S_2 have approximately equal kinetic energies.

The 4 TL and 3 TL films are thin enough that the substrate must be included to account for all the CLSs. In the theoretical calculations, which are in reasonable agreement with the measured shifts, the Si substrate is treated as a continuous medium with dielectric constant ε_{sub}=11.7, and placed a distance d_i=0.8Å from the nucleus of the interface Ca atom. The interface Ca atom *I* has charge q_{Ca}=+2, the same as for the bulk Ca atoms. The interface Madelung shifts were assumed to be the same as at the surface, which was -0.013 eV for the interface F atom I_1, and only 0.31 eV for the interface Ca atom *I*. This assumes that there is a negatively charged layer between the Si and the Ca, a point which will be discussed further below.

We were able to observe reliable CLSs for Ca LMM Auger and Ca 2p electrons both at the surface and interface for the 3 and 4 TL films. At the surface, there is agreement with theory for both Ca shifts; therefore we can conclude that the initial state shift $e\Delta\Phi_M$ and final state shift ΔR for Ca are predicted correctly by our model. For F SCLSs, we could only get reliable measurements for the Auger electron splittings, so that we can only determine that the predicted total $\Delta E_{AE} = e\Delta\Phi_M + 3\Delta R$ is in agreement with experiment.

At the 3 and 4 TL interfaces, agreement between theory and experiment is acceptable, although greater deviations from theory are present for Ca atoms than for F atoms. The calculated extra-atomic contribution overestimates the Ca LMM shift, and underestimates the Ca 2*p* shift. The opposite sign of these discrepancies indicates that the intra-atomic corrections due to residual chemical shifts must involve corrections to both the initial and

final state; the discrepancies are small, however, so that the large interface core-level shift is determined primarily by screening from the Si substrate and only secondarily through residual chemical shifts.

We modelled the interface Ca as having an ionic charge q_{Ca}=+2, which is the same for all Ca atoms in the film. This is contrary to the expectation that since a F layer is absent from the interface, an extra electron is available to be bound to the interface Ca atom, reducing the Ca charge to q_{Ca}=+1. This is also contrary to the interpretation of near-edge x-ray absorption fine structure measurements by Himpsel *et al.* [Him86, Him91], who concluded that q_{Ca}=+1. On the other hand, theoretical calculations by Salehpour *et al.* [Sal91] show that 80% of the charge density of the extra electronic state is distributed over the first two substrate Si bilayers, which supports the assumption q_{Ca}=+2. Furthermore, our model rules out large departures of q_{Ca} from +2, which would create larger ICLSs than we observe for the F atoms I_1 and I_2, both from the altered Madelung potential near the interface, and from the altered polarizability of the Ca atom. Of these, the latter is most important. Upon going from the closed-shell configuration $3s^2 3p^6$ to $3s^2 3p^6 4s$, the Ca polarizability in the interface layer increases by approximately an order of magnitude. We estimate, then, that for each 0.1 electron added to Ca, the F KVV I_1 and I_2 electrons display an additional ICLSs of ~-1.4 eV and ~-0.7 eV, respectively. Even in the absence of all of the Si relaxation, a value of $q_{Ca} \approx +1.8$ is sufficient to account for the entire observed F KVV ICLSs. Placing the Si at a reasonable distance from the CaF_2 film forces $q_{Ca} \approx +2$.

For the oxidized 3 TL film, we were able to estimate the altered SCLSs before and after exposure to oxygen, which are presented for CaF_2 in Table 6.01. Eqs. (6.02a, b) may be inverted to yield ΔR and $e\Delta\Phi_M$ in terms of the measured values of ΔE_{AE} and ΔE_{PE}. Performing this inversion for the measurements in Table 6.01, we find that for surface F atoms, $\Delta R \approx$ -1 eV and $e\Delta\Phi_M \approx$ 0.7 eV. For surface Ca atoms, $\Delta R \approx$ -1 eV and $e\Delta\Phi_M \approx$ -0.7 eV. These shifts cannot be accounted for by simply covering the CaF_2 with a

dielectric layer, since the relaxation energies for F and Ca are so similar; any simple theory predicts large differences between F and Ca CLSs due to the proximity of F to the overlayer. Therefore, we conclude that there are significant chemical interactions between CaF_2 and the oxygen layer.

Finally, we compare the unburied to buried interface core levels by examining the relaxation and Madelung energies for a single CaF bilayer and for a bilayer buried under 3 TLs of CaF_2. For Ca 2*p*, the predicted shift between unburied (I_0) *vs.* buried (I_1) Ca atoms is the same as the SCLS between surface (*S*) and bulk (*B*) Ca atoms. Experimentally, we find a shift of the same direction, but of a much smaller magnitude (0.2 eV).

For F atoms, we expect that upon burying the interface layer, the 1*s* electron becomes more bound ($e\Delta\Phi_M > 0$) due to electrostatic interaction with the overlayers, while the 1*s* electron becomes less bound ($\Delta R < 0$) due to the additional polarization of the overlayers in the presence of the core hole. Using (6.02a, b), the predicted photoelectron and Auger shifts are

$$\begin{aligned}\Delta E_{\mathrm{F\ 1s}} &= e\Delta\Phi_M + \Delta R \\ &= -1.05 + 0.53 = -0.52\ \mathrm{eV}\ \ (\mathrm{theory})\end{aligned} \tag{6.4a}$$

$$\begin{aligned}\Delta E_{\mathrm{F\ KVV}} &= e\Delta\Phi_M + 3\Delta R \\ &= -1.05 + 1.59 = 0.54\ \mathrm{eV}\ \ (\mathrm{theory})\end{aligned}. \tag{6.4b}$$

From the experimental shifts $\Delta E_{\mathrm{F\ 1}s}$=-1.30 eV, $\Delta E_{\mathrm{F\ KVV}}$=-0.84 eV, we can invert Eqs. (1) and (2) to determine the experimental shifts $e\Delta\Phi_M$ = -1.5 ± 0.5 eV and ΔR = 0.23 ± 0.3 eV. Although the overall agreement with experiment is somewhat poor, the signs of the predicted shifts $e\Delta\Phi_M$ and ΔR are correct. We observed with XPD that the exposed interface Ca layer has the same XPD pattern as the surface Ca atom, except that the modulation strength is ~50% weaker for the former case. This observation, along with the observed sharpening of interface XPS peaks upon burial, suggests that the exposed interface layer has a significant disorder in the F atom position. This disorder in the exposed interface layer may account for

the deviation between experiment and theory.

6.4.2 SrF_2 CLSs

Table 6.02 summarizes the SCLSs measured for the islanded SrF_2 film, which we estimated to have islands of average thickness 6 TLs on the Si-Sr-F layer. The SCLSs are only sensitive to atoms within the islands, so that the measurements may be compared with the 8 TL CaF_2 results. Interestingly, the observed SCLSs for CaF_2 and SrF_2 are identical within the experimental uncertainties. As in the case of CaF_2, the SrF_2 F KVV shifts remain unresolved.

It is surprising that the measured SCLSs for SrF_2 and CaF_2 are so similar. The increased number of electrons on the Sr atoms should lead to greater polarizability and hence greater relaxation energies, altering the SCLSs. It is important, however, to consider the precise locations of the film atoms. For example, the increased distance between Sr and F atoms due to the larger lattice constant of SrF_2 compensates for the enhanced polarizability, while at the same time altering the Madelung potential. An additional difference between the CaF_2 and SrF_2 is the strain field due to mismatch between the film and substrate lattice constants, which will also affect the extra-atomic contributions. To explore these effects further, we considered the effect of tetragonal strain, or lattice distortion on the SCLSs.

Figure 6.14 shows the predicted CaF_2 and SrF_2 SCLSs (solid and dashed lines, resp.) as a function of the lateral lattice constant $a_{\|}$. The relaxation parts of the calculation have been corrected for the finite electron escape depth as discussed above. The normal lattice constants are constrained by (2.26). It is important to note that most of the dependence on $a_{\|}$ in the figure are due to variations in the Madelung potential; ΔR varies by at most 10% over the indicated range, while $\Delta\Phi_M$ can vary by 100% over the same range. The most consistent value of the lateral lattice constant with our SrF_2 data is $a_{\|}\approx 1.08$, for which (i) the predicted Sr 3d shift agrees with the experimental measurement, and (ii) the F KVV shifts are both equal, although the predicted shift is somewhat smaller than the observed SCLS. For CaF_2,

Geometry	Atom	Photoelectrons		Auger Electrons	
		Theory	Expt.	Theory	Expt.
Islands	F (S_1)	-0.58	?	0.45	0.64 ± 0.08
w/Exposed	Sr (S)	0.64	0.63 ± 0.08	...	...
Interface	F (S_2)	0.14	?	0.46	0.64 ± 0.08[a]

[a] Not resolved from S_1

Table 6.02. Summary of SrF_2 SCLSs. Experimental and theoretical (parentheses) values are reported in eV, where positive shifts correspond to higher binding energy (lower kinetic energy) than a reference peak. Theoretical calculations assumed $a_{\|}$=1.08.

on the other hand, the theoretical SCLSs do not vary much over the relatively limited range of allowed lattice constants, so that we cannot easily distinguish the lateral lattice constant from the SCLSs.

The film strain may be measured independently. We observed with LEED that all SrF_2 films thicker than ~1 layer are relaxed to $a_{||} \approx 1.08$, which is in agreement with our interpretation above. This indicates that the films are under tensile strain, consistent with our earlier study with LEED and X-ray standing wave fluorescence [Den91] as well as with ion channelling measurements [Li92]. This means that the growth temperature mismatch is retained after cooling to room temperature; interfacial defects prevent the relaxation of overlayer atoms from $a_{||} \sim 1.08$ to $a_{||} \sim 1.068$ [Has85]. The theoretical SCLSs for $a_{||}=1.08$ from Figure 6.14 have therefore been placed in Table 6.02.

For CaF_2, on the other hand, we had assumed pseudomorphic growth ($a_{||} = 1$) in Table 6.01 (compressive strain), which is supported by the absence of additional LEED spots as for SrF_2, by x-ray scattering results [Won93, Luc92] on similar films showing $a_{\perp}=1.013$ (so that from Eq, (13) $a_{||} =1$) and by plan-view transmission electron microscopy studies, which show no Moiré fringes at these thicknesses [Hes94, Won93].

6.5 Summary and Conclusions

The relationship between atomic structure and core level spectroscopy was examined for thin ionic insulator films of CaF_2 and SrF_2 on Si(111) by measuring surface core level shifts and comparing to an electrostatic model where all the observed shifts are due to geometric, or extra-atomic effects. The assignment of the surface peaks was confirmed with x-ray photoelectron diffraction and also by surface modification by oxidation and by Si or SrF_2 deposition. In our model, the two principal effects are the electrostatic Madelung potential at and the polarization response of the insulator to the core hole. We found that this model is adequate to describe the observed surface shifts without resorting to intra-atomic or chemical shifts at the surface. We also found that even at the interfaces between the insulators

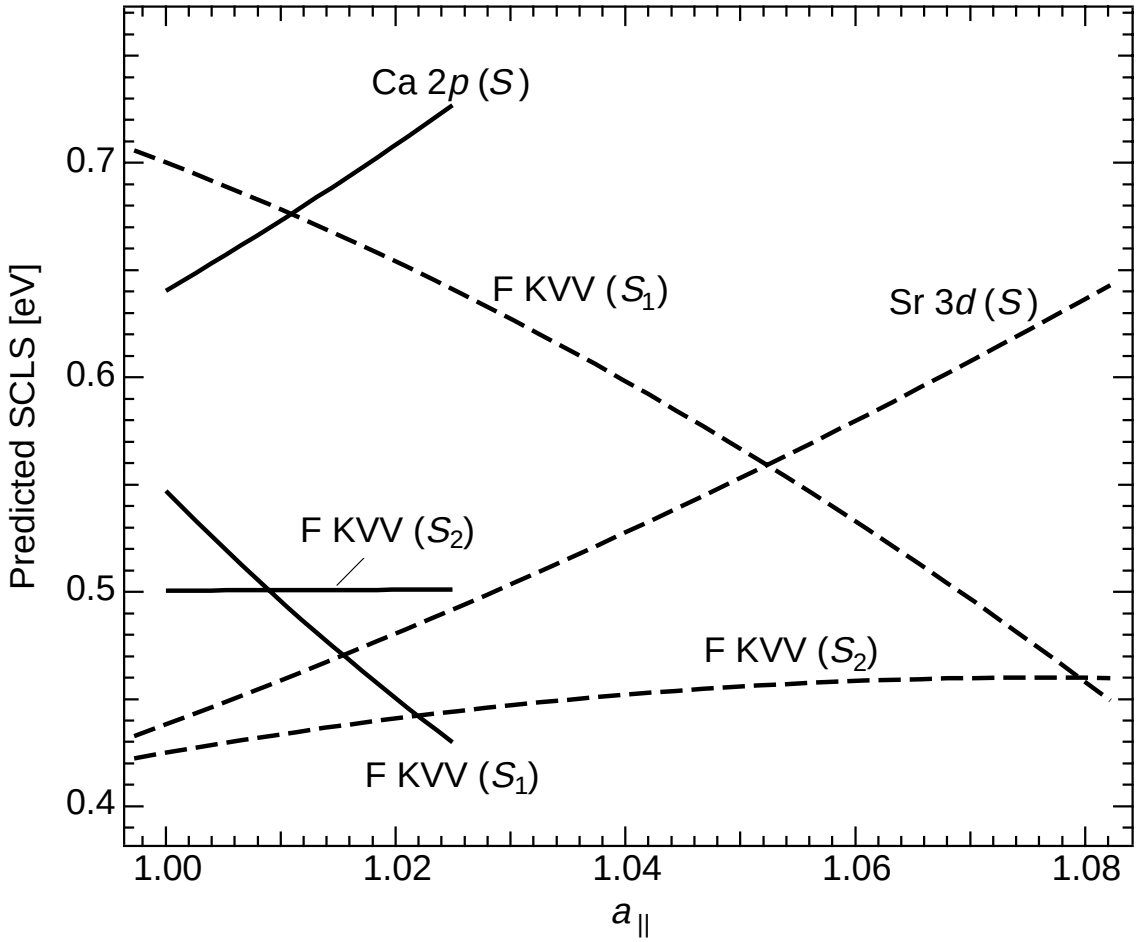

Figure 6.14. Predicted CaF_2 (solid) and SrF_2 (dashed) surface core-level shifts for strained films, corrected for finite escape depth. Shifts are calculated as a function of $a_{\|}$, the lateral lattice constant relative to the Si substrate. The normal lattice constant $a_{\perp}$ is constrained as described in the text.

and substrate, where strong chemical interactions are expected to occur, that the model accounts for most of the observed shift. This is because the electronic interface state is distributed through the upper Silicon layers, where they may be easily incorporated into a continuum dielectric layer. These results illustrate the relative importance of the relaxation response in modelling the core-level shifts in ionic insulators.

We also included strain due to mismatch between film and substrate lattice constants into our calculation. Within our model, we were able to show that the SrF_2 films' lateral lattice constant is greater than the natural lattice constant of the SrF_2 crystal, a result which is consistent with our LEED measurements.

Appendix A

Tetragonal Distortion of Cubic Crystal Overlayers

In this appendix, we consider the strain response of a cubic crystal to a homogenous planar stress field. Such a stress field occurs when a thin film of a cubic material like CaF_2 or SrF_2 is commensurate with a lattice-mismatched substrate. It is assumed that the substrate thickness >> overlayer thickness so that the stress of the overlayer on the substrate causes negligible substrate deformation. Figure A.01 illustrates the situation for a film under compressive stress. In (a) the overlayer and substrate are not in contact so that both lattices are cubic; the overlayer has lattice constant *a*. When the film is bonded to the substrate, the lateral and perpendicular lattice constants have been altered to

$$a_{\parallel}=(1+\varepsilon_{xx})a \tag{1a}$$

$$a_{\perp}=(1+\varepsilon_{zz})a \tag{1b}$$

where ε_{xx} and ε_{zz} are elements of the strain tensor to be defined below. We know that $a_{\parallel}$ is given by the lattice mismatch of the materials; we seek the relationship between $a_{\perp}$ and $a_{\parallel}$.

We start with the classic treatment by Landau and Lifshitz [Lan86]. For a material with strain field **u** (defined such that the distances d**x** and d**x**' between two points in the material before and after stress is applied are related by d**x**'=d**x**+d**u**), we define the symmetrical strain tensor (to lowest order) as:

$$\varepsilon_{ik} \equiv \frac{1}{2}\left(\frac{\partial u_i}{\partial x_k} + \frac{\partial u_k}{\partial x_i} \right) \tag{2}$$

The microscopic forces within a material are assumed to act locally, i.e. that the net force on any volume element is given by the force on the surface of the volume element. The force **F** applied to a surface element d**s** is given as

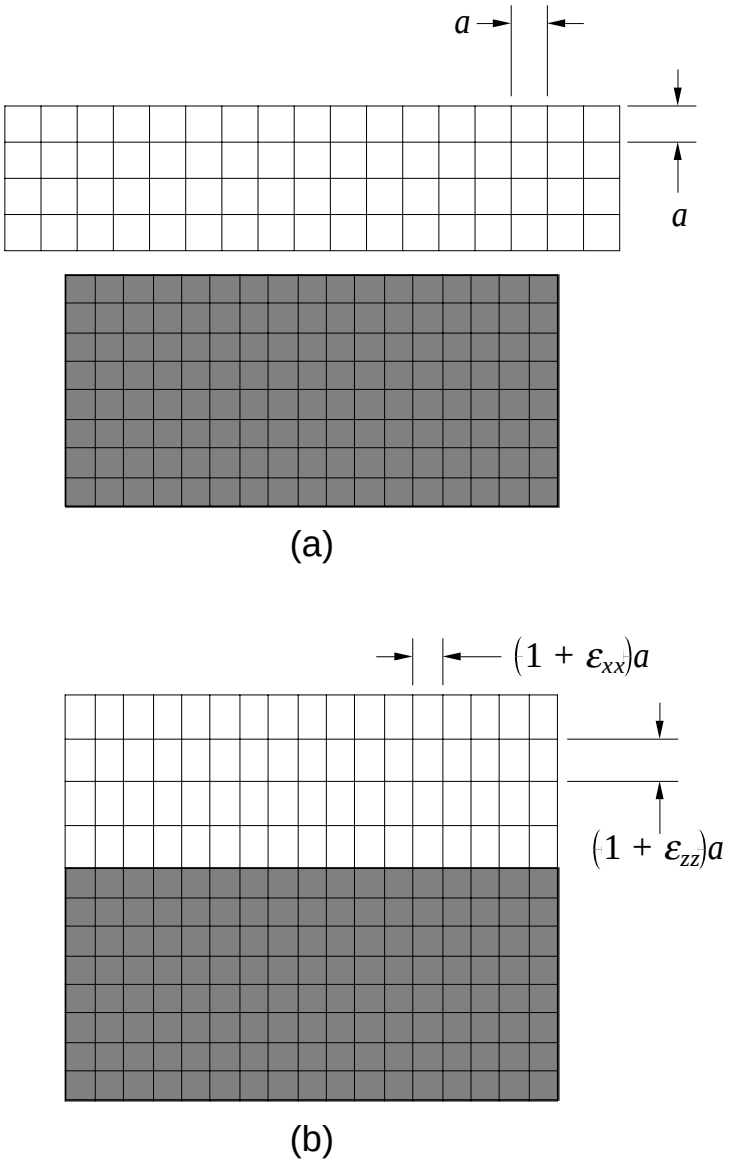

Figure A.01. Example of tetragonal strain in epitaxial systems. (a) a free film, lattice mismatched to the substrate, has cubic lattice constant a. (b) the commensurate film under compressive strain ε_{xx} undergoes an expansion ε_{zz} in the *z*-direction.

$$F_i = \sigma_{ik} ds_k \tag{3}$$

where σ_{ik} are elements of the stress tensor.

From thermodynamics, the change in free energy of a medium is given by

$$d\mathcal{F} = -SdT + pdV. \tag{4a}$$

The analogous equation in terms of the stress and strain tensors is

$$d\mathcal{F} = -SdT + \sigma_{ik} d\varepsilon_{ik} \tag{4b}$$

so that the stress and strain tensors are related through

$$\sigma_{ik} = \left(\frac{\partial F}{\partial \varepsilon_{ik}} \right)_T . \tag{5}$$

The general form for the free energy in an anisotropic solid (written within the summation rule for indices) is

$$F = \tfrac{1}{2} C_{iklm} \varepsilon_{ik} \varepsilon_{lm} \tag{6}$$

where the fourth-rank tensor C_{iklm} is called the *elastic modulus tensor*. The number of independent elements in this tensor is at most 21; this is a result of the symmetry of the strain tensor ($\varepsilon_{ik} = \varepsilon_{ki}$) such that $C_{iklm} = C_{kilm}$ etc. The number of independent elements may further be reduced for cubic crystals by considering the additional symmetries present: the three 4-fold axes in O_h-class lattices, or the four 3-fold axes in T- or T_d-class lattices. In either case, the free energy Eq. (6) reduces to

$$\begin{aligned} F = {} & \frac{1}{2} C_{11} (\varepsilon_{xx}^2 + \varepsilon_{yy}^2 + \varepsilon_{zz}^2) + C_{12} (\varepsilon_{xx}\varepsilon_{yy} + \varepsilon_{xx}\varepsilon_{zz} + \varepsilon_{yy}\varepsilon_{zz}) \\ & + 2C_{44} (\varepsilon_{xy}^2 + \varepsilon_{yz}^2 + \varepsilon_{yz}^2) \end{aligned} \tag{7}$$

where $C_{11} \equiv C_{xxxx}$, , $C_{12} \equiv C_{xxyy}$ and $C_{44} \equiv C_{xyxy}$.

We now apply these equations to find the relation between the stress tensor elements ε_{xx} and ε_{zz}. For films grown in the [001] direction, the stress tensor retains only diagonal elements; from Eqs. (5) and (7) we see that the strain tensor is also diagonal, so that these equations reduce to the matrix equation,

$$\vec{\sigma} = \begin{pmatrix} \sigma_{xx} \\ \sigma_{yy} \\ \sigma_{zz} \end{pmatrix} = \begin{pmatrix} C_{11} & C_{12} & C_{12} \\ C_{12} & C_{11} & C_{12} \\ C_{12} & C_{12} & C_{11} \end{pmatrix} \begin{pmatrix} \varepsilon_{xx} \\ \varepsilon_{yy} \\ \varepsilon_{zz} \end{pmatrix}. \tag{8}$$

For the case under consideration, uniform tensile or compressive stress in the *x*-*y* plane results in strain in the *z*-direction. In this case, we consider $\vec{\sigma}$=(1, 1, 0). The solution of Eq. (8) for the strain is then

$$\begin{aligned} \varepsilon_{zz} &= -A\varepsilon_{xx} \\ A &= 2C_{12} / C_{11} \end{aligned}. \tag{9}$$

Another important situation which may be analyzed is the inverse case: pressure is applied in the *z*-direction and we wish to know how much strain results in the *x*-*y* plane. With $\vec{\sigma}$=(0, 0, 1), the solution to Eq. (8) becomes,

$$\begin{aligned} \varepsilon_{xx} &= -\nu\varepsilon_{zz} \\ \nu &= C_{12} / (C_{11} + C_{12}) \end{aligned}, \tag{10}$$

where ν is called the *Poisson ratio* of the material. Comparison of Eqs. (9) and (10) shows that A and ν are related through

$$A = 2\nu / (1 - \nu). \tag{11}$$

For crystal growth in the [111] direction, the stress and strain tensors will also be diagonal; however the elastic modulus tensor is tabulated only for the (*x*, *y*, *z*) basis. Therefore Eq. (7) must be transformed into the rotated basis (*x*', *y*', *z*'):

$$\begin{aligned} \hat{x}' &= (\hat{x} - \hat{y}) / \sqrt{2} \\ \hat{y}' &= \left(\frac{\hat{x}}{\sqrt{6}} + \frac{\hat{y}}{\sqrt{6}} - \hat{z}\sqrt{\frac{2}{3}} \right). \\ \hat{z}' &= (\hat{x} + \hat{y} + \hat{z}) / \sqrt{3} \end{aligned} \tag{12}$$

These vectors are assembled into the similarity transform P such that

$$\varepsilon = P\varepsilon' P^{-1}$$
$$= \frac{1}{6}\begin{pmatrix} 3\varepsilon'_{xx}+\varepsilon'_{yy}+2\varepsilon'_{zz} & -3\varepsilon'_{xx}+\varepsilon'_{yy}+2\varepsilon'_{zz} & 2(-\varepsilon'_{yy}+\varepsilon'_{zz}) \\ -3\varepsilon'_{xx}+\varepsilon'_{yy}+2\varepsilon'_{zz} & 3\varepsilon'_{xx}+\varepsilon'_{yy}+2\varepsilon'_{zz} & 2(-\varepsilon'_{yy}+\varepsilon'_{zz}) \\ 2(-\varepsilon'_{yy}+\varepsilon'_{zz}) & 2(-\varepsilon'_{yy}+\varepsilon'_{zz}) & 4\varepsilon'_{yy}+2\varepsilon'_{zz} \end{pmatrix} \tag{13}$$

After substituting into Eq. (7), we apply $\sigma'_{ik} = (\partial F / \partial \varepsilon'_{ik})_T$. This yields the system of equations

$$\vec{\sigma}' = \begin{pmatrix} \sigma'_{xx} \\ \sigma'_{yy} \\ \sigma'_{zz} \end{pmatrix}$$
$$= \begin{pmatrix} \frac{C_{11}+C_{12}+2C_{44}}{2} & \frac{C_{11}+5C_{12}-2C_{44}}{6} & \frac{C_{11}+2C_{12}-2C_{44}}{3} \\ \frac{C_{11}+5C_{12}-2C_{44}}{6} & \frac{C_{11}+C_{12}+2C_{44}}{2} & \frac{C_{11}+2C_{12}-2C_{44}}{3} \\ \frac{C_{11}+2C_{12}-2C_{44}}{3} & \frac{C_{11}+2C_{12}-2C_{44}}{3} & \frac{C_{11}+2C_{12}+4C_{44}}{3} \end{pmatrix} \begin{pmatrix} \varepsilon'_{xx} \\ \varepsilon'_{yy} \\ \varepsilon'_{zz} \end{pmatrix}. \tag{14}$$

For the case of uniform stress in the *x*-*y* plane, $\vec{\sigma}'$=(1, 1, 0), we find

$$\varepsilon'_{zz} = -A\varepsilon'_{xx}$$
$$A = 2(C_{11}+2C_{12}-2C_{44}) / (C_{11}+2C_{12}+4C_{44}). \tag{15}$$

For stress applied in the z'=[111]-direction, we find

$$\varepsilon'_{xx} = -\nu\varepsilon'_{zz}$$
$$\nu = (C_{11}+2C_{12}-2C_{44}) / 2(C_{11}+2C_{12}+C_{44}). \tag{16}$$

We verify that Eq. (11) holds for films grown in the [111] direction as well as in the [001] direction.

Table A.01 summarizes experimental values for the elastic modulus tensor and the resulting parameters ν and A for Si, CaF_2 and SrF_2. The parameters were taken from the literature [Hel66, Ho67]. One can see by comparing the values for the [111] and [001] directions that the crystals are quite anisotropic.

Table A.01. Elastic modulus parameters and resulting elastic coefficients for the [001] and [111] directions in Si, CaF_2, and SrF_2.

	Coefficients, 10^{11} dyn/cm^2		
	C_{11}	C_{12}	C_{44}
Si	16.6	6.4	7.96
CaF_2	16.4	4.7	3.39
SrF_2	12.35	4.3	3.13

	Poisson Ratio		"*A*" Coefficient	
	[001]	[111]	[001]	[111]
Si	0.278	0.180	0.771	0.440
CaF_2	0.223	0.326	0.573	0.966
SrF_2	0.258	0.305	0.696	0.878

Appendix B

Satellite Emission Features in Core-Level Spectra of Interface Atoms

B.0 Introduction

Complete fitting of core-level spectra requires an understanding of the peaks' lineshapes, as discussed in Chapter 3. We found that the core-level emission peaks of Ca and Sr atoms bonded to Si at the CaF_2 or SrF_2 on Si(111) interface had neighboring satellite peaks which differed from those of bulk atoms; these satellites impacted the curve-fits of spectra of films that had both bulk and interface atoms. An example of this is given in Figure B.01. This curve shows the Ca $2p_{3/2}$ difference spectrum $\mathcal{S}_{\text{on-off}}$ for a 3 layer film (see diagram) where the surface Ca signal has been subtracted off as discussed in §5.1. The lineshapes and the spin-orbit deconvolution used in the fit were the same ones discussed in Chapter 4. The peak labelled "interface" clearly has incorporated in it a strong satellite feature shifted approximately 4.5 eV to higher binding energy, and we seek to explain the existence of this peak. In this appendix, various possible explanations for this and similar satellite peaks are proposed; we then compare and contrast these alternative models.

In §4.1.6, we introduced the concept of intrinsic *vs.* extrinsic electron energy losses in connection with inelastic loss tails, and how their identification may be used to gain information on the electronic properties of materials. The same intrinsic/extrinsic concept also applies to understanding satellite peaks. Intrinsic loss peaks give very local information on the electronic states near a core hole, while extrinsic loss peaks give more information on the bulk electronic states. In this Appendix, we offer competing intrinsic/extrinsic models for the Ca and Sr satellites, and derive experimental properties of the solids within these models.

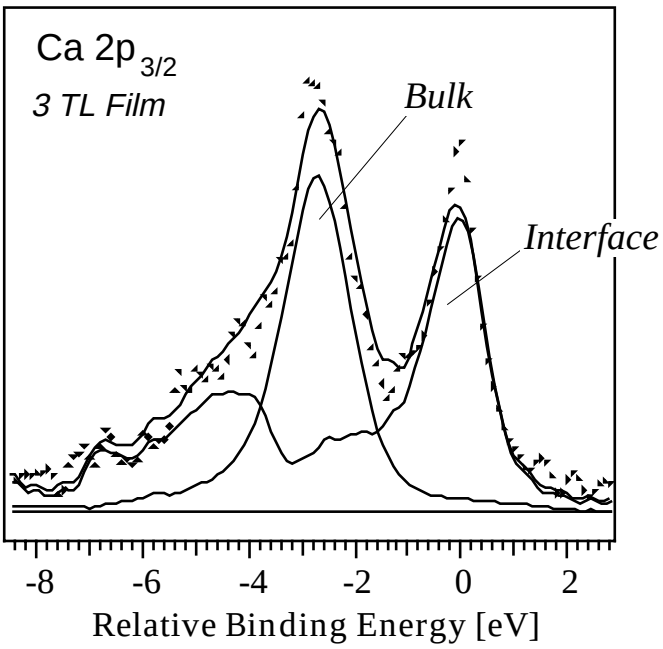

Figure B.01. Interface Ca $2p_{3/2}$ satellite in a three layer CaF_2/Si(111) film (11/3/92), where the surface Ca signal has been subtracted. See Figure C.02 for our working model for the interface structure.

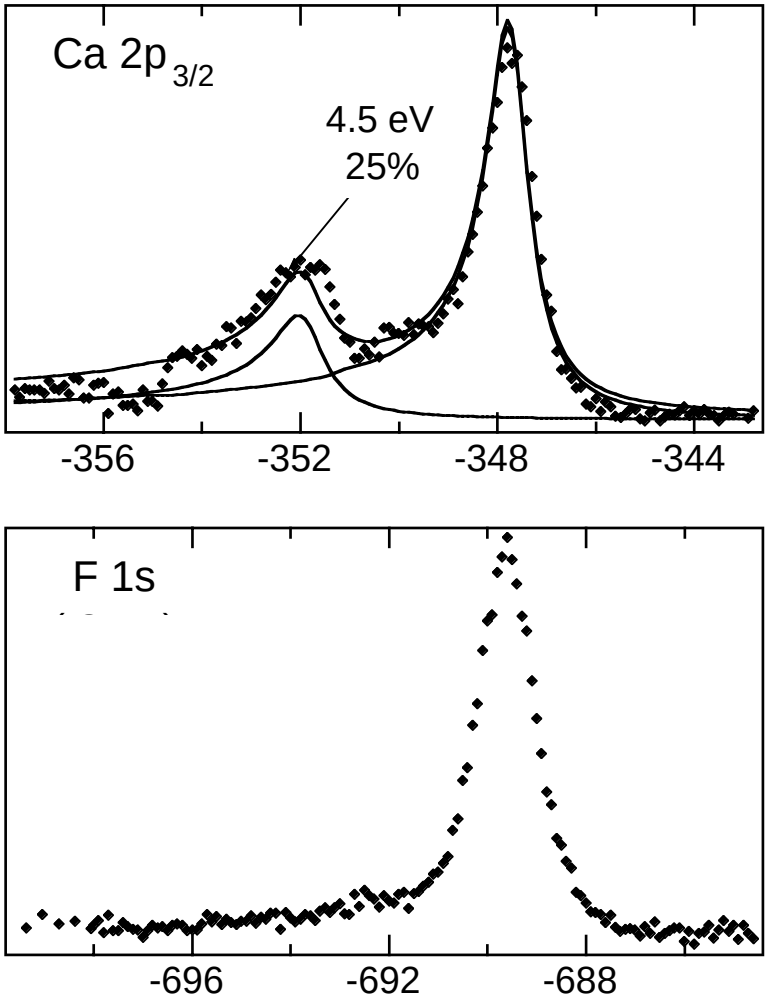

Figure B.02. Comparison of ML Ca and F spectra in the inelastic loss region (10/2/91). Only the Ca 2p spectrum displays the large inelastic loss feature.

B.1 Data

To investigate the interface electronic structure, we grew single-layer films of CaF_2 and SrF_2 on Si(111) at 650 to 700°C. Because of the chemical reaction during growth, these films consisted of reacted F-Ca-Si or F-Sr-Si layers. This structure is known from prior work [Rie86, Olm87, Zeg90, Den91] and it is also evidenced by XPD studies in this thesis.

In Figure B.02 we show Ca $2p_{3/2}$ and F 1*s* core-level XPS spectra in such films. (Spin-orbit deconvolution parameters for this Appendix are tabulated in Table 4.01.) Clearly the Ca 2*p* spectrum shows a large satellite, while the F 1*s* does not. Furthermore, the substrate Si 2*p* peak also does not show the satellite, either with Mg K_α x-rays ($h\nu$=1254 eV), or with soft x-rays from a synchrotron ($h\nu$=135 eV). This suggests that the satellite is intrinsic to the Ca atom; the excitation represented by the satellite is locally created near the core-hole and cannot be excited by electrons passing through the interface layer. Another observation is that the spin-orbit splitting for the satellite peak appears to be slightly larger (a few tenths of an eV) than the splitting for the main peak. This is manifested as a slight "kink" on the high-binding energy tail of the satellite peak, which is an artifact of the deconvolution algorithm when the main and satellite peaks have slightly different spin-orbit splittings. Finally, we observe that the Ca 2*p* peaks have a metallic-like asymmetry to them, which is demonstrated by the curvefits to the data. We have used the Doniach-Sunjic lineshape, which accounts for the many-electron interaction between free electrons and the core hole in metal XPS spectra [Don70].

Figure B.03 shows Sr 3*p*, 3*d*, 4*p* and F 1*s* core level spectra for a single Sr-F bilayer on Si(111). [The film from which the Sr 4*p* was acquired was slightly thicker and had partially formed a F-Sr-F triple layer atop the interface layer; the spectrum was acquired with synchrotron radiation at SSRL]. The Sr core levels were spin-orbit deconvolved according to the parameters in Table 4.01. In the Sr 3*p* and Sr 3*d* spectra, the satellite is present, but it is absent in the Sr 4*p* spectrum; the F 1*s* again shows no such satellite. The small shoulder on

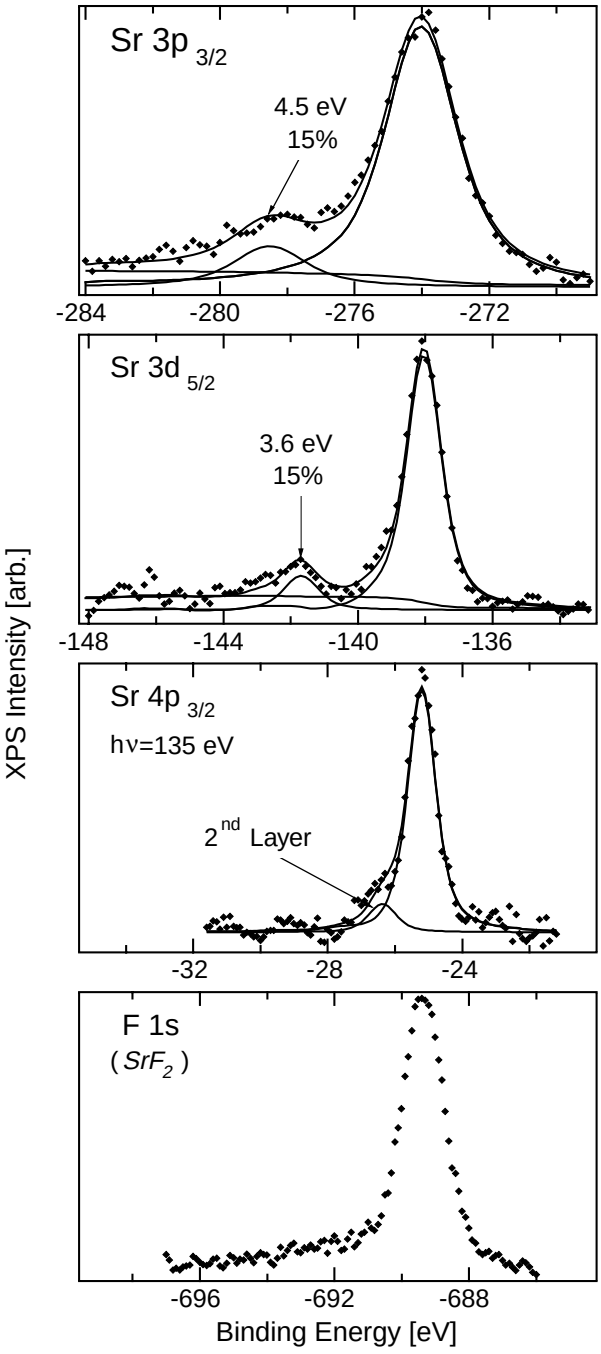

Figure B.03. Comparison of ML Sr and F spectra in the inelastic loss region. Only the Sr 3p and Sr 3p spectra display the inelastic loss feature. All data are from sample 10/3/92 except the Sr 4p data from sample 7/14/91.

the Sr 4*p* is attributed to the second-layer emission, although it cannot be ruled out that there is a small satellite component as well. The metallic character to the core-level lineshape that was present in CaF_2 on Si(111) is also apparent in the SrF_2 on Si(111) spectra. Here the metallic tails are represented as a step-like background proportional to the integral of the peaks.

The above results establish the existence of an intrinsic satellite excitation localized to the Ca or Sr core hole. We next consider three different models which might explain the observed peaks.

B.2 Molecular-Orbital Model

Figure B.04 summarizes the electronic states in the CaF_2 on Si(111) system. Bulk CaF_2 has a large (~12 eV) band-gap with a F 2*p*-derived valence band, and a Ca 4*s*/3*d*-derived conduction band [Hea80, Eva89]. Formation of the solid is through ionic bonds in which the two Ca 4*s* electrons are transferred to each of the two F atoms in the CaF_2 molecule. At the interface, there is a missing F atom, so that an extra electron, which would have been transferred to it, is available for covalent bonding with Si. Theoretical [Nat88, Fuj89, Sal91, Oss91] and experimental [Avo89, Hei89, Mcl89, Bou92] work has shown that this electron and the extra Si dangling bond orbitals form a bonding/anti-bonding pair state, with a bandgap of ~2.4 eV.

Figure B.05 is an energy level diagram of this bonding state in a molecular picture, and shows what happens in the absence or presence of a Ca 2*p* core hole. Our model is based on that of de Boer *et al.* [Deb84], and has been used successfully to model satellites of bulk transition metal compounds. The bonding state is comprised by the interaction of the Si 3*p* dangling bond and the Ca 4*s*/3*d* occupied state. The energy of the Ca state relative to the Si state is given by the parameter *A*. The Hamiltonian describing the mixture of the two states is

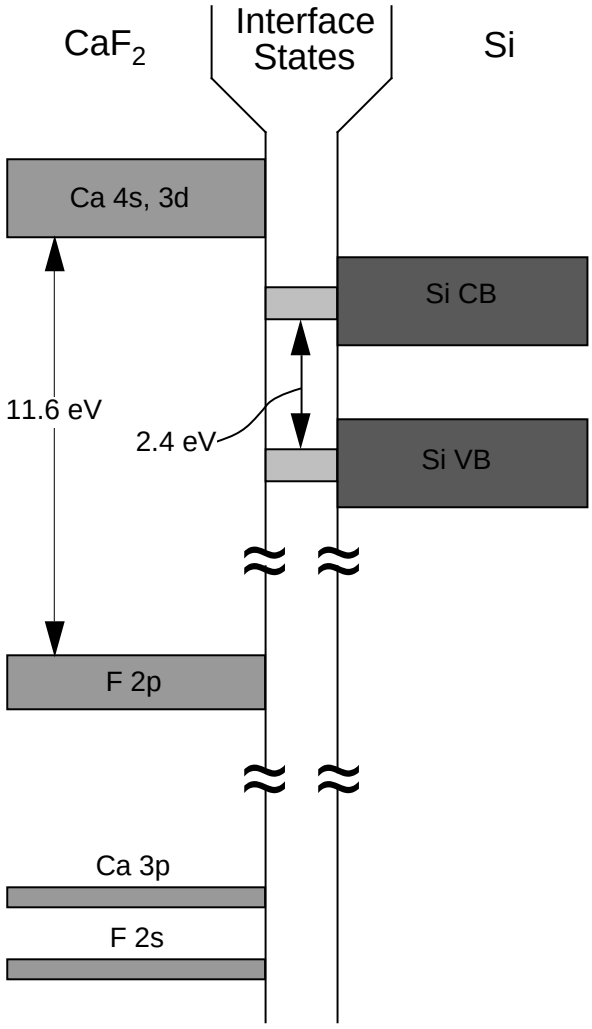

Figure B.04. Schematic energy level diagram for CaF_2 on Si(111).

$$H = \begin{pmatrix} A & T \\ T & 0 \end{pmatrix}, \tag{B.1}$$

where T is the interaction energy of the two states and the basis states are the unperturbed Ca 4*s*/3*d* and Si 3p states. The zero of energy is defined at the Si dangling bond level.

For the unperturbed bond, simple arguments relate T and A to the bonding/anti-bonding "gap" E_G. First, we argue that $A \approx 0$. When the fluoride and the Si are in contact (but without interaction) then each of the two surface states are metallic, since each of the surface unit cells has an odd number (1) of electrons per unit cell. Therefore the Fermi levels, which are pinned to these non-interacting surface states, will be aligned via charge movement, a fact that will not change when the chemical interaction takes place. But we don't assume $A=0$, calculate it from our data below and examine the consequences. It would be an unphysical model if our data was outside the range $0<|A|<E_G$; our interpretation shows that |A| is reasonably small within the molecular model . Solution of the eigenvalue problem $H\Psi=E\Psi$ yields the following energies of the bonding and anti-bonding states:

$$E = \frac{1}{2}\begin{cases} A - \sqrt{A^2 + 4T^2} & bonding \\ A + \sqrt{A^2 + 4T^2} & anti-bonding \end{cases}. \tag{B.2}$$

In the molecular model, the interface state bandgap E_G is equated to the difference in energy between the bonding and anti-bonding levels. This is only a rough approximation to the actual electronic states, which have reasonable dispersion (~0.5 eV across the Brioullin zone). Since this bandgap has been measured experimentally [Avo89, Hei89], we can solve for the parameter T as a function of A:

$$T = \frac{1}{2}\left[E_G^2 - A^2\right]^{1/2}. \tag{B.3}$$

After the creation of the Ca 2*p* core hole, the interaction between the Ca 3*d* electron and Ca 2*p* hole causes the Ca 3*d* electron to lower its energy by the value Q. This large "collapse" is due to the fact that in Ca, the centrifugal term in the atomic Hamiltonian $l(l+1)/r^2$ gives rise

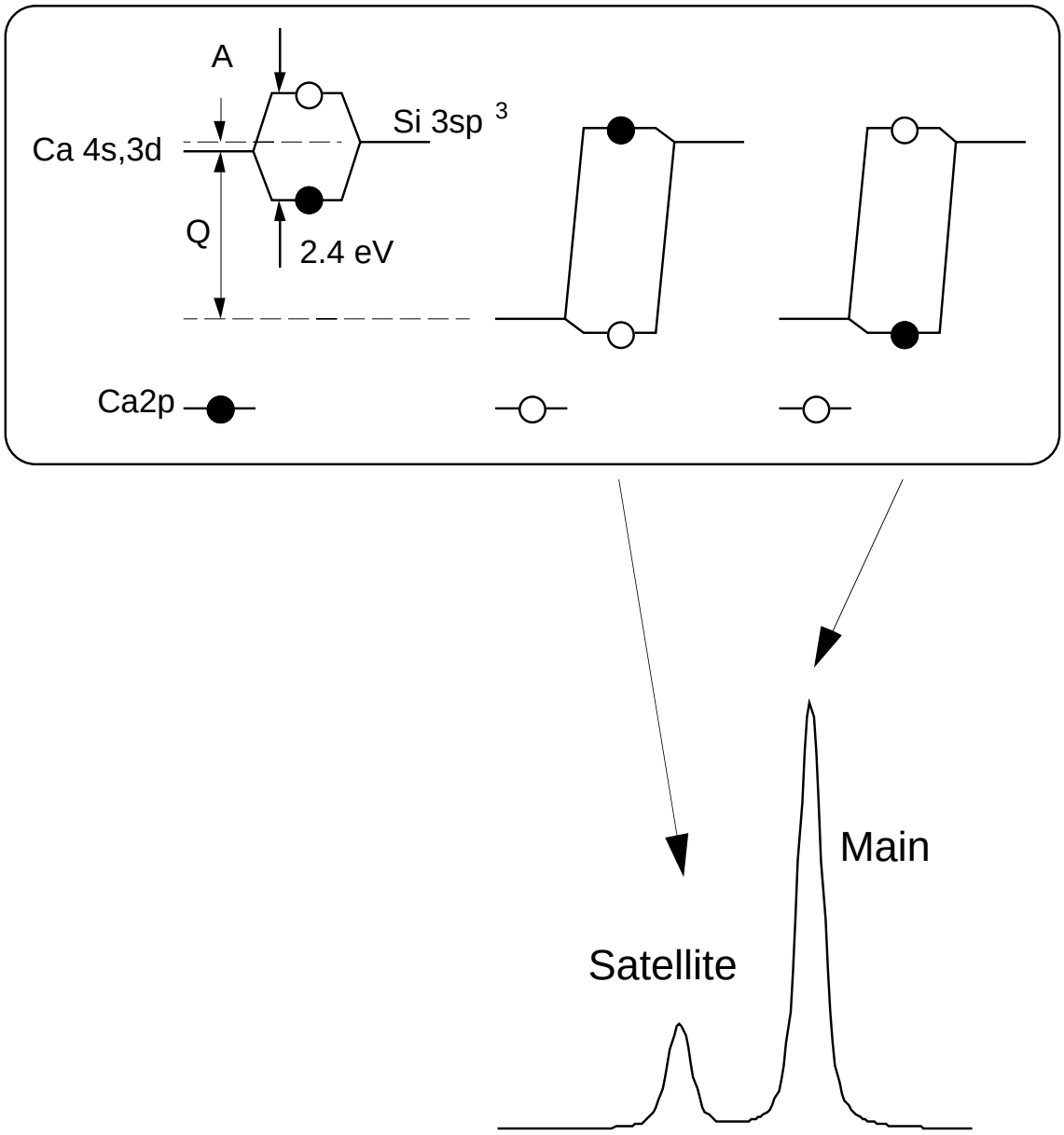

Figure B.05. Energy level diagram in the molecular model. After core-hole creation, the Ca 3d level collapses to lower energy. This creates the possibility of excitation from the 3d-like level to the Si 3p-like level.

to a potential barrier for the 3*d* electron, which acts to keep the 3*d* away from the nucleus. Upon creation of the core hole, the centrifugal barrier is overcome by the attractive force towards the core hole, and the 3*d* level falls in towards the nucleus [Rau68]. A Hartree-Fock calculation by Mansfield [Man76] for atomic Ca gives the value Q=3.75 eV.

After creation of the core hole, then, the interaction Hamiltonian between Ca and Si states becomes

$$H = \begin{pmatrix} A-Q & T_f \\ T_f & 0 \end{pmatrix}, \tag{B.4}$$

where the basis states are still the unperturbed Ca 4*s*/3*d* and Si 3*p* states. The Si 3*p* level is assumed not to change because of the screening of the core hole by the semiconducting substrate. After the core hole is created, the interaction energy becomes T_f. Solution of this equation for the new bonding and anti-bonding energies gives

$$E = \frac{1}{2}\begin{cases} (A-Q) - \sqrt{(A-Q)^2 + 4T_f^2} & bonding \\ (A-Q) + \sqrt{(A-Q)^2 + 4T_f^2} & anti-bonding \end{cases}, \tag{B.5}$$

with energy splitting

$$\Delta E_f = \sqrt{(A-Q)^2 + 4T_f^2}\,. \tag{B.6}$$

The Hamiltonians (B.1) and (B.4) may be solved for the eigenstates as well as the eigenenergies. The normalized eigenstates are

$$\begin{aligned} |i_b\rangle &= \left(1 + (A-E_G)^2/4T^2\right)^{-1/2}\left[\frac{(A-E_G)}{2T}|Ca\rangle + |Si\rangle\right] \\ |f_b\rangle &= \left(1 + (A-Q-\Delta E_f)^2/4T_f^2\right)^{-1/2}\left[\frac{(A-Q-\Delta E_f)}{2T_f}|Ca\rangle + |Si\rangle\right], \\ |f_a\rangle &= \left(1 + (A-Q+\Delta E_f)^2/4T_f^2\right)^{-1/2}\left[\frac{(A-Q+\Delta E_f)}{2T_f}|Ca\rangle + |Si\rangle\right] \end{aligned} \tag{B.7}$$

where $|i_b\rangle$ is the initial state bonding level, and $|f_b\rangle$, $|f_a\rangle$ are the two possible final state bonding and anti-bonding levels. The relative probability of these final states is given by

$$R = \left|\langle f_a|i_b\rangle / \langle f_b|i_b\rangle\right|^2, \tag{B.8}$$

which can be computed directly from (B.7).

Given that T is known from (B.3), and if we assume that T_f=T, then the model contains only two parameters Q and A. The measured quantities are the satellite splitting ΔE_f and the satellite relative magnitude R. We can use the two equations (B.6) and (B.8) to solve for the unknowns Q and A numerically given the two experimental observables. Table B.01 shows results for T_f=T. For CaF_2 we used the interface state bandgap E_G=2.4 eV as measured by Himpsel *et al.* [Him89]. The solution for Q, 3.61 eV, is very close to the predicted value Q=3.75 eV due to Mansfield [Man76]. The solution for A, -0.20 eV, is small as argued above.

For Sr, the model is similar to Ca, except that it is the 5*s*/4*d* state which collapses towards the core hole. Since the bandgap before the core-hole creation is unknown, we have calculated the parameters Q and A for various values of E_G in Table B.01. We find that Q is larger for the Sr 3*p* hole than for the Sr 3*d* hole. This is to be expected if the Sr 3*p* hole is more localized than the Sr 3*d* hole. The parameter A on the other hand, should be independent of core hole, since it characterizes the initial-state bandgap. We find that this is possible for E_G~1.0 eV, at which Q for Sr 3*p* ≈ Q for Ca 2*p*. For this band-gap, A≈-0.6 eV, which is not excessively far from zero. This value of Q implies a relatively weak interaction between the initial Sr 5*s*/4*d* level and the Si dangling bond.

We have also considered the possibility that 0 < T_f< T. This is expected to be the case if the overlap with the Si 3*p* state decreases after the *d* wavefunction collapses. Figure B.06 summarizes the effect of varying T_f. In (a), we see that the values of $Q(x)$ and $A(x)$, where 0 < x=T_f/T < 1 do not take on any unphysical values throughout the entire range of x and indeed do not change drastically with x.

Table B.01. Theoretical results for the molecular model for $T_f = T$. ΔE_f and R are the observed satellite splitting and relative height; E_G is the interface bandgap used in the calculation, and Q, A are the theoretical parameters in Figure B.05.

	Experiment		Bandgap	Theory	
Level	ΔE_f [eV]	R	E_G [eV]	Q [eV]	A [eV]
Ca 2p	4.5	0.25	2.4	3.61	-0.20
Sr 3p	4.5	0.15	1	3.82	-0.61
			2	3.17	-0.70
			3	3.05	-0.32
Sr 3d	3.6	0.15	1	2.94	-0.56
			2	2.51	-0.53
			3	2.45	+0.42

For SrF_2, we must consider both the unknown band gap and the unknown value of x (Figure B.06(b)-(c)). Considering the case x=1 above, we found that the bandgap E_G = 1 made both the Sr 3*p* and Sr 3*d* measurements consistent with each other. We find that E_G = 1 makes the measurements consistent for all $0 < x < 1$ since the $A(x)$ curves are still approximately equal for this bandgap. We conclude that the molecular model gives reasonable values for the parameters Q and A for all values of x for SrF_2.

An assumption in this section has been that the initial state has only two interacting levels, i.e. that the 4*s* and 3*d* levels are nearly degenerate. This is a reasonable assumption considering theoretical calculations that show the band broadening to overlap these two levels [Hea80, Eva89]. But, it is far from clear whether this is reasonable in the final state, since the 3*d* level collapses inwards much more than the 4*s* level. A more refined model would consider interactions of three final states and not two. This would be invoked if the Si 3*p* level has little interaction at all (i.e. $T_f \rightarrow 0$) with the collapsed 3*d* level and that the final state consists

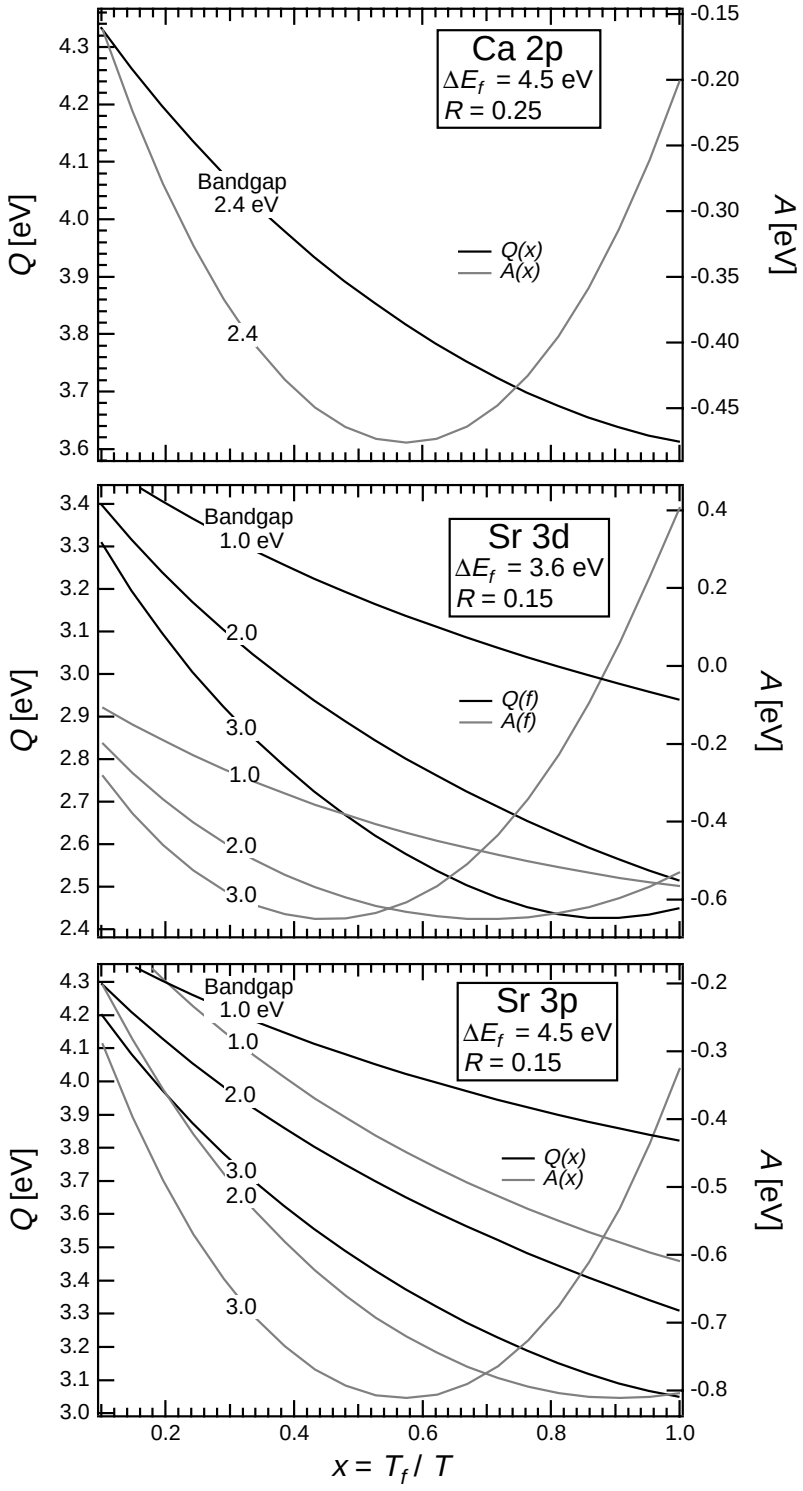

Figure B.06. Theoretical results for the molecular model for $T_f \leq T$. Plotted are the computed Q, A parameters (defined in the text and Figure B.05) for various bandgaps E_G.

of transitions just between $3d \rightarrow 4s$ levels. But if this were the case, there would be very little difference in the physics involved—we would still be considering final-state transitions from a localized $3d$ to a (fairly) delocalized orbital.

B.3 Atomic Model

One question raised by the last model is the extent to which the $3d$ electron is localized in the presence of the core hole. If it is localized too much, perhaps the excitation observed as the loss feature is due to a multiplet interaction between the $3d$ electron and the core hole. Effects of the rest of the solid would then be reduced to weaker crystal-field effects which are secondary in importance to the atomic interactions. In this section we comment on this possibility by analyzing the near-edge x-ray absorption fine structure (NEXAFS) experiment and theoretical calculations of Himpsel *et al.* [Him91]. This experimental technique measures the detailed x-ray absorption edge of the transition Ca $2p \rightarrow$ Ca $3d$ unoccupied states above the Fermi level in CaF_2 on Si(111). The transition is strong because of the Ca $3d$ state's collapse in the presence of the Ca $2p$ core hole, which creates significant overlap between the two wavefunctions. This transition is split for several reasons:

(i) The cubic, eight-fold crystal field splitting in bulk CaF_2 splits the singly-occupied $3d$ level into a triply degenerate t_{2g} manifold and a doubly-degenerate e_g manifold.

(ii) The interaction of the excited $3d$ electron and the vacated $2p$ core hole leads to additional multiplet splitting. Theoretically, the transition from the singlet $2p^6 3d^0$ (J=0) to triplet $2p^5 3d^1$ (J=1) state has three observable lines.

Figure B.07(a) illustrates these effects in the NEXAFS experiment for bulk Ca atoms. In Figure B.07(b), we see the additional effects which occur at the interface. First, the arrangement of ligand electron wavefunctions is different, so that experimentally, Himpsel *et al.* observed the reversal of the order of the e_g and t_{2g} manifolds (as though the cubic environment had become octahedral around the interface Ca atom). Second, the final-state multiplet interaction is different. Before x-ray absorption, the $4s/3d$ orbital is occupied by an

electron. To the outer electrons, the Ca 2*p* hole is localized enough to appear as an extra positive nuclear charge. Therefore, after core hole creation, we expect the outer levels to be arranged as that of Sc^+, in which there is a single occupied 3*d* electron and a single 4*s* electron (this is known as the "Z+1" rule). These two states interact with the core hole to create a range of fine-structure multiplet splittings. Combining crystal-field and atomic multiplet splittings, the interface Ca atom theoretically has 29 observable lines [Him91].

We wish to assess the relative strengths of the two effects, namely crystal field splitting of the 3*d* level *vs.* multiplet interactions between the 3*d* electron/2*p* hole. Himpsel and coworkers' NEXAFS data suggests that for bulk Ca atoms the crystal field splitting and the multiplet splitting become equally unimportant: his absorption data reveal a single sharp peak with small (~5%) satellites of both types distributed < 2 eV from the main absorption line. For the interface Ca atom, however, Himpsel *et al*. found that the crystal-field splitting dominated the observed spectrum: there was a large, barely resolved absorption feature ~25% of the height of the main peak, located ~1 eV to lower photon energy. The satellite strength was accounted for mostly by crystal field splitting only. Both theoretically and experimentally, it was concluded that multiplet splitting was small and that the 3*d* level was delocalized enough so that crystal field splitting could be the only important effect.

Photoemission experiments in bulk CaF_2 are not affected by either crystal field or atomic multiplet splitting because in the final state there is a free electron, not a localized 3*d* electron which can interact with the ligands or the core hole (Figure B.07(c)). However, the presence of the extra Ca 3*d* electron at the interface atom before photoemission can potentially lead to these effects (Figure B.07(d)). In this model, the final state consists of excitations to different perturbed 3*d* states reasonably localized to the interface Ca atom. This is in contrast to the model of the previous section where the excitation was from a hybrid Ca 3*d*/Si 3*p* bonding state to a Ca 3*d*/Si 3*p* anti-bonding state. These two models, the Ca-Si molecular model of the previous section and the atomic model of this section, can be viewed

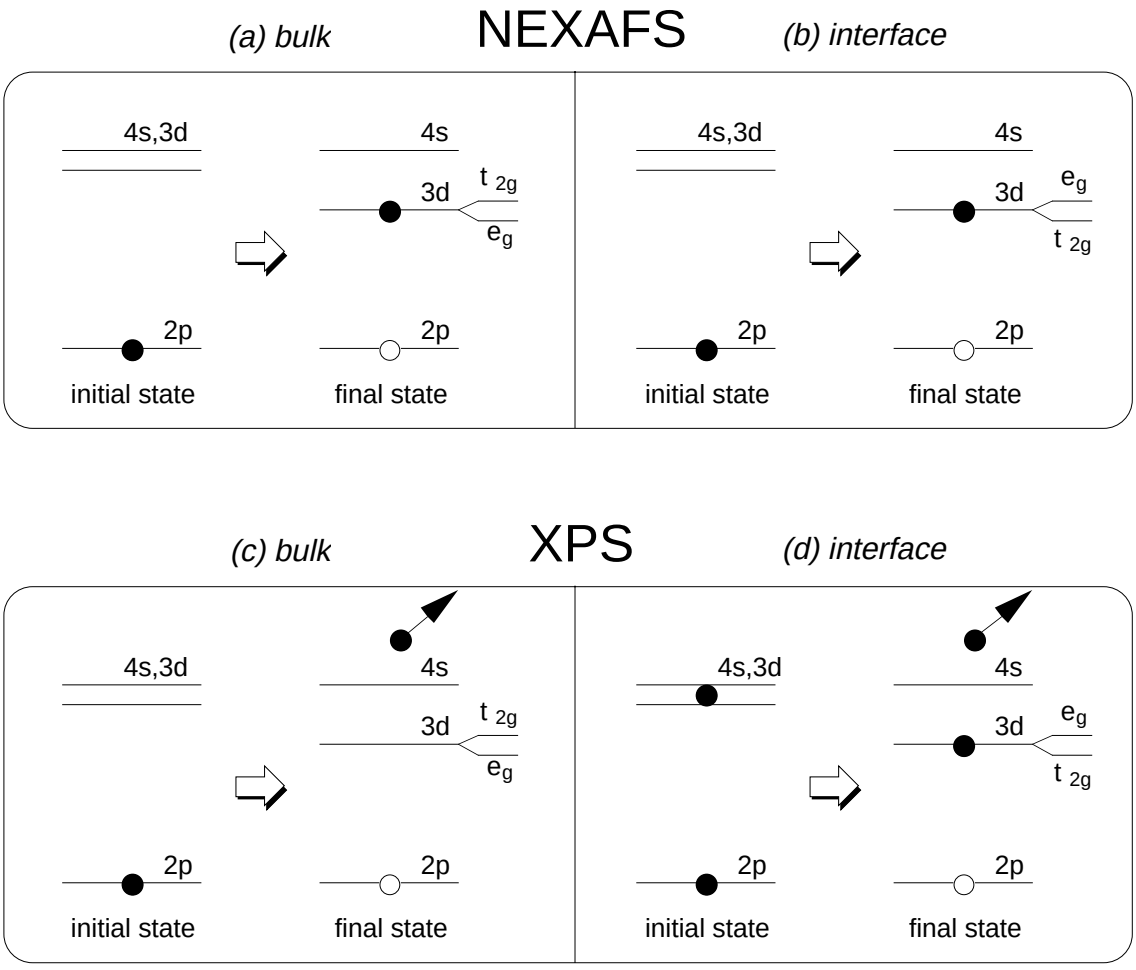

Figure B.07. Comparison of NEXAFS and XPS spectra. Shown are NEXAFS and XPS energy level diagrams for (a, c) bulk and (b, d) interface Ca or Sr atoms at the CaF_2 or SrF_2 on Si(111) interface.

as opposite extremes of possible excitations of the 3*d* electron. In the molecular model, the localized Ca 3*d* electron is transferred towards the Si atom, while in the atomic model, the Ca 3*d* stays localized to the interface Ca atom.

Next, I assess the type of splittings that can occur at the interface atom in photoemission. The crystal field splitting in absorption (B.07(b)) and photoemission (B.07(d)) should be the same, since the local interfaces structures in the Himpsel *et al.* experiment and in ours should be the same. If the atomic multiplet splitting were a concern, we would be concerned with the final state in B.07(a), which is closer to that in (d) as far as the electron configuration is concerned. But we have already seen that the multiplet coupling is not strong enough to account for any strong satellite features, so we only consider the crystal field splitting. But here, too, we must consider the crystal field splitting to be an unlikely cause of our observed satellite. The main reason is that although the splitting leads to a peak of strong enough magnitude to account for our data, the shift (~1 eV) is much smaller than the observed shifts in our photoemission spectra (~3.5-4.5 eV).

B.4 Dielectric Response Model

We now consider a simple model for the satellite peaks that approaches the problem from the point of view of extrinsic losses. Although we have already demonstrated that the loss features are most likely intrinsic excitations, this model is attractive because it is conceptually simple, and because it relates directly to an existing measurement of the interface dielectric response [Him89]. Also, it is difficult to characterize this model as being purely "extrinsic" since the dielectric response of a two-dimensional state very near to the core-hole is being probed, and may in fact be a modified response because of the core hole's presence.

First, we consider what is known about the interface electronic structure as illustrated in Figure B.08. The valence band dispersion was measured with angle-resolved photoemission, and the width of the band was $W_v \approx 0.6$ eV [Mcl89]. The bottom of the conduction

band is $E_G \approx 2.4$ eV above the valence band, as measured with second harmonic generation (SHG) by Heinz *et al.* [Hei89] and scanning tunnelling spectroscopy [Avo89]. The conduction band has been calculated to curve upward [Sal91, Oss91]. An experimental measurement using inverse photoemission [Bou92] found a conduction band that curved *downwards* although this result is called into question by the vulnerability of the CaF_2 films to electron damage during the experiment. We will then assume the simple band structure illustrated in Figure B.08, with a conduction band width W_c.

The imaginary part of the dielectric function ε_2 is proportional to the joint density of states (JDOS) [Coh88 and references therein]. The JDOS for parabolic bands in two dimensions is constant; for the interface bands at the CaF_2/Si(111) interface, the JDOS is plotted in Figure B.09(a). We assumed a total width of $W_c + W_v = 2.2$ eV. In addition to determining the band gap E_G, the SHG experiment also found a two-dimensional exciton resonance ~150 meV below the two-dimensional bandgap E_G. We have for completeness

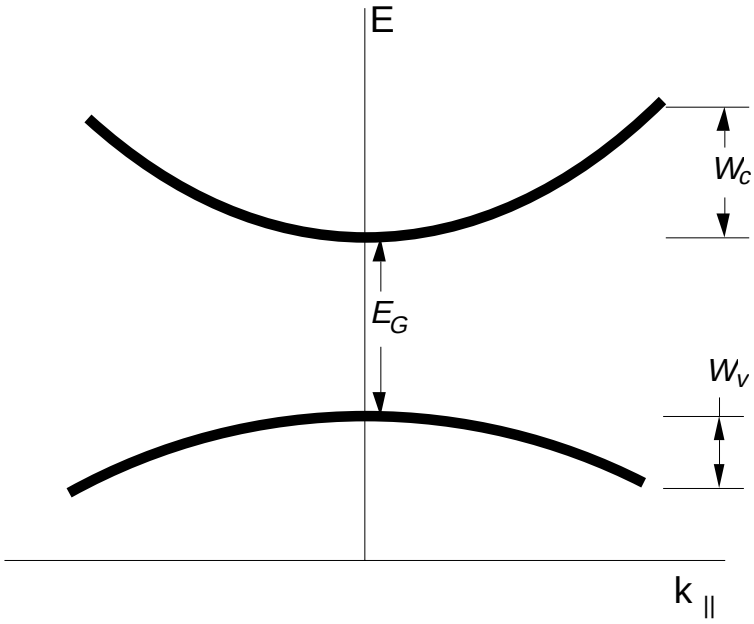

Figure B.08. Interface state band structure for CaF_2 on Si(111). The diagram is schematic and approximates the hexagonal Brillouin zone as circular.

included this resonance as a sharp peak preceding the square JDOS. From this composite function, we can determine the real part of the dielectric function ε_1 using the Kramers-Kronig relationship; this function is plotted in Figure B.09(b).

SHG and electron loss spectroscopy both probe the complex dielectric function. The SHG spectrum is proportional to $|\chi^{(2)}(\omega)|$, the absolute value of the second-order susceptibility tensor [She84]. This quantity was assumed by Heinz *et al.* to be proportional to $|\varepsilon(\omega)|$, which is plotted in B.09(c); this function peaks near the leading edge of the absorption and adequately describes the observed SHG data.

Within this model, the inelastic loss spectrum observed in photoemission is proportional to the quantity Im $\varepsilon(\omega)^{-1}$. As discussed in chapter 4, this function describes the inelastic scattering spectrum for electrons travelling through a medium and is plotted in Figure B.09(d). After convoluting this function with a simulated core-level peak, we arrive at a predicted lineshape (B.09(d)) which compares favorably with the experimental observation for interface Ca 2*p* spectra (B.09(e)). Presumably similar agreement could be obtained for SrF_2/Si(111) data if the interface band structure in that system were known, except that this model would not explain the different splittings for Sr 3*d* and 3*p* satellites.

B. 5 Critique of Models

Table B.02 summarizes the pros and cons of the models discussed in this section. The molecular model accounts for the observed shifts with reasonable parameters. Not only is the relative magnitude explained, but the different shifts for various Sr core levels may also be understood. Furthermore, the molecular model has seen success in application to other transition metal halides, where the *d-d* interactions are more complicated [e.g. Deb84]. One concern is the simplification of the model to just two levels—although this would seem warranted by the data which presents just two peaks. Another concern is that for consistent results among Sr core levels, it was assumed that the Sr-Si interface state band gap was quite small (~1 eV) which is less than half the gap in the case of Ca-Si. This may be a minor

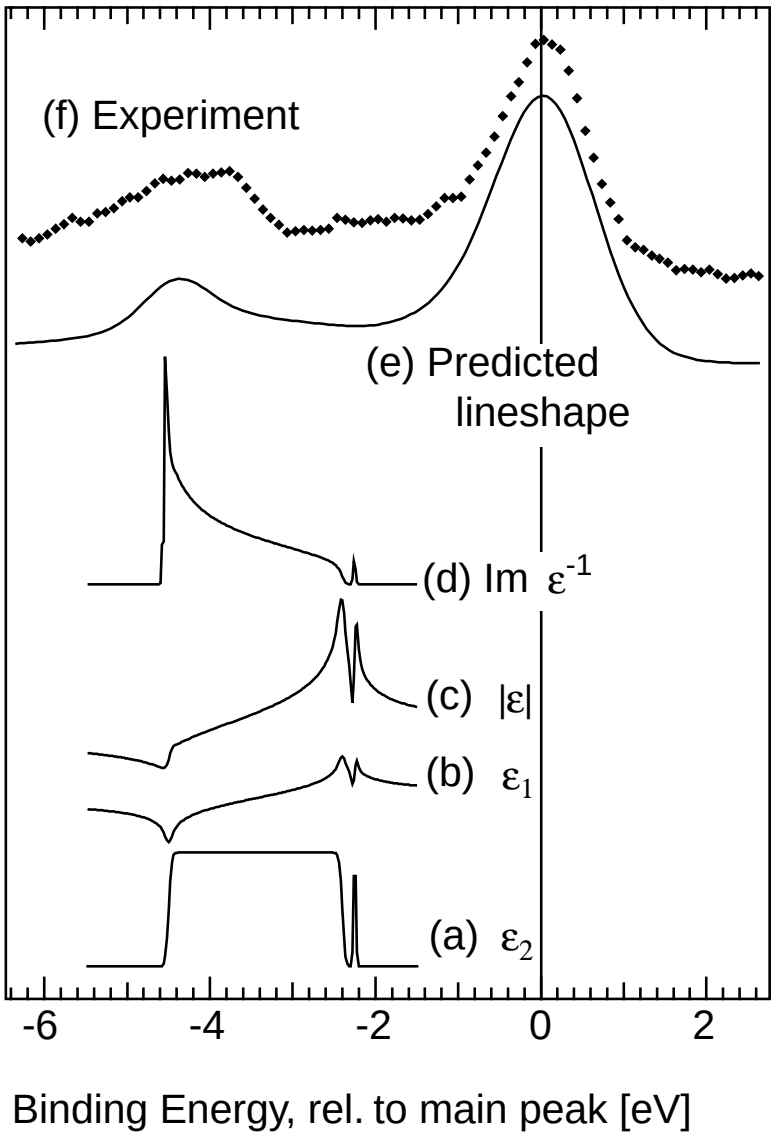

Figure B.09. Dielectric response functions for the CaF2/Si (111) inteface state. (a-b) Complex dielectric function $\varepsilon=\varepsilon_1+i\varepsilon_2$. (c) $|\varepsilon| \propto$ second harmonic generation spectrum, (d) Im $\varepsilon^{-1} \propto$ electron energy loss spectrum.

concern, since the bulk SrF2 band gap is also less than the bulk CaF_2 band gap by ~1 eV. Therefore, we favor the molecular model over the other models in this Appendix.

The atomic model presents two different possible explanations, both of which are perturbations on the *d* electron wave function: *p*/*d* multiplet splitting and crystal-field splitting. These effects explain the NEXAFS data [Him89] well, but the predicted satellites have either too small a shift or too small a magnitude. One open question remains as to why our large satellite feature was not seen in the NEXAFS spectra.

The dielectric response model explains the interface Ca 2*p* lineshape, but fails to account for the different splittings observed among the Sr core levels. Furthermore, the model predicts that Si core levels should have the same satellite feature, since these electrons necessarily pass through the same interface layer with similar (1150 *vs.* 900 eV) kinetic energy.

Table B.02. Comparison of various models for interface satellite peaks.

	PRO	**CON**
Molecular Model	Reasonable numerical values Larger splitting for deeper core holes Intrinsic to Ca atom--predicts no Si or F losses	Predicts small Sr-Si interface state bandgap
Atomic Model (Multiplet/Crystal Field)	Explains NEXAFS data	Multiplet satellites are too weak Crystal-field satellites have too small a shift
Dielectric Response Model	Reasonable numerical values Predicts no F loss peaks	Predicts Si loss peaks Predicts same shift for all Sr core levels

Appendix C

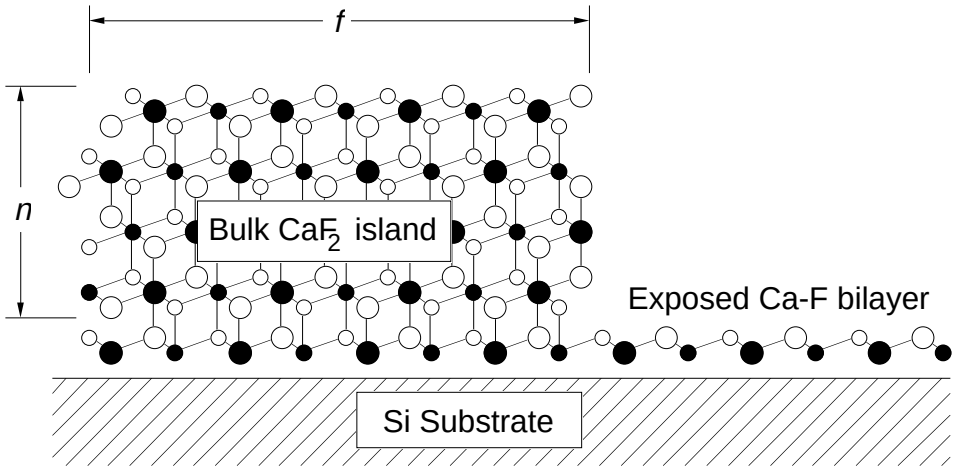

Figure C.01. Simplified island morphology. CaF_2 or SrF_2 films consist of islands atop a reacted Si-Ca-F or Si-Sr-F bilayer. *n*=average island thickness, *f*=total coverage (~0=highly islanded, ~1=completely flat film). In the example shown, *n*=4 and *f*≈0.6.

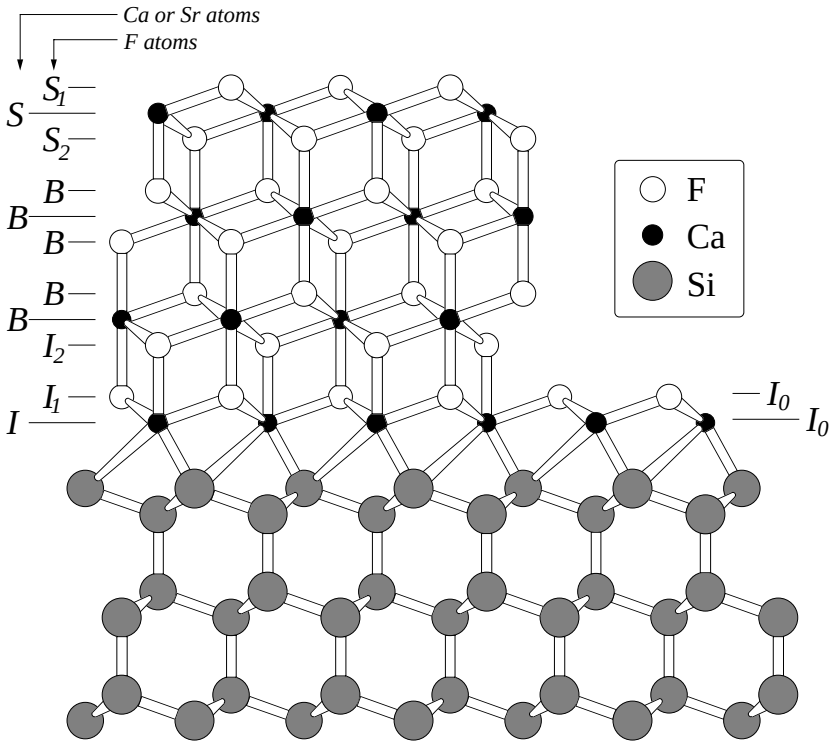

Figure C.02. Labelling convention for Ca (or Sr) and F atoms. The exposed interface atoms are designated with a subscript zero to distinguish them from atoms in the island.

Table C.01. CaF_2 on Si(111) sample growth summary. The morphology is defined by the parameters *n* and *f*, where *n* is the island height and *f* is the fractional coverage of the interface layer due to islands. The total coverage is $N=1+nf$.

Sample			Growth			Morphology		
#	Notes	Fermi Level [eV]	time [s]	flux [Å/min]	Temp [°C]	*f*	*n* [TL]	*N* [TL]
2/3/91		5.46	10	36	750	0.32	2.6	1.8
2/5/91		5.35	8.5	36	750	0.21	1.6	1.3
3/1/91		"	15	36	750	0.41	3.3	2.4
3/3/91		"	20	36	750	0.62	3.9	3.4
7/2/91	SSRL		9	38	750			
9/1/91		4.36						
10/3/91		3.28	180	6	775	0.5	6.8	4.4
10/4/91		"	120	6	775	0.42	5	3.1
1/1/92		"	90	5	<200	0.94	1.8	2.7
3/1/92		"	90	5	600	0.37	4.3	2.6
3/2/92		"	75	5	450	1	1.5	2.6
3/4/92		3.16	30	5	450	0.2	1	0.8
3/5/92		"	20	5	450	0.1	1	0.5
4/7/92	TEM, r	"	960	5	775			
6/4/92		"	12	50	450	1.3	2.5	4.6
6/5/92		"	8	50	700	0.75	2	2.5
		"						
7/1/92		3.15	75	5	750	0.35	2.2	1.8
7/2/92		"	10	36	750			
7/3/92	TEM	"	60	52	750			
7/4/92		"	6	52	750	0.32	2.3	1.8
8/1/92		3.5	8	50	700	0.58	2.1	2.3
8/2/92		"	105	5	450	1.1	2.1	3.4
9/1/92		"	15	52	700	0.95	3.3	4.1
9/2/92		"	11	52	700	0.82	2.3	2.9
9/3/92		"	8	50	650	0.81	1.7	2.4
9/4/92		"	3	110	700	0.52	2	2.1
10/1/92		"	3	110	600	1.2	1.6	2.9
10/2/92		"	3	50	700			8
11/3/92		"	11	50	700			3
2/2/93	miscut	"	54	52	700			
5/1/93		"	30	51	300			
5/4/93	(metal)	"	15	52	650			
5/4b/93	SrCap	"	16	21	400			
6/1/93	holo	"	30	52	650			
6/2/93	templ	"	15	52	650			
		"	15	52	300			
6/3/93		"	15	52	650			
6/3b/93	SrCap	"	15	26	400			
7/2/93		"	15	52	650			
7/2b/93	SiCap	"	300	2	300			
7/3/93		"	52	15	650			
6/15/92	LBL	· · ·	12	30	720	0.24	2.7	1.6
7/13/92	LBL	· · ·	32	30	720	0.88	4.8	5.2
7/14/92	LBL	· · ·	24	30	720	0.45	3.9	2.8

Notes: **holo**=CaF_2 hologram data, **LBL**=grown/characterized at LBL, **r**=re-evaporation regime, **SiCap**=capped sample with Si, **SrCap**=capped sample with SrF_2, **SSRL**=grown/characterized at SSRL, **templ**="template" growth method.

Table C.02. SrF_2 on Si(111) sample growth summary. Types-*A* and -*B* orientation are rotated either 0° or 180° about the [111] axis relative to the Si substrate. LEED=low energy electron diffraction.

	Growth			Structure	
Sample	time [s]	flux [Å/m]	temp. [°C]	Orientation	LEED
7/14/91	60	6	750	———	———
11/1/91	120	50	775	B[a]	———
11/2/91	120	5	750	B[a]	———
11/5/91	180	5	750	A+B	1×1 + 1×1[b]
10/3/92	5	34	700	A?	5×1
11/0/92	8	34	700	———	5×1 + 1×1[b]
11/1/92	8	33	RT[c]	A+B	fuzzy 1×1
11/2/92	8	34	700	B	5×1 + rosettes + 1×1[b]?
3/1/93 [d]	96	42	400	———	fuzzy 1×1
3/2/93	15	52	700	B	1×1 + 1×1[b]
3/3/93	81	52	450	B	———

[a]Determined from $\phi = 0°$ XPD only
[b]Second set of LEED spots with ~7% larger lattice constant
[c]Uncalibrated temperature, probably 25°C < T < 300°C
[d]4°-miscut Si(111) wafer

References

Alv92 J. C. Alvarez, K. Hirano, A. Yu Kazimirov, M. V. Kovalchuk, A. Ya Kreines, N. S. Sokolov, and N. L. Yakovlev, Semicond. Sci. Technol. 7, 1431 (1992).

Arm67 B. H. Armstrong, J. Quant. Spectrosc. Radiat. Transfer 7, 61 (1967).

Asa83 T. Asano and H. Ishiwara, Appl. Phys. Lett. **42**, 517 (1983).

Asa83b T. Asano, H. Ishiwara, and N. Kaifu, Jpn. J. Appl. Phys. **22**, 1474 (1983).

Asa83 T. Asano, H. Ishiwara, and N. Kaifu, Jap. J. Appl. Phys. **22**, 1474 (1983).

Ash81 J. C. Ashley and V. E. Anderson, J. Electron Spectr. and Rel. Phenom. **52**, 285 (1990).

Avo89 Ph. Avouris and R. Wolkow, Appl. Phys. Lett. **55**, 1074 (1989).

Bar88 J. J. Barton, Phys. Rev. Lett. 61, 1356 (1988).

Bar92 J. J. Barton and L. J. TerminelloPhys. Rev. B **46**, 13548 (1992).

Bar93 N. C. Bartelt, T. L. Einstein, E. D. Williams, J.-J. Métois, J. C. Heyraud, C. Alfonso, and J. M. Bermond, Bull. Amer. Phys. Soc. **38**, 567 (1993).

Bat88 J. L. Batstone, J. M. Phillips, and E. C. Hunke, Phys. Rev. Lett, **60**, 1394 (1988).

Bec81 F. Bechstedt and K. Hübner, Phys. Stat. Sol. (a)**67**, 517 (1981).

Bec82 F. Bechstedt, Phys. Stat. Sol. (b)**112**, 9 (1982).

Ben90 H. Bender, Surf. Interface Anal. **15**, 767 (1990).

Blu63 G. D. Blue, J. W. Green, R. G. Bautista, J. L. Margrave, J. Chem. Phys. **67**, 877 (1963).

Bri77 *Handbook of X-ray and Ultraviolet Photoelectron Spectroscopy*, edited by D. Briggs (Philadelphia: Heyden, 1977).

Bri83 D. Briggs and M. P. Seah, *Practical Surface Analysis by Auger and X-reay Photoelectron Spectroscopy* (New York: John Wiley, 1983).

Bro78 F. C. Brown, R. Z. Bachrach, and N. Lien, Nucl. Instrum. Methods **152**,

73 (1978).

Bro88 R. Browning, M. A. Sobolewski, and C. R. Helms, Phys. Rev. B **38**, 13407 (1988).

Cad80 P. Cadman and G. M. Gossedge, J. Electron Spectr. and Rel. Phenom. 18, 161 (1980).

Car78 *Photoemission in Solids I: General Principles*, edited by M. Cardona and L. Ley (New York: Springer, 1978).

Car78b M. Cardona and L. Ley, in *Photoemission in Solids I: General Principles*, edited by M. Cardona and L. Ley (New York: Springer, 1978).

Cat82 C. R. A. Catlow, M. Dixon, and W. C. Mackrodt, in *Computer Simulation of Solids*, edited by C. R. A. Catlow and W. C. Mackrodt (Berlin: Springer, 1982).

Cha76 D. Chattarji, *The Theory of Auger Transitions* (New York: Academic Press, 1976).

Cha91 S. A. Chambers, Advances in Physics, 1991 40, 357 (1991).

Che92 J. Chevrier, Le Thanh Vinh, and A. Cruz, Surface Science Letters **268**(1-3), L261-266 (1992).

Chi86 T. C. Chiang, G. Kaindl, and T. Mandel, Phys. Rev. B **33**, 695 (1986).

Cho91 C. C. Cho and H. Y. Liu, Mat. Res. Symp. **221**, 87 (1991).

Cho92 C. C. Cho, T. S. Kim, B. E. Gnade, and H. Y. Liu, Appl. Phys. Lett. **60**, 338 (1992).

Cit72 P. H. Citrin and T. D. Thomas, J. Chem. Phys. **57**, 4446 (1972).

Cit83a P. H. Citrin, G. K. Wertheim, and Y. Baer, Phys. Rev. B **27**, 3160 (1983).

Cit83b P. H. Citrin, and G. K. Wertheim, Phys. Rev. B **27**, 3176 (1983).

Coh88 M. L. Cohen and J. R. Chelikowsky, *Electronic Structure and Optical Properties of Semiconductors* (New York: Springer-Verlag, 1988).

Con51 E. U. Condon and G. H. Shortley, *The Theory of Atomic Spectra* (UK: Cambridge University Press, 1951).

Cou90 R. Courths, J. Noffke, H. Wern, and R. Heise, Phys. Rev. B **42**, 9127 (1990).

Die92 P. Dietz, C. A. Ramos, and P. K. Hansma, J. Vac. Sci. Technol. B **10**, 741 (1992).

Dol90 C.M. Doland and R. J. Nemanich, J. Mater. Res. **5**(12), 2854 (1990).

Don70 S. Doniach and M. Sunjic, J. Phys. C: Solid St. Phys. **3**, 285 (1970).

Deb84 D. K. G. de Boer, C. Haas, and G. A. Sawatzky, Phys. Rev. B **29**, 4401 (1984).

Den91 J. D. Denlinger, M. A. Olmstead, E. Rotenberg, J. R. Patel, and E. Fontes, Phys. Rev. B **43**, 7335 (1991).

Den93 J. D. Denlinger, PhD Thesis, University of California, Berkeley 1993.

Den93b J. D. Denlinger, Eli Rotenberg, Uwe Hessinger, M. Leskovar, and M. A. Olmstead, Appl. Phys. Lett. 62, 2057 (1993).

Den93c J. D. Denlinger, Eli Rotenberg, Uwe Hessinger, M. Leskovar, and M. A. Olmstead, in *Common Themes and Mechanisms of Epitaxial Growth (Proceedings of the Spring 1993 meeting, San Francisco, CA)*, P. Fuoss, J. Tsao, D. W. Kisker, A. Zangwill, and T. F. Kuech (Pittsburgh: MRS, 1993).

Die92 P. Dietz, C. A. Ramos and P. K. Hansma, J. Vac. Sci. Technol. B **10**(2), 741 (1992).

Dra76 S. R. Drayson, J. Quant. Spectrosc. Radiat. Transfer **16**, 611 (1976).

Ege87 W. F. Egelhoff, Jr., Surf. Sci. Reports **6**, 253 (1987).

Ege90 W. F. Egelhoff, Jr., CRC Crit. Rev. Sol. State Matl. Sci. **16**, 213 (1990).

Eva89 R. A. Evarestov, I. V. Murin, and A. V. Petrov, J. Phys:Condens. Matter **1**,6603 (1989).

Fad68 C. S. Fadley, S. B. G. Hagstrom, M. P. Klein, and D. A. Shirley, J. Chem. Phys. **48**, 3779 (1968).

Fli75 R. Flitsch and S. I. Raider J. Vacuum Sci. Technol. **12**, 305(1975).

Fri90 D. J. Friedman and C. S. Fadley, J. Electr. Spectr. and Rel. Phen. **51**, 689 (1990).

Fuj89 H. Fujitani and S. Asano, Phys. Rev. B **40**, 8357 (1989).

Gre92 T. Greber, J. Osterwalder, D. Naumovic, A. Stuck et al., Phys. Rev. Lett., 69, 1947 (1992).

Has85 S. Hashimoto, J.-L. Peng, W. M. Gibson, L. J. Schowalter, and R. W. Fathauer, Appl. Phys. Lett. **47**, 1071 (1985).

Hea80 R. A. Heaton and C. C. Lin, Phys. Rev. B **22**, 3629 (1988).

Hei89 T. F. Heinz, F. J. Himpsel, E. Palange, and E. Burstein, Phys. Rev. Lett. **63**, 644 (1989).

Hel66 K. H. Hellwege and A. M. Hellwege, eds. *Landolt-Börnstein Numerical Data and Functional Relationships in Science and Technology*, v.III/1 (Berlin: Springer, 1966), Section 1.2.

Hes94 U. Hessinger, J. D. Denlinger, E. Rotenberg, M. Leskovar, and M. A. Olmstead, to be published.

Hil76 J. M. Hill, D. G. Royce, C. S. Fadley, L. F. Wagner, and F. J. Grunthaner, Chem. Phys. Letters **44**, 225 (1976).

Him81 F. J. Himpsel, D. E. Eastman, P. Heimann, B. Reihl, C. W. White, and D. M. Zehner, Phys. Rev. B **24**,1120 (1981).

Him83 F. J. Himpsel, G. Hollinger, and R. A. Pollack, Phys. Rev. B **28**, 7014 (1983).

Him86 F. J. Himpsel, U. O. Karlsson, J. F. Morar, D. Rieger, and J. A. Yarmoff, Phys. Rev. Lett. **56**, 1497 (1986).

Him88 F. J. Himpsel, F. R. McFeely, A. Taleb-Ibrahimi, J. A. Yarmoff, and G. Hollinger, Physical Review B **38**, 6084 (1988).

Him89 F. J. Himpsel, T. F. Heinz, A. B. McLean, E. Palange, and E. Burstein, J. Vac. Sci. Technol. B 7(4), 879 (1989).

Him91 F. J. Himpsel, U. O. Karlsson, A. B. McLean, L. J. Terminello, F. M. F. de Groot, M. Abbate, J. C. Fuggle, J. A. Yarmoff, B. T. Thole, and G. A. Sawatzky, Phys. Rev. B **43**, 6899 (1991).

Hin88 V. Hinkel, L. Sorba, and K. Horn, Surf. Sci. **194**, 597 (1988).

Ho67 P. L. Ho and A. L. Ruoff, Phys. Rev. **161**, 864 (1967).

Hoh85 G. Hohlneicher and H. Plum, J. Electron Spectrosc. Relat. Phenom. **37**, 209 (1985).

Hon93 Y. Hong and T. R. Dillingham, J. Vac. Sci. Technol. A **11**(4), 2298 (1993).

Hud93 L. T. Hudson, R. L. Kurtz, S. W. Robey, D. Temple, and R. L. Stockbauer, Phys. Rev. B **47**, 10832 (1993).

Ike77 I. Ikemoto, K. Ishii, S. Kinoshita, and H. Kuroda, J. Electron Spectrosc. Relat. Phenom. **11**, 251 (1977).

Ish79 A. Ishizaka, S. Iwata, and Y. Kamigaki Surface Science **84**, 355 (1979).

Ish81 H. Ishiwara and T. Asano, Appl. Phys. Lett. **40**, 66 (1981).

Ish86 A. Ishizaka, and Y. Shiraki, J. Electrochem. Soc. **133**, 666 (1986).

Jab90 A. Jablonski and S. Tougaard, J. Vac. Sci. Technol. **A8**(1), 106 (1990).

Jac82 K. Jacobi and H. H. Rotermund, Surf. Sci **116**, 435 (1982).

Jac86 J. D. Jackson, *Classical Electrodynamics*, 2nd ed. (New York: John Wiley, 1986).

Jac88 K. Jacobi, Phys. Rev. B **38**, 6291 (1988).

Jan89 A. R. Jani, G. S. Tripathi, N. E. Brener, and J. Callaway, Phys. Rev. B **40**, 1593 (1989).

Kao90 C. C. Kao and R. P. Merrill, J. Phys. Chem. Solids **52**, 909 (1991).

Kat91 M. Katayama, B. V. King, E. Nomura, and M. Aono, Vacuum **42**, 321 (1991).

Kit86 C. Kittel, *Introduction to Solid State Physics*, 6th ed. (New York: John Wiley, 1986).

Kla74 M. Klasson, A. Berndtsson, J. Hedman, R. Nilsson, R. Nyholm, and C. Nordling, J. Electron Spectroscopy 3,427 (1974).

Koe74 D. D. Koelling, F. M. Mueller, and B. W. Veal, Phys. Rev. B **10**, 1290 (1974).

Kow92 B. J. Kowalski, J. Phys.:Condes. Matter **4**, 10353 (1992).

Kum89 M. Kumagai and T. Takagahara, Phys. Rev. B **40**, 12359 (1989).

Lan86 L. D. Landau and E. M. Lifshitz, *Theory of Elasticity*, 3rd ed. (UK:Pergammon Press 1986), Chapter 1.

Lan92 E. Landemark, C. J. Karlsson, Y. C. Chao, and R. I. G. Uhrberg, Phys. Rev. Letters **69**(10), 1588 (1992).

Lat91 A. V. Latyshev, A. B. Krasilnikov, A. L. Aseev, L. V. Sokolov, and S. I. Stenin, Surface Science **254**, 90 (1991).

Law88 K. Lawniczak-Jablonska and M. Heinonen, J. Phys. **F18**, 2451 (1988).

Les94 M. Leskovar, E. Rotenberg, M. A. Olmstead, to be published.

Li92 W. Li, A. P. Taylor, and L. J. Schowalter, Mat. Res. Soc. Proc. **263**, 433 (1992).

Liu89 R. Liu, C. G. Olson, A.-B. Yang, C. Gu, D. W. Lynch, A. J. Arko, R. S. List, R. J. Bartlett, B. W. Veal, J. Z. Liu, A. P. Paulikas, and K. Vandervoort, Phys. Rev. B **40**, 2650 (1989).

Lor52 H. A. Lorentz, *Theory of Electrons*, 2nd ed. (New York: Dover, 1952).

Luc92 C. A. Lucas and D. Loretto, Appl. Phys. Lett. **60**, 2071 (1992).

Luc93 C. A. Lucas, G. C. L. Wong, D. Loretto, Phys. Rev. Lett. **70**,1826 (1993).

Luc93b C. A. Lucas and G. C. L. Wong, private communication.

Luc93c C. A. Lucas, G. C. L. Wong, D. Loretto, unpublished.

Mcl89 A. B. McLean and F. J. Himpsel, Phys. Rev. B **39**, 1457 (1989).

Mcl90 A. B. McLean, J. Phys:Condens. Matter **2**, 1027 (1990).

Mah80 G. D. Mahan, Phys. Rev. B **21**, 4791(1980).

Mah91 F. Mahmood, H. Ahmed, M. Suleman, and M. M. Ahmed, Jap. J. Appl. Physics, Part 2 **30**(8A), L1418 (1991).

Mey90 A. K. Myers-Beaghton and D. D. Vvedensky, Phys. Rev. B **42**, 5544 (1990).

Mön86 W. Mönch, Solid State Commun. **58**, 215 (1986).

Mor90 G. Moretti, Surf. Interface Anal. **16**, 159 (1990).

Mot38 N. F. Mott and M. J. Littleton, Trans. Faraday Soc. **34**, 485 (1938).

Mot40 N. F. Mott and R. W. Gurney, *Electronic Processes in Ionic Crystals* (Oxford: Clarendon Press, 1940).

Mus89 J. Mustre de Leon, J. J. Rehr, C. R. Natoli, C. S. Fadley, and J. Osterwalder, Phys. Rev. B **39**, 5632 (1989).

Nat88 K. Nath and A. B. Anderson, Phys. Rev. B **38**, 8264 (1988).

Nyh91 R. Nyholm, J. N. Andersen, J. F. van Acker, and M. Qvarford, Phys. Rev. B **44**, 10987 (1991).

Olm87 M. A. Olmstead, R. I. G. Uhrberg, R. D. Bringans, and R. Z. Bachrach, Phys. Rev. B **35**, 7526 (1987).

Olm90 M. A. Olmstead and R. D. Bringans, Phys. Rev. B **41**, 8420 (1990).

Oss91 S. Ossicini, C. Arcangeli, and O. Bisi, Phys. Rev. B **43**, 9823 (1991).

Pen74 J. B. Pendry, *Low Energy Electron Diffraction: The theory and its application to surface structure* (New York: Academic Press, 1974).

Pen76 D. R. Penn, Phys. Rev. B **13**(12), 5248 (1976).

Pen87 D. R. Penn, Phys, Rev. B **35**(2), 482 (1987).

Pon86 F. A. Ponce, G. B. Anderson, M. A. O'Keefe, and L. J. Schowalter, J. Vac. Sci. Technol. B4, 1121 1986).

Pre86 W. H. Press, B. P. Flannery, S. A. Teukolsky, and W. T. Vetterling, *Numerical Recipes: The Art of Scientific Computing* (Cambridge: Cambridge University Press, 1986), p.418ff.

Pri87 C. Priester, G. Allan, and M. Lannoo, Phys. Rev. Lett. **58**, 1989 (1987).

Rau68 A. R. P. Rau, and U. Fano, Phys. Rev. **168**, 7 (1968).

Rea77 J. M. Reau, C. Lucat, G. Campet, J. Claverie, and J. Portier, Electrochem. Acta **22**, 761 (1977).

Reh91 J. J. Rehr, J. Mustre de Leon, S. I. Zabinsky, and R. C. Albers, J. Am. Chem. Soc. **113**, 5135 (1991).

Rie86 D. Rieger, F. J. Himpsel, U. O. Karlsson, F. R. McFeely, J. F. Morar, and J. A. Yarmoff, Phys. Rev B **34**, 7295 (1986).

Rod90 P. Rodriguez-Hernández and A. Muñoz, J. Electron Spectr. Rel. Phenom. **52**, 155 (1990).

Ros91 N. Rosenberg, M. Tholomier, E. Vicario, and N. Doghmane, Surface Science **254**, 289 (1991).

Rot92 E. Rotenberg and M. A. Olmstead, Phys. Rev. B **46**, 12884 (1992).

Rot93 E. Rotenberg, J. D. Denlinger, Uwe Hessinger, M. Leskovar, and M. A. Olmstead, J. Vac. Sci. Technol. B **11**(4), 1993 (in press).

Rot93b E. Rotenberg, J. D. Denlinger, M. Leskovar, U. Hessinger, and M. A. Olmstead, Phys. Rev. B (submitted).

Sai87 K. Saiki, T. Tokoro, and A, Koma, Jap. J. Appl. Phys. **27**, 1386 (1988).

Sal90 U. Salzner, P. von Ragué Schleyer, Chem. Phys. Lett. **172**, 461 (1990).

Sal91 M. R. Salehpour, S. Satpathy, and G. P. Das, Phys. Rev. B **44**, 8880 (1991).

Sal92 D. K. Saldin, G. R. Harp, B. P. Tonner, Phys. Rev. B **45**, 9629 (1992).

Sat89 S. Satpathy and R. M. Martin, Phys. Rev. B **39**, 8494 (1989).

Sea79 M. P. Seah and W. A. Dench, Surface Interface Anal. **1**, 2 (1979).

Sch85 L. J. Schowalter and R. W. Fathauer, J. Vac. Sci. Tech. **A4**, 1026 (1985).

Sch89 P. A. Schultz and R. P. Messmer, Surf. Sci. **209**, 229 (1989).

Sch89b L. J. Schowalter and R. W. Fathauer, CRC Crit. Rev. Sol. State. Matls. Sci. **15**, 367 (1989).

Sha88 V. M. Shatalov, O. F. Panchenko, O. M. Artamonov, A. G. Vinogradov, and A. N. Terekhov, Solid State Comm. **68**(8), 719 (1988).

She84 Y. R. Shen, *The Principles of Nonlinear Optics* (New York: Wiley, 1984).

Shi78 D. A. Shirley, in *Photoemission in Solids I*, M. Cardona and L. Ley, eds. (New York: Springer, 1978).

Sie67 K. Siegbahn et al., *Atomic, Molecular, and Solid State Structure Studied by Means of Electron Spectroscopy, ESCA* (Uppsala, Sweden: Almqvist and Wiksell, 1967).

Sin90 S. Sinharoy, Thin Solid Films **187**, 231 [1990].

Sob79 I. I. Sobelman, *Atomic Spectra and Radiative Transitions* (Berlin: Springer, 1979).

Sto88 N. G. Stoffel, P. A. Morris, W. A. Bonner, D. LaGraffe, M. Tang, Y. Chang, G. Margaritondo, and M. Onellion, Phys. Rev. B **38**, 213 (1988).

Sze90 L. von Szentpály and P. Schwerdtfeger, Chem. Phys. Lett. **170**, 555 (1990).

Tak85 K. Takayanagi, Y. Yanishiro, M. Takahashi, S. Takahashi, J. Vac. Sci. Technol. A**3**, 1502 (1985).

Tas80 P. W. Tasker, Journal de Physique Colloque **C6**, 488 (1980).

Ter93 L. J. Terminello and J. J. Barton, Bull. Amer. Phys. Soc. **38**(1), 364 (1993).

Tok85 H. Tokutaka, K. Nishimori, and H. Hayashi, Surface Science **149**, 349 (1985).

Tan90 S. Tanuma, C. J. Powell, and D. R. Penn, J. Electron Spectr. and Rel. Phenom. **52**, 285 (1990).

Tes53 J. R. Tessman, A. H. Kahn, and W. Shockley, Phys. Rev. **92**, 890 (1953).

Tof88 A. L. Tofterup, Surface Science **227**, 157 (1990).

Tou88 S. Tougaard, Surf. Interface Anal. **11**, 453 (1988).

Tro88 R. M. Tromp and M. C. Reuter, Phys. Rev. Lett. **61**, 1756 (1988).

Tro93 R. M. Tromp, private communication.

Tsu85 K. Tsutsui, H. Ishiwara, T. Asano, and S. Furukawa, Appl. Phys. Lett. **46**, 1131 (1985).

Väy90 I. J. Väyrynen, J. A. Leiro, and M. H. Heinonen, J. Electron Spectr. and Rel. Phenom. **51**, 555 (1990).

Vos89 M. Vos, F. Xu, and J. H. Weaver, J. Appl. Phys. **66**, 2467 (1989).

Wag75 C. D. Wagner, Faraday Discuss. Chem. Soc. **60**, 291 (1975).

Wan80 J. C. Wang, Phys. Rev. B **22**, 2725 (1980).

Wan84 K. Wandelt and J. E. Hulse, J. Chem. Phys. **80**, 1340 (1984).

Wat81 R. E. Watson, J. W. Davenport, M. L. Perlman, and T. K. Sham, Phys. Rev. B **24**, 1791 (1981).

Wat83 R. E. Watson, J. W. Davenport, Phys. Rev. B **27**, 6418 (1983).

Wat92 M. Watanabe, S. Muratake, T. Suemasu, H. Fujimoto, S. Sakamori, M. Asada, and S. Arai, J. Electronic Materials **21**, 783 (1992).

Wei81 F. Weissman and K. Müller, Surf. Sci. Rep. **105**, 251 (1981).

Whi68 E. E. Whiting, J. Quant. Spectrosc. Radiat. Transfer **8**,1379 (1968).

Wil88 W. G. Wilke, V. Hinkel, W. Theis, and K. Horn, Phys. Rev. B **40**, 9824 (1988).

Won93 G. C. L. Wong, D. Loretto, E. Rotenberg, M. A. Olmstead, and C. A. Lucas, Phys. Rev. B **48** (15 August 1993), in press.

Xu89 F. Xu, M. Vos, and J. H. Weaver, Phys. Rev. B **41**, 8429 (1989).

Zeg90 J. Zegenhagen and J. R. Patel, Phys. Rev. B **41**, 5315 (1990).

Zeg93 J. Zegenhagen, private communication.